Variability and trends of Arctic water vapour from passive microwave satellites
Special role of Polar lows and Atmospheric rivers

Inaugural-Dissertation
zur
Erlangung des Doktorgrades
der Mathematisch-Naturwissenschaftlichen Fakultät
der Universität zu Köln

vorgelegt von
ANA RADOVAN
aus Dugopolje
Köln
2020

Berichterstatter:

Prof. Dr. Susanne Crewell
Prof. Dr. Roel Neggers

Tag der mündlichen Prüfung: 5. Oktober 2020

Abstract

Water in the vapour phase is the most important component of the hydrological cycle. It is formed by processes of evaporation and sublimation during which a lot of energy as latent heat is absorbed from the atmosphere. Through atmospheric large and small scale circulation, this energy is transported and released elsewhere through the process of condensation. Water vapour is the most important greenhouse gas (GHG) due to its abundance and its effectiveness in absorbing longwave radiation. In the light of global climate change, it is of great importance to identify trends of water vapour amounts in the atmosphere and its variability.

Climate change in terms of the near-surface temperature is most pronounced in the Arctic, known as Arctic Amplification. Since most of the Arctic are either open ocean or sea-ice covered surfaces, only sparse ground-based observations, mostly confined to land areas are available. Therefore, one must resort to usage of the satellite based observations which offer a great advantage by their large spatial coverage. For water vapour assessment, passive microwave satellites are well suited due to their ability to sense water vapour under clear and cloudy sky conditions independent of sun light.

A number of products of integrated water vapour (IWV) from various satellites are available. However, these are often inconsistent and prone to have biases due to various assumptions and uncertainties of *a priori* data included in the retrieval algorithms. According to the Clausius-Clapeyron relation, water vapour is constrained by the saturation vapour pressure which is constrained only by the temperature.

Therefore, this thesis investigates the hypothesis that brightness temperatures (T_bs) from spaceborne passive microwave instruments can be used as a proxy for water vapour trends. To test this hypothesis, satellites based T_bs are compared to synthetic T_bs derived from the Arctic System Reanalysis (ASR). To enable the comparison, the ASR has been evaluated in T_b space by employing the Passive and Active Microwave TRAnsfer forward model (PAMTRA). Moreover, T_bs from sounding channels were correlated with corresponding IWV based on the weighted absolute humidity profiles peaks. The hypothesis is tested for the dry, cold and sun-absent winter season (January) and the sun-return transitional spring season (May).

The results show that T_bs from frequency channels can explain trends in the corresponding IWV columns derived from ASR for regions with significant positive trends for both, T_b and IWV since high correlation coefficients, reaching 0.98, have been found. This is true for different time scales, daily, monthly and for the period of 17 years (2000-2016). The exception to this has been found for May for daily time scale for frequency channel dominated by the signal from the upper troposphere lower stratosphere (UTLS). For this combination of T_bs and IWV correlations tend to be weaker and at some locations even negative. This is consistent with theoretical calculations and observational studies which report a cooling in the UTLS region for increasing IWV. However, T_bs from the corresponding channel seem less reliable in explaining trends of the corresponding IWV derived from the ASR. This indicates the importance of other processes relevant in the UTLS region during spring.

Furthermore, this thesis investigates synoptic features which are associated with water vapour transport and precipitation. Previous studies have shown that Arctic cyclone activity during winter has a large impact on the sea ice melt in the following seasons making them important players in the complex feedback mechanism of the climate change in the Arctic. However, the life cycle of the most intense of such cyclones, also known as polar lows (PL) are not yet fully understood. To analyse their dynamics, this thesis investigates different environmental conditions (and their combination) between genesis and maturity stage of January PLs. PLs with overall lower thermal instability between the surface and 500 hPa during formation stage are typically accompanied by higher and steeper lapse rates throughout the boundary layer. Therefore these PLs were fostering convective development. However, as observed for a few cases, a decreased thermal instability alongside a simultaneous decrease of convection coincides with high relative humidity (mostly above 90%). Furthermore, higher relative humidity at lower levels during genesis stage promoted stronger winds at the maturity stage.

Besides water vapour turn over associated with Arctic cyclones, atmospheric rivers (ARs) transport major amounts of moisture from tropical and extratropical regions into the Arctic. Studies have shown that about 90% of the total mid-latitude vertically integrated water vapour transport (IVT) is related to these synoptic features. To study the influence of ARs on PL precipitation, an event with a coupled AR and PL is compared to an event which featured only a PL. The AR had a strong influence on the PL resulting in higher snow amounts on the order of $\sim 4\mathrm{kg/m^2}$ higher wind speeds and a longer distance traveled during its life cycle, compared to the PL only case.

Zusammenfassung

Wasserdampf ist der wichtigste Bestandteil des Wasserkreislaufs. Er entsteht durch Verdampfungs- und Sublimationsprozesse, bei denen viel Energie als latente Wärme aus der Atmosphäre absorbiert wird. Durch groß- und kleinskalige atmosphärische Zirkulation wird die aufgenommene Energie transportiert und an anderer Stelle als Kondensationswärme freigesetzt. Aufgrund seines hohen Vorkommens und seiner starken Absorption langwelliger Strahlung stellt er das wichtigste Treibhausgas dar. Angesichts des globalen Klimawandels ist es somit von großer Bedeutung, Trends des Wasserdampfgehalts in der Atmosphäre und seine Variabilität zu studieren.

In Bezug auf die oberflächennahe Temperatur ist der Klimawandel in der Arktis am stärksten ausgeprägt. Dieses Verhalten wird als arktische Verstärkung bezeichnet. Da es sich bei den meisten Teilen der Arktis entweder um offene Ozean- oder Meereisoberflächen handelt, stehen nur wenige bodengebundene Beobachtungen zur Verfügung, die sich hauptsächlich auf das Festland beschränken. Daher ist es notwendig auf Satellitenfernerkundung zurückzugreifen, die einen großen Vorteil durch die Möglichkeit zur flächendeckenden Erkundung bietet. Für die Erfassung von Wasserdampf eignen sich passive Mikrowellensatelliten aufgrund ihrer Fähigkeit, Wasserdampf sowohl unter klaren als auch unter bewölkten Bedingungen unabhängig vom Sonnenlicht zu detektieren.

Eine Reihe von Produkten basierend auf verschiedenen Satelliten ist für integrierten Wasserdampf (IWV) verfügbar. Diese Produkte sind jedoch häufig inkonsistent und neigen aufgrund verschiedener Annahmen und Unsicherheiten von a priori Daten, die in die Berechnungsalgorithmen einfließen, zu systematischen Fehlern. Gemäß der Clausius-Clapeyron-Gleichung ist Wasserdampf durch den Sättigungsdampfdruck begrenzt, der wiederum nur durch die Temperatur begrenzt ist. Daher untersucht diese Arbeit die Hypothese, dass Helligkeitstemperaturen (T_bs) von satellitengestützten passiven Mikrowelleninstrumenten als Proxy für Wasserdampftrends verwendet werden können. Um diese Hypothese zu testen, werden satellitenbasierte T_bs mit synthetischen T_bs, die aus der sogenannten „Arctic System Reanalysis“ (ASR, Reanalyse des arktischen Systems) abgeleitet werden, verglichen. Um den Vergleich zu ermöglichen, wurde die ASR im T_b-Raum unter Verwendung des Vorwärtsoperator „Passive and Active Microwave TRAnsfer“ (PAMTRA) ausgewertet. Darüber hinaus werden T_bs aus verschiedenen Spektralkanälen mit dem entsprechenden IWV gemäß gewichteter Peaks in Profilen der absoluten Feuchtigkeit korreliert. Die Hypothese wird für die durch die Abwesenheit der Sonne geprägte, kalte und trockene Wintersaison (Januar) und für die vorsommerliche, unter Einfluss von Sonnenstrahlung stehende Übergangsjahreszeit (Mai) getestet.

Die Ergebnisse zeigen, dass T_bs von Spektralkanälen, die vom Signal aus der unteren Troposphäre dominiert werden, Trends in den entsprechenden IWV-Säulen, die von der ASR abgeleitet wurden, für Regionen mit signifikanten positiven Trends für T_b und IWV erklären können, da ein hoher Korrelationskoeffizient von 0,98 festgestellt werden konnte. Für Mai zeigt der Spektralkanal, der vom Signal der oberen

Troposphäre und unteren Stratosphäre (UTLS) dominiert wird, eine schwächere und negative Korrelation zwischen T_bs und IWV. Dies steht im Einklang mit theoretischen Berechnungen und Beobachtungsstudien, die eine Abkühlung in der UTLS-Region für erhöhten IWV berichten. T_bs aus dem entsprechenden Kanal scheinen jedoch weniger zuverlässig bei der Erklärung von Trends des entsprechenden IWV zu sein, der aus der ASR abgeleitet wurde. Dies ist ein Zeichen für die Bedeutung anderer Prozesse, die im Frühjahr in der UTLS-Region relevant sind.

Darüber hinaus untersucht diese Arbeit synoptische Phänomene, die mit Wasserdampftransport und Niederschlag verbunden sind. Frühere Studien haben gezeigt, dass die Aktivität arktischer Zyklonen im Winter einen großen Einfluss auf die Meereisschmelze in den folgenden Jahreszeiten hat, was sie zu wichtigen Akteuren im komplexen Rückkopplungsmechanismus des Klimawandels in der Arktis macht. Der Lebenszyklus der intensivsten Zyklonen, die auch als Polar Lows (PL) bekannt sind, ist jedoch noch nicht vollständig geklärt. Um ihre Dynamik zu analysieren, untersucht diese Arbeit verschiedene Umgebungsbedingungen (und ihre Kombination) zwischen Genese und ausgereiften Stadium der im Januar auftretenden PLs. Es zeigt sich, dass PLs, die insgesamt eine geringere thermische Instabilität zwischen der Oberfläche und 500 hPa während ihrer Bildungsphase aufweisen, typischerweise mit höheren und steileren atmosphärischen Temperaturgradienten in der gesamten Grenzschicht einhergehen. So förderten diese PLs eine konvektive Entwicklung. Wie in einigen Fällen beobachtet, tritt jedoch eine verminderte thermische Instabilität bei gleichzeitiger Abnahme der Konvektion simultan mit einer hohen relativen Luftfeuchtigkeit (meist über 90%) in Erscheinung. Darüber hinaus begünstigte eine höhere relative Luftfeuchtigkeit in den unteren Schichten während der Zyklogenese stärkere Winde der vollständig entwickelten Zyklone.

Neben der Wasserdampffluktuation in Verbindung mit arktischen Zyklonen transportieren sogenannte „atmospheric rivers“ (ARs, atmosphärische Flüsse) große Mengen an Feuchtigkeit aus tropischen und extratropischen Regionen in die Arktis. Studien haben gezeigt, dass etwa 90% des gesamten vertikal integrierten Wasserdampftransports (IVT) in mittleren Breitengraden mit diesen synoptischen Systemen zusammenhängen. Um den Einfluss von ARs auf den Niederschlag durch PLs zu untersuchen, wird in einer Fallstudie ein an einen AR gekoppeltes PL mit einem einzeln auftretenden PL verglichen. Der AR hatte einen starken Einfluss auf das PL, sodass größere Schneemengen in der Größenordnung von $\sim 4\text{kg/m}^2$, höhere Windgeschwindigkeiten und eine längere zurückgelegte Strecke während seines Lebenszyklus festgestellt werden konnten im Vergleich mit dem einzeln auftretenden PL.

Contents

1 Introduction

1.1 Water vapour

Water vapour is the component of the hydrological cycle (Figure 1.1) that comes in the gaseous form. This enables it to travel fast through the atmosphere, governed by the atmospheric motions, redistributing energy in the form of latent heat from one place to another. In that way, as an important part of the atmospheric dynamics it influences the global circulation and climate. Although its amount in the atmosphere is only 0.25 % on average (Stevens and Bony, 2013; Fionda et al., 2019) without it, the life as we know it, would not be possible.

Depending on the environmental conditions (temperature and pressure), water vapour will condense to form clouds and subsequently precipitation, or it will be released by either evaporation or sublimation. Through these processes the energy in the form of latent heat is either absorbed (evaporation and sublimation) or released (condensation).

The process of condensation, is controlled by the saturation water vapour pressure, e_s which is controlled only by the temperature. This means that at higher temperatures, the molecules of water are gaining more kinetic energy and are having higher probability to break the hydrogen bonds and „escape“ the liquid or solid state. Generally, this is what is meant by "warmer air will be able to hold more water vapour" often found in textbooks. The relation between saturation vapour pressure and the

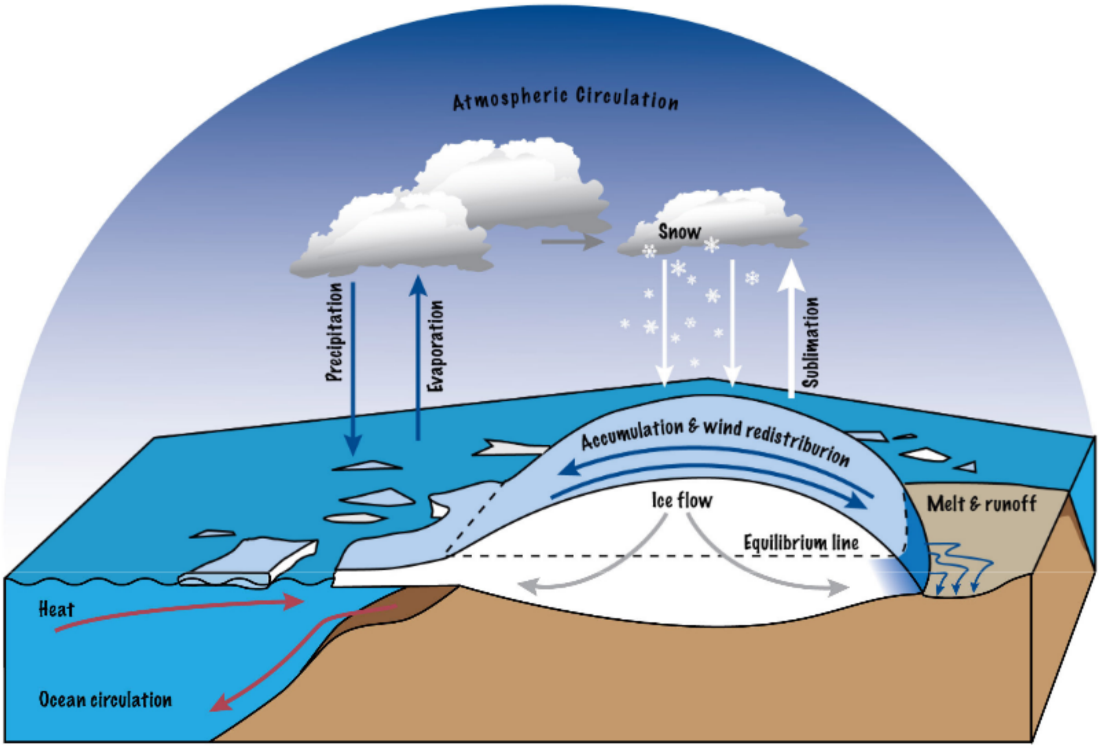

Figure 1.1: *Scheme of hydrological cycle in the Arctic taken from http://geography.exeter.ac.uk/opensource/cryosphere/*

temperature is know as the Clausius-Clapeyron equation defined by:

$$e_s(T) \approx e_0 \cdot exp\left[\frac{L}{R_v} \cdot \left(\frac{1}{T_0} - \frac{1}{T}\right)\right]. \tag{1.1}$$

L is the latent heat of vaporization, $R_v = 461\ JK^{-1}kg^{-1}$ the water vapour gas constant, $T_0 = 273.15\ K$ the water freezing temperature and $e_0 = 0.611\ kPa$ is the reference saturation vapour pressure (usually at the triple point - 0 °C). With the Clausius-Clapeyron equation one can show that the increase in the temperature will lead to an increase in the water vapour, of roughly 7 % per 1 K warming (Trenberth et al., 2003; Skliris et al., 2016). This relation and its scaling in simulations of climate change is further investigated by O'Gorman and Muller (2010). They found deviations from Clausius-Clapeyron scaling for relative and specific humidity for tropics and mid-latitude regions, especially over land.

The uneven solar heating of the Earth, together with Earth's rotation drives the atmospheric circulation. Since water vapour content is highly constrained by the temperature, its distribution over globe resembles the atmospheric circulation and is very variable, ranging only from trace amounts at the poles or deserts to 70 kg/m^2 in the tropics. Moreover due to higher temperatures close to the surface, most of water vapour is confined to the lower parts of the troposphere. This high amount of water vapour evaporated from the oceans, is what in the tropics, enables the development of strong tropical cyclones. After the ascend of the evaporated water vapour, due to collision of the trade winds from southern and northern hemisphere, the lifted parcel of the air cools and condenses creating the large cloud bands of the cyclone. A similar process helps is governing the Arctic cyclones where two air masses of highly different temperature, one cold coming from the ice surfaces, also know as the cold air outbreak (CAO) and other coming from the relatively warm ocean surface collide (Kolstad et al., 2008). During these cyclones events a huge amount of precipitation is formed (mostly in the form of snow) and in the process of condensation the water vapour has been removed from the atmosphere.

1.1.1 Water vapour and recent climate change

Climate on Earth has been changing in response to external forcings and internal feedbacks across a wide range of timescales going through warm (Early Eocen - 50 million years ago) and cold (last interglacial 129–116 thousand years ago) periods (Burke et al., 2018). However, climate changes after industrial revolution (beginning of 17th century), in terms of the temperature increase, are not in accordance with "natural changes" and Milanković's cycles (related to solar radiation) for this century. The first notion of the anthropogenic, that is human induced climate change was mentioned by British scientist Guy Callendar in 1938 where burning of fossil fuel was linked to green house "blanket" effect proposed by French scientist J. Fourier in 1824 (Chao and Feng, 2018). It is worth mentioning that Swedish scientist Svante Aarrhenius in his work from 1896 has already shown the influence that an increase in carbon dioxide (CO_2) has on the global temperature, although not directly mentioning relation with fossil fuel burning. Latter, various studies, such as from Manabe and Wetherlad (1967) and Charney (1973), that used different models with varying or doubled amounts of CO_2, showed that temperature under these conditions will increase. However, Manabe and Wetherlad (1967) found values in between 1.3°C (for fixed absolute humidity) and 2.4°C (for fixed relative humidity). This relation of temperature sensitivity to CO_2 has as well been investigated by Sawyer (1972) and Broecker (1975) and various other studies afterwards.

Today, when it is known that the main source of the global temperature increase is human induced, world-wide policy makers united under the United Nations Framework Convention on Climate Change (UNFCCC) and the Paris Agreement (2015) in attempt to prevent further temperature increase by developing more clean energy sources and by reducing the usage of sources who's principal by product is CO_2.

The physics behind the CO_2 and temperature increase is that CO_2 is a very good absorber of the outgoing longwave radiation (OLR) in the thermal infrared region (IR). Meaning, the light photons that are re-emitted by Earth (and other objects) are being absorbed by the CO_2 molecule whose energy than increases due to excitation of the molecule's electrons that start to vibrate faster and in that way produce heat.

However, other gases like chlorofluorocarbons (CFC) and hydrofluorocarbons (HCFC), more known under the name freons (used in refrigerators, hair sprays etc.) that have been restricted in 1987 under Montreal Proctocol, methane CH_4, nitrous oxide (N_2O) and water vapour (although not a forcing) are also high contributors to warming. All these gases are known under the common name - Green House Gases (GHGs). What highlights the concern for our future climate more, is that once in the atmosphere, the molecules of these gases are having relatively long lifetime in the atmosphere, ranging from around a week for H_2O through 10 years for CH_4 to couple of centuries for N_2O (Montzka et al., 2011; Liu et al., 2016; Prather et al., 2012, 2015; Rigby et al., 2013).

Although water vapour in itself is not a forcing of the temperature increase, it is the most important GHG as it alters the effect (temperature increase) caused by other GHGs (Chung et al., 2014). For instance, when CO_2 increases, so does the IR opacity of the atmosphere, which in turn as well raises the altitude from which thermal radiation is emitted to space (Stevens and Bony, 2013). Such a change produces imbalance in Earth's radiation budget that can be restored either by increasing the temperature or the planetary albedo (Stevens and Bony, 2013). In the former, following the Clausius-Clapeyron's equation, water vapour will create a positive feedback loop by increasing the temperature even more. This is very alarming since water vapour is also the most abundant GHG and in comparison to CO_2, is more efficient in absorbing the longwave radiation (LW) (Lacis et al., 2013).

In comparison to pre-industrial time (1880), annual temperature has increased by 0.07 $°C\ dec^{-1}$ while after 1981 this increase is more than double and is of 0.18 $°C\ dec^{-1}$ (NOAA, 2019a) based on the Global Historical Climatology Network version 2 (GHCNv2) data set. However, observations from the Microwave Sounding Units (MSUs) and the Advanced Microwave Sounding Units (AMSUs) for the period between 1978 and 2002 show an even higher increase in the global temperature of 0.22°C to 0.26 °C with and without diurnal cycle correction, respectively (Vinnikov and Grody, 2003).

All of the above raises the necessity for more concise modeled climate projections which are still having discrepancies (Monckton et al., 2015; Eyring et al., 2019; Block et al., 2019). However, most of the climate models agree that we are entering new climate phase with increased temperatures where different Representative Concentration Pathways (RCP) scenarios in models project the increase in between 1.0 to 4.5 °C by the end of this century (Nazarenko et al., 2015). Similar results have been shown by using the new Coupled Model Intercomparison Project 6 (CMIP6) climate model runs which instead of RCPs use new Shared Socioeconomic Pathways (SSPs) that yield increases in temperature in between 1.33°C and 4.60°C for the period 2081-2100 (Tokarska et al., 2020). Moreover, the region that is most sensitive to temperature changes and shows the highest warming is the Arctic. Therefore, the role of water vapour in changing Arctic is the subject of this thesis.

1.1.2 Arctic Amplification - role of water vapour

The region over which the increase in near surface temperature is most amplified is the Arctic. There, the near-surface air temperature, for the past few decades, had risen to more than double the increase of the global mean value (Shindell and G.Faluvegi, 2009; Cohen et al., 2014; Wendisch et al., 2017). This phenomena is defined as the Arctic Amplification (Serreze and Francis, 2006a; Serreze and Barry, 2011) and due to its limited understanding, nowadays is a topic of large scientific research efforts. One of them is a German project called the "Arctic Amplification: Climate Relevant Atmospheric and Surface Processes and Feedback Mechanisms $(AC)^3$" (Wendisch et al., 2017) under which the work for this dissertation was performed. Within $(AC)^3$ the role of various mechanisms is investigated, with main contributors being:

1. **reduced albedo:** Due to massive sea-ice melt, the Arctic is losing its high albedo and therefore the ability to reflect solar radiation as effectively as in the past. This as a consequence has more darker ocean left behind which is a better absorber of the shortwave radiation (SW) leading to a warming of the upper oceanic layer and subsequently through process of evaporation, leads to

2. **increased water vapour**. As mentioned above, the increase of water vapour for a consequence has enhanced retention of OLR and thus further temperature increase. This subsequently leads to increased sea-ice melt and cloudiness. However, increased cloudiness and water vapour are partially also due to

3. **moisture intrusions into the Arctic from lower latitudes**. Moisture intrusions into the central Arctic (above 70°N) are closely related with transient eddies that account for 81% of meridional moisture flux in winter and for 92% in summer (Jakobson and Vihma, 2009). It has been shown by Woods et al. (2013) and Woods and Caballero (2016) that these intrusions can increase a local heating in the central Arctic for up to 20 K and can foster melt in the marginal sea ice zone. In addition to local evaporation, moisture from lower latitudes changes the stratification of the atmosphere leading to:

4. **increase in lapse-rate** and therefore positive lapse-rate feedback (Pithan and Mauritsen, 2014; Payne et al., 2015). In a warmer Arctic, stable stratification (especially in non-summer months), suppresses vertical mixing and warming

> remains largely confined to a thin near-surface layers. Such conditions in the lower troposphere result in a larger warming of the lower than of the upper troposphere, leading to a smaller increase in OLR compared to vertically uniform warming, and thus to further warming (Goosse et al., 2018).

The mentioned contributors and vast majority of possible interactions in between them on a local and regional spatial and temporal scales are investigated in order to solve the puzzle of Arctic Amplification whose complete source is still uncertain. However, what is certain is that model projections show a continuing positive temperature trend and by 2050, Arctic could face an ice-free summer and thus the complete change of the ecosystem (Overland and Wang, 2013).

For the period between 1979 - 2014 it has been shown that the September sea-ice extent is shrinking by 13.4 % per decade when referenced to the mean September extent for the period 1981–2010 (Serreze and Stroeve, 2015). This is very concerning since the changes in the Arctic are not having only local effect but are far more reaching and unpredictable. Many studies have tried to find the connection between Arctic amplification and sea-ice loss with the mid-latitude weather changes and extremes during summer, autumn and winter months (Petoukhov and Semenov, 2010; Francis and Vavrus, 2012; Cohen et al., 2014; Coumou et al., 2018).

However, in order to understand the Arctic amplification effects on mid-latitudes, it is crucial to first understand the changes that are happening on the local scales, in this context, the Arctic. The highest temperature increase over the Arctic was observed during winter months (Cohen et al., 2014; Wendisch et al., 2017) when the polar night is present and low-level stability is increased. This reduces the mixing of the atmospheric column and enhances the retention of released latent heat from the ocean that was accumulated during summer (Screen and Simmonds, 2010; Screen et al., 2011)). Moreover, formation of specific humidity inversions (increase of moisture with height) during winter has been shown to serve as a moisture source for cloud formation and persistence by feeding a cloud decoupled from the surface with moisture from above (Nygård et al., 2014; Vihma et al., 2016).

An increase in surface heating of 10-25 W/m^2 during the warm air advection over sea-ice accompanied with surface inversion has been observed (Tjernström et al., 2015, 2019). Furthermore, during winter for the 2003-2014 period, these inversions have been detected for 90% of the time (Naakka et al., 2018). The additional heat as a consequence has delayed sea-ice refreezing time in late autumn and earlier melt onset in spring. Consequently, this leaves the Arctic with a reduced area of the multi-year thick ice (of 50 % less for the 5 m thick ice (Hansen et al., 2013; Renner et al., 2014) and more easy to melt, young thin ice (especially evident in Chukchi, Beaufort and East Siberian Seas (Stroeve and Notz, 2018).

Rinke et al. (2017) showed that the anomalous winter warming over the Arctic Ocean has been greatly influenced by the increased frequency and duration of cyclonic activity due to larger amounts of water vapour they transport from the lower latitudes increasing the storm's cyclogenesis and persistence. One of the strongest cyclones in the Arctic are polar lows, also know as the hurricanes of the Arctic due to their destructiveness and resemblance to tropical cyclones. However, the complete understanding of key mechanisms of these intense and short-lived cyclone's development and persistence is still unclear. Moreover, the increased cyclonic activity and the availability of water vapour intrusions showed to be connected with enhanced sea-ice melt during summer (Screen et al., 2011; Knudsen et al., 2015; Ding et al., 2018) and earlier melt onset during spring (Kapsch et al., 2013; Devasthale et al., 2013; Kapsch et al., 2018).

Strong moisture intrusions, nowadays mostly referred as atmospheric rivers, a term first used by Zhu and Newell (1994), are the narrow corridors of poleward enhanced water vapour transport. Although widely researched in mid-latitudes (Schneider et al., 2006; Newman et al., 2012; Guan and Waliser, 2015, 2017; Waliser and Guan, 2017), their importance in the Arctic hydrological cycle is likely large, however up to recently they didn't got much of the attention (Vázquez et al., 2018; Nash et al., 2018; Komatsu et al., 2018). The atmospheric rivers into the Arctic are also affecting the temperature inversion layer that is most frequent in winter which than further enhance surface warming (Tjernström et al., 2019). Woods et al. (2013) and Woods and Caballero (2016) showed that atmospheric rivers induced warming, not mentioning temperature inversions, further increases lapse-rate feedback. The above once again highlights the importance of investigating the water vapour changes and the variability in the Arctic and therefore the necessity of its accurate measurement.

1.2 State of the Art of water vapour measurements

The importance that water vapour has on a various dynamical and thermodynamic processes in the Arctic, whether as a forcing or a feedback mechanism, has been explained above. From there it can be concluded that the accurate measurements of water vapour are highly significant. However, monitoring the water vapour over such a remote region as the Arctic, presents a great challenge, since most of the Arctic area is open ocean and/or sea ice covered surface.

Setting up the meteorological stations in an inhospitable environment is often very challenging or almost impossible task, especially during winter, when thick sea-ice is very hard to break and transportation of the instruments becomes even more problematic (Comiso and Hall, 2014). Therefore, existing in situ measurements, mostly radiosondes, providing long time record, are usually deployed only on coastal Arctic area and hence, present only point measurements leaving a large gap over the Arctic Ocean. Moreover, these long term data records, such as radiosonde can have gaps or artificial shift in time series due to the station being removed, changes in instrument type or operating procedure (Chen and Liu, 2016). However, they do provide very fine temporal resolution and accuracy for validation of other data sets.

One of the examples of usage of radiosonde data for validation has been performed by Weaver et al. (2019) where comparison of the upper troposphere and lower stratosphere (UTLS) water vapour from Atmospheric Chemistry Experiment (ACE) satellite measurements with coincident ground-based measurements taken at a high Arctic observatory at Eureka, Nunavut, Canada has been investigated. To get a full coverage and fill the gaps between point measurements, one must resort to remote sensing measurement techniques made by satellites.

Today it has been over 60 years since the launch of the first meteorological satellite in low Earth orbit (LEO) Television Infra-Red Observation Satellite (TIROS-1) on

1st of April 1960 and more than 40 years since the launch of Nimbus-7 in 1978, where Nimbus stands for the "rain cloud" (web links: (OSCAR; ESA, a)). Since then, a large number of satellites have been launched for various purposes (communications, Earth observation satellites, navigation, space science, and other). However, many of the launched meteorological satellites are carrying different instruments that are specifically designed to get the information on different parts of atmosphere and/or its constituents.

Water vapour can be measured by satellites using number of techniques. Most important are those relaying on the Earth's emission of the water vapour molecule in the thermal infrared (IR; 1 to 100 microns) and microwave (1 m to 1 mm, or 0.3 to 300 GHz) part of the spectrum (Crewell, 2006). Through that spectrum water vapour shows certain absorption characteristics. However the absorption spectrum of water vapour is very complex in general and can happen in three different types of transition: rotational, vibrational and electronic (Quintanilla, 2014), where rotational transition is most important for dipole molecule such as H_2O in IR and microwave part of the spectrum. From the rotational transition two rotational spectral lines (22.235 GHz and 183.310 GHz) are mostly used for microwave measurements (Gaut, 1968; Liebe et al., 1993; Liljegren et al., 2005; Westwater et al., 2005; Rosenkranz, 1998).

Knowing the absorption lines of the gas, channels with different sensitivity (frequency) are selected for instrument construction that will be carried by the satellite. This radiance measured by the instrument in the form of voltage is through Planck's law (Planck, 1901) connected with kinetic temperature of radiating object (gas) and converted to so called brightness temperature, T_b.

Although most of the water vapour absorption is taking place in the IR spectrum, the majority of the satellites measuring in that spectral range such as the Moderate Resolution Imaging Spectroradiometer (MODIS), the Infrared Atmospheric Sounding Interferometer (IASI) (Schlüssel and Goldberg, 2002), the Spinning Enhanced Visible Infra-Red Imager (SEVIRI), the Atmospheric Infrared Sounder (AIRS) or the near IR and visible MEdium Resolution Imaging Spectrometer (MERIS) are not able to penetrate most of the thick clouds (signal is getting attenuated) and the large amounts of water vapour below the clouds are left undetected. Although IASI shows a high accuracy of integrated water vapour (IWV) retrieved values (for near-nadir only radiances) it is still limited to the clear-sky scenes only (Aires et al., 2011a) as MODIS.

Passive microwave sounders such as the Advanced Microwave Sounding Unit -B (AMSU-B; launched in 1998) flown on the National Oceanic and Atmospheric Administration (NOAA) polar orbiting satellites NOAA-15, -16, -17, the Microwave Humidity Sounder (MHS; on NOAA-18, -19, MetOp-A and -B) or more recently launched (18 November, 2017) NOAA-20 (Joint Polar Satellite System (JPSS) in comparison to IR imagers are able to penetrate even the thickest of the clouds in their window channels and offer a good spatial coverage (with $\sim$ 14 overpasses a day) over the Arctic region during both, day and night with a good resolution of only $\sim$ 15 km at nadir. More details about these instruments and theirs scanning technique can be found in chapter 2.

The observations from these satellites are used for better description of air temperature and humidity, and their assimilation into numerical weather prediction (NWP) helps better constrain models in regions where scarce observations are assimilated, such as Arctic (Sapucci et al., 2013; Karbou et al., 2014; Randriamampianina et al., 2019). Today, we have the ability of using more than 20 years of data available from mentioned satellite sounders in order to improve and investigate atmospheric water vapour spatial and temporal changes in connection to climate and the Arctic amplification. However, the signal that comes from the satellite is not directly the value of the parameter of interest but it has to be retrieved by usage of some sophisticated methods, such as optimal estimation method (OEM) (Rodgers, 1976, 2000).

When investigating water vapour spatial and temporal changes most of the time what is being analysed is the IWV (also called precipitable water (PWV) or total column water vapour (TCWV)), which is the amount of water vapour contained in the atmospheric column of 1 m^2 from the surface to the top of the atmosphere (TOA). Reason for this are certain instruments limitations such as low vertical, spatial or temporal resolution. In the case of passive microwave satellites used in this thesis vertical resolution is limited and fine resolution profiles are very hard and complex to retrieve.

Although there is a long record of various meteorological satellite measurements, often times the retrievals are made only over global oceans (Mieruch et al., 2014; Mears et al., 2018) due to very complex surface emissivity in the microwave spectrum. Although retrievals that cover both land and ocean surfaces are possible, these are often prone to wet biases over land when compared to ground based microwave radiometers or radiosondes (Lindstrot et al., 2012, 2014). Another possibility for retrieval of IWV over both kinds of the surfaces exist from Constellation Observing System for Meteorology, Ionosphere, and Climate (COSMIC) that uses Global Positioning System (GPS) radio occultation limb sounding (Kuo, 2005; Wee and Kuo, 2015). However using these instruments and technique, the retrievals although with good vertical resolution suffer from very coarse spatial and/or temporal resolution. Moreover, long term IWV data are often times a combination from multiple satellites sensors where proper calibration between instruments is critical. Therefore the Global Energy and Water cycle Exchanges (GEWEX) Data and Assessments Panel (GDAP) initiated the GEWEX Water Vapor Assessment (G-VAP) whose main objective is to quantify the current state of the art in water vapor products that are being constructed for climate applications (Schröder et al., 2016, 2018).

G-VAP also includes the retrospective analyses (reanalyses), which are basically spatially and temporally discontinuous observations and model state fields merged onto the common and continuous spatial and temporal state fields. Various reanalyses are existing today, and most used for water vapour studies are the Modern-Era Retrospective analysis for Research and Applications, Version 2 (MERRA-2, Gelaro et al., 2017; Bosilovich et al., 2017, the Japanese 55-year Reanalysis (JRA-55; Kobayashi et al. 2015), the Climate Forecast System Reanalysis (CFSR; Saha et al. 2010), the European Centre for Medium-Range Weather Forecasts (ECMWF) Re-Analysis Interim (ERA-I; Dee et al. 2011), the most recent ECMWF Reanalysis 5th Generation Description (ERA-5; Hersbach et al. 2020) and specially tuned for Arctic conditions the Arctic System Reanalysis (ASR; Bromwich et al., 2010, 2018).

Schröder et al. (2016) showed that the highest relative standard deviation of IWV between long-term data sets is present over the Arctic and Antarctic region, which besides complexity of the polar regions is also due to relatively small values of IWV. In the study by Rinke et al. (2019) where reanalyses data for the 1979-2016 period were used to investigate trends in IWV above 70°N, the largest trend of 0.33 ± 0.18 kg/m^2 dec^{-1} was found in August. However they found that reanalyses are not consistent among each other considering magnitude of the trends where difference between reanalyses can be of 0.5 kg/m^2 dec^{-1}, especially in summer months.

Using the global satellite retrieved IWV data and their comparison with radiosonde (RS; 1450 worldwide stations), microwave radiometer (MWR) and/or Global Positioning System (GPS) measurements (point measurements), shows dry or moist biases (Trent et al., 2018) and large root-mean square errors (RMSE) reaching 3.84 kg/m^2 (Chen and Liu, 2016). Moreover, such a comparison of satellite retrieved IWV with point measurements over the whole Arctic region is even more challenging and hardly investigated so far. Although advances are made in retrieving the IWV over the ice surfaces by usage of the ASMU-B and MHS sensors, still there are issues in retrieving higher amounts of IWV during summer (Melsheimer and Heygster, 2008; Perro et al., 2016; Scarlat et al., 2018).

From the above it can be concluded that retrieving IWV from satellite observations still presents a great challenge due to high and variable surface emissivity in the microwave region. Further, due to the underdetermination of the problem various assumptions and *a priori* data information needs to be included into the retrieval algorithms. Therefore, the retrieved values are prone to biases when compared to other data sets, e.g. to radiosonde, GPS, Fourier transform spectrometer (FTIR) or microwave ground-based radiometers (MWR) (Bobylev et al., 2008; Palm et al., 2010; Alraddawi et al., 2017). Although advances in IWV retrievals from AMSU-B and MHS satellites have been made (Melsheimer and Heygster, 2008; Scarlat et al., 2018; Perro et al., 2016) still there are no long-term data set of IWV necessary to investigate long-term spatial and temporal changes of water vapor.

Therefore to study long-term climate change reanalyses based on various data assimilation are vastly used. In atmospheric data assimilation, this information typically includes both, observations from a variety of sources, such as ground-based stations, ships, airplanes, satellites and forecasts from numerical weather prediction (NWP) models. These reanalyses provide comprehensive, gridded estimates of atmospheric conditions at regular intervals over long time periods which makes them very attractive and convenient to use (Parker, 2016). For the purpose of this dissertation, the Arctic System Reanalysis (ASR) (Bromwich et al., 2010, 2018) specially tuned for the Arctic region has been used to create long-term data set of IWV.

1.3 Thesis hypotheses

As can be noted from the above, retrieving WV from the satellite sensors still presents a great challenge where passive MW observations from AMSU-B and MHS depend on the absorption and emission by atmospheric gases and scattering from hydrometers at higher frequencies and on surface emission and scattering for lower frequencies. Due to various assumptions necessary in the IWV retrieval, the resulting values often show either dry or moist biases when compared to other data sets (mostly with radiosonde (RS) and microwave radiometer (MWR) measurements; point measurements) (Mota et al., 2019). In attempt to avoid various assumptions made in the retrieval algorithms and following from the Clausius-Clapeyron's equation 1.1 that saturation vapour pressure is constrained only by the temperature, following hypothesis has been made:

> **Hypothesis 1**: Long-term brightness temperatures (T_bs) can be used as a proxy for water vapour spatiotemporal trends in the Arctic.

In order to test this hypothesis, an IWV data set that provides realistic T_b fields and is consistent with satellite's T_b is also needed. For the development of the IWV data set, the ASR reanalysis was chosen since it is the most recent reanalyses data set based on the Polar Weather Research and Forecasting Model (WRF) and is specially tuned for the Arctic region (Bromwich et al., 2010, 2018).

Due to cyclone's and therefore polar low's influence on the sea-ice melt and the necessity of theirs timely forecast, especially of short-lived polar lows, it is of importance to find theirs key governing and persistence mechanisms to be able to better predict theirs strength and severity in terms of the wind speed. Moreover, due to atmospheric rivers into the Arctic, it is of interest to asses theirs influence on the polar low severity in terms of precipitation since it is one of the key factors that determines visibility during severe storm events. From here two additional hypotheses have been made:

> **Hypothesis 2**: Through investigation of multiple important environmental conditions of polar lows during genesis stage, it is possible to find the most important one/or the combination of that enables/enable further persistence of the polar low to its maturity stage and determines its severity in terms of the wind speed.
>
> **Hypothesis 3**: A concurrent occurrence of an atmospheric river can increase the severity of polar low in terms of precipitation.

1.4 Thesis focus and structure

Following the above made hypotheses, the focus of this thesis will be on the:

1. Creation of a gridded brightness temperature (T_b) data set from the AMSU-B and MHS sensors flown on several satellites to match the temporal and spatial resolution of the ASR. As the largest increase in temperature over the Arctic is observed during winter months, January has been chosen as representative of the winter season to study long term spatial and temporal changes and variability as the daily cycle of T_b and water vapour. Additionally, since largest changes in the Arctic are happening during the transitional period between winter and summer, when the solar radiation is slowly increasing and the heating of the surface and melting of the ice is starting it is of interest, as for January, to investigate the long term spatial and temporal changes and variability as well

as the daily cycle of T_b and of water vapour in this period. As a representative for this transitional period that is starting in spring the month of May has been chosen.

2. Identification of relation between different altitude IWV and T_b by usage of the ASR. This investigation was preformed by conversion of the ASR output in the T_b space using the Passive and Active Microwave TRAnsfer forward model (PAMTRA) (Mech et al., 2020) which set up the model for realistic measurements of AMSU-B and MHS radiances at theirs frequency channels around strong water vapour absorption line, 183.31 GHz.

3. Creation of the IWV data set using ASR reanalysis variables for different column heights. Each column base height corresponds to AMSU-B's and MHS's sounding channels weighting function peaks translated to weighted absolute humidity functions peaks which willbe explained in chapter 5. After, the IWV columns are correlated with the observed T_b. In this way, a change of IWV through most of the atmospheric column can be analyzed.

4. Investigation of the key mechanisms for the polar low development and persistence due to theirs effect on the latent heat release during winter when the highest increase in the temperature is observed. Since winter is also the season of the polar lows with highest frequency of occurrence in January, this is the month chosen for the investigation. For this analysis only the ASR has been used since many kinematic and dynamic variables can not be inferred from the satellites instruments used in this study.

5. Investigation of the amount of precipitation of polar lows, more specifically, snow in connection with the enhanced moisture supply from the atmospheric rivers. Here as well only data from the ASR will be used.

The above points that this thesis will tackle are sorted through 8 chapters. Following this one, the second chapter will concentrate on the description and explanation of passive microwave sensor scanning technique and data acquisition of both, AMSU-B and the MHS as well as detailed description of the ASR. In Chapter 3 radiative transfer theory and the radiative transfer, more specifically microwave forward model used in this thesis, PAMTRA, will be described followed by the Chapter 4 that will present methods used to derive long term data sets of both, T_b from satellites and IWV from the ASR. In Chapter 5 the analysis of derived long-term data sets mentioned above and the assessment of simulated T_b will be laid out. Herein, first three points will be addressed and the hypothesis 1 will be tested. In Chapter 6, the investigation of the key mechanisms of PL cyclogenesis and persistence will be explained followed by the atmospheric river's influence on the PL precipitation presented in Chapter 7. The Chapters 6 and 7 therefore address the last two points of the focus of the thesis and hypotheses 2 and 3 will be tested. In the last chapter, Chapter 8, will be summarized the results and future perspectives will be laid out.

2 Passive microwave instruments onboard satellites and the Arctic System reanalysis

"Remote sensing", simply defined, is the collection of information about an object without being in direct contact with as defined by Evelyn Pruitt (Pruitt, 1979). Although remotely observing and permanently recording the objects of interest was possible way back in the early 19th century with the invention of photography, the modern remote sensing did not started until the Second World War and the usage of the infrared sensitive instruments and radar technology (Rodgers, 2012). Throughout years and technological advancement, such as satellite launches, the usage of this kind of technology has became recognized in various areas ranging from day to day life to climate applications. In the light of the modern climate change and Arctic Amplification, where polar night lasts for almost half of the year, passive microwave instruments are of great value and importance since contrary to active, they do not require a light source to make the measurements. Moreover, passive microwave instruments are able to provide the information on water vapour through the entire atmospheric column in the presence of clouds; contrary to IR techniques whose information on water vapour is obscured by clouds and therefore limited only to clear sky situations (Berg et al., 1999; Lanzante and Ghars, 2000; Lin et al., 1998; Crewell, 2006; Vaquero-Martínez et al., 2018). However, as mentioned in the previous chapter, retrieving IWV from satellite observations still presents a challenge due to variable surface emissivity in the microwave and the need of various assumption in the retrieval algorithms. Therefore, the retrieved values are prone to uncertainties when compared to in situ measurements. Reanalyses which include observations from a variety of sources—ground-based stations, ships, airplanes, satellites and forecasts from numerical weather prediction (NWP) models provide gridded estimates of atmospheric conditions at regular intervals over long time periods are vastly used. For the purpose of this dissertation, the Arctic System Reanalysis (ASR) (Bromwich et al., 2010, 2018) specially adapted for the Arctic region has been used to create long-term data set of IWV. This reanalysis and passive microwave instruments, namely AMSU-B and MHS mentioned above will be the focus of this chapter.

2.1 Passive microwave instruments onboard satellites

Passive microwave radiometry, although first developed for the radio - astronomical purposes in 1940s (Sharkov, 2003) has later on became an essential tool for probing the atmosphere and gaining more information on it's constituents. These instruments, as their name says, measure in the microwave frequency range (3 - 300 GHz or 10 - 0.1 cm) and are well suited to sense the radiation affected by emission and absorption by atmospheric gases but as well the one scattered from atmospheric particles such as droplets or ice crystals.

Since the launch of the Mariner-2 in 1960 for probing the Venus's atmosphere (Barath et al., 1964) by carrying microwave radiometer and it's track mode of measurements (only nadir-viewing antenna), novel techniques and ways of scanning were developed. The existing types of measurement can be grouped in: 1) track type (cross, along and conical) system, 2) imagers and 3) sounders. However, it should be noted that modern sensors are often times combining the ways of scanning modes and today we have cross or along track sounders, conical scanning imagers or conical scanning imager sounders. One of the first notable conical scanning imagers is SSM/I launched in 1987 onboard the Defense Meteorological Satellite Program (DMSP), a program designed to study oceanographic and solar-terrestrial physics environments (ESA (b)).

The SSM/I instrument flies in a near-polar orbiting, Sun-synchronous orbit at an altitude of approximately 860 km. It's conical way of scanning uses constant antenna boresight angle of 45° (Fennig et al., 2019). With this angle it scans a sector of 102.4° and with an Earth' incidence angle (EIA) of 52.94° it provides a swath width of about 1400 km. The orbit inclination of 98° and orbital period of 102 minute, allows the SSM/I to provide a full coverage between 87.5° N-S in two to three days and over the Arctic region almost twice per day (Hollinger et al., 1987; Wentz, 1991; Berg et al., 2013). With the frequencies of 19.35 (V,H), 22.23 (V), 37 (V,H) and 85.5 (V,H) GHz, where V and H denote vertical and horizontal polarization, the SSM/I is able, with the help of retrieval algorithms, to give the information about precipitation (Wentz and Spencer, 1998), sea-ice cover (Kern and Heygster, 2001), near-surface wind speed (Wentz, 1992; Flamant, 2003), IWV (Alishouse et al., 1990), cloud liquid water (Weng and Grody, 1992; Karstens et al., 1994) and snow cover (Crawford et al., 1992; Fiore and Grody, 1992; Grandell and Hallikainen, 1994; Tedesco et al., 2004). Its footprint size depends on channel frequency and varies from 74 × 40 km for 19.35 GHz to 16 × 13 km for 91.7 GHz. Later, in 2003, the SSM/I's successor, the Spatial Sensor Microwave Imager-Sounder (SSMIS) was launched with 27 frequency channels from which seven are identical to those of SSM/I. However, SSMIS has a slightly wider scan angle, 144°, and therefore wider swath width of 1700 km in comparison to SSM/I's.

The SSM/I and SSMIS instruments can be used for number of purposes, however, they were primary designed to provide the information on precipitation intensity at surface (OSCAR). Retrievals of IWV from these instruments are only possible over the ocean surfaces due to its lower and less variable emissivity when compared to land (Schulz et al., 1993; Zuidema and Joyce, 2008; Mears et al., 2018). Similarly, IWV retrieved from the Japanese instrument Advanced Microwave Scanning Radiometer-Earth Observing System (AMSR-E) with frequencies 6.9, 10.7, 18.7, 23.8, 36.5, 89.0

GHz, is available only over ocean surfaces (Kazumori et al., 2012; Zabolotskikh, 2017). IWV accuracy is typically about 1-2 kg/m^2 (Cimini et al., 2012; Li et al.). Attempts to derive IWV over land using neural-network approach shows accuracy of 2.39 kg/m^2 (Basili et al., 2010).

To respond to the need to sound the vertical humidity profile different instruments were required. For this purpose, the AMSU-B was designed and later on it's successor, the MHS. The AMSU-B and MHS are working on higher frequencies than SSM/I, SSMIS and AMSRE-E. Both instruments are of high importance to NWP models and operational weather forecasting and will be described in the following section.

2.2 AMSU-B and MHS sounders

AMSU-B and MHS are crosstrack, continuous line scanning, total power radiometers. These instruments are the atmospheric sounders (also called profilers) due to their ability to give the information on multiple levels of the atmosphere. They were launched onboard NOAA-K, -L and -M satellites (AMSU-B) as a part of the Polar-orbiting Operational Environmental Satellite (POES) constellation and the European Meteorological Operational satellites (MetOP-A and MetOp-B; MHS) as a complementary part of NOAA's POES constellation. Providing afternoon or morning service with their Sun-synchronous orbit means that these satellites are crossing certain point (observing the same scene) at the equator at the same local solar time (LST) each day, at 14:00 from NOAA-K, -L and -M and at 09:30 LST for the European MetOp-B satellites.

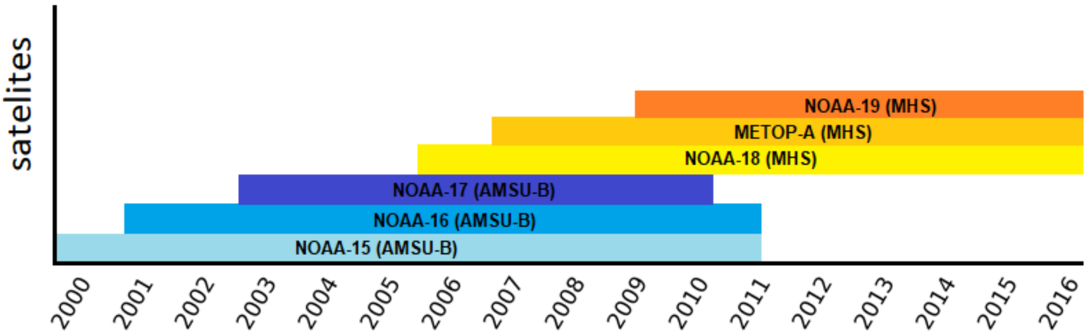

Figure 2.1: *Timeline of NOAA's and MetOp's satellite operation of AMSU-B and MHS instruments. Shown are only those used in this study.*

As mentioned above, the sounders were designed primarily to provide the information about vertical humidity profiles. They are able to do so by sensing the emitted radiation in five double-side band, vertically polarized frequencies centered around 89 GHz, 150 GHz, 183.31 ± 1 GHz, 183.31 ± 3 GHz, 183.31 ± 7 GHz for AMSU-B. For the MHS frequencies 157 GHz and 190.31 GHz were used instead of the AMSU-B's 150 GHz and 183.31 ± 7 GHz (Figure 2.2). Moreover, only 183.31 ± 1 GHz and 183.31 ± 3 GHz frequencies of the MHS are double side band and in contrast to AMSU-B, are having horizontal polarization. A double side band means that the radiation received at the instrument is not directly detected but downcoverted by mixing it with a stable signal at the line central frequencies. In this so called heterodyne principle two side bands, one below and one above the central frequency are combined (Figure 2.2). For 89 and 150 GHz the intermediate frequency (IF) is so low that the two side bands can be considered as one. The first two frequency channels from both instruments, namely 89 and 150 GHz (or 157 GHz for MHS) are called window channels due to their ability to sense the radiation emitted by the surface since at these frequencies the atmosphere is more transparent. The last three frequency channels are centered around the strongly opaque water vapour absorption line, 183.31 GHz, and are therefore able to provide information about water vapour at higher altitudes. These five frequencies from both instruments are sometimes denoted by their channel numbers, ranging from 16 to 20. The frequencies closest to the absorption line (most sensitive to WV) observe coldest T_b as their emission comes from higher and therefore colder altitude (Figure 2.2).

The higher frequency channels of AMSU-B and MHS are also sensitive to frozen hydrometeors and can be used for the retrieval of precipitation, snow and ice (Zhao and Weng, 2002; Weng et al., 2003; Kummerow et al., 1996; Ferraro et al., 2005; Vila et al., 2007; Kim et al., 2008; Tomaso et al., 2009; Noh et al., 2009; Sanò et al., 2015; Meng et al., 2017; Edel et al., 2019). Especially for scenes with high amounts of snow, scattering process lead to strong depression in T_b at frequencies above 150 GHz. This is most prominent for the channel at 183.31 ± 7 GHz which can penetrate deeper in the cloud than the frequencies above (Burns et al., 1997). Hence, further interest has risen in exploitation of AMSU-B and MHS frequencies such as to detect strong tropical cyclones and polar lows by usage of T_b differences between certain frequency channels (Hong, 2005; Melsheimer et al., 2016). From the above it can be concluded that these instruments are well suited to observe the atmospheric structure under all types of weather conditions.

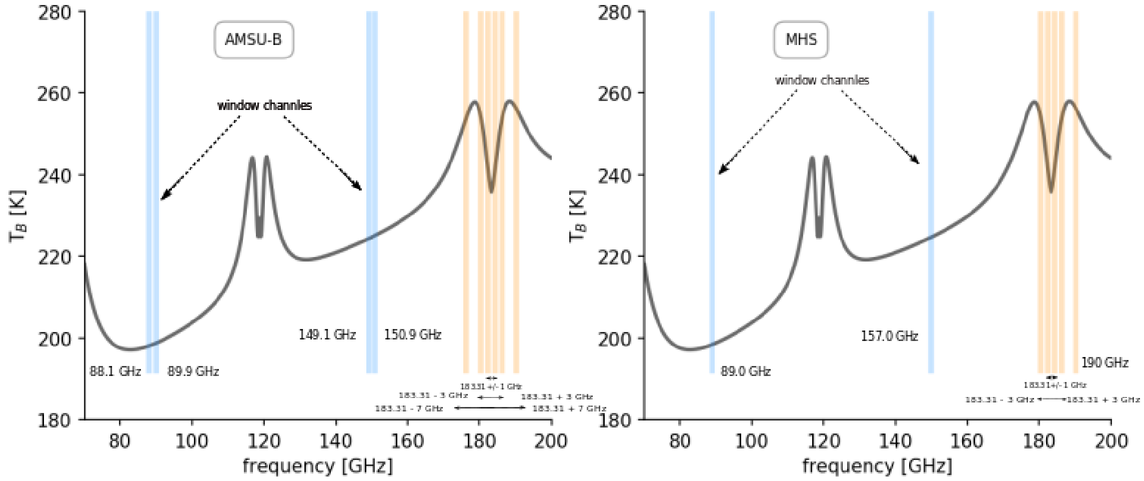

Figure 2.2: *Brightness temperatures, T_b, for AMSU-B (left) and MHS (right) frequencies for nadir viewing angle. Vertical lines indicate passbands for window (blue) and sounding (orange) channels. T_bs are simulated for one exemplary Arctic profile (78°N 7°E) in May taken from ASR under clear sky conditions using the PAMTRA (Mech et al., 2020) microwave forward model.*

2.2.1 Scanning technique

In order to measure the microwave signal an antenna that receives the upwelling radiance of the objects of interest is needed. For AMSU-B and MHS the antenna system consists of an offset paraboloidal beryllium main reflector that is placed in a cylindrical shroud with a 21.9 cm diameter aperture. The main reflector makes one complete rotation every 8/3 s (2.666 s) to direct upwelling radiation in a plane perpendicular to the satellite track onto the secondary mirror (Hewison and Saunders, 1996). This redirection is done via a hyperbolic subreflector to a quasi-optic feed which splits the incoming radiation into the three bands centred at 89, 150 and 183.3 GHz. These frequency bands are then down-converted, amplified and filtered to the required pre-detection bands. The 183.3 GHz receiver separates the signal into three different IF, namely 183 ± 1, ± 3 and ± 7 GHz (Vangasse et al., 1996).

During one rotation of the reflector, 90 Earth views within ± 48.95° of nadir are sampled, each separated by 1.10° in a cross track direction and by 17.6 km in along-track direction and are referred to as field of view (FOV) 1 to 90 (Figure 2.3).

One complete AMSU-B measurement takes 19 ms, with 18 ms integration time and 1ms dump time. During integration time (18 ms), the sub-satellite point moves about 125 m, whereas the main reflector of AMSU-B's antenna rotates about 1.04°. This rotation causes a shift of the footprint center equivalent to the size of the instantaneous field of view (IFOV) itself and hence leads to a significant broadening (therefore elliptical shape) of the effective field of view (EFOV) in cross-track direction (Bennartz, 2000).

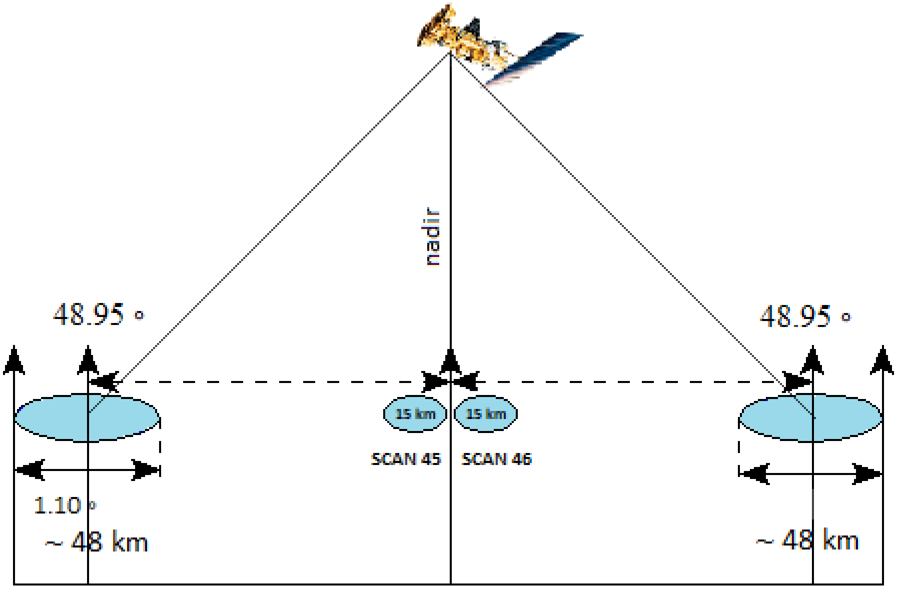

Figure 2.3: *AMSU-B and MHS cross scanning technique scheme.*

At each Earth view, the measured Earth view counts - which are proportional to the energy striking the detector area per unit time, that is radiance, are converted to an equivalent T_b by Planck's law (more details can be found in A.1). The spatial resolution of these pixels (IFOV's), is changing with the viewing angle, starting from the innermost at nadir of ~ 16 km (circular) to the outer most of around 26 × 48 km (elliptical). With this resolution, the width of the swath of one scan line is approximately 2300 km. The T_b's swath width from five different frequency channels of the MHS instrument are shown in Figure 2.4 (a). With this design, geometry and nodal period of 102 minutes these satellites are able to provide global coverage once per day with 14.2 orbits (ascending and descending) (Figure 2.4 (b)). However, for the higher altitudes such as Arctic, many swaths overlap and therefore more frequent sampling of the same area occurs.

It is worth mentioning that due to the Earth's eastward rotation, the satellite track is translated westward with each pass and repeats the same orbital configuration every 9th day. Specifics about AMSU-B and MHS instruments can also be found in Table 1.

Table 1: *AMSU-B and MHS instrument central frequencies (f), bandwidth, polarization and horizontal resolution and the altitude of the satellite they are onboard.*

AMSU-B			**MHS**		
Central f [GHz]	**Bandwidth [MHz]**	**Polarization**	**Central f [GHz]**	**Bandwidth [MHz]**	**Polarization**
89 ± 0.9	1000	V	89	2800	V
150 ± 0.9	1000	V	157	2800	V
183.31 ± 1	500	V	183.31 ± 1	500	H
183.31 ± 3	1000	V	183.31 ± 3	1000	H
183.31 ± 7	2000	V	190.31	2200	V
Horizontal res. $[km]$	~ 16 (nadir) to 48 (edge of swath)				
Altitude $[km]$	~ 830 km				

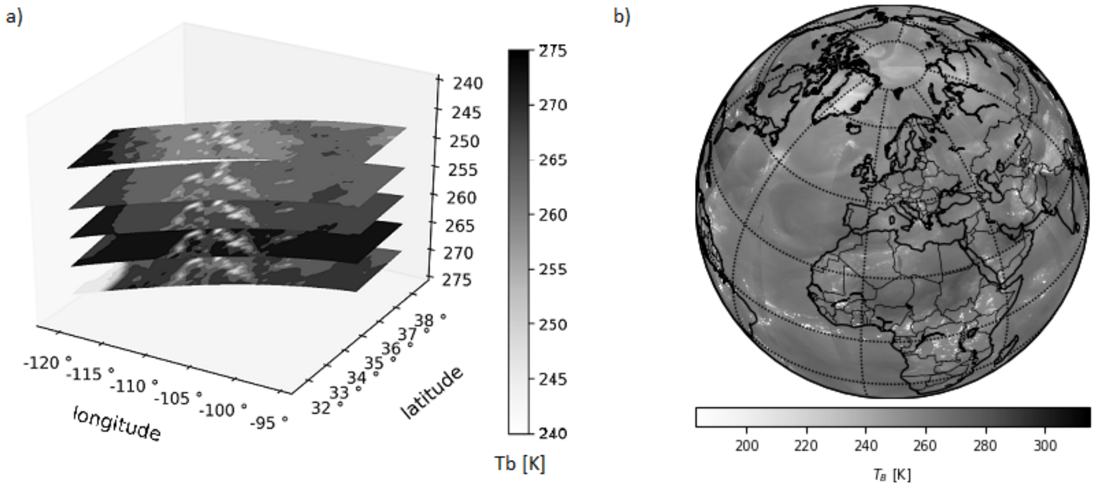

Figure 2.4: *(a) Example images of the 5 MHS frequency channels for part of one orbit (shown is also width of the swath). (b) Daily global coverage illustrated here for T_b at 190 GHz from MHS onboard NOAA-18 for the 1st of May 2016 .*

The AMSU-B and MHS instruments were designed to have a nominal lifetime of approximately 5 years, however, they have been operational for much longer. They are prone to orbital drift resulting in changes in observation conditions and overpass

times. The largest change in equator overpass time was noted for NOAA-16 where initial equator crossing time in 2003 was 14:00 LTS and in 2011 reached 19:30 LTS (Courcoux and Schröder, 2015). Moreover, geolocation errors are also present due to various possible sources (angular misalignment of the sensor spin axis with the spacecraft zenith, sample timing offsets, nonuniform spin rate, antenna deployment offsets, spacecraft ephemeris, and approximations of the geolocation algorithm in the Ground Data Processing Software) (Poe et al., 2008) as well as due to radio frequency interference (RFI).
Over the years, various studies have been devoted to identification or removal of the biases caused by these errors and the implementation of correction methods such as geolocation correction by Moradi et al. (2013b) or RFI correction by (Atkinson, 2001). Furthermore, enhanced values of the noise equivalent differential temperature (NEΔT) were identified by Hans et al. (2017) and for the purpose of this thesis such observations rendered as unusable were removed.
Due to different factors influencing the quality of the T_b measurements, there was a need for a consistent dataset that can be used for climatological purposes. Such a data set is called Fundamental Climate Data Record (FCDR) and the one used in this study is detailed in the next section.

2.2.2 Fundamental Climate Data Record - FCDR

The AMSU-B and MHS FCDR dataset used in this study has been produced by the National Climatic Data Center (NCDC) at NOAA/NESDIS/Center for Satellite Applications and Research (STAR). The satellites included into FCDR production are AMSU-B's on NOAA-15, -16 and 17 and MHS's on NOAA-18 and 19 and MetOp-A. Although, MetOp-B has been launched in 2012 it was not included into the production of this FCDR. The procedure in producing the level 1c dataset, that is FCDR, is such that level 1b data (l1b) provided by NOAA's Comprehensive Large Array-data Stewardship System (CLASS) were processed in six steps following Ferraro and Moradi (2016):

1. **Reading in the data** - l1b data from NOAA CLASS were compiled in which the Earth scene, warm (black body target inside instrument) and the cold count (cold space background target) are included together with ancillary data (land mask, local zenith angle, latitude and longitude, date and time and type of orbit (ascending or descending)).

2. **The geolocation correction** is based on the comparison between the ascending and descending orbits for pixels within 150 km from the shoreline by minimizing the number of pixels along the coastlines where the T_b difference between ascending and descending orbit is greater than a threshold of 30 K. The threshold needs to be greater than the daily range of the land surface temperature (20 K). The processing was performed by varying the attitude (pitch, roll, and yaw) starting from zero until the minimum number of pixels surpassing the threshold was reached (Moradi et al., 2013b).

3. **Inter-satellite correction** - was completed by using T_b averages over the tropical ocean (30° S to 30° N; as a warm end), Arctic and Antarctica ($>$ 75° S

and $>$ 75° N; as the cold end) from a reference satellite (NOAA-17 for AMSU-B and NOAA-18 for MHS) and the target satellite. Scatter plots between both were created and a linear regression performed to determine the slope and intercept. These correction coefficients were calculated for the monthly mean data.

4. **Radiance calculation** - Radiance is usually calculated from the combination of earth scene count and the accompanying count-to-radiance conversion coefficients.

5. **T_b generation** - After calculating the radiances, the Radio-Frequency-Interference (RFI) and antenna pattern correction (APC) coefficients were used to convert the originally measured antenna temperature (T_a) to T_b for AMSU-B/MHS by applying Planck function with the central frequencies of the specified channels. The APC were directly taken from the ATOVS and AVHRR Pre-processing Package (AAPP) as described by Hewison and Saunders (1996).

6. **The output** - is written in the netcdf format with approximately 8 MB per file (orbit) which contains the following information: latitude, longitude, scan time, and scan time since 1998, surface type, orbital mode, earth incidence angle, solar zenith angle, corrected T_b data for the 89 GHz, 157 GHz, 183 +/-1 GHz, 183 +/-3 GHz and 183 +/- 7 GHz channels, and quality flags.

For the relevant instruments the launch dates, their operationality, the switch off time and the recommended times to use them can be found in Table 2.

Table 2: *Satellites (first column) and instruments onboard them (second column) used in this study. Listed are dates of satellite launches (fourth column) and operationality (either still active (ACT) or end of life (EOL)). Last two columns note best time to use the data set as noted in Ferraro et al. (2018) and NOAA (2019b) and known issues of certain satellite Hans et al. (2017), respectively.*

Platform	**Instrument**	**Launch**	**Operational/Turned off**	**Best time to use**	**known issues**
NOAA-15	AMSU-B	13 May 1998	EOL - 28 Mar 2011	Jan 2000 - Dec 2010	cold NEΔT $>$ 2.5 K mid Sep 2010 gain falls to 0
NOAA-16	AMSU-B	21 Sep 2000	EOL - 09 Jun 2014	Jan 2001 - Dec 2010	strong orbital drift in 2007 changing in pattern for the observables related to the solar beta angle
NOAA-17	AMSU-B	24 Jun 2002	EOL - 10 Apr 2013	Jan 2003 - Dec 2009	channels 3,4,5 huge cold NEΔT of 2000 K and higher
NOAA-18	MHS	20 May 2005	EOL - 2016	Jun 2005 - Dec 2016	
NOAA-19	MHS	06 Feb 2009	ACT	Feb 2009 -	from 22 Jun 2009 (increase in NEΔT makes channel 3 unusable for majority of purposes)
MetOp-A	MHS	19 Oct 2006	ACT	Jan 2006 - Dec 2016	(issues since 26 March 2014)

2.3 Arctic System Reanalysis (ASR): version 1 and 2

ASRv1(v2) is a 3-hourly regional reanalysis with a horizontal resolution of $\sim 30(15)$ km and 29(34) pressure levels (10 hPa upper boundary) available for the 2000-2016 period. Both versions are produced using the polar optimized Weather Research and Forecasting Model (WRF) version 3.6.0, also called Polar WRF (PWRF). It is a limited area model for which ERA-I data were used as lateral boundary conditions. PWRF is based on the Pennsylvania State University (PSU)-National Center for Atmospheric Research (NCAR) Fifth-generation Mesoscale Model (MM5) (Grell et al., 1994), the WRF-variational data assimilation (WRF-Var) and High Resolution Land Data Assimilation (HRLDAS) tuned for polar regions (Bromwich et al., 2010).

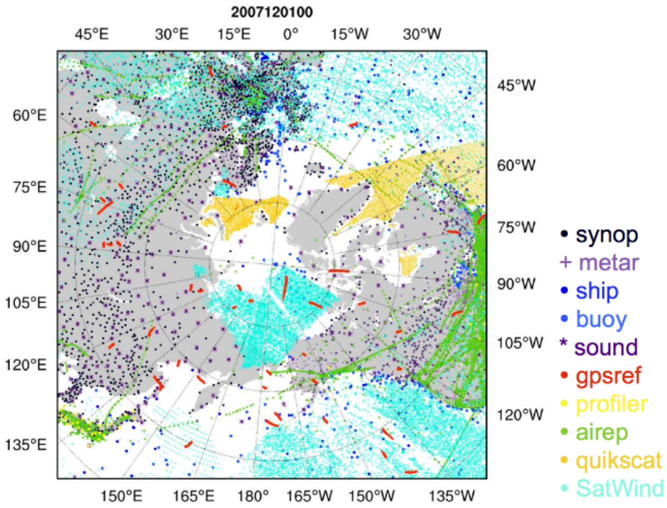

Figure 2.5: ASRv2 assimilated data including synoptic surface observations (black dots), METAR airport observations (purple pluses), ship observations (royal blue dots), buoys (navy blue dots), radiosondes (purple asterisks), global positioning system refractivity observations (red dots), wind profiler (yellow dots), aviation in-flight weather report (green dots), QuikScat sea-surface winds (orange dots), and satellite atmospheric motion vectors (aqua dots) (Bromwich et al., 2018).

The tuning of the WRF meant implementing a number of key physical schemes that are modified for the polar regions in order to capture features unique to extensive ice sheets, such as steep coastal margins, thermal properties of snow and ice, explicit ice phase microphysics, optimized turbulence (boundary layer) parameterization and improved treatment of heat transfer through snow/ice surfaces (Hines and Bromwich, 2008; Barlage et al., 2010). For the cloud microphysics with ice, snow, and graupel, but also liquid cloud and rain processes (Tao and Simpson, 1993; Tao et al., 2003) the Goddard microphysics scheme (Goddard Space Flight Center (GFSC)) has been used while for the cumulus parameterization the Kain-Fritsch scheme (Kain and Fritsch, 1990, 1993; Kain, 2003) has been adapted.

ASRv2 uses a staggered Arakawa grid-C with 721 x 721 grid points on a north-polar stereographic projection which chooses a latitude whose scale doesn't change, in the this case, 60°N. Grid points below 60°N are stretched further apart with lower boundary at 40°N, and points further north are pushed closer together. In the end the map is distorted with a scrunched up north due to points above 60°N being pushed closer together and stretched out equator due to points below 60°N being further apart (Figure 2.5). In the vertical direction, Polar WRF uses a terrain-following dry hydrostatic-pressure coordinate.

Both ASRs use a three-dimensional-variational data assimilation system (3D-Var). The non-radiance assimilated data are shown on Figure 2.5 and include: synoptic surface observations, Meteorological Terminal Air Report (METAR) airport observations, ship observations, buoys, radiosondes, global positioning system refractivity observations, wind profiler, aviation in-flight weather report, QuikScat sea-surface winds, and satellite atmospheric motion vectors. Besides these, the radiances from various satellites for different purposes were as well assimilated, including: MODIS (vegetation), High-resolution Infrared Radiation Sounder (HIRS3 and HIRS4), AMSU-A (channels 5-9; temperature sensitive), AMSU-B (channels 3-5; humidity sensitive), SSM/I, AMSR-E (Bromwich et al., 2018). However, channels 3-5 from AMSU-B, namely 183.31 ± 7, ± 3 and ± 1 GHz were assimilated only for the clear sky scenes while cloudy/precipitating scenes were screened out using quality control procedure such as scatter-index, difference between channel 1 (89 GHz) and 2 (150 GHz) or during the background check (Z. Liu and J.D. Keller - personal communication)

When compared to independent observations, the WRF showed good performance for surface variables with mean sea level pressure (MSLP) having the best performance, while poor performance is shown for near surface wind speed due to inadequate modeling of local wind effects and obstructions (Bromwich et al., 2010). When compared to ERA-I, which has coarser temporal (6 hourly) and horizontal resolution ($\sim$ 79 km), even the first version of the ASR has improved modeling of moisture and near-surface wind fields as shown by Radovan et al. (2019) in polar lows study while the remaining variables showed similar behavior as ERA-I (Wilson et al., 2011, 2012). In terms of cyclone activity, (Tilinina et al., 2014) showed that the ASRv1, during winter, detects 28% more cyclones than ERA-I. A similar result was shown in (Akperov et al., 2018), where it was found that the new version of ASR, the ASRv2, resolves more small and shallow cyclones. Since ASR, when compared to ERA-I, proved to be more reliable in the above studies, and since at the time of starting the research for this thesis the ECMWF Reanalysis 5th Generation (ERA-5) was not released, the choice of using the ASR is justified.

3 From electromagnetic wave to Radiative Transfer Model (RTM)

To understand properties of atmospheric constituents and the information that reaches the measuring instruments, it is necessary to understand physical processes of the source from which we receive the radiation. The part of the physics that studies energy transfer in the form of electromagnetic (EM) radiation is called radiative transfer (RT). Moreover, the radiative transfer equation (RTE) that combines absorption, emission and scattering processes of EM radiation propagating through a medium is typically so complex and therefore a derivation of simple RTE starting from Maxwell's equations and the EM wave to its complex form including scattering will be presented. Due to RTE complexity, an analytical solution is not possible and we must resort to the usage of numerical models. These RT models (operators) are used as a tool for sensitivity studies as a testbed for designing new instrument capabilities, for the development of retrieval algorithms of various atmospheric parameters, such as liquid water path (LWP), integrated water vapour (IWV), rain rates (RR) and etc.. Additionally, an RT model needs to be used for assimilation of the observations into the NWP models. The model used in this thesis for conversion of the ASR model space in T_b observation space is the Passive and Active Microwave TRAnsfer model (PAMTRA) and its applications will be explained in the second part of this chapter. The following text is mainly based on the work by Janssen (1993); Rybicki and Lightman (2004); Drusch and Crewell (2006); Mishchenko (2003, 2006); Ellison (2006) and the description of forward model PAMTRA by Mech et al. (2020).

3.1 From electromagnetic wave to brightness temperature

The electromagnetic (EM) waves are composed of oscillating electric and magnetic fields. In an homogeneous, isotropic, linear and nonabsorbing medium with real permittivity ε and real magnetic susceptibility μ and without radiation sources, transverse electrical $\mathbf{E}$ and magnetic fields $\mathbf{H}$ (under the time-harmonic plane wave solution) of traveling monochromatic electromagnetic wave can be expressed in the form:

$$\mathbf{E}(\mathbf{r},\mathbf{t}) = \mathbf{E_0}\,\mathbf{exp}(\imath\mathbf{k}\cdot\mathbf{r} - \imath\omega t) \tag{3.1}$$

and

$$\mathbf{H}(\mathbf{r},\mathbf{t}) = \mathbf{H_0}\,\mathbf{exp}(\imath\mathbf{k}\cdot\mathbf{r} - \imath\omega t) \tag{3.2}$$

where $\mathbf{E_0}$ and $\mathbf{H_0}$ are complex vectors, $\mathbf{r}$ is the position vector and $\mathbf{k}$ is a complex wave vector pointing in the direction of wave travel and is equal to $\omega\sqrt{\mu_0\varepsilon}$, where μ_0 is magnetic permeability of free space ($\mu_0 = 4\pi \times 10^{-7} Hm^{-1}$) and ω is the angular frequency (3.1).

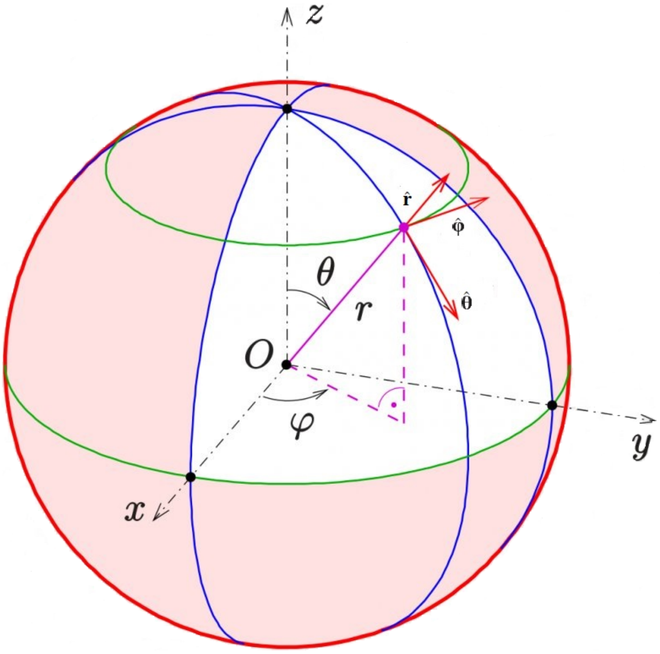

Figure 3.1: *Polar coordinate system describing polarization and the propagation of the transverse EM wave. Downloaded from: www.favpng.com*

With the assumptions made above, the instantaneous transverse electrical field $\mathbf{E}$ for any monochromatic EM wave traveling in the direction perpendicular to the defined plane is the sum of its components ($\mathbf{E}_\theta$ and $\mathbf{E}_\phi$):

$$\begin{aligned}\mathbf{E}(\mathbf{r},\mathbf{t}) &= \mathbf{E_0}\,exp(\imath\mathbf{k}\cdot\mathbf{r} - \imath\omega t)\\ &= \mathbf{E}_\theta(\mathbf{r},\mathbf{t}) + \mathbf{E}_\varphi(\mathbf{r},\mathbf{t}).\end{aligned} \tag{3.3}$$

In order to describe polarization, a concept of coherency matrix will be used which is applicable regardless the particular band of the electromagnetic spectrum considered (Gil, 2014). For this purpose we consider the complex amplitudes of the electric field $E_\theta(t)$, that does not vary as fast as the harmonic oscillations of the time factor $-\imath\omega t$ and can be reshaped to:

$$\mathbf{E}(\mathbf{r},\mathbf{t}) = \begin{bmatrix}\mathsf{a}_\theta exp\left(i\phi_\theta\right)\\ \mathsf{a}_\varphi exp\left(i\phi_\varphi\right)\end{bmatrix}\mathbf{exp}\left(\imath k\mathbf{n}\right) \tag{3.4}$$

where a_θ and a_φ are the amplitudes, and ϕ_θ and ϕ_φ are the phases of the complex amplitudes E_θ and E_φ, respectively.

The coherency matrix ρ, of monochromatic light is equal to:

$$\rho = \begin{bmatrix} \rho_{11} & \rho_{12} \\ \rho_{21} & \rho_{22} \end{bmatrix} = \frac{1}{2}\sqrt{\frac{\epsilon}{\mu}} \begin{bmatrix} \mathsf{E}_{0\theta}\mathsf{E}^*_{0\theta} & \mathsf{E}_{0\theta}\mathsf{E}^*_{0\varphi} \\ \mathsf{E}_{0\varphi}\mathsf{E}^*_{0\theta} & \mathsf{E}_{0\varphi}\mathsf{E}^*_{0\varphi} \end{bmatrix}, \tag{3.5}$$

where asterisks denote the complex-conjugate value. The elements of ρ have the dimension of monochromatic energy flux (W/m^2) and can be grouped in a 4 x 1 coherency column vector:

$$\mathbf{J} = \begin{bmatrix} \rho_{11} \\ \rho_{12} \\ \rho_{21} \\ \rho_{22} \end{bmatrix} = \frac{1}{2}\sqrt{\frac{\epsilon}{\mu}} \begin{bmatrix} \mathsf{E}_{0\theta}\mathsf{E}^*_{0\theta} \\ \mathsf{E}_{0\theta}\mathsf{E}^*_{0\varphi} \\ \mathsf{E}_{0\varphi}\mathsf{E}^*_{0\theta} \\ \mathsf{E}_{0\varphi}\mathsf{E}^*_{0\varphi} \end{bmatrix}. \tag{3.6}$$

The radiation varies rapidly and randomly in amplitude and direction and it can be 1)linear, where components of the **E** oscillate in phase, 2) circular, where components of **E** oscillate with a phase difference of 90°, and more general 3) elliptical, where the tip of the **E** describes the ellipse as it oscillates. Since these oscillations are so rapid and it is not possible to measure swift change of the phase angles and imaginary components, we instead measure the average polarization (direction of EM field) of time-averaged radiation over unit frequency range, defined as Stokes parameters (I, Q, U, V):

$$\mathbf{I} = \mathbf{DJ} = \frac{\mathbf{1}}{\mathbf{2}}\sqrt{\frac{\epsilon}{\mu}} \begin{bmatrix} \mathsf{E}_{0\theta}\mathsf{E}^*_{0\theta} + \mathsf{E}_{0\varphi}\mathsf{E}^*_{0\varphi} \\ \mathsf{E}_{0\theta}\mathsf{E}^*_{0\theta} - \mathsf{E}_{0\varphi}\mathsf{E}^*_{0\varphi} \\ -\mathsf{E}_{0\theta}\mathsf{E}^*_{0\varphi} - \mathsf{E}_{0\varphi}\mathsf{E}^*_{0\theta} \\ -i\left(\mathsf{E}_{0\varphi}\mathsf{E}^*_{0\theta} - \mathsf{E}_{0\theta}\mathsf{E}^*_{0\varphi}\right) \end{bmatrix} = \begin{bmatrix} I \\ Q \\ U \\ V \end{bmatrix}. \tag{3.7}$$

Here, I, Q, U and V are total flux density (intensity), degree of polarization, the phase (plane) of polarization and the ellipticity, respectively. In the above term we must replace amplitudes and phases with their time averages:

$$\begin{bmatrix} I \\ Q \\ U \\ V \end{bmatrix} = \begin{bmatrix} \mathsf{a}_\theta{}^2 + \mathsf{a}_\varphi{}^2 \\ \mathsf{a}_\theta{}^2 - \mathsf{a}_\varphi{}^2 \\ -2\mathsf{a}_\theta\mathsf{a}_\varphi cos\left(\phi\right) \\ -2\mathsf{a}_\theta\mathsf{a}_\varphi sin\left(\phi\right) \end{bmatrix} = \begin{bmatrix} \mathsf{I}_\theta + \mathsf{I}_\varphi \\ \mathsf{I}_\theta - \mathsf{I}_\varphi \\ \mathsf{I}_{-45} + \mathsf{I}_{45} \\ \mathsf{I}_{\mathsf{rcp}} + \mathsf{I}_{\mathsf{lcp}} \end{bmatrix}, \tag{3.8}$$

where I_θ and I_φ are horizontal and vertical polarizations, I_{-45} and I_{45} are polarization for ±45° angle and $\mathsf{I}_{\mathsf{rcp}} + \mathsf{I}_{\mathsf{lcp}}$ are right and left circular polarizations. I is a total flux density, no matter of the polarization preference. Therefore the total flux density can be expressed as:

$$I = \sqrt{Q^2 + U^2 + V^2}. \tag{3.9}$$

This relation holds true for the polarized EM wave, where the phases between components are fixed. However for the light source, coming from the Sun or any other natural source of emission that interacts with other radiating objects whose phases are random, there is no preferred orientation. Thus the EM field is unpolarized and therefore the above relation does not hold anymore.

Planck and blackbody radiation

Every body that has a temperature higher than absolute zero (0 K) does emit radiation. In order to understand heat radiation and its laws, it was necessary to forge a theoretical concept in which all radiation falling on the object is absorbed. This has been first proposed by Gustav R. Kirchhoff (1985) by imagining an object that at thermodynamic equilibrium does emit all radiation that has fallen on it (been absorbed). Such an idealized object is called blackbody which in order to mathematically model the electrical field of the radiation of the object is imagined as a enclosed cavity with a small hole through which only negligibly radiation can enter/exit and therefore negligibly affect the thermal equilibrium condition. This term is purely conventional and the black hole is the closest to this imaginative object since it absorbs all of the radiation falling in it. In Rayleigh-Jeans approximation, where emission is proportional to absolute temperature, spectral brightness of blackbody radiation is defined by:

$$\mathsf{B}_\nu = \frac{2kT\nu^2}{c^2} = \frac{2kT}{\lambda^2} \tag{3.10}$$

where k is the Boltzmann constant (k = 1.3806 $\cdot 10^{-23} JK^-1$), ν the frequency of all modes (can be considered as independent harmonic oscillators) of oscillating waves that have average energy $\langle E \rangle$ = kT, c the speed of light ($c = 2.99792458 \cdot 10^8$ m/s) and λ is the wavelength. The above relation for high frequency range leads to a well-known paradox called ultraviolet catastrophe. In order to solve this paradox, Planck, in his 'act of despair' had to give up the idea of deterministic physics in which the energy of all possible modes are continuously distributed and embrace the statistics of particles in which light is both at the same time, wave and particle. In this new theory, that opened the door to modern quantum physics, energy levels are quantized and must obey:

$$E = nh\nu, \qquad \text{n = 1,2,3,...} \tag{3.11}$$

where n is a number of photons and h is the Planck constant (h = 6.626 $\cdot$ $10^{-34} Js$) following from the Heisenberg's uncertainty principle as a product of uncertainty of coordinate and momentum. Now, similar to the continuous Boltzmann probability distribution, energy per mode is calculated by summing over only permitted discrete energies:

$$\langle E \rangle = \frac{\sum\limits_{i=0}^{\infty}(nh\nu P(nh\nu)}{\sum\limits_{i=0}^{\infty}(P(nh\nu)} = \frac{\sum\limits_{i=0}^{\infty} nh\nu exp\left(-\frac{nh\nu}{kT}\right)}{\sum\limits_{i=0}^{\infty} exp\left(-\frac{nh\nu}{kT}\right)}, \tag{3.12}$$

where $P(nh\nu) = P(E)$ is the probability that any mode has the energy E. After solving the sum (A.2), we come to the term for spectral brightness of the blackbody:

$$B_\nu(\nu, T) = \frac{2h\nu^3}{c^2} \frac{1}{exp(\frac{h\nu}{kT}) - 1}. \tag{3.13}$$

This term is also called specific intensity of radiation I_ν, which is a function of direction. However, no real object is a true blackbody and therefore will not emit the whole frequency spectrum. To measure the radiance of a specific object we define brightness temperature T_b which is the temperature a blackbody in thermal equilibrium should be at with it's surrounding in order to emit the same radiation observed by our object of interest:

$$T_b^{-1} = \frac{k}{h\nu} ln \left[1 + \frac{e^{\left(\frac{h\nu}{kT}\right)} - 1}{j} \right], \tag{3.14}$$

where j is the emissivity which for the non black body is lower than 1. This is the temperature that is provided as product from satellite observations from which later on, various atmospheric features can be obtained by usage of retrieval algorithms.

3.2 Radiative Transfer Equation

In order to understand the radiation coming from some distant object and to derive T_b, we first need to understand the processes that modify this radiation while propagating from that object (source) to our instrument. In its way from the source to the instrument, various processes and interactions with other atmospheric constituents can take place that can affect the radiation we receive. These processes include energy being: 1) taken by absorption, 2) added by emission from some other radiative source or 3) scattered by various constituents of the atmosphere. In the following text it will be explained how these processes add to the mathematical complexity of the radiative transfer equation (RTE) and which "exact" and approximate methods can be used to derive its solution.

3.2.1 RTE in free space

If we consider a ray of light traveling along distance s, through an empty space and through the solid angle $d\Omega$ in the infinitesimal time dt, and falling on the surface of area dA at some angle $d\theta$ and at the narrow frequency band ν, the intensity I_ν at the surface is equal to:

$$I_\nu \equiv \frac{dE}{dt\, cos\theta\, d\nu\, dA\, d\Omega}. \tag{3.15}$$

The change of radiation or spectral intensity during the travel along distance s without scattering, absorption or emission is equal to:

$$\frac{dI_\nu}{ds} = 0 \tag{3.16}$$

This means that no radiation, for this specific ray, has been lost and that the intensity is conserved and independent of distance. This however does not mean that the intensity should be constant through the space, since it can be different for different parallel rays or different directions. This conservation of intensity stays true even if the ray gets reflected of any kind of mirror (convex or concave) or magnifier. If this were not true, the intensity rule (3.16) would violate the laws of thermodynamics.

3.2.2 RTE including gaseous absorption

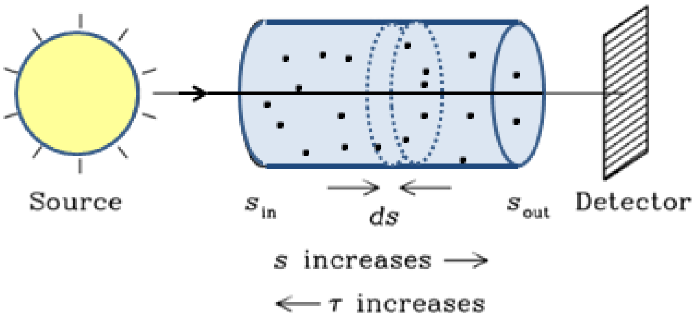

Figure 3.2: *Absorption between a source and a detector. The coordinate along the ray increases from s_{in} at the input end of the absorber to s_{out} at the output end of the absorber. The optical depth τ is measured in the opposite direction, starting from $\tau = 0$ at s_{in} and increasing as s decreases. Adapted from Essential Radio Astronomy (ERA) courses (ERA)*

In contrast to previous subsection, now we shall assume that on the way of the light ray travel there are some particles in a medium that act as absorbers of the photons. The probability of a photon being absorbed is proportional to the infinitesimal distance traveled, ds, and the efficiency of the particles to absorb a photons from a light ray is given by the photon mean free path. However, instead of using mean free paths, it is more natural to use the term extinction coefficient, which is inverse of the mean free paths since what we observe after light ray has been passing through the medium is the radiation that has been partially extincted. Another term mostly used for the same parameter is opacity. The denser the medium, the smaller is the mean free path (greater opacity) (Fig. 3.2) and less photons to be absorbed at the end of the medium. Now, the intensity at the output side can be written as:

$$\frac{I_\nu(s)}{I_\nu(s)} = -\alpha_\nu(s)ds \tag{3.17}$$

where α_ν is the linear absorption coefficient with the units of inverse length. Than the optical depth between two points, s_{in} and s_{out}, along a ray can be expressed as the following integral:

$$\begin{aligned} \int_{s_{in}}^{s_{out}} \frac{dI_\nu(s)}{I_\nu(s)} &= -\int_{s_{in}}^{s_{out}} \alpha_\nu(s)ds \\ \frac{I_\nu(s_{out})}{I_\nu(s_{in})} &= e^{\left[-\int_{s_{in}}^{s_{out}} \alpha_\nu(s)ds\right]} \\ &= e^{-\tau(s)}. \end{aligned} \tag{3.18}$$

The direction of integration is chosen to be negative so that optical depth, τ is positive, that is it increases as we look deeper into the absorber. If $\tau \gg 1$ we say that the absorber is optically thick and if $\tau \ll 1$ we say that the absorber is optically thin. The whole expression on the right hand side of the 3.18 is called the transmission, which is the radiation that managed to pass through the medium. The formal RTE for the purely absorbing and non-emitting medium can be written in the form:

$$dI_\nu(s_{out}) = I_\nu(s_{in})e^{-\tau(s)}. \tag{3.19}$$

3.2.3 RTE including absorption and emission

If we now assume that the medium through which the light ray is passing also adds some radiation to the ray, than the RTE must also include the emission part and is now given by:

$$\frac{dI_\nu(s)}{ds} = j_\nu(s) - \alpha_\nu(s)I_\nu(s). \tag{3.20}$$

The j_ν is the emissivity coefficient in cgs units erg s^{-1} cm^{-3} Hz^{-1} ster^{-1}. In local thermodynamic equilibrium (LTE) where system is at some temperature T, no matter how small or big the opacity, the intensity should everywhere be equal, that is $I_\nu = B_\nu(T)$. From the RTE, that means that $dI_\nu/ds = 0$:

$$j_\nu(s) - \alpha_\nu(s)I_\nu(s) = j_\nu(s) - \alpha_\nu(s)B_\nu(s) = 0. \tag{3.21}$$

That is:

$$\frac{j_\nu}{\alpha_\nu} = B_\nu(T). \tag{3.22}$$

This is Kirchhoff's law which says that a medium in thermal equilibrium can have any emissivity j_ν and extinction α_ν, as long as their ratio is equal to the Planck function. By using the Kirchhoff law, the RTE can be written in the form:

$$\frac{dI_\nu(s)}{ds} = \alpha_\nu(s)\left[B_\nu(T(s)) - I_\nu(s)\right] \tag{3.23}$$

If we now define the "source function":

$$S_\nu \equiv \frac{j_\nu}{\alpha_\nu}, \tag{3.24}$$

where source function for LTE is actually the Planck function for black body radiation B_ν, than in a similar way as the above expression (3.23) we can write the RTE for a case independent of whether there is LTE or not:

$$\frac{dI_\nu(s)}{ds} = \alpha_\nu(s)\left[S_\nu(s) - I_\nu(s)\right]; \tag{3.25}$$

Weighting function

For well mixed gases in the atmosphere, such as O_2, CO_2, CH_4 or N_2O, with well known concentration, a measured upwelling radiance (emission) is basically the sum of surface emission and contributions from the individual atmospheric heights, weighted by the corresponding weighting function. Weighting function determines how much one atmospheric layer contributes to the measured signal. Weighted profile of e.g. temperature or some other atmospheric parameter x, at height s, is expressed by using a weighting function W which is defined as:

$$W_x(s) = \lim_{\substack{\delta x \to 0 \\ \delta s \to 0}} = \frac{\delta T_b}{\delta B(T_b)} \frac{\delta B(T_b)}{\delta x \delta s}, \tag{3.26}$$

where δx is the perturbation in the atmospheric parameter x, δs is the layer thickness at height s, δT_b is the resulting change in T_b and $\delta B(T_b)$ is the resulting change in the Planck radiance (Schroeder and Westwater, 1992).
For temperature, the weighting function is given by:

$$W(T(s)) = \frac{\delta\tau(s)}{\delta s}\frac{\delta B(T_b(s))}{\delta T(s)}. \tag{3.27}$$

where $\delta\tau = \delta(T_b(s))/\delta B(T_b(s))$. In the microwave frequency region, dominant absorbers in the troposphere are water vapour H_2O, oxygen O_2 (Van Vleck, 1947a,b) and nitrogen dioxide N_2 (Huffman and Larrabe, 1968). Wheres close to the surface absorption by H_2O is dominant, at higher altitudes, N_2 becomes significant absorber especially for the frequencies around resonance of H_2O and O_2 (Kunzi et al., 2010). In order to solve the weighting function equation, the absorption coefficients are needed. In this thesis these were taken from Rosenkranz (1998) Radiative Transfer Model (RTM). The largest contribution, that is, the strongest signal satellite instrument gets from a certain channel, is from the level where τ changes most rapidly with the altitude, that is where atmosphere becomes opaque.

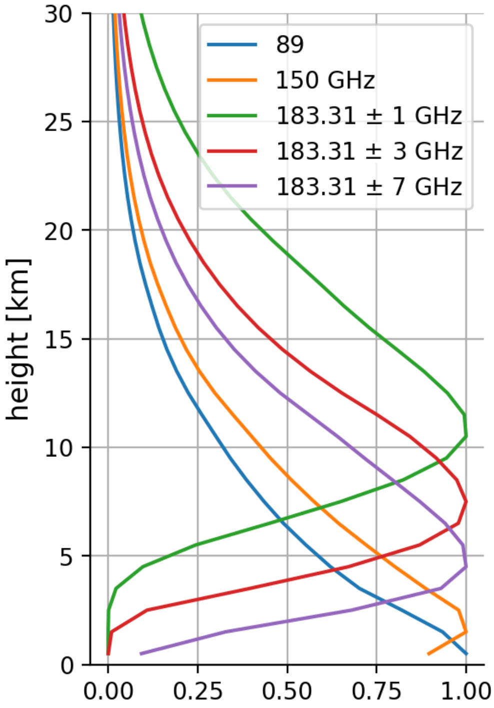

Figure 3.3: *Humidity weighting functions for the AMSU-B channels, namely, 89 GHz (blue), 150 GHz (orange), 183.31 ± 7 GHz (purple), 183.31 GHz ± 3 GHz (red) and 183.31 ± 1 GHz (green)*

This is indicated by a weighting function peak. Humidity weighting functions for the AMSU-B instrument for standard atmosphere are presented in the Fig. 3.3. It can be seen that lower frequencies, such as 89 and 150 GHz are having a peak at, or very close to the surface, meaning the information from these channels is coming from the surface or layers very close to it. However, these frequencies are not well suited for sensing water vapour but rather for precipitation relying on scattering effect due to which a decrease in T_b is observed or emission (Tomaso et al., 2009). In microwave region, frequency usually used for sensing water vapour close to surface is 22.24 GHz. However, this frequency lacks sensitivity for for cold and dry atmospheric conditions, such as Arctic (Westwater et al., 2005). In contrast, channels around strong water vapour absorption line at 183.31 GHz, show strong sensitivity for such conditions and therefore in this study only these sounding frequencies will be used. From Fig. 3.3 it can be seen that peaks of the weighting functions for these frequencies are at higher altitudes, meaning that the information is mostly coming from the higher layers in the atmosphere.

Calculating weighting functions for given composition of the atmospheric state, such as temperature, pressure, relative humidity and density of the cloud (excluding the scattering), it is possible to retrieve the temperature an instrument with certain antenna specification and with chosen frequency would observe prior to its construction. This is very useful since in that way building of the instrument is more cost-efficient.

3.2.4 RTE including absorption, emission and scattering

In a real case scenario in the atmosphere various particles that affect radiation traveling towards the detector are present. Most common particles encountered in the atmosphere are aerosols (organic or inorganic origin), water droplets, ice crystals, snow or graupel vastly studied in the meteorology and known under common name - hydrometeors. While traversing, radiation comes into contact with these particles, it gets absorbed and/or scattered in all directions which makes the solution of the RTE quite complicated. However, often the medium is considered homogeneous if it consists of particles which size is smaller than the radiation wavelength.
In this kind of medium, the total radiation received by a detector is reduced due to absorption and scattering of photons. Therefore, the total opacity (extinguishing) is equal to the sum of absorption α_ν^{abs} and scattering α_ν^{scat} coefficients:

$$\alpha_\nu^{ext} = \alpha_\nu^{abs} + \alpha_\nu^{scat} \tag{3.28}$$

and the ratio of α_ν^{scat} and α_ν^{ext} is called the "single-scattering albedo":

$$\eta_\nu = \frac{\alpha_\nu^{scat}}{\alpha_\nu^{ext}}. \tag{3.29}$$

Similarly we can define photon destruction probability as:

$$\epsilon_\nu = 1 - \eta_\nu. \tag{3.30}$$

Emission coefficient like the absorption coefficient, also consist of two contributions, emissive and scattered part:

$$j_\nu = j_\nu^{emis} + j_\nu^{scat}. \tag{3.31}$$

Now, the source function S_ν can be written in a form that includes above mentioned parameters for absorption, emission and scattering:

$$\begin{aligned} S_\nu = \frac{j_\nu}{\alpha_\nu} &= \frac{j_\nu^{emis} + j_\nu^{scat}}{\alpha_\nu^{abs} + \alpha_\nu^{scat}} && (3.32) \\ &= \epsilon_\nu \frac{j_\nu^{emis}}{\alpha_\nu^{abs}} + \eta_\nu \frac{j_\nu^{scat}}{\alpha_\nu^{scat}} && (3.33) \\ &= \epsilon_\nu S_\nu^{abs} + \eta_\nu S_\nu^{scat} && (3.34) \end{aligned}$$

For isotropic scattering (meaning the intensity of light radiated is the same in all directions) ($j_\nu^{scat}/\alpha_\nu^{scat} = J_\nu$) and thermal emission at some temperature T ($j_\nu^{emis}/\alpha_\nu^{scat} = B_\nu(T)$), the source term can be written in a form:

$$S_\nu = \epsilon_\nu B_\nu(T) + \eta_\nu J_\nu = \epsilon_\nu B_\nu(T) + (1 - \epsilon_\nu) J_\nu \tag{3.35}$$

Similar to Eq. 3.25, the RTE now reads:

$$\frac{dI_\nu}{ds} = \alpha_\nu \left[S_\nu - I_\nu \right]. \tag{3.36}$$

and by using Eq. 3.35:

$$\frac{dI_\nu}{ds} = \alpha_\nu \left[\epsilon_\nu B_\nu(T) + (1-\epsilon_\nu) J_\nu - I_\nu \right] \tag{3.37}$$

Since J_ν is the angle-averaged intensity at frequency ν and the formal solution for RTE takes in consideration all possible angles, J_ν needs to be integrated over all the angles (that is over a space angle, Ω):

$$J_\nu = \Lambda \left[S_\nu \right] \tag{3.38}$$

where Λ is a notation for integral over whole space. Now, the source function can be written in the form:

$$S_\nu = \epsilon B_\nu(T) + (1-\epsilon_\nu) \Lambda S_\nu \tag{3.39}$$

or in the integral form by using the expression for $\epsilon_\nu = -\alpha_{scat}/\alpha_{ext}$ from Eq. 3.28 and 3.29 and knowing that the source function for thermodynamic equilibrium is the Planck function $B_\nu(T) = I_\nu$:

$$S_\nu = \epsilon_\nu B_\nu(T) + \int_{4\pi} \frac{\alpha_\nu^{scat}}{\alpha_\nu^{ext}} I_\nu(s, \theta', \phi') d\Omega', \tag{3.40}$$

where term $\alpha_\nu^{scat}/\alpha_\nu^{ext}$ under integral is already defined single-scattering albedo and scattering is governed by a so-called "normalized phase-function" that can be written in the form:

$$\frac{\alpha_\nu^{scat}}{\alpha_\nu^{ext}} = \frac{1}{4\pi} \int_{4\pi} p(\theta, \phi, \theta', \phi') d\Omega \tag{3.41}$$

and which represents the radiance transfer from direction (θ', ϕ') to the direction (θ, ϕ) from a propagation path. Therefore the minus sign in front of the integral has been left out.
Putting the integral form for the source function S_ν back into (3.36) we get:

$$\frac{dI_\nu(s)}{ds} = \alpha_\nu \left[\epsilon_\nu B_\nu(T) + \tfrac{1}{4\pi} \int_{4\pi} p(\theta, \phi, \theta', \phi') I_\nu(s, \theta', \phi') d\Omega' - I_\nu \right]. \tag{3.42}$$

The RTE in the above form also applies for the Rayleigh-Jeans regime where I_ν can be replaced with brightness temperature T_b and Planck function B_ν with T. Taking into consideration the extinction coefficient in α_ν and dropping the ν subscript, we get:

$$\frac{dT_b(s)}{ds} = -\alpha^{ext}(s) T_b(s) + \alpha^{abs} T(s) + \frac{\alpha^{ext}}{4\pi} \int_{4\pi} p(\theta, \phi, \theta', \phi') T_B(s, \theta', \phi') d\Omega'. \tag{3.43}$$

This is the RTE in integro-differential form that includes propagation of T_b in all directions due to interactions with other particles on its way. These interactions have to be taken into account by calculating the probability of their occurrence.

As stated above, this makes the RTE solution very complex and therefore various methods for its approximate solution exist, such as: single scattering approximation (applicable for optically thin medium (τ less than 0.1) (Mishchenko et al., 2007), two-stream approximations (e.g. Eddington and Delta-Eddington approximations where angle of the incident radiation and angular dependence of phase function are important) (Coakley Jr. and Chýlek, 1974; Joseph et al., 1976), and the "exact" solutions such as: Discrete-ordinate technique (radiation field is decomposed into a coherent- determines the optical characteristics of the medium, and incoherent - related to the processes of multiple light scattering parts) (Chandrasekhar, 1946; Afanas'ev et al., 2020), adding-doubling technique and statistical Monte Carlo method named due to a chance of certain event happening (Metropolis, 1987). The idea of Monte Carlo method is to follow the path of a photon from one scattering event to the next, and to use random numbers to decide in which direction the photon will proceed after each scattering event. This is achieved by sampling optical depth from the probability distribution. First work on this topic was presented by Avery and House (1968). Below, however only the formal solution of RTE will be provided since Monte Carlo method and its application in RTE solution is beyond the scope of this thesis.

3.2.5 A formal solution of RTE

The equation for optical depth Eq. 3.19 between two points can be also expressed with usage of the extinction coefficient:

$$\tau(s_{in}, s_{out}) = -\int_{s_{in}}^{s_{out}} \alpha_\nu(s')ds' \tag{3.44}$$

or in a differential form:

$$d\tau = -\alpha_\nu(s)ds. \tag{3.45}$$

Now combining Eqs. 3.25 and 3.45 we have:

$$\begin{aligned} dI_\nu &= d\tau(I_\nu - S_\nu) \\ \frac{dI_\nu}{d\tau} &= I_\nu - S_\nu / \cdot e^{-\tau} \\ \frac{d}{d\tau}(e^{-\tau} I_\nu(\tau)) &= -e^{-\tau} S_\nu. \end{aligned} \tag{3.46}$$

Integrating the above expression from surface $\tau = \tau_s$ to the top of the atmosphere $\tau = 0$ (since we consider a detector on an instrument that is onboard satellite and therefore the optical path τ, at the very end of radiation travel will be equal to 0), we get:

$$I_\nu(\tau = 0) = I_\nu(\tau = \tau_s)e^{-\tau_s} + \int_0^{\tau_s} e^{-\tau} S_\nu(\tau) d\tau. \tag{3.47}$$

In Rayleigh-Jeans approximation the above expression becomes:

$$\begin{aligned} T_b(0) = {} & T_b(\tau_s)e^{-\tau_s} + \\ & + \int_0^{\tau_s} \left[(1-\eta)T(\tau) \ + \frac{1}{4\pi} \int_{4\pi} p(\theta, \phi, \theta', \phi') T_B(s, \theta', \phi') d\Omega' \right] e^{-\tau} d\tau. \end{aligned} \tag{3.48}$$

This equation is the *formal solution* of the RTE and not a solution in a true sense since in general case the source function and the intensities at the boundaries depend on the unknown intensity of radiation emitted by the media.

3.2.6 Scattering regimes

Since in our media we are now dealing with particles and scattering, it is more convenient to use parameters that we can relate to the particle properties such as size. In these terms, a cross section σ, which for a spherical particle is equal to πr^2, where r is the radius of spherical particle is used.

However, real particles are not perfect spheres and we have to take into consideration their shape and complex index of refraction $m(\lambda)$ which is wavelength dependant and has dimensionless imaginary part, k (connected to absorption) and real part n (connected to scattering):

$$m(\lambda) = n(\lambda) + k(\lambda) \tag{3.49}$$

For values of $k = 0$ at some wavelength, the material could scatter everything but would not have absorptive properties and if such material would also have $n = 0$ it would be invisible. Real particles do not have $k = 0$ and are always absorbing to some degree. However, liquid water and ice or glass for visible wavelengths are very close to this value, having k of order 10^{-8}.

Materials whose k value approaches zero are called dielectrics. Another important parameter relating particle size and the wavelength is the size-parameter:

$$\chi = \frac{2\pi r}{\lambda} \tag{3.50}$$

that depending on the particles radius a tells us which regime for particle scattering should be used. From here it follows:

$$\chi \begin{cases} \ll 1, & \text{Rayleigh scattering,} \\ \simeq 1, & \text{Mie scattering,} \\ \gg 1, & \text{geometric scattering.} \end{cases}$$

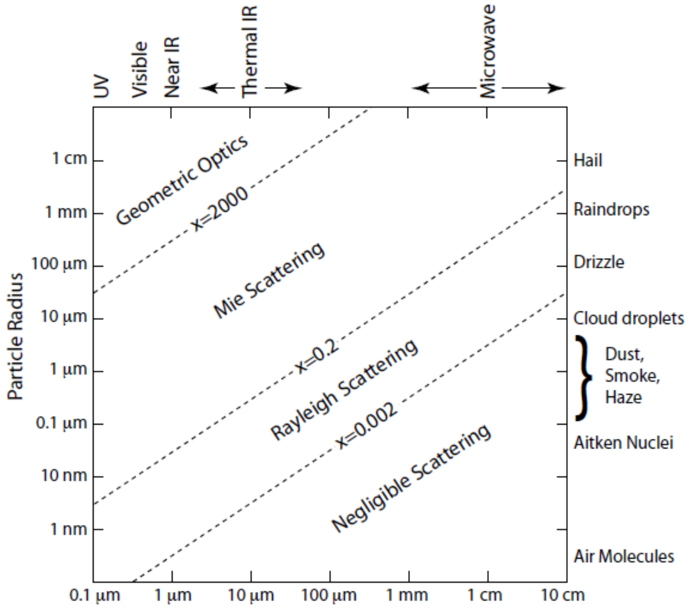

Figure 3.4: *Relation between particle size, radiation wavelength and scattering behavior of atmospheric particles: approximate regime boundaries are indicated as dashed lines. (Petty, 2006)*

The relation of particle size, shape and scattering regime for different atmospheric profiles is presented in the Fig. 3.4. A Rayleigh scattering is applicable for scattering by molecules and small aerosols. For the microwave region, the Lorentz-Mie theory can be used to calculate single-scattering properties of spherical particles, however for a different shapes a *T-matrix* method (Mishchenko et al., 1996) or discrete-dipole approximation (DDA) (Draine and Flatau, 1994) can be used. The last kind of scattering, a geometric scattering is applicable for scattering by large cloud droplets and ice crystals. In the following text first two regimes will be briefly introduced.

Rayleigh scattering

For a small particles ($\chi \ll 1$) as noted above, to calculate particle's scattering cross-section we can use a Rayleigh scattering theory. The angular phase function from Eq. 3.41 is simply a probability that a photon will be scattered from its initial position through the angle θ.

For elastic scattering such as Rayleigh scattering, where the amount of backward and forward scattered radiation is equal, the probability is P(cosθ) = 1/2. In Rayleigh-Jeans approximation the intensity is given by:

$$I_R = I\frac{2\pi {n_0}^4}{\lambda}\frac{r^6}{2D^2}\left(\frac{\varepsilon - \varepsilon_0}{\varepsilon + 2\varepsilon_0}\right)^2 (1 + cos^2\theta) \tag{3.51}$$

where R stands for Rayleigh and D is the distance between the particle and the observer (Lockwood, 2016). Derivation of the above term can be found in the appendix (A.3).

Lorentz-Mie theory

Mie theory or also called Mie-Lorentz or Mie-Lorentz-Debye scattering owes its different naming due to Mie's application of Maxwell's equations to calculate light scattering from spherical particles (Mie, 1908) that was already shown by Ludwig Lorentz in 1890 and soon after Mie, by Peter Debye (Debye, 1909).

It is the theory that solves one of the most important problems in the optics, that is the absorption and scattering of light by a small sphere of arbitrary size and refractive index. Moreover, it provides a first-order description of optical effects in non-spherical particles. Since the derivation of the differential cross section for particles in the Mie-Lorentz scattering regime is complicated and beyond the scope of this thesis, the idea to derive it and its detailed solution can be found in Bohren and Huffman (1998) while in the appendix only a brief derivation can be found (A.4).

Due to complex solution for particle scattering in microwave region the computation time for solving RTE can be long. Therefore it is of importance to create a good numerical solution due to a finite precision floating-point arithmetic of the computers. One of such models, Radiative Transfer 4 (RT4) (Evans and Stephens, 1995) is implemented in PAMTRA model used in this study and is presented below.

3.3 Radiative transfer model PAMTRA

Radiative transfer models for data assimilation are one of the most complex and computationally most expensive models. Nevertheless weather forecast centres require fast radiative transfer models to assimilate the huge amount of observations from various satellites. Moreover, RTMs are a key tool in testing the capabilities for new sensor designs as well as for the development of retrieval algorithms. Today, many radiative transfer models for calculating the RTE solution in the microwave region are available. However, the majority are developed only for some specific instrument. Publicly available are Atmospheric Transmission at Microwaves (ATM) (Pardo et al., 2001), Atmospheric Radiative Transfer Simulator (ARTS) (Buehler et al., 2005a; Eriksson et al., 2011; Buehler et al., 2018), Radiative Transfer for the

TIROS Operational Vertical Sounder (RTTOV)(ECMWF, Andersson et al., 1998) or Community Radiative Transfer Model (CRTM) (Ding et al., 2011).

Since the above models are mostly designed for a specific purpose (e.g. specific satellite instrument), there was a need for a more flexible model that will be able to calculate passive microwave (or active) radiative transfer from either ground, airborne or satellite applications. This was unified in PAMTRA foreward model that for the passive microwave uses RT4 Evans and Stephens (1995) code that enables polarized radiative transfer calculations for non-spherical and oriented particles. In this code the absorption model for water vapour continuum by Rosenkranz (1998) was implemented and further extended using modifications by Turner et al. (2009).

PAMTRA uses the approximation of a plane-parallel atmosphere, solves 1D RT equation and assumes a horizontally homogeneous atmosphere with hydrometeors. What distinguishes PAMTRA from other models is its flexibility to work on various Cloud Resolving Models (CRMs) outputs which apply one-moment or two-moment schemes, or in-situ measured hydrometer properties. Additionally, it allows implementation of various absorption and scattering models by the user, such as Liebe et al. (1993) or Rosenkranz (1998) for absorption or Self-similar Rayleigh Gans (Hogan et al., 2017), Mie or Rayleigh model for particles scattering.

With these characteristics, by using PAMTRA it is possible to simulate radiances at any given height in the atmosphere at any angle and its mentioned flexibility allows its usage for the evaluation of new NWP models or reanalyses using model-to-observation approach (Keil et al., 2006; Böhme et al., 2011). The code is written in FORTRAN90 but is wrapped by a Python framework that offers a more user friendly environment for setting up and running the simulations (Mech et al., 2020).

In order to solve the RTE, the effects of boundary conditions need to be known since the equation with the assumption of a plane-parallel atmosphere using finite differences, where layers between each plane are discretized is what is being solved in the model. For the upper boundary the background temperature is the cold cosmic temperature of 2.73 K. However, for the lower boundary, which is the surface, the emissivity, especially for lower frequencies of microwave has to be taken into consideration. The emission from the water surfaces (including foam, roughness produced by waves or swells) is relatively well known but for highly variable land surfaces (sea ice age, snow, canopy, soil moisture etc.) is more challenging. Therefore, the RTM needs to include assumptions on the nature of the surface reflection, such as Lambertian (fixed emissivity independent of viewing angle) or Fresnel (depending on the reflection and refraction of part of radiation with the medium). Moreover, to solve the RTE, gas absorption and single scattering properties for hydrometeors need to be specified in PAMTRA. This is done by providing PAMTRA with input data such as temperature, relative humidity (RH) and pressure profiles. The flow chart of PAMTRA RTE calculation is shown in the Fig. 3.5 and explained in the following text.

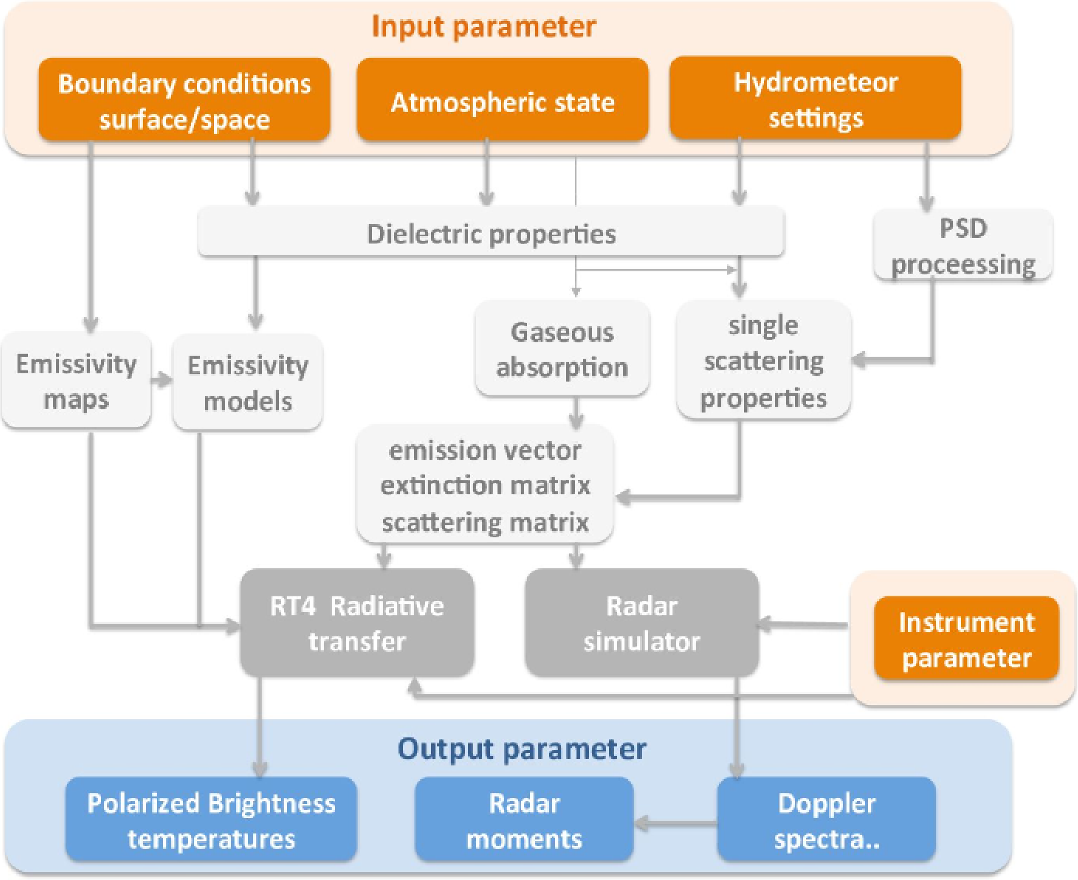

Figure 3.5: *Flowchart of the PAMTRA steps in the calculation of the RTE. Orange boxes are needed input parameters, white and gray boxes denote various models for hydrometers scattering, surface emissivity or gaseous absorption, while the blue boxes stand for the output parameters of PAMTRA (Mech et al., 2020)*

.

PAMTRA work flow

Atmospheric state including hydrometeors

As mentioned above, to solve RTE, PAMTRA needs input data describing the atmospheric state which is provided in the form of vertical profiles of temperature, RH and pressure. Additionally atmospheric information close to the surface (such as: wind speed, 2 meter temperature and specific humidity) can as well be given as an input. Beside these variables, to calculate simulations for "cloudy" atmosphere a hydrometer description, such as cloud liquid water and ice, rain, snow and graupel can be given as input as well. These variables can be defined for each layer of the atmosphere and are described by the particle size distribution (PSD), also called drop size distribution (DSD).

Particle size distribution (PSD)

PSD is the distribution of the particle number of different sizes (diameter or volume). For a considered volume, the PSD is often characterized by an exponential decrease of drop number for increasing drop size. Often, due to its flexibility modified gamma distribution (MGD) (Deimendjian, 1963) is used and is given by:

$$n(r) = ar^{\alpha} e^{-\beta r^{\gamma}} \tag{3.52}$$

where α, β and γ are positive constants. The exponential distribution and the three-parameter gamma distribution (obtained by setting α and b to 0 and γ to 1) is used for description of snow and rain (Marshall and Palmer, 1948):

$$N(r) = N_0 e^{-qr} \tag{3.53}$$

where N_0 and q are intercept and slope parameters, respectively.
For PSD recently Hansen and Travis (1974) and Ulbrich (1983) PSD are also used in RTM models for Earth and exoplanets atmosphere (Sterzik et al., 2020; Bailey et al., in preparation).
In PAMTRA, few distributions are available that can be set up by user including: monodisperse, the inverse exponential, the MGD and log-normal distribution. In the PSD calculation, one or two parameters are left unknown depending on the settings. PAMTRA can derive these parameters by resolving the system of equations for the moments, M_k that are given by the NWP or reanalyses models output. Currently, PAMTRA can take three different quantities related to the PSD moments: 1) total number concentration $N_T = M^0$, 2) the effective radius $r_e = M^3/2M^2$ and 3) the mass mixing ratio $w = aM^b$ (where a and b are the parameters of the power-law defining the mass-size relation $m(D) = aD^b$) (Mech et al., 2020).

Boundary conditions

As mentioned above, for the upper boundary cosmic temperature of 2.73 K has been taken. However for the surface emissivity with high variability depending on the surface type, and therefore affecting the radiation by surface reflection and scattering, different relations have been implemented.
In PAMTRA, there are different kind of surfaces considered, such as Lambertian, Fresnel or specular. A Lambertian surface defines a diffusely reflecting surface where surface appears equally bright from all viewing angles (Nayar et al., 1989). For land surfaces, the specular reflectance (where angle of incidence and reflection are the same such as of freshly fallen snow (Harlow, 2009)) is used together with the surface emissivity derived using the Tool to Estimate Land Surface Emissivity from Microwave to Submillimeter Waves (TELSEM^2) tool (Aires et al., 2011b; Wang et al., 2017). TELSEM^2 is linked to a climatology of monthly emissivity estimates and provides a parameterization of the surface emssivity up to 700 GHz. It is derived from satellite observations from SSM/I, SSMIS and AMSU-B. Reflectance over water surfaces is affected by wind induced roughness and over sea and ocean surfaces additionally by salinity. Therefore in PAMTRA, the Tool to Estimate Sea-Surface Emissivity from Microwave to Submillimeter Waves (TESSEM^2) (Prigent et al., 2016) expanding community model FAST microwave Emissivity Model (FASTEM) (Liu et al., 2011) to higher frequencies is implemented. For a model to know over which kind of surface a T_b has to be calculated, a landmask has to be provided. For a purpose of this thesis, this has been taken from the ASR.

Gaseous absorption

In the atmosphere various gases are present that interact with the radiation and the absorption coefficient describing that interaction have to be included in PAMTRA. The absorption of gases relevant for microwave region can be divided in absorption by resonant lines of H_2O, O_2, N_2 and O_3 and water vapour continuum. In PAMTRA, as mentioned above, Rosenkranz (1998, 2015) absorption model was used for water vapour continuum while Liljegren et al. (2005) is used for resonant line of H_20 at 22 GHz.

Single-scattering properties

For a plane-parallel and optically thin atmosphere with no thermal sources, the probability of light being scattered more than once is very small so that multiple scattering, with good approximation, can be ignored. In PAMTRA, for liquid hydrometeors such as cloud droplets, drizzle or rain drops, the single-scattering properties are calculated using Mie scattering. To calculate liquid water refractive index, PAMTRA utilizes Turner et al. (2016) model. However, other models, such as Ray (1972); Liebe et al. (1993); Stogryn (1995) and Ellison (2006) are also possible and are left to users choice.

For frozen hydrometeors, such as ice crystals, graupel, snowflakes or rimed particles that have different orientations and densities, since no snowflake is identical, complexity of their natural interaction with radiation is still under research and presents large uncertainties in radiative transfer models. For ice mass retrieval, the larger error follows from the uncertainty of the microphysical state of the particle, such as shape, size, phase and orientation (Eriksson et al., 2015). And while shape is not a critical aspect for purely liquid particles, the deviation from a strict spherical shape increases with droplet size and fall speed. However, for frozen hydrometeors, particle shape is very variable (Heymsfield and McFarquhar, 1996; Heymsfield et al., 2013). Moreover, a small volume will never consist of only one particle of one phase, but it is a rather a mixture of particles of different properties.

Since it is not possible to know all the microphysical properties of every single particle in rapidly changing volume mixture a shape model is used. For ice, usually consideration of solid spheres (Mie theory) is used or soft particle approximation (SPA) for a mixture of ice and air, where ice particles are considered as spheroids (treated through T-matrix by Mishchenko et al. (1996) and air fraction is fixed (or derived from some parametric relationship between particle size and effective density) (Eriksson et al., 2018). Single-scattering properties of frozen hydrometeors with arbitrary shape can be calculated using DDA. There are couple of DDA databases available such as Liu (2008); Hong et al. (2009) and Nowell et al. (2013) that are publicly available and which radiative transfer models can incorporate.

In PAMTRA, for DDA method it is possible to choose between Liu (2008) and Hong et al. (2009). However, recently a novel approximation, called Self-similar Rayleigh-Gans Approximation (SSRGA; Hogan and Westbrook 2014; Hogan et al. 2017) has been included in PAMTRA and is the model used in this thesis for description of ice and snow particles scattering properties of arbitrary shapes. In this approximation, the electric field experienced at any point in the particle is approximated by the incident field and neglecting the interaction between dipoles. The backscatter cross-section than can be numerically estimated from a 1D description of the structure of the particle in the direction of the incident wave (Hogan et al., 2017). In Hogan and Westbrook (2014) it was shown that for realistic aggregates, a 1D function has a self-similar structure and hence that its power spectrum can be represented by a power law.

After, atmospheric state, boundary conditions and hydrometer description have been provided and models for calculation of gases and hydrometers interaction with radiation has been described, the RT4 code described above can be utilized to calculate desired product. In this thesis, a desired product are simulated T_bs from satellite instruments, namely AMSU-B and MHS. In order to produce simulated T_bs the input for PAMTRA was taken from ASR version 2 described in Chapter 2 (Section 2.3).

4 Methods

Satellite observations of brightness temperature and IWV allows us to gain a deeper understanding of the variability and trends of water vapour in the Arctic. However, there are also a number of challenges. To investigate spatiotemporal changes of observed and simulated T_b and the reanalysis IWV, long term data records first need to be processed. Due to satellites change in performance over time certain channels show errors in T_bs introduced by increased noise equivalent differential temperature (NEΔT). NEΔT can be defined as the standard deviation of the calibrated scene T_b when viewing a uniform scene of constant temperature such as cold target - space view for samples of defined integration time Thus, T_b from channels affected by this kind of error needs to be removed from the data record. Additionally, orbital observations of T_b from cross-track satellite instruments need to be interpolated on a uniform spatio temporal grid.

T_b observations are used directly to study WV variability and trends. In order to compare with ASR, synthetic T_bs are calculated using the forward model PAMTRA. To better relate T_bS to water vapour, column values can be calculated from ASR. This chapter explains the methods to fulfill aforementioned tasks, and provides the description of the set up of PAMTRA for this study with a help of a case study.

4.1 Processing of AMSU-B and MHS FCDR

In order to develop a long term data set from satellite instruments, AMSU-B and MHS, certain processing of these data has to be done. Since the orbital data received from these instruments are satellite's swaths, they do not posses the same geographical locations nor grid at which the successive swaths can be easily combined. Therefore, it is necessary to first put all individual pixels on a common grid. This has been performed by resampling the data to a predefined grid. For the purpose of this thesis, the common grid is the ASR's north-polar stereographic projection with $\sim$ 15 km horizontal resolution. A method for data resampling has been adapted from Python SatPy library using the nearest-neighbour method from the pyresample module (Nielsen, 2020).

The instruments, as mentioned in Chapter 2 have 5 channels scanning at 89 GHz, 150 GHz, 183.31 ± 1 GHz, 183.31 ± 3 GHz, 183.31 ± 7 GHz frequencies for AMSU-B and similar for the MHS, where frequencies 157 GHz and 190.31 GHz were used instead of the AMSU-B's 150 GHz and 183.31 ± 7 GHz. The signal for these channels is received at 90 ° scanning angles, 48.5 ° to the left and 48.5 ° to the right side of the nadir point. This means, that the viewing angle is different for different pixels along the scan line and at the edge of the swath a wider layer of the atmosphere is scanned.

Since the atmospheric limb effects should depend only on the viewing angle, they should on average be symmetric around the nadir point. This, however does not have to be the case in the real world scenario and due to inhomogeneity, instrument and surface effects significant scan asymmetries can be present. These effects can lead to a limb darkening or limb brightening effect of T_b's at the edge of the swath (Goldberg et al., 2001; Greenwald et al., 2018).

The analysis of the effect of the viewing angle on T_b has revealed that scan asymmetries can be as high as -9.4 K (-2.95 K) for 183.31 ± 3 (183.31 ± 7) GHz channel on the NOAA-15 (Buehler et al., 2005b). Similar behaviour with lower effect (of 1 K to 3 K for the three sounding channels) is noted for the other satellites carrying AMSU-B and MHS instruments. Moreover, it was shown that the asymmetries were progressing during the studied 2000 - 2005 period. A cause for these asymmetries is not yet completely understood but partial explanation could be due to changes in the RFI characteristics (Buehler et al., 2005b).

4.1.1 Spatial resampling

The effects of limb darkening and brightening mentioned above have to be removed because the effect of 1 K difference in the upper troposphere can lead to a difference of 7 % in relative humidity (Buehler, 2005). Moreover, in studies for the detection of deep convective clouds and convective overshooting it was found that pixels at the edge of the swath sensed at a higher viewing angle have a profound effect on the detection algorithm (Hong, 2005; Rysman et al., 2017; Funatsu et al., 2018) which could lead to a less reliable screening of the convective cores for humidity retrieval.

Therefore, in addition to resampling, 9 pixels from each side of the swath have been removed. An example of removing and resampling for one orbit is shown in the Fig. 4.1. It can be noted that the effect of resampling for the full swath width (-0.29 K)leads to a minor changes in mean T_b for the reduced swath width (-0.05 K).

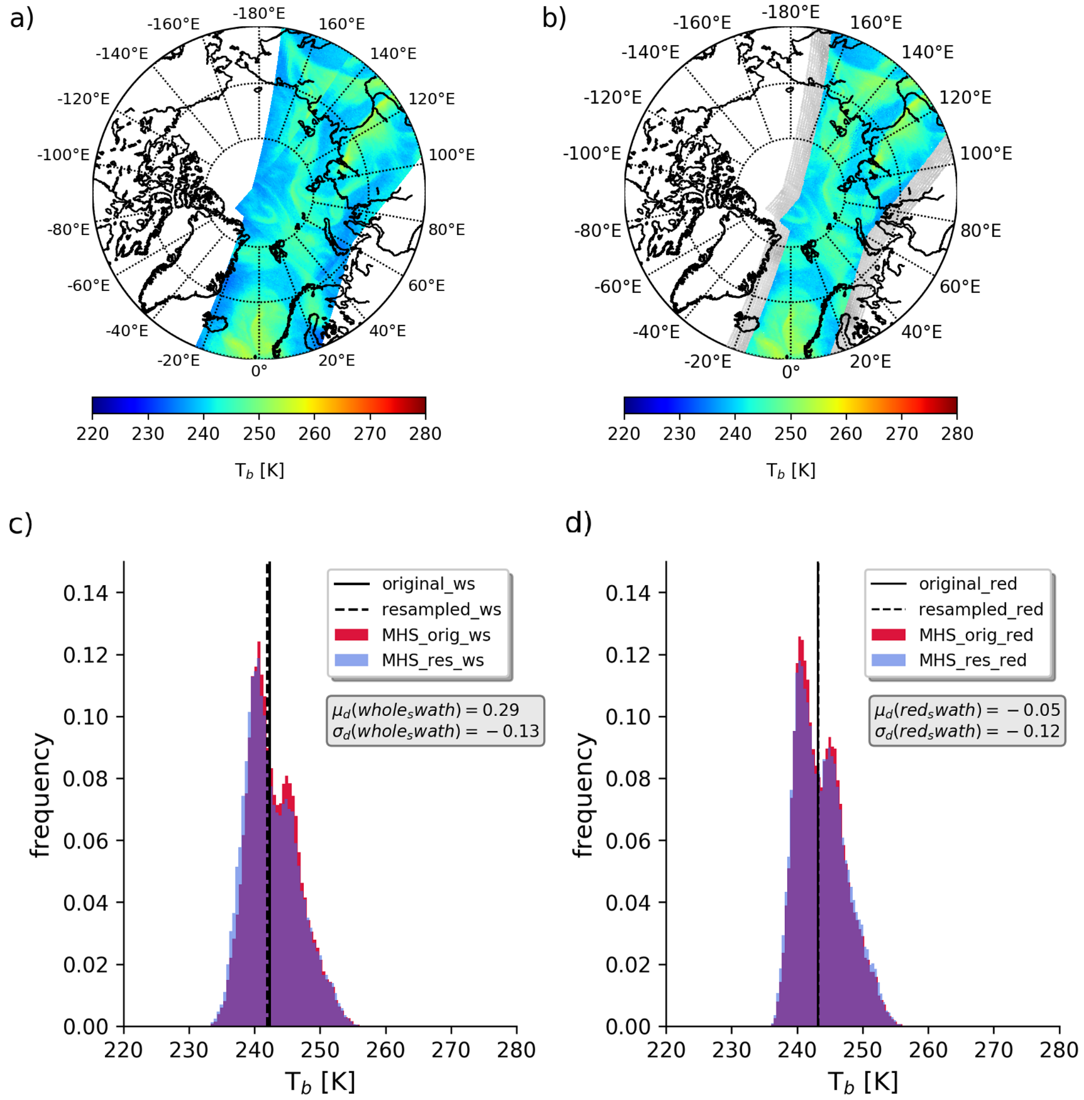

Figure 4.1: *T_b at 183.31 ± 1 GHz for one orbit from NOAA-17 on 2 May, 2007 between 02:27 and 04:22 UTC. On the upper panels, the full width of the swath of the original data (a) and the resampled one with the cut out parts of the swath in gray (b) are shown. The histograms show the original (red) and the resampled (blue) full swath width (c) and the original and resampled reduced swath width for 9 pixels (d). Vertical lines show the median for the original (full line) and the resampled (dashed line)*

4.1.2 Temporal resampling

In order to make the analysis for temperature trends and their variability easier, hourly data have been produced from ∼ 90 minute orbit files. Since start and end time of each orbit are not always the same this can lead to an hour for which there is no coverage over 60 °N for that specific satellite. This, however, does not mean that the data for that hour are not available from other satellites.

The time resampling of one orbit file is presented in Fig. 4.2. This particular orbit from NOAA-17 (2 May, 2007) starts at 02:27 UTC and ends at 04:27 UTC, meaning that from this orbit three files for three different hours are produced. To obtain hourly data the orbit is cut between the start time and the next full hour, in this case at 03:00 UTC. The next file produced is a file of T_bs between 03:00 UTC and 04:00 UTC and the last one is between 04:00 and 04:27 UTC. Missing data over the Arctic between 03:00 and 04:00 UTC means that this satellite, NOAA-17, was scanning latitudes lower than 60 °N.

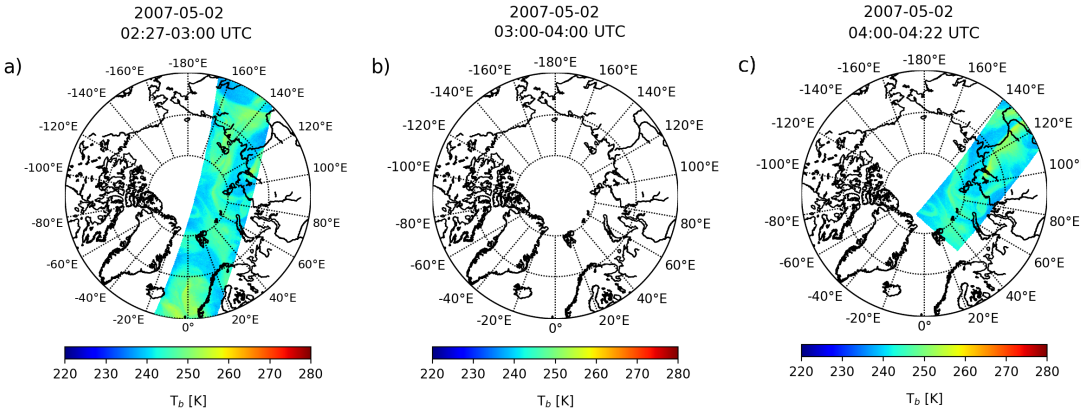

Figure 4.2: *Same orbit as in Fig. 4.1 illustrating time resampling for three different hours.*

4.1.3 Removal of data strongly affected by increased NEΔT

The FCDR data produced by NCDC, described in detail in Chapter 2 (Section 2.2.2) are used for the purpose of this research. However, not all of the available data from FCDR were used due to certain issues with satellite's performance during their lifetime. One of the issues is the error in received T_b introduced by increased noise equivalent differential temperature (NEΔT). This has been investigated in a study by Hans et al. (2017) and is explained below.

Generally, for the instruments used in this study, two NEΔT are derived, cold and warm. The cold and warm NEΔT refer to the count noise originating from statistical estimation in the number of counts (digitized voltage output) from the instruments view on the cold (deep space view (DSV)) or warm calibration target (internal on-board (OBCT)). This fluctuation in the number of counts corresponds to radiometer sensitivity dT, when looking at cold or warm scenes. It is worth mentioning that by using the DSV counts, the T_b contributing to antenna temperature, T_a, is very weak and the remaining temperature contribution to the T_a is of instrumental origin. The NEΔT was investigated (Hans et al., 2017) for the lifetimes of the satellites and the best time to use the data is presented in table 3.

Table 3: *AMSU-B and MHS year for certain frequency channels and satellites after which data is not recommended to use due to issues reported in Hans et al. (2017). NOAA satellites are designed in short by N and the satellite number.Dash/none designation in table represent data that are usable/not usable for the entire period.*

FREQUENCY	N15	N16	N17	N18	N19	METOP-A
183.31 ± 1	2001	2005	2009	-	none	-
183.31 ± 3	2003	2005	2009	-	-	-
183.31 ± 7 (190.31)	2007	2005	2009	-	-	-

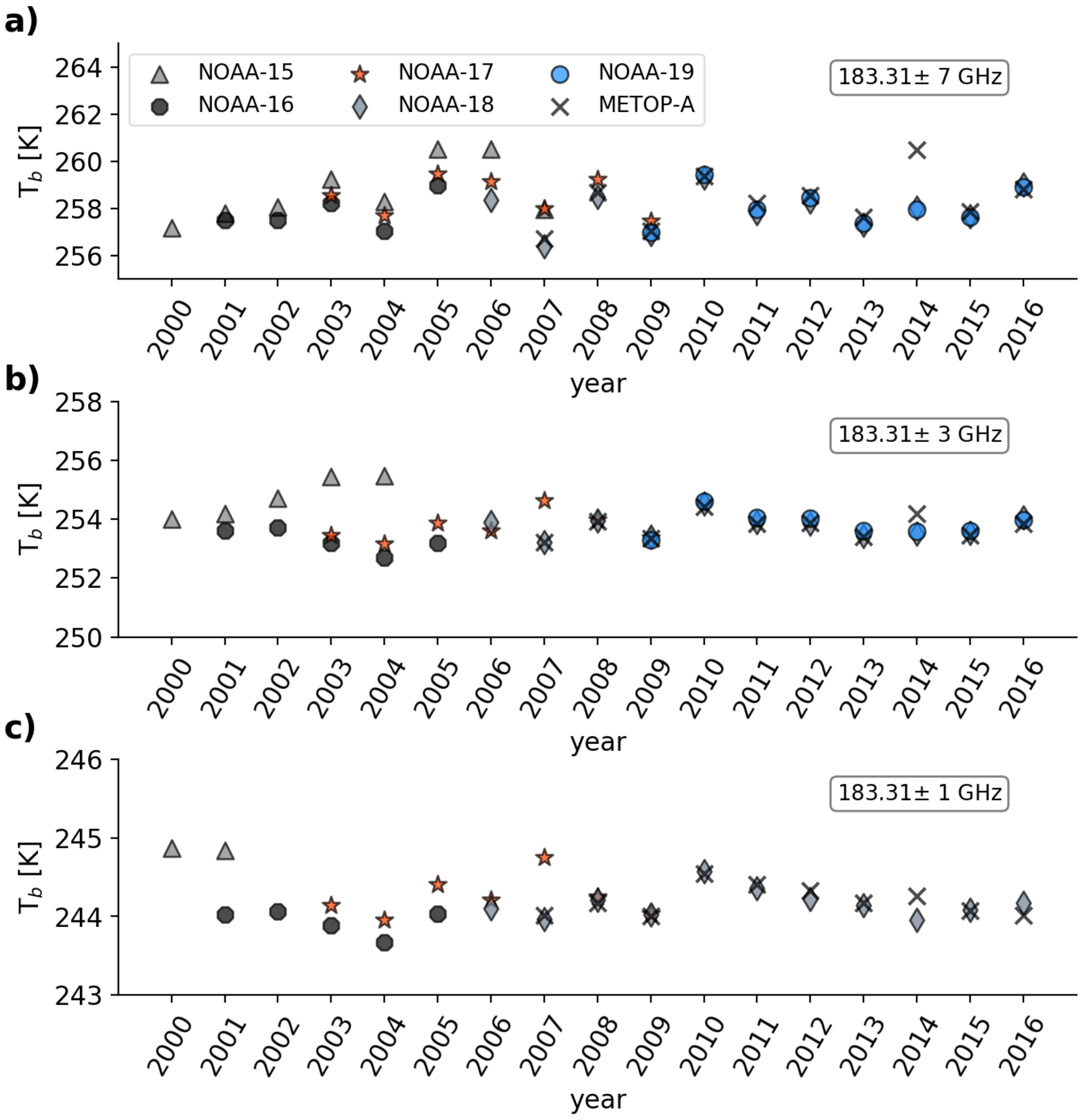

Figure 4.3: *Monthly mean Arctic T_bs for May from NOAA-15 to NOAA-19 and METOP-A satellites for three frequencies channels around 183.31 GHz after removal of those years and frequencies for which the respective satellite suffered from substantial noise effects.*

4.2 Calculation of long term data set of IWV from ASRv2

In this research, the interest is on spatiotemporal changes of the IWV that is defined by:

$$IWV = \int_{z_i}^{z_f} \rho_v(z)\, dz \tag{4.1}$$

where ρ_v is the absolute humidity, z_i and z_f are the lowermost and uppermost height of reanalysis pressure levels. The above equation can be expressed in numerical form as:

$$IWV = \sum_{i=0}^{N-1} \frac{{\rho_v}^{i} + {\rho_v}^{i+1}}{2} \left(z^{i+1} - z^{i}\right) \tag{4.2}$$

However, IWV is not directly provided in the ASRv2 and it has to be calculated by using variables that are provided, namely T, geopotential height (GPH), terrain height (orography) and RH.

Moreover, ASRv2 has pressure level coordinates, meaning that vertical profiles are given from the "base" surface, which in the ASRv2 is always 1000 hPa. This, however causes the profiles to be provided at 1000 hPa even in the case of a high mountainous area where the first pressure level in reality is quite smaller (eg. Greenland elevation of $\sim$ 3200 m). Therefore, the ASRv2 vertical profiles had to be filtered by an orography following field first in order to prevent overestimation of IWV. Besides modifying T and RH profiles, it is necessary to perform this procedure for other variables (pressure and hydrometeors mass mixing ratios) that are used as input for PAMTRA. This procedure is presented in the following text.

Deriving geometrical height filed

Creating the geometrical height field can be achieved by subtracting the topographic height in units of meter from the GPH which is provided in units of meter by the ASRv2 as well. This is possible since GPH is given with:

$$GPH = \frac{1}{g_0} \int_{surf}^{z} g(\phi, z) dz \tag{4.3}$$

where g_0 is the Earth gravity constant at standard mean sea level ($g_0 = 9.80991 m/s^2$), $g(\phi, z)$ is the acceleration due to gravity that is changing with altitude and z is the geometric altitude. The term under the integral is the geopotential, Φ, which is the gravitational potential energy per unit mass at the elevation z. In this way, the geopotential height can be explained as the gravity-adjusted height.

After the geometric height is calculated, the vertical profiles can be cut for the levels that show invalid values of height. The result for the modified temperature field for the mountainous region in Siberia between 80° - 100° E and 60° - 70° N is presented at the Mercator projection in the Figure 4.4. It is worth mentioning that the elevation in this region can be up to 1200 m which corresponds to about 850 hPa in this region. This means that parts of the vertical profiles below this pressure field will be filtered out.

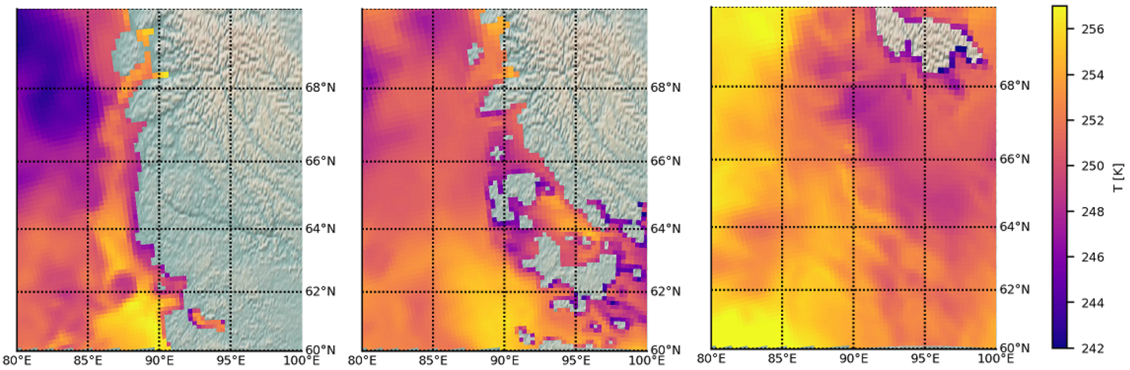

Figure 4.4: *Orography following temperature field from the ASRv2 for 7 Jan, 2009 at 0000 UTC for the 1000 hPa (left), 950 hPa (middle) and 900 hPa (right) pressure levels*

Similar calculation of geometric height can be achieved by using the mean sea level pressure (MSLP) where invariant pressure fields from the ASRv2 can be subtracted from the MSLP and for the layers with invalid values of pressure, profiles can be filtered out.

4.3 Case study simulation: Polar low - 7 Jan, 2009

A polar low case that occurred on January 7, 2009 has been chosen to show both, the ability of the reanalysis to resolve small scale processes and PAMTRA's ability to simulate corresponding T_b. This specific case was chosen because it was one of the most severe storms in terms of wind speed that reached 35 m/s and the system formed two cores of low pressure that present a great challenge in tracking algorithms.

4.3.1 Setting up PAMTRA forward model

Following the PAMTRA flow chart (Figure 3.5), after profiles from ASR have been processed for input to the PAMTRA, additional settings have to be given to the forward model such as setting microphysical specifications for different types of hydrometeors. In the ASRv2, there are 5 types of hydrometeors given as dimensionless mass mixing ratios: cloud liquid water, rain water, snow, ice and graupel.

The microphysical specifications to PAMTRA need the moments of the PSD, either the total number concentration, the effective radius, the mass concentration, or a mixture of any two. Additionally, the diameter of the smallest and larges particles in order to calculate absorption and scattering properties for a given class of hydrometeors as well as the the a and b parameters from the mass-size relation (in SI units) have to be provided. After these specification have been prescribed, the scattering model has to be chosen for liquid and frozen hydrometeors.

If only liquid phase is included, the density and the a and b parameters of the mass-size relation will be ignored as hydrometeors are assumed spherical. The aspect ratio and canting angle (hydrometeor's orientation relative to some fixed frame of reference) are set as missing values because single scattering properties are calculated with Mie theory which assumes spherical particles and uses a log normal distribution. For snow, an exponential PSD is chosen with the intercept (slope) parameter that is temperature dependent. Moreover, for frozen hydrometeors, SSRGA scattering model has been chosen.

The boundary conditions for top and the bottom layer of the plane-parallel atmosphere as mentioned in the Section 3.3.1 have to be prescribed. This has been done by including the surface emissivity as monthly means for land and sea using the TELSEM^2 (Wang et al., 2017) and TESSEM^2 (Prigent et al., 2016) models. Moreover, for the sea ice covered surface the emissivity value of 0.75 has been prescribed following Wang et al. (2017).

In PAMTRA T_b are simulated for 30 different angles starting from 0° (nadir view) to 180° (space view). Later, the simulated T_b's can be interpolated to the closest observation angles.

4.3.2 Simulations of T_b

In Fig. 4.5 the observations (top) and simulations (bottom) of T_b for the mentioned polar low case at 09:00 UTC are presented for the 5 AMSU-B frequencies. PAMTRA simulated T_bs have been interpolated to the closest observations angles using the nearest-neighbor method to make simulations closer to the observations. Figure 4.5 also shows column amounts of WV and the different hydrometeors to illustrate their contribution to T_b.

Without an atmosphere T_b would be determined by surface emissivity and temperature. However, in cases of a thick cloud or precipitation, the atmosphere is not completely transparent at these frequencies and the signal from cloud and precipitation is significantly contaminating the sounder's field of view (Eyre, 1990; Engelen and Stephens, 1998; Greenwald and Christopher, 2002). A strong liquid signal with enhanced T_b for the 150 GHz and slightly weaker for 89 GHz channel can be noted around polar low cores at 72°N 28°E and 72°N 35°E. Usually this signal is coming mostly from the surface.

This contamination of the field of view is present in the case of this polar low that exhibits a thick precipitating cloud band surrounding the warm core. This contamination is most notable for the 183.31 ± 7 GHz frequency channel, where convective cores containing frozen hydrometeors lead to strong scattering and are therefore visible as a decrease in T_b.

At higher frequencies and thus higher altitudes, a strong signal from frozen hydrometeors (mostly ice) can be noted as a strong depression in T_b that can show differences of 40 K between the warm core of the cyclone and the outer cold cloud band. In the simulations, the general structure of the polar low is well captured. However, some features are missing such as the more pronounced liquid signal at 150 GHz and the double convective cores at higher frequencies for which the simulations show only the bigger one. The liquid water signal manifested in the simulations as increased T_b at 89 and 150 GHz frequencies (Fig. 4.5 middle) is, however, in accordance with the liquid water input (Fig. 4.5 bottom) from ASRv2 given for the PAMTRA simulations.

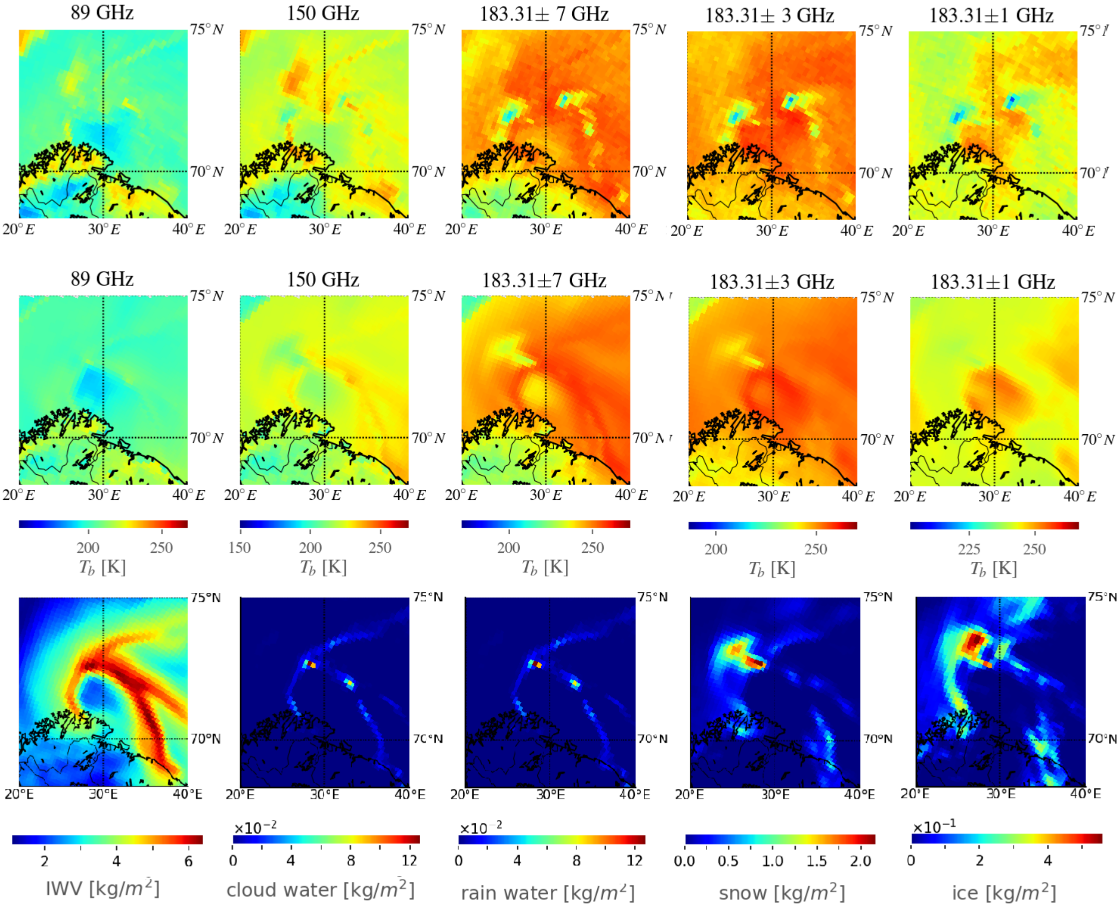

Figure 4.5: *Polar low case observed on Janury 7, 2009 at 09:00 UTC with AMSU-B (top) observations and PAMTRA simulations (middle). Shown are all 5 frequencies channels from AMSU-B, in order from left to right: 89 GHz, 150 GHz, 183.31 ± 7 GHz, 183.31 GHz ± 3 GHz and 183.31 ± 1 GHz. The bottom row shows column integrated values of water vapour, cloud and rain water, and of snow and ice (from left to right)*

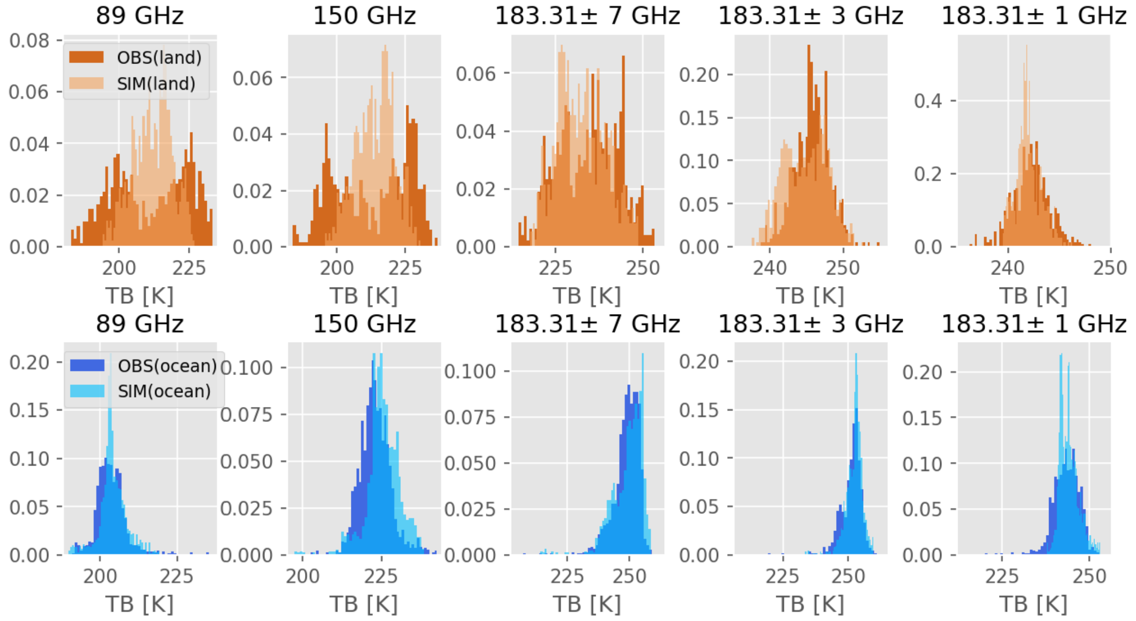

Figure 4.6: *Histograms of observed (dark shade) and simulated (light shade) T_bs over land (top) and sea (bottom) from 5 ASMU-B frequencies in the same order as in the Fig. 4.5*

A similar behaviour can be found for the higher frequencies considering the integrated values of frozen hydrometeors, where high amounts of snow (up to 4 $\mathrm{kg/m^2}$), ice (0.5 $\mathrm{kg/m^2}$) and graupel (0.035 $\mathrm{kg/m^2}$) are represented as one convective core. A possible explanation for these discrepancies between observations and simulations could be due to the parameterization of the precipitation processes in the ASRv2.

Moreover, a sea-ice signal at a 89 GHz frequency (Fig. 4.5) with enhanced T_b can be noted in the upper left corner of the observations. This is not present in the simulations as ASR classifies these pixels as open ocean. The general good agreement between the observations and the simulations is also shown for both land and ocean separately in Fig. 4.6 for all AMSU-B frequencies. A better agreement between the simulations and the observations is achieved over ocean compared to over land or a sea-ice covered surfaces. This example underlines the challenge in the representation and parameterization of highly variable surface emissivity (sea-ice, fresh snow, soil moisture etc.) in ASR, especially close to the abrupt change of orography.

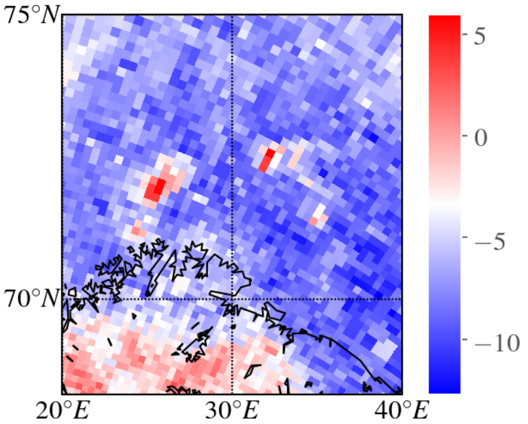

Figure 4.7: *Brightness temperature difference between 183.31 ± 1 and 183.31 ± 3 GHz channels for the same scene as in Fig. 4.5. PL convective cores are visible in red.*

The feature of the strong T_b depression in the convective cores of the polar low mentioned earlier can be used for the detection of deep convective clouds where different temperature thresholds are chosen, depending on the study. Some of the first studies based on thermal IR channels were done by Hall and Vonder Haar (1999), Fu et al. (1990), Gettelman et al. (2002) and Liu and Seo (2013). More important, it was found by Burns et al. (1997) using microwave frequencies, that the difference between 183.31 ± 1 and 183.31 ± 3 GHz channels can be used for the detection of convective cores which can be filtered out subsequently for water vapour retrievals. Later on this method was extended by Hong (2005) who included a lower frequency channel, namely 183.31 ± 7 GHz, and found an inverse relation:

$$\Delta T_{17} \geqslant \Delta T_{13} \geqslant \Delta T_{37} > 0K. \tag{4.4}$$

where:

$$\begin{aligned} T_{17} &= T_{b,183\pm1} - T_{b,183\pm7}, \\ T_{13} &= T_{b,183\pm1} - T_{b,183\pm3}, \\ T_{37} &= T_{b,183\pm3} - T_{b,183\pm7}, \end{aligned} \tag{4.5}$$

This detection is presented in Fig. 4.7, where red clusters of ΔT_b represent the convective cores of a polar low.

5 Brightness temperature as a proxy for water vapour in the Arctic

The previous chapters have explained the importance of studying water vapour in the Arctic as well as the methods used for this study. This chapter addresses the first hypothesis:

> **Hypothesis 1**: Long-term brightness temperatures (T_bs) can be used as a proxy for water vapour spatiotemporal trends in the Arctic.

using the following approach. Firstly observations of long term (2000-2016) AMSU-B and MHS climate data records and ASRv2 IWV are analysed as monthly means in order to check for their long-term spatial distribution resemblance. Secondly, the analysis of significant trends including their regional distribution is performed followed by sensitivity studies of satellites sounding frequencies that explain how T_b relates to water vapour. This is further substantiated by deriving synthetic T_b from ASRv2 using the forward operator PAMTRA. In this way the relation between long-term IWV and T_b spatiotemporal trends from ASRv2 will be illustrated.

It is worth mentioning that T_b is mainly affected by temperature and humidity. However in this thesis the focus is on analysing water vapour and the possibility for it to be approximated by T_b. Therefore this part of the thesis addresses hypothesis one. Analysis has been done for both months of interest, namely May and January. As it was mentioned in the beginning of this thesis, January has been chosen for the investigation as a representative month for the winter season when Arctic amplification is the strongest. During January polar night is present and the atmosphere is relatively stable with strong temperature and humidity inversions but with reduced cloud cover in comparison to other seasons (Chernokulsky and Mokhov, 2012; Kay et al., 2016). Contrary to January, solar radiation in May persists through almost 24 h a day and the Arctic atmosphere is becoming more unstable and turbulent. The warmed atmosphere leads to the beginning of the sea-ice melt. This further leads to higher amounts of water vapour and consequently more clouds formation. Additionally, the amount of moisture transported into the Arctic by atmospheric rivers increase (Nash et al., 2018). Due to these differences these two selected months are the focus of the following research.

5.1 T_b spatiotemporal trends and variability

This study focuses on months of January and May. However, in order to get a general overview, the Arctic wide ($> 60°$) yearly cycle as a 17-year (2000-2016) mean of T_b is presented in Fig. 5.1. Herein composites of AMSU-B's and MHS's T_b at 183.31 ± 3 GHz are shown for all months while composites of T_bs from 183.31 ± 1 GHz and 190.31 GHz frequency channels are shown only for the months of interest (Fig. 5.2), and their yearly cycle can be found in the appendix (B.1). For lower frequencies further away from the central one (183.31 GHz), the two instruments, AMSU-B and MHS have slightly different frequencies. Therefore composites of T_b's for 183.31 ± 7 (AMSU-B) and 190.31 GHz (MHS) are besides their joined product of T_b, as well shown separately (B.1).

Although these two frequencies are very similar, the differences between them can be of 1 K for May and slightly greater than 1 K for January for an arbitrary chosen Arctic profile (Fig. 5.3). Moreover, the 183.31 ± 7 GHz frequency channel senses slightly deeper into the atmosphere than the 190.31 GHz frequency channel and therefore could be more affected by hydrometers. Furthermore, the post processed dataset from these two instruments is available for different time periods. Thus AMSU-B's 183.31 ± 7 GHz frequency channel has a valid period between 2000 and 2009 while MHS's 190.31 GHz frequency channel has a valid period between 2006 and 2016. January and May T_b means for these two periods and frequencies as well as the difference for their overlap period (2006-2009) are shown in the appendix (Fig. B.3).

In the Fig. 5.1, 183.31 ± 3 GHz mean T_b are shown. What can be identified is that the mean temperature difference between winter and summer months is about 45 K. The reason for this, besides generally warmer atmosphere, is the altitude from which this channel (183.31 ± 3 GHz frequency) receives most of its signal. The altitude ($\sim$ 7 km) emits most strongly during summer while during winter, when the atmosphere is very dry, this channel can penetrate deeper through the relatively transparent atmosphere and receives strongest signal from much lower altitudes, around $\sim$ 5 km. However, parts of the signal can also be received from the high topography surfaces, thus the strong signal over Greenland is much more pronounced during winter than during summer (especially in July) when the atmosphere gets more opaque. The vertical contribution to the T_b will be investigated in more detail through weighting functions later in section 5.2. Moreover, due to the generally cold and dry atmosphere, larger variability can be identified during winter than during summer months. During winter, differences between most of the Arctic land and ice covered area and North Atlantic and Bering Strait can be of 20 K. Especially cold areas are noted over high orography such as Greenland or Verkhoyansk range (in Siberia) regions while especially warmer structures are noted over variable topography of the Yukon range and McKenzie river basin. The reason for these warmer structures could be due to subpolar high pressure systems and low-level temperature inversions in this region (Cao et al., 2008). These are not observed in summer due to more homogeneous atmosphere at the altitudes from which the signal for this channel is received.

In figure Fig. 5.2 (left), T_bs at 183.31 ± 1 GHz frequency are shown. What can be immediately noted is that differences between May and January T_b are not as large as the ones seen for 183.31 ± 3 GHz frequency. The reason for this, as for the previous

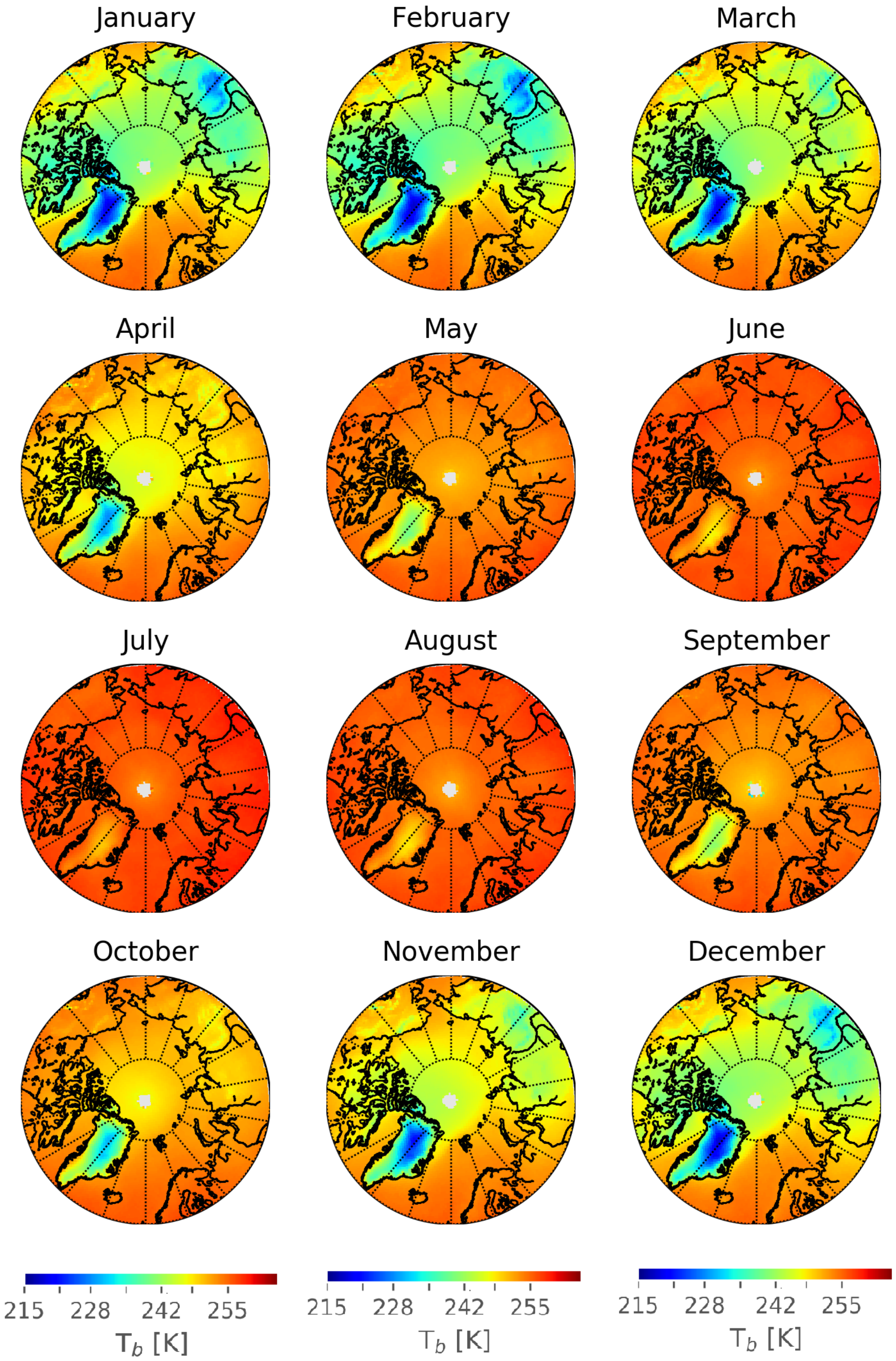

Figure 5.1: *Mean monthly T_b from all available satellites for 183.31 ± 3 GHz during 2000-2016 period.*

channel, is the signal emission altitude, which in May is ~ 10 km and gets lower during winter, ~ 9 km. For such high altitudes, especially in the Arctic, where amounts of water vapor can be found only in trace amounts, this sounding channel shows differences, excluding high Greenland region, between summer and winter months of at most 12 K. However these high altitudes, are for Arctic regions already part of upper troposphere-lower stratosphere region (UTLS). Therefore, T_b temperature is beside water vapour affected by dynamical processes such as strong jets and stratospheric meridional circulation.

T_b for the 183.31 ± 1 GHz frequency, studied over a period of 17 years, shows coldest regions during winter months over Siberia, Canadian archipelago and Central Arctic while warmer regions are concentrated over Alaska, North Atlantic and North Pacific. During summer this difference in the T_b field is not so pronounced. One possible explanation could be lower tropopause height observed in summer which is characterized by higher temperatures (Kishore et al., 2006). Another reason could be the more opaque atmosphere due to Sun light which drives stratospheric chemistry through photochemical processes and subsequently increases the UTLS water vapour. Some of the processes such as breaking of methane (CH_4) with hydroxide (OH) or molecular hydrogen (H_2) and CH_4 oxidation (Parmentier et al., 2013; Thölix et al., 2016; Winterstein and Jöckel, 2020) for a consequence have formation of the water vapour. However, stratospheric chemistry is very complex and the explanation of these processes is beyond the scope of this research.

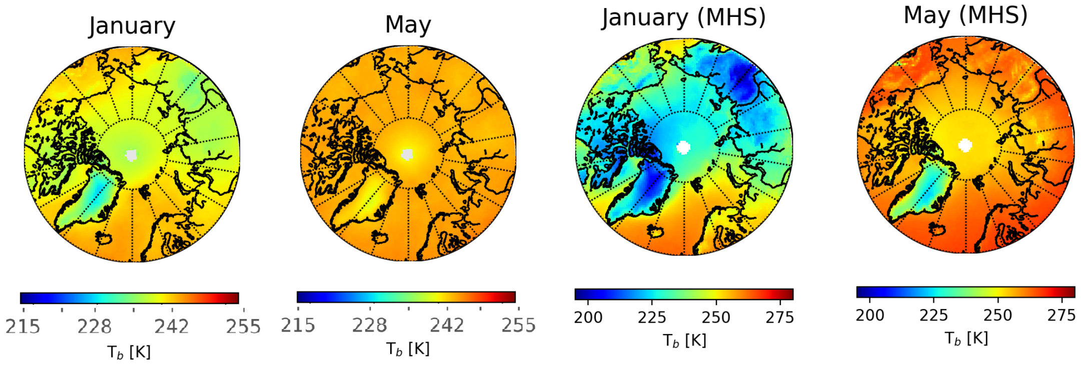

Figure 5.2: *Mean monthly T_b composites from all available satellites for 183.31 ± 1 GHz during 2000-2016 period for January (leftmost) and May (left) and 190.31 GHz frequency channel for January (righ) and May (rightmost) only from MHS during 2006-2016 period.*

Fig. 5.2 (right) shows T_b for the 190.31 GHz channel for January and May. A stronger variability in comparison to T_b maps from the 183.31 ± 3 GHz channel, during both months can immediately be noted. This variability is more pronounced in between months, which can be of 70 K, but as well intramonthly. During January a difference between cold Siberia or Canadian Archipelago (~ 200 K) and warmer North Atlantic can be of 65 K. The reason for this, as for previous channels, is the signal emission altitude. This channel can penetrate deeper than those mentioned above (183.31 ± 1 GHz and 183.31 ± 3 GHz). Therefore, during winter the signal receiving altitude is ~ 2.5 km with some contribution from the surface due to broad weighting functions. Furthermore, when the amounts of water vapour are very low during winter, this channels can penetrate sometimes even to the surface. In such conditions, the received signal is harder to interpret since it can be affected by surface emissivity and low level liquid clouds. Similarly to the previous case (183.31 ± 3 GHz channel), when the atmosphere is more opaque in summer due to increased amount of water vapour and cloudiness in May, intramonthly variability is less pronounced and is of $\sim$ 10 K.

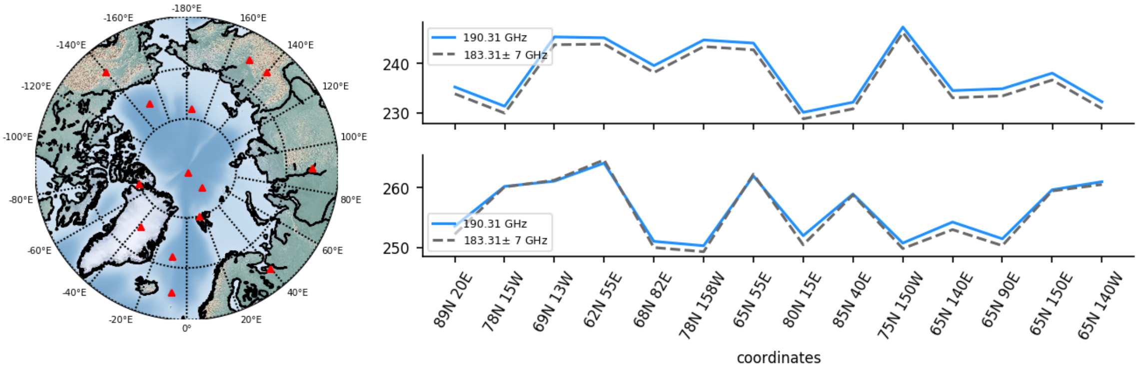

Figure 5.3: *Simulated T_bs for 183.31 ± 7 GHz (dashed gray line) and 190.31 GHz (full blue line) frequency channels for different coordinates shown on map (left) for January 7, 2009 (top) and May 11, 2007 (bottom).*

5.1.1 Winter month - January

Trends of T_b were calculated using the non-parametric Mann Kendall trend test (Kendall, 1975) for each pixel based on monthly means derived from all available satellites and their overpasses for each frequency. Although the climatological term trend refer to a time span of 30 years, here the term trend will be used for 17 years change since trend is still a tendency within a certain time period. In this section the combination of AMSU-B's and MHS's lower channel frequencies, 183.31 ± 7 and 190.31 GHz, respectively, are shown as joint product but as well separately (Fig. 5.4) to test for spatial differences in trends from the two instruments and periods. T_b trends across the Arctic range between -0.2 to 0.8 K/dec for the 183.31 ± 7 and 190.31 GHz joint product, between -0.1 to 0.4 K/dec for 183.31± 3 GHz and between -0.05 to 0.3 for 183.31 ± 1 GHz frequency channels. The estimated trend over all Arctic locations is significant on the 90 % confidence level.

Trends from these instruments doubled in comparison to those found from other passive microwave satellite instruments such as Advanced Microwave Sounding Unit -A (AMSU-A) and Microwave Sounding Unit (MSU) for 1978 - 2002 period as reported by Vinnikov and Grody (2003). It needs to be mentioned that trends found by Vinnikov and Grody (2003) uses instrument that scan at different frequencies that those used in this study. Moreover, regions of positive and negative trends are consistent among channels, indicating robustness of these findings. This is true even for a joined product of two slightly different frequencies (183.31 ± 7 and 190.31 GHz). Regions that experience significant warming since 2000 are Central Arctic, East Siberia with East Siberian and Chukchi Seas (herein after north-east Arctic), Canadian Archipelago, Fram Strait and north-east Greenland. Positive trends, besides lower altitude from which emitted radiation is sensed for joined product, most probably arise due to increase in water vapour as a consequence of other processes that are enhancing water vapour positive feedback loop. Some of these processes, beside sea ice melt over East Siberian region and sea are a large Eurasian river discharge of fresh water for which increase of 7% has been found (Peterson, 2002). Due to higher specific heat capacity of fresh water, these regions stay warmer for longer period enabling longer retention of evaporated moisture in the air. Additionally, due to permafrost thawing a large amount of CH_4 is released, which together with water vapour alters warming locally (Walter et al., 2006).

However, negative T_b trends have also been observed over North Atlantic and north-west Russia. A significant decrease in T_b, that is cooling, over these regions could be present due to water vapour removal by condensation and increase of mid- and low-level cloud optical thickness in these regions. Cooling observed over North Atlantic has as well been reported by (Gervais et al., 2019; Chemke et al., 2020) in whose study large-ensemble atmospheric simulations with the Community Earth System

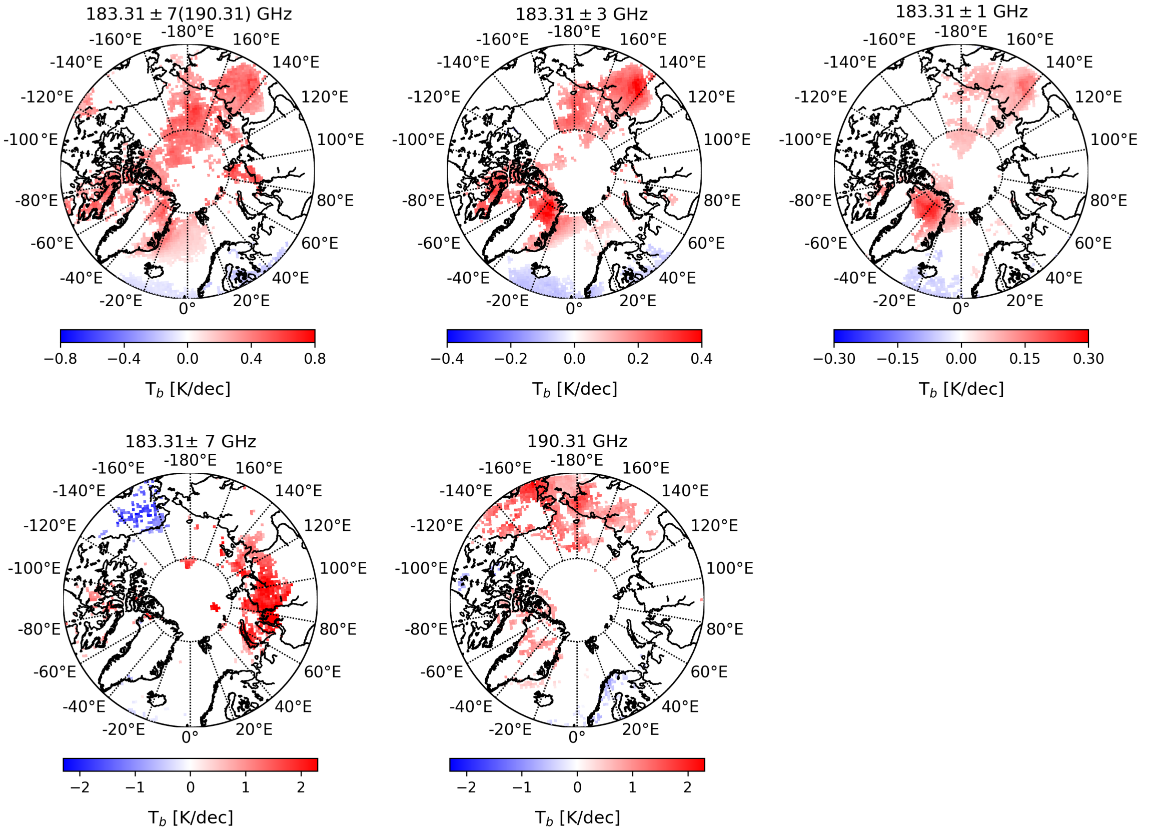

Figure 5.4: *Top: T_b trends for January during 2000-2016 period from all satellites overpasses for joined AMSU-B's 183.31 ± 7 GHz and MHS's 190.31 GHz frequency channels (left), 183.31 ± 3 GHz (middle) and 183.31 ± 1 GHz (right). Bottom: January T_b trends from AMSU-B's 183.31 ± 7 GHz (left) during 2000-2009 period and MHS's 190.31 GHz (right) frequencies during 2006-2016 period. Shown are only trends that are significant at 90% confidence level.*

Model (CESM) were used. Due to specific shape of cooling region, they termed it as "Atlantic Warming Hole". In another, more recent study by Gong et al. (2020), a decrease of latent heat over Greenland, Barents and Kara Sea that as a consequence has a decrease in the temperature has as well been shown.
This negative trend observed over North Atlantic and north-west Russia in winter could as well be due to polar vortex and jet stream shifting more to the east over Euroasian continent (Zhang et al., 2016) or increased stratospheric water vapour that has tendency to cool the lower troposphere (Solomon et al., 2010). Moreover, a negative trend in IWV over North Atlantic has been found by Ho et al. (2018) using WindSat data from 2006-2013.

In order to investigate the robustness of the joint product, that is, combined lower frequencies (183.31 ± and 190.31 GHz), trends from AMSU-B and MHS frequencies for two different periods are investigated, see Fig. 5.5 bottom. During the 2000-2009 AMSU-B period, positive trends over Canadian Archipelago, Siberian and Russian land and coastal region can be seen while negative trends are observed over Alaska and few grid points over North Atlantic (Fig. 5.4).

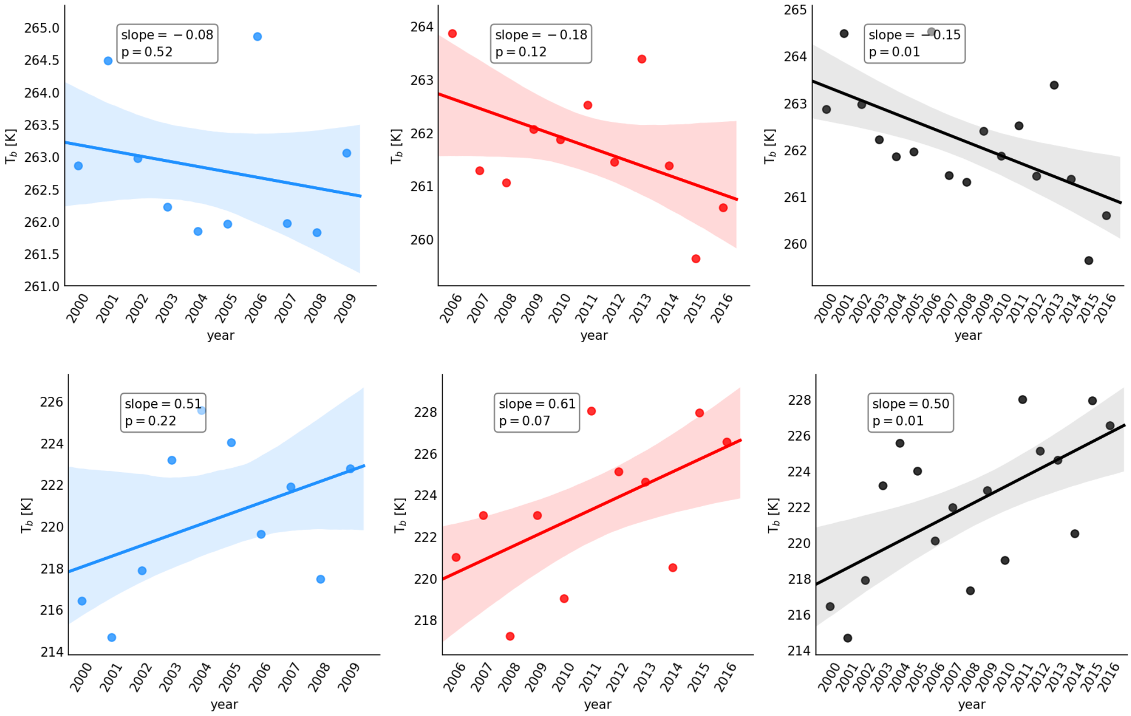

Figure 5.5: *T_b trend over North Atlantic (between 60° N-62° N and 15° W-5° W) (top) and NE Arctic (60° N-80° N and 130° E-180° E) (bottom) for January for: 183.31 ± 7 GHz frequency during 2000-2009 period (left), 190.31 GHz frequency during 2006-2016 period (middle) and joint product during 2000-2016 period (right) for the respective period. Trends in K/respective period and their p values are shown in the upper left corners of each panel.*

Found T_b trends, both negative and positive over same regions as here, have also been reported by Comiso and Hall (2014), however for August 1981 to November 2012 period, for which surface temperature from Advanced Very-High-Resolution

Radiometer (AVHRR) satellite were used. Although surface temperature and T_b are not directly comparable it is an indication that found trends in this study are valid since those are derived from the frequency channel scanning lower parts of the atmosphere. During MHS 2006-2016 period, positive trends over Chukchi Sea, Alaska, East Siberia, North Pacific and parts of Greenland and Canadian Archipelago are found (Fig. 5.4 (bottom right)). Over Alaska, positive trends from MHS observations are concentrated mostly around the area where negative trend were observed for the AMSU-B period before. In addition, negative trends are noted over Norway and North Atlantic south of Island. A difference in the trends between the two different periods irrespective of the region, however do not differ and range in between -2 to 2.3 K/dec (Fig. 5.4 (bottom)). From these trends it can be concluded that after 2009 significant warming shifts from Siberian, Laptev and Kara Seas to the north parts of the Arctic while significant cooling from northern part of the Atlantic shifts more eastward and over Norway.

To test differences between the joint product and for different periods, an area over the North Atlantic (between 60°N-62°N and 15°W-5°W) and an area over North-east (NE) Arctic (60°N-80°N and 130°E-180°) have been taken into consideration. Fig. 5.5 shows that over the North Atlantic negative trends during both, 2000-2009 and 2006-2016 periods were indeed present. However for 2000-2009 period the significance is lower, $\sim$ 50% while for the 2006-2016 period it increases to $\sim$ 90%. For the joint product, significance for found negative trend of -0.08 K/dec increases further and reaches 99% confidence level.

This indicates that, although the trend for the first period has a lower confidence level, the joint frequency product is in agreement with the second period where high statistical significance has been found. Moreover, larger consistency with 183.31 ± 1 and 183.31 ± 3 GHz is achieved for joined product. Similar was found for NE Arctic region, where positive trends of 0.5 and 0.6 K/dec for first and second period respectively are significant on $\sim$ 80% confidence level while statistical significance increases for the joint product and reaches 99% confidence. The results from joined product of two lower scanning frequencies deserve more thorough investigation and comparison with other data sets.

5.1.2 Spring month - May

During May, significant positive trends in T_b can be noted over Alaska, Beaufort Sea, north-west Russia, Barents and Kara seas and over region from both sides of Lena river (around 120°E) while significant negative trends are found over Siberia, Bearing Strait, Central Arctic ocean, Nunavut and Baffin Bay, Fram Strait and North Atlantic (Fig. 5.6). These trends range from -0.2 to 0.6 K/dec for 183.31 ± 7 and 190.31 GHz joint product, between -0.15 to 0.2 K/dec for 183.31 ± 3 GHz and between -0.2 to 0.2 K/dec for the 183.31 ± 1 GHz frequency channels.

In comparison to January (Fig. 5.4), a reversed sign of the trend for 183.31 ± 3 GHz can be noted for some regions such as Nunavut, parts of Baffin Bay and Central Arctic ocean. These regions show significant positive trends in January while in May (Fig. 5.6) these regions seem to be cooling. For the same frequency, an opposite effect has been found over parts of north-west Russia which shows decrease in January while in May this area experienced warming. The T_b trend for 183.31 ± 1 GHz as well shows a reversed sign in May over Fram Strait, Nunavut and tip of north-east Greenland. These regions show signs of warming in January but experience cooling in May.

The positive T_b trend of the joint product over Alaska and Beaufort sea could be due to increased bottom sea ice melt (Perovich et al., 2008; Perovich and Richter-Menge, 2015) and subsequent stronger evaporation and anticyclonic circulation over Beaufort Sea (Moore, 2012). Found negative trends over North Atlantic and Siberia could be explained due to removal of water vapour by condensation from increased low- and mid- level cloud formation. Besides increased cloud formation (Jun et al., 2016), there is possibility of increase in cloud optical thickness and cloud liquid water (CLW) over some regions in the Arctic. However, this is hard to verify since cloud optical thickness retrievals have the highest uncertainty over bright surfaces at low sun angles which are predominant conditions during spring and fall (Wang and Key, 2005). The increased cloudiness in warming climate over Arctic acts in a way to enhance negative feedback on surface temperature as predicted by different studies using model simulations (Roeckner et al., 1987; Tselioudis et al., 1992; Lin et al., 2006; Gettelman and Sherwood, 2016; Ceppi et al., 2017). Indeed, it has been shown that increased temperature and evaporation lead to increased cloudiness in the Arctic during summer and reduced cloudiness in winter (Wang and Key, 2003; Schweiger, 2004). However, different regions of the Arctic show different responses to increased temperature and water vapour in respect to cloud formation and their microphysical

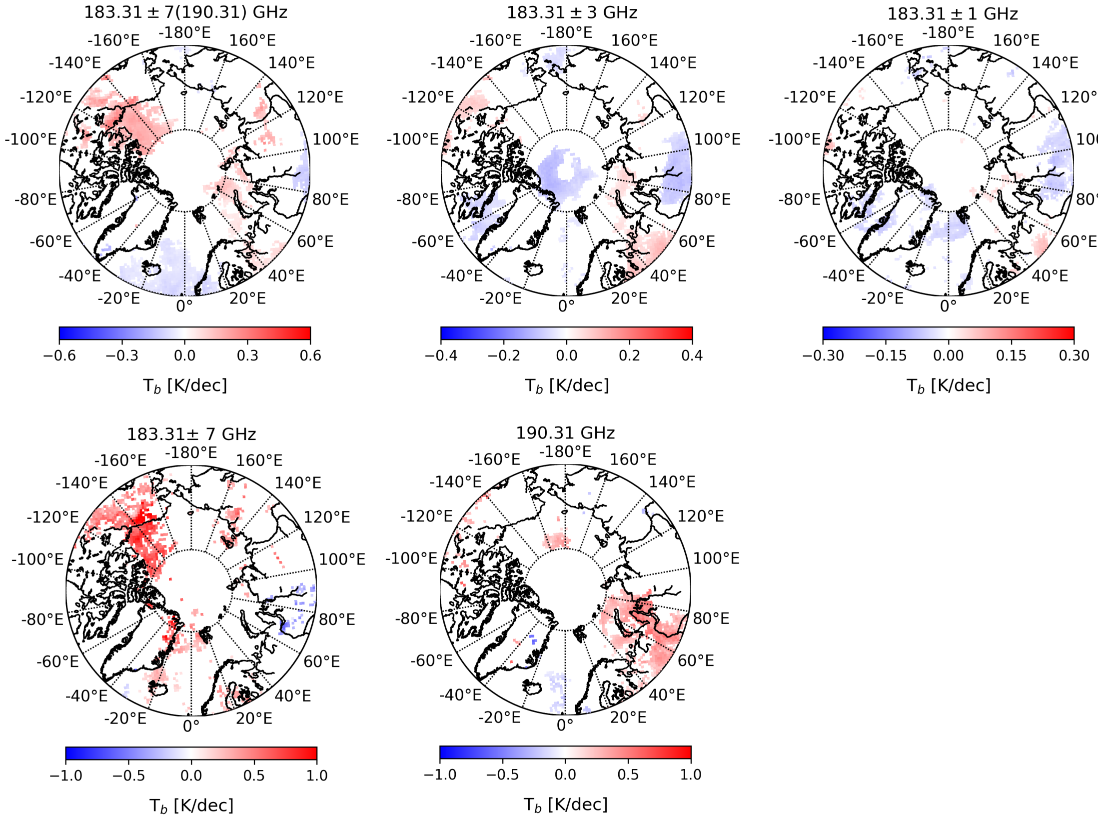

Figure 5.6: *As in Fig. 5.4 only for May.*

properties. In a study by Kay et al. (2016) for the 2000-2015 period a negative trend in shortwave radiation has been found over North Atlantic. Another, more recent study by He et al. (2019) has shown linear increase of cloud coverage with the area of ice-free water during the melt seasons. The presence of clouds damp the positive albedo effect and in that way partially compensates for the loss of high sea ice albedo. Here, as for January, trends for the joint product of lower frequencies shows to be in agreement with higher altitude sensing frequencies over Barents and Kara Seas, north-west Russia, Siberia and parts of Alaska while the rest of regions although in agreement are showing much less area covered with significant trends. Therefore trends for lower frequencies, are as well shown separately for their corresponding two periods (Fig. 5.6 (bottom)). For the 2000-2009 period an increase over Alaska and Beaufort Sea consistent with the joint product in figure Fig. 5.6 (upper left) can be noted. Additionally, for this period an increase in T_b over Fram Strait region can be seen which is not evident in joint product.

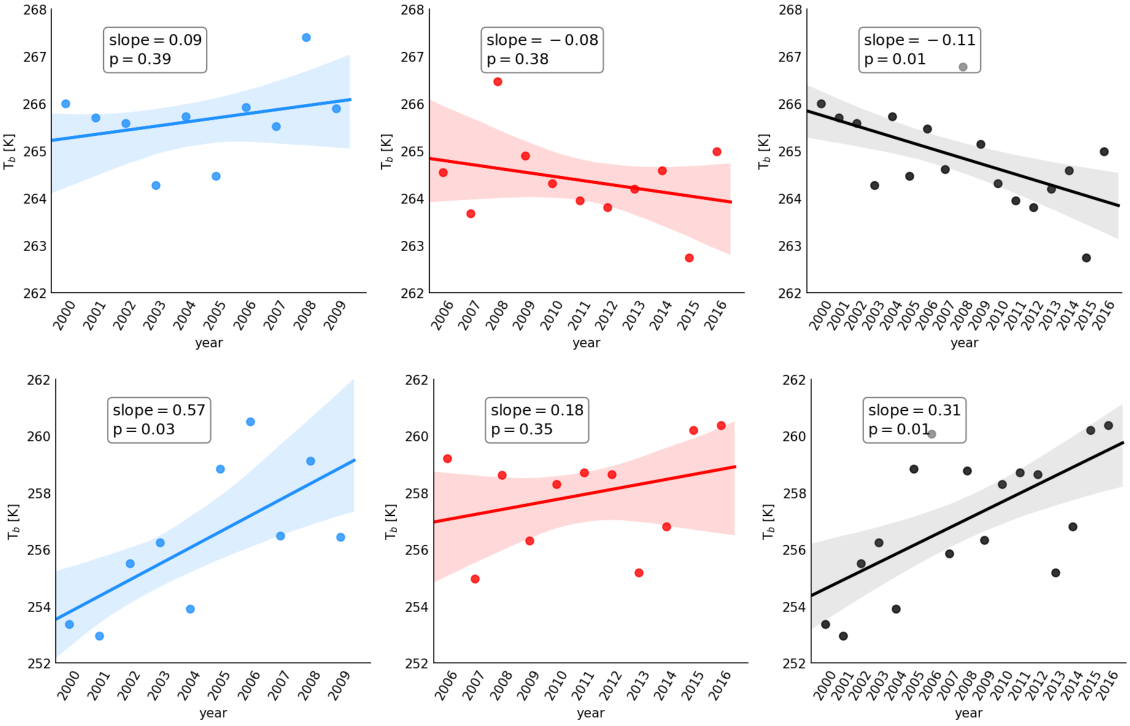

Figure 5.7: *Similar to 5.5 only for North Atlantic (between 60° -65° N and 15° W-5° E) (top) and over Alaska (between 67° -80° N and 120° W-160° W) for May.*

However, this warming over Fram Strait could possibly be explained by an increase in stratospheric water vapour in UTLS region which enhances cooling of the stratosphere but has warming effect on surface (Maycock et al., 2011, 2014). This explanation agrees well with the decrease of T_b found for 183.31 ± 1 GHz frequency over this region. During 2006-2016 period over Alaska, an increase in T_b can be noted, however covering only few grid points in comparison to the first period or the one found in the joint product. Moreover, a positive trend over Beaufort sea for the first period is not present in the second period. However, an increase over north-west Russia, Barents and Kara Seas is in agreement for all frequencies and periods, making this signal consistent. Most evident difference for these periods is lack of negative trend over North Atlantic region, which is shown for the joint product and is not in agreement with T_b changes for higher frequencies. To test signal for joined product from lower frequencies in May, two regions are chosen for deeper investigation, one that shows positive, Alaska, and the other that shows a negative trend, North Atlantic. In figure 5.7 trends during 2000-2009, 2006-2016 and the whole period of 17 years are shown. Herein negative trends over north Atlantic during 2000-2009 and 2006-2016 period indeed were present. However they are significant on lower confidence level, $\sim 60\%$, while joint product shows significance with confidence level greater of 99%. The similar is found for the positive trend over Alaska region. Nonetheless, trends for separate periods for Alaska have higher statistical significance than those found over North Atlantic. This indicates that although the trend for the joint product shows greater statistical value, the investigation revealed that this results from with two different period that separately show lower confidence. Although negative trend over the North Atlantic is only present for joined product and is not evident in other frequency channels these can be explained by UTLS water vapour increase. Therefore, it would be of interest to check for changes in water vapour to test this significance further. For this reason, and the hypothesis that T_b can be used as a proxy for water vapour changes, in the following chapter T_b sensitivity for each of the frequency channels will be tested.

5.2 Weighting functions and water vapour sensitivity

To test T_b sensitivity to water vapour, ASR will be used as a testbed and regions that show significant trends were choosen for the investigation and are shown in Fig. 5.8. Although a significant trend has been observed over north-east Greenland 5.4, sensitivity to water vapour low amounts at this altitude is hard to interpret due to high and complex orography and is not considered here. Furthermore, water vapour retrieval in such high elevated regions is prone to larger errors when compared

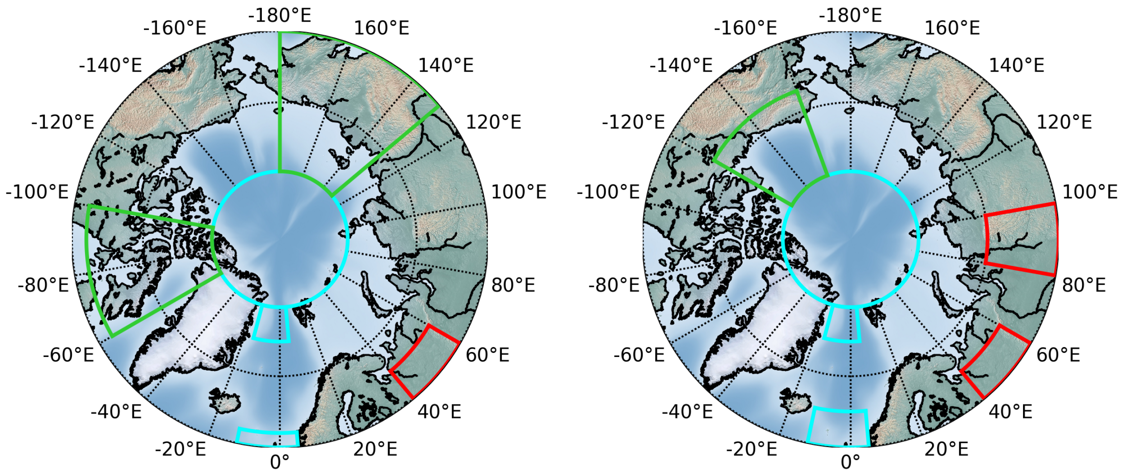

Figure 5.8: *Identified regions of significant T_b changes for January (left) and May (right). Colors denote regions that encompass both, land and ocean (green), only ocean (cyan) and only land (red).*

to more flat surfaces since the influence from surface emissivity is large. For these reasons sensitivity studies to humidity for this area was excluded from the analysis. Altogether, there are six regions of interest for both January and May months (Fig. 5.8). Testing has been performed by calculating weighting functions for AMSU-B frequencies with focus on sounding channels by increasing specific humidity for 20%. Input profiles of height, pressure, T and RH are taken from the ASRv2 and are used as 17 years means for each region.To investigate humidity sensitivity for the different frequency channels, RH input was calculated for increased values of specific humidity as mentioned above. The reason for using RH as input steams from technical necessity where weighting functions were calculated using RH. Moreover, code for calculation of weighting function has option to directly calculate perturbed RH profiles for given specific humidity perturbations. In addition another variable for expressing humidity was used, absolute humidity (AH). Reason for using yet another form of humidity is that IWV was calculated using AH profiles. After weighting functions are calculated these are than multiplied by AH, hereinafter weighted AH (AH$_w$). Such AH$_w$ profiles by its peaks can provides us with the information about the level at which certain channel is most sensitive to water vapour, since to that level largest weight is given. Each of the AH$_w$ profiles corresponds to a certain channel weighting function that AH was multiplied by. Moreover, from peak level of the AH$_w$ it is possible to read out temperature T, to which simulated T$_b$

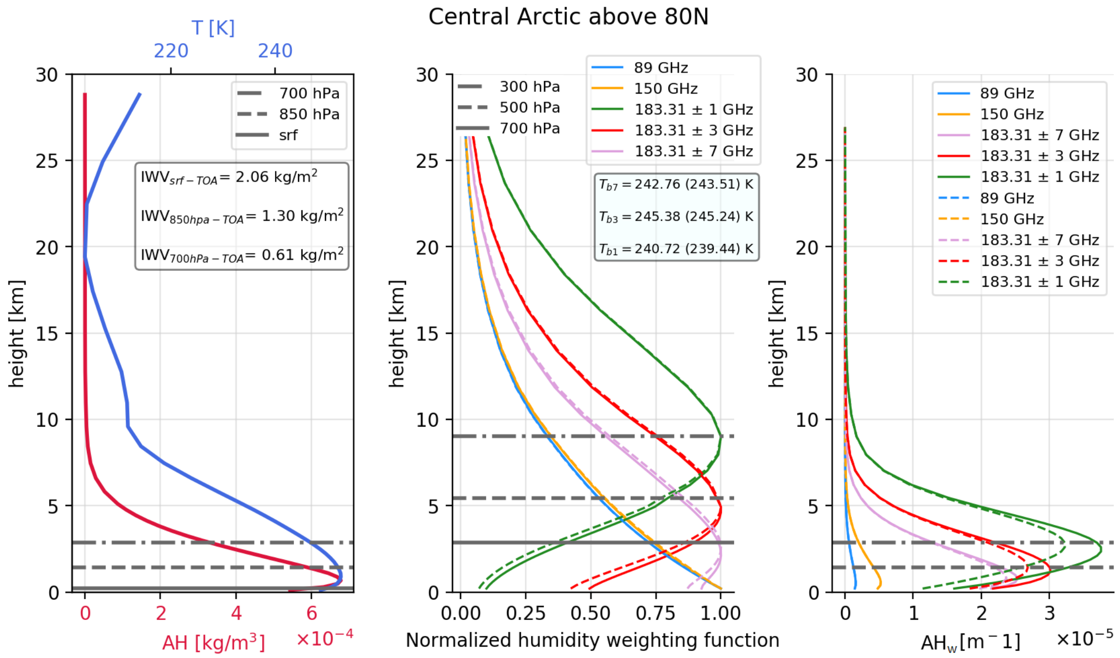

Figure 5.9: *17-year mean input profiles of T and absolute humidity (AH) with IWV values for 3 different column heights (left), normalized weighting functions for 5 AMSU-B frequencies for mean profiles (full line) and for 20 % increased specific humidity (dashed) (middle) and AH$_w$ for mean (solid) and 20% increased humidity (dashed) (right). In the middle plot T$_b$ values for mean and perturbed (in brackets) state of RH are indicated. Plots are shown for Central Arctic region in January over sea ice surface.*

for certain channels should be in close agreement. Change in the T_b for perturbed weighting function relative to unperturbed T_b gives us the sensitivity of T_b for changes in humidity. The sensitivity study described above for the Central Arctic region for the January climatological mean is shown in the Fig. 5.9. It can be seen that the atmosphere during January is extremely dry and for the region above 80°N IWV from surface to top of the atmosphere (TOA) has a climatological mean of only 2.06 kg/m^2. This, however is expected during January, when mean temperature, calculated using ASR, does not go above 250 K ($\sim$ -23°C).

Weighting functions of sounding channels for 20% increased humidity are slightly lifted to higher altitude, indicating that emission comes from higher altitudes. The reason for this is the more opaque atmosphere that saturates channels faster. The altitude from which the two most opaque sounding channels (183.31 ± 1 and 183.31 ± 3 GHz) receive their strongest signal has a lower temperature leading also to a slightly lower T_b (Fig. 5.9). The T decrease is not observed for window channels (89 and 150 GHz) since these are not affected by scattering from liquid and ice particles (Bennartz and Bauer, 2003; Kneifel et al., 2010; Xie et al., 2012; Chen and Bennartz, 2020). Moreover, it can be noted that weighting function profiles, even for sounding channels, do not always start close to 0 (no surface effect) meaning that signal is contaminated by emissivity from surface (profile starts for values greater than 0). For January, when the Central Arctic atmosphere is especially dry, the 183.31 ± 7 (190.31) GHz frequency channel is strongly affected by the surface which has a variable emissivity of different types of sea ice (albedo and age). Moreover, these two similar channels (183.31 ± 7 and 190.31 GHz) are often used for improvement of ice and snowfall retrieval due to their sensitivity to frozen particles (Meng et al., 2017; Edel et al., 2019). This means that retrieval of IWV from these frequencies gets much harder and will lead to large errors if surface emissivity and influence of

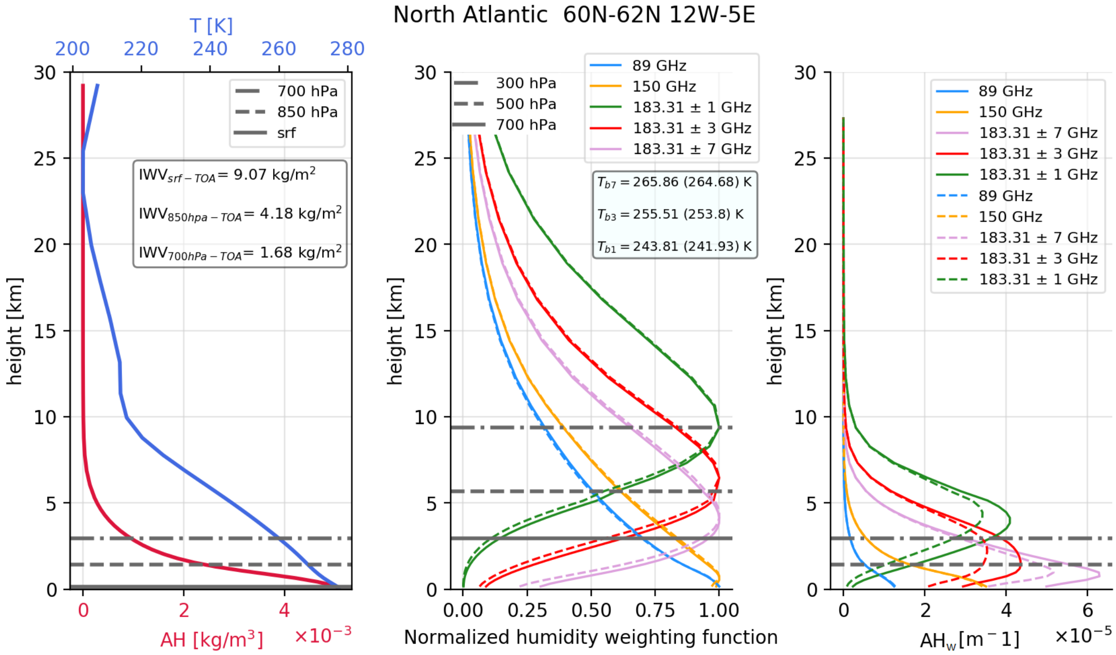

Figure 5.10: *As in Fig. 5.9 only for the North Atlantic region (January).*

hydrometers to received signal are not taken into account. Therefore many IWV retrieval studies focus only on the higher altitude sounding frequency, 183.31 ± 1 GHz and relate this to the UTLS region (Buehler, 2005; Moradi et al., 2010, 2013a, 2015). Compared to the dry Central Arctic, the region over North Atlantic for same frequencies (183.31 ± 7 (190.31) GHz) is almost not affected by the surface (Fig. 5.10). This could be due to higher moisture in this region that in comparison to Central Arctic is ice free throughout the year. Furthermore, the North Atlantic region experiences strong moisture transport from lower latitudes (Nash et al., 2018). This region should therefore contain larger amounts of humidity leading to strong channel saturation which translates to higher altitudes of weighting function peaks. This is indeed observed by looking at the 17-year mean IWV amount which for this region reaches value of approximately 9 kg/m^2 in comparison to the Central Arctic IWV of 2 kg/m^2. This findings suggest that, over this region, it would be possible to retrieve IWV from lower altitude scanning frequencies with larger confidence in comparison to Central Arctic region even during January.

Looking at the weighting functions, one can notice that peaks for each of the sounding frequencies for climatological mean profiles are positioned at a certain altitude. Hence during January (Fig. 5.9), 183.31 ± 7 GHz receives strongest signal from around 2.5 km, 183.31 ± 3 GHz at around 5 km and 183.31 ± 1 GHz at around 9 km altitude. This approximately translates to 700 hPa, 500 hPa and 300 hPa for frequency channels, respectively. It needs to be mentioned that although the strongest signal comes from the altitude at which peaks are, the peaks are not completely narrow but are somewhat broadened. This means that the signal is a composite over a wider altitude range and also includes contributions from altitudes below the peaks. Therefore, one can notice that AH$_w$, for e.g. 183.31 ± 1 GHz frequency channel, mainly is below 5 km. This is reasonable since more water vapour is concentrated in the lower parts of the atmosphere. Therefore to asses water vapour, the column between lower and

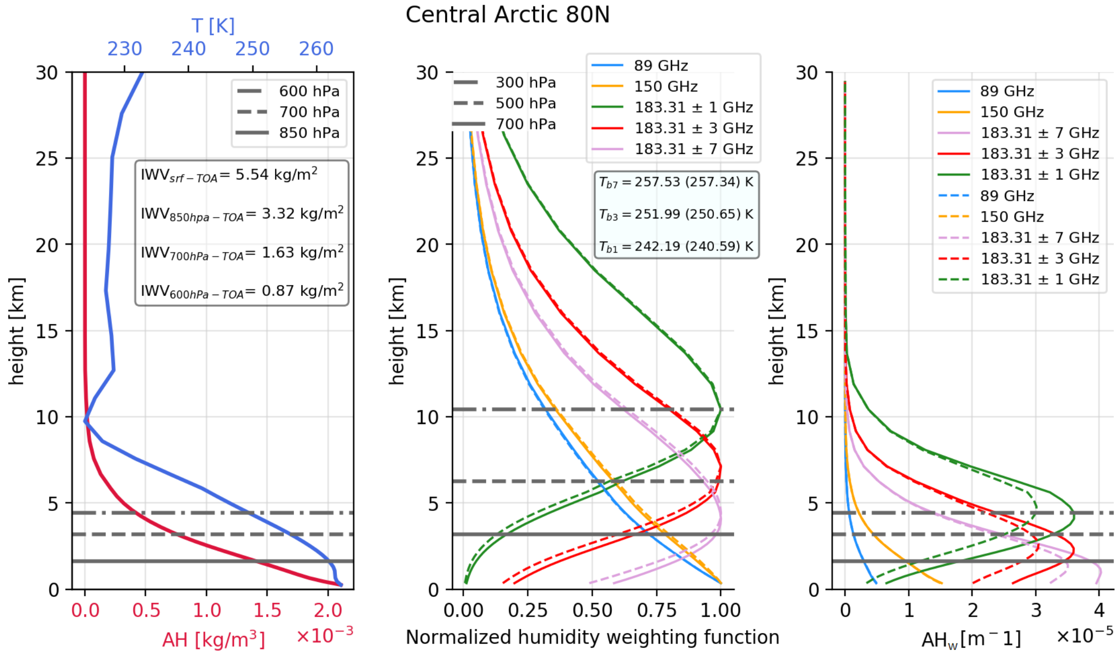

Figure 5.11: *As in Fig. 5.9 only for May.*

upper boundary of the most broadened part of AH_w peak provides an indication. However, it needs to be highlighted that the assessment of water vapour by T_b is difficult since lower and upper boundary of the AH_w broadened part are changing from profile to profile. In summery, T_b of weighting function peak indicates the level from which strongest signal is received by a certain channel and that pressure levels for weighting function peaks for each frequency are almost constant for all profiles.

In contrast to taking the boundaries of the width of weighting function to asses water vapour, it is possible to use T_b from different channels and correlate it with the IWV from the level to which T_b of the weighting function peak translates to the AH_w peak level to top of the atmosphere (TOA). In the example (Fig. 5.9), the weighting function for nadir view for the 183.31 ± 1 GHz frequency channel peaks at 300 hPa and shows a T_b of 240.71 K. The 300 hPa level corresponds to the level of the AH_w at $\sim$ 2.6 km or 700 hPa. Comparing this T_b value with the input, it can be seen that T_b of the 183.31 ± 1 GHz frequency channel peak closely corresponds to the physical T at $\sim$ 2.6 km (700 hPa). It needs to be highlighted that this is only value for that specific level. Therefore to use T_b as a proxy for IWV, IWV can be calculated for columns whose base corresponds to AH_w peak level to TOA. Furthermore, it can be noted that T_b for 183.31 ± 7 GHz frequency is lower than for 183.31 ± 3 GHz frequency channel possibly due to lower altitude humidity inversions during January over Central Arctic (Fig. 5.9). Similar low level humidity inversions were noted for the Canadian Archipelago and the NE Arctic regions (Fig. B.5). Same sensitivity study has been performed for May for the same regions, Central Arctic (Fig. 5.11) and North Atlantic (Fig. 5.12). During May, IWV values over Central Arctic region are more than double in January and reach 5.54 kg/m^2. Due to the more humid atmosphere in May, the strongest signal receiving altitude (weighting function peak) is positioned at higher altitudes for all channels.

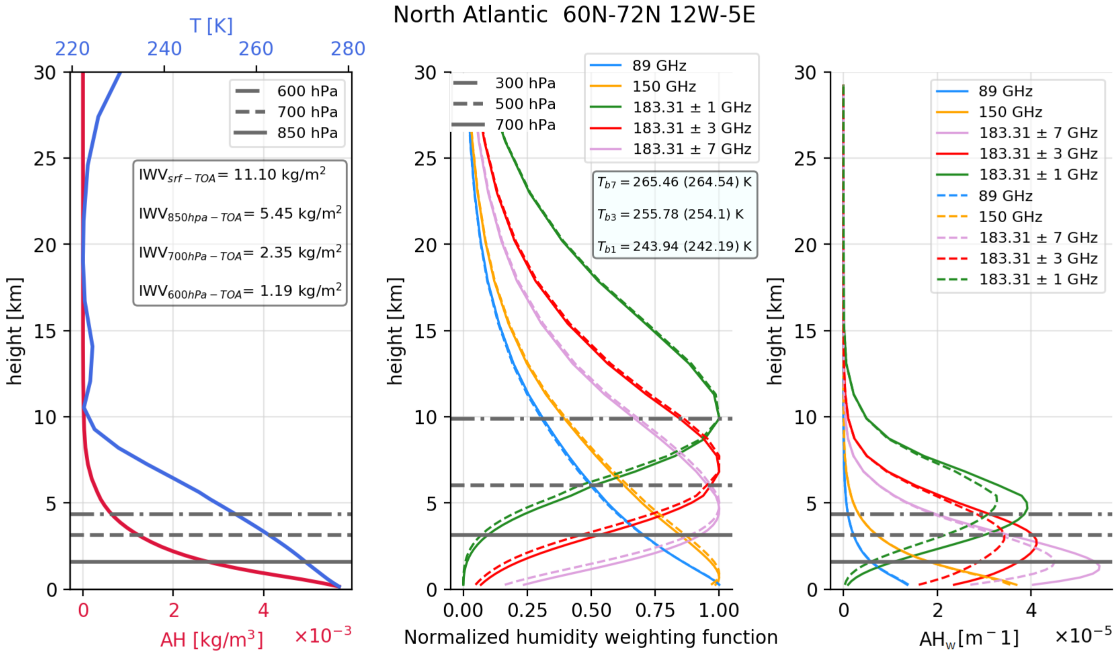

Figure 5.12: *As in Fig. 5.10 only for May.*

In comparison to January, peaks of weighting functions are lifted by about 2 km. Here, no indication of humidity inversions appear. For the North Atlantic region in May (Fig. 5.12), IWV can reach values of 11.1 kg/m^2. Also, the weighting function shows that 183.31 ± 7 GHz frequency is not affected by the surface, indicating that retrieval of IWV over this region should be more reliable. Moreover, largest weight for IWV is coming from water vapour that can be sensed with this channel (AH$_w$ profile). Sensitivity studies as above have as well been performed for other regions and can be found in the appendix (Fig. B.6 and Fig. B.7).

From the above inspection it can be concluded that three sounding channels receive the strongest signal from different altitudes. Moreover, these channels 183.31 ± 7 GHz, 183.31 ± 3 GHz and 183.31 ± 1 GHz have peaks at approximately same pressure levels for 17-year mean profiles, 700 hPa, 500 hPa and 300 hPa. These levels in AH$_w$ profiles translate to different levels in different month that are taken as a base level for corresponding IWV columns. In that way, IWV for three different atmospheric layers are calculated for both months and are correlated with corresponding frequency channel T$_b$ (Table 4). This allows for testing of the hypothesis that T$_b$ can be used as a proxy for water vapour.

Table 4: *Frequency channels and corresponding IWV column for January and May based on AH$_w$ functions peak levels.*

frequency [GHz]	**IWV column**	
	January	**May**
183.31 ± 7	surf-TOA	850 hPa-TOA
183.31 ± 3	850 hPa-TOA	700 hPa-TOA
183.31 ± 1	700 hPa-TOA	600 hPa-TOA

5.3 IWV spatiotemporal changes and variability

The importance of water vapour and its effects in warming climate has been described in the introduction and in this section spatiotemporal changes of IWV from ASR for three different atmospheric columns (Table 4) will be presented. As mentioned in the previous section, these three different IWV columns have a lower boundary that correspond to the level of the AH$_w$ function peak and span vertically up to TOA. To get a general overview, first the yearly cycle of IWV and its one standard deviation (STD) for different parts of the atmosphere are presented in the Fig. 5.13. Herein, whole atmospheric column is described by surf-TOA IWV, middle part of the atmosphere is described by 700 hPa-TOA IWV while upper parts are described by 500 hPa-TOA and 300 hPa-TOA (UTLS region) IWV.

As expected, IWV shows lowest amounts during winter, and starts to increase as the Sun returns in early spring and initiates warming of the atmosphere and sea ice melt. Maximum values are observed in summer (July) when sea ice has melted significantly, a large values of latent heat is released due to convectional condensation brought by meridional cyclonic activity (Serreze and Barrett, 2008; Knudsen et al., 2015; Crawford and Serreze, 2017; Semenov et al., 2019) and when moisture transport into the Arctic is increased (Nash et al., 2018).

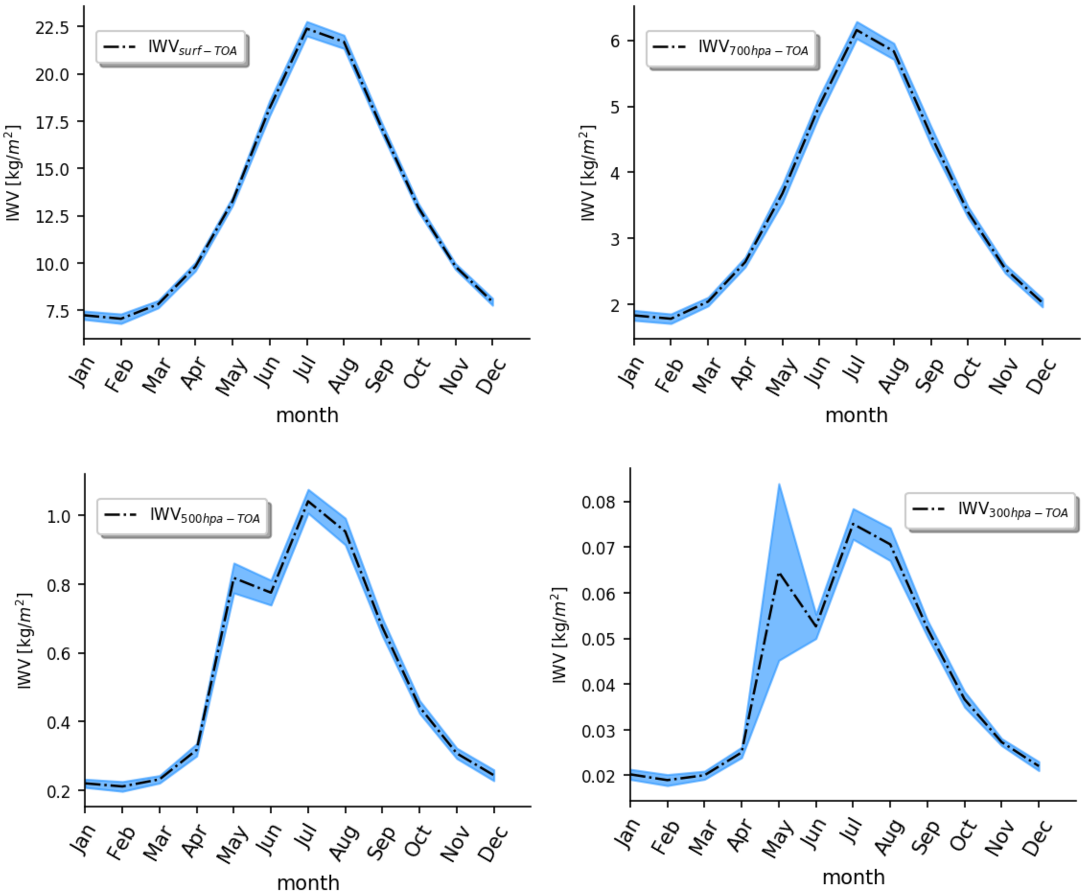

Figure 5.13: *Yearly cycle of Arctic wide IWV from ASR during the 2000-2016 period for four atmospheric layers: between surface-TOA (upper left), 700 hPa-TOA (upper right), 500 hPa-TOA (lower left) and 300 hPa-TOA (lower right). Blue shading shows one STD from the mean value.*

As the summer ends and the Sun starts to set during autumn, reduced amount of the IWV are observed. This yearly cycle is evident for all IWV columns (Fig. 5.13). Furthermore, what can be immediately noted is a striking high variability during May for higher altitude columns, especially for $IWV_{300-TOA}$. Above this level, which is already the UTLS region, an increase of water vapour can act to initiate radiative cooling (Manabe and Strickler, 1964; Manabe and Wetherald, 1975; Gillett et al., 2003; Maycock et al., 2011). In the UTLS, water vapour is present only in trace amounts and expressed in parts per milion (ppm), therefore even small changes in water vapour will produce strong variability. Investigation of IWV and temperature in ASR revealed that during May 2004 especially high values of IWV have been present in the UTLS while temperatures were below 240 K (not shown). At the end of the year, temperatures were extremely low, below 195 K, and the winter 2004/2005 was reported as the coldest since 1960 (Rex et al., 2006; Manney, 2005).

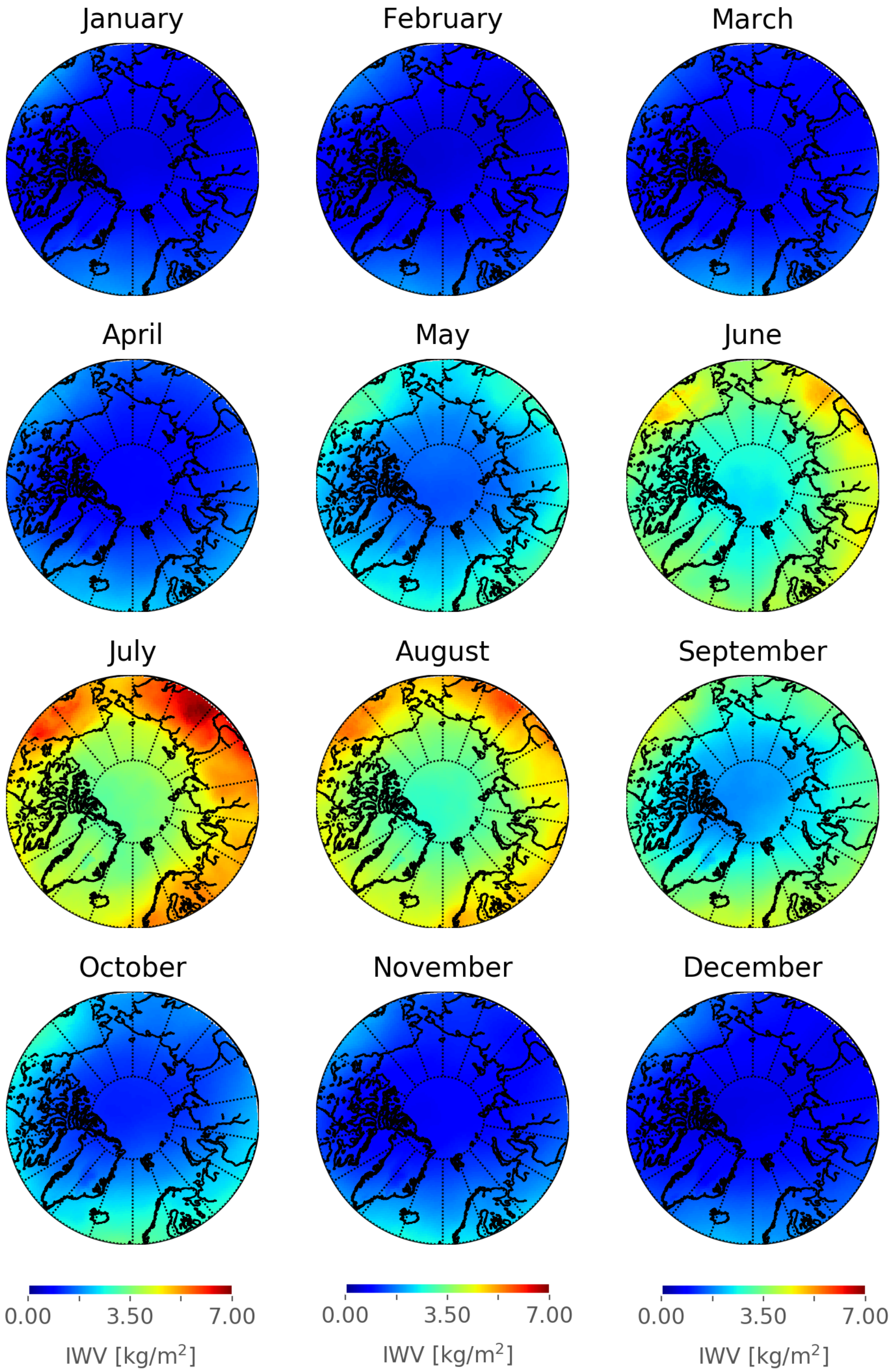

Figure 5.14: *Monthly means of* $IWV_{700hPa-TOA}$ *during 2000-2016 period.*

Cooling induced by increase in water vapour in the UTLS region also enhances the strength of the polar vortex. In this way it prolongs its lifetime and delays its breaking in spring (Maycock et al., 2020) affecting atmospheric dynamics. Moreover, during 2004/2005 the winter polar vortex broke in two parts (Chshyolkova et al., 2007), theoretically leaving a corridor for moisture intrusions into the stratosphere (driven by planetary waves) that acts to decrease UTLS temperatures.

Besides water vapour initiated cooling of UTLS region, the enhanced stratospheric water vapour is also very important component for the Arctic ozone loss that induces warming of the lower stratosphere, especially in winter (Feck et al., 2008; Polvani et al., 2020). Additionally, increased water vapour in the stratosphere as well enhances formation of polar stratospheric clouds (15 -24 km) and subsequently depletion of ozone (Solomon, 1999; Vogel et al., 2011). Nonetheless, our understanding of the response of the complex stratospheric processes due to global warming is still uncertain and requires more attention.

From the figure Fig. 5.13 and the description above, the choosen months for investigation, January and May, seem to be reasonable to illustrate different Arctic conditions. Besides showing Arctic wide averaged yearly cycle of IWV, it is of importance to check for its spatial variability as well. Therefore in addition, the yearly cycle as maps of monthly means of the Arctic for IWV$_{700hPa-TOA}$ is shown in Fig. 5.14 while IWV$_{surf-TOA}$ can be found in the appendix (Fig. B.8).

Following temperature, during winter, very low amounts of IWV for 700 hPa-TOA can be found across the whole Arctic region, not rising above $\sim$ 2.5 kg/m^2. In contrast, during summer these amounts can reach values of 7 kg/m^2. This is a relatively high amount given the fact that globally $\sim$ 50% of the water vapour is concentrated close to surface and below 850 hPa, and more than 90% below 500 hPa (Peixoto and Oort, 1992).

During spring, more specifically - May, a sudden increase in water vapour can be noted, marking a transitional period between more stable and calm winter to more active summer season. The increase between April and May is of 2 kg/m^2 for the 700 hPa-TOA column and more than 6 kg/m^2 for surface-TOA column (Fig. B.8). The strongest increase is observed over north Siberia and Alaska that continues to show especially high values during summer. As mentioned above (Section 5.1) over these regions a significant evaporation after land snow melt from Siberian Verkhoyansk range and Yukon region can occur.

How does IWV follow T$_b$?

Above the Arctic wide mean yearly cycle of IWV through different parts of the atmosphere has been presented (Fig. 5.13). In addition maps of monthly means of IWV has been shown for the 700 hPa-TOA (Fig. 5.14) while the the total atmospheric column (IWV$_{surf-TOA}$) can be found in the appendix (Fig. B.8). Now, the focus is on resemblance of mean IWV spatial patterns to those noted in T$_b$ means. This is presented in Fig. 5.15 and Fig. 5.16 for January and May respectively.

During January (Fig. 5.15) strong spatial variability can be noted in both, T$_b$ for all frequencies and all IWV columns. Low values of IWV for all columns are observed trough most of the Arctic region excluding parts of Alaska, North Atlantic and Pacific

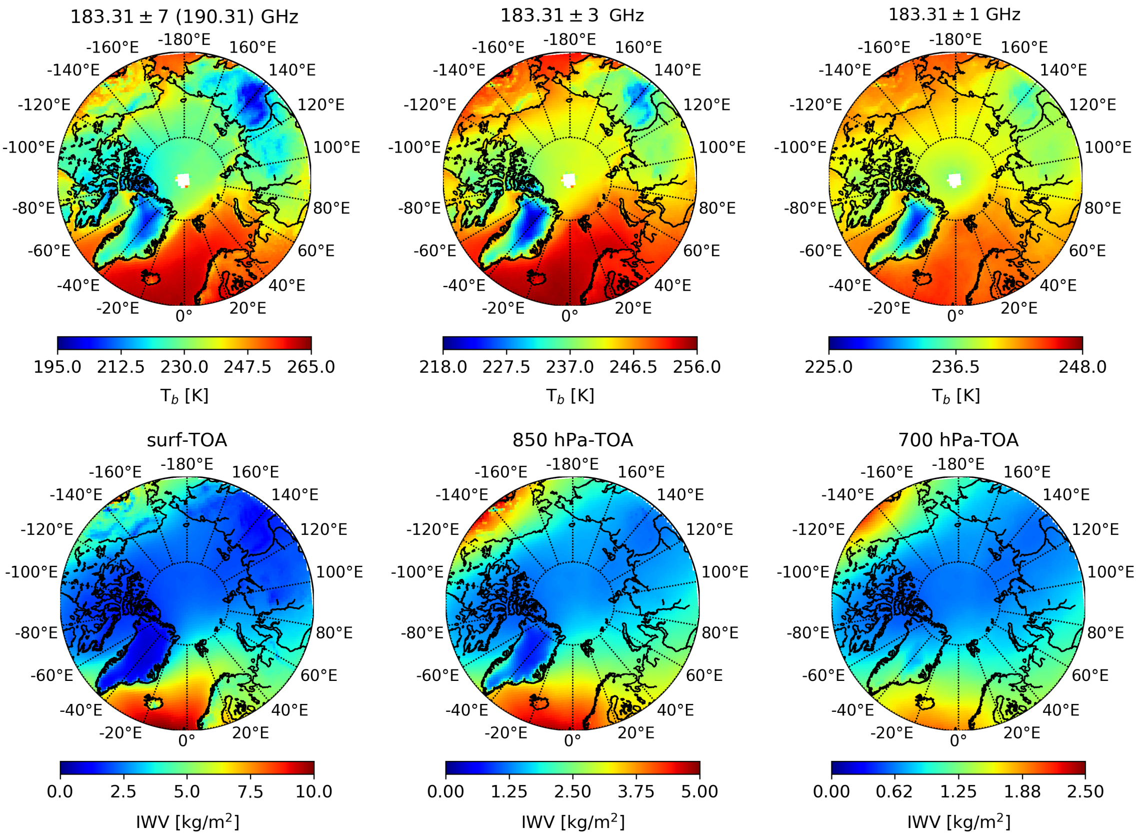

Figure 5.15: *Mean T_b for 2000-2016 period for 183.31 ± 7 GHz, 183.31 ± 3 GHz and 183.31 ± 1 GHz frequency channels (top) and corresponding IWV columns from surf-TOA, 850 hPa-TOA and 700 hPa-TOA (bottom) during January.*

ocean where extremely high values, reaching 10 kg/m^2 for full atmospheric column are found over open ocean. These spatial structures follow T_b of corresponding frequency channels. Even small local structures of increased T_b over Alaska region for all frequency channels are evident in increased values of corresponding IWV columns. Due to the very small changes in IWV over Siberian Verkhoyansk range, $\text{IWV}_{700hPa-TOA}$ column shows slightly lower resemblance to T_b for the high 183.31 ± 1 GHz frequency channel.

Nonetheless, for the whole Arctic region, IWV spatial patterns seems to follow those of T_b well. Moreover, it can be seen that half of the $\text{IWV}_{surf-TOA}$ is contained above 850 hPa level ($\sim$ 3 km) which is in agreement with Peixoto and Oort (1992). Furthermore, spatial structure of IWV found here are in agreement to those found by Rinke et al. (2019) and Nygård et al. (2019, 2020).

Similar resemblance of IWV column patterns to corresponding T_b is observed for May (Fig. 5.16). Here, however, the pattern of high values of IWV for all columns is more circular and located between 60°-70°N latitude. In comparison to the Central Arctic Ocean and seas, values over this latitude belt can be more than double, i.e. for $\text{IWV}_{850hPa-TOA}$ difference can reach almost 5 kg/m^2. These higher amounts of IWV could, besides lower latitudes and therefore warmer atmosphere, be explained by fast evapotranspiration of growing vegetation over the land area and evaporation from sea-ice free oceans in comparison to lower evaporation or sublimation over

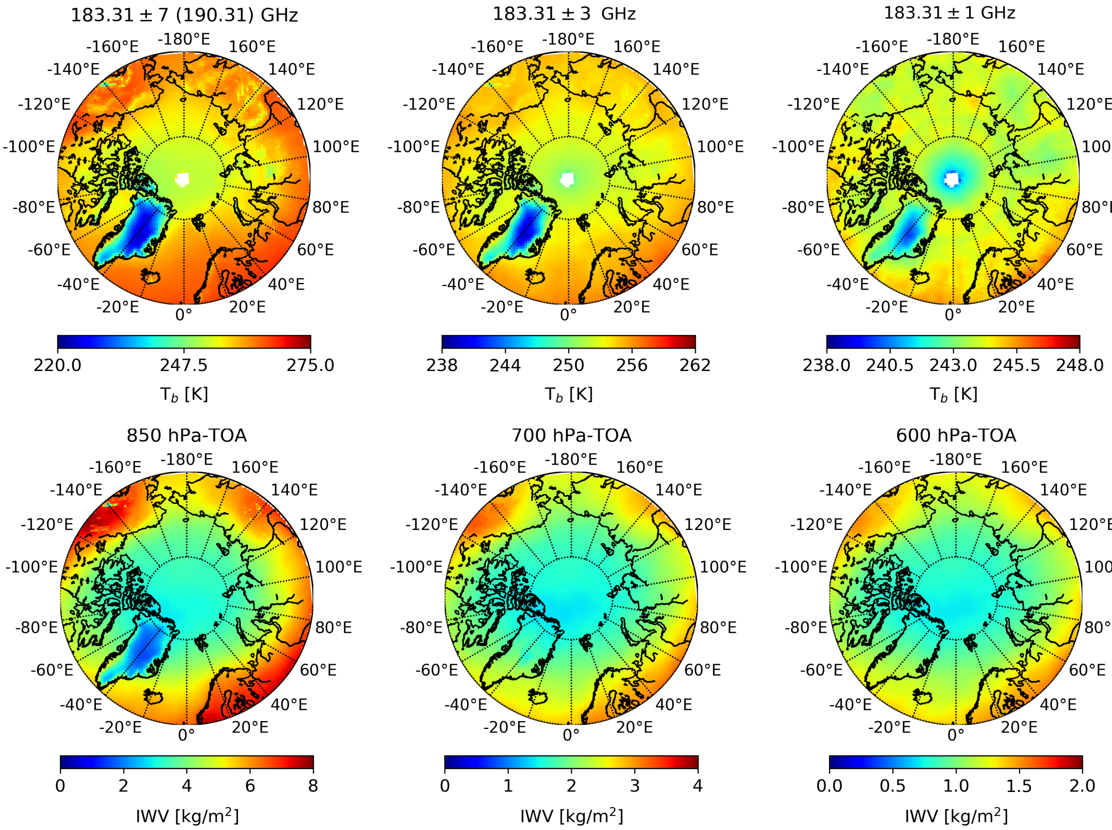

Figure 5.16: *As in Fig. 5.15 only for May.*

Central Arctic Ocean and sea ice covered surfaces. In addition increase of moisture transport into the Arctic is noted for the transitional season, especially May (Nash et al., 2018). The above implies that IWV spatial variability follows the one observed in T_b field. Besides this conclusion, in this research it is of interest to investigate how do IWV trends follow those of T_b. Therefore in the following section trends of IWV columns for corresponding T_b frequency channels will be presented.

5.3.1 Winter month - January

Fig. 5.17(top) shows trends of IWV columns for January over the 2000-2016 period as well as $IWV_{surf-TOA}$ (bottom) for two different periods in respect to T_bs from two different instruments, AMSU-B (183.31 ± 7 GHz) and MHS (190.31 GHz).

IWV trends range from -0.08 to 0.08 kg/m^2 dec^{-1} for $IWV_{surf-TOA}$. Most pronounced positive trends can be found over Fram Strait, Siberia, small portion over Alaska, northern part of Bearing Sea, Greenland and Canadian Archipelago. These trends are in agreement with the T_b joint product of 183.31 ± 7 GHz and 190.31 GHz (Fig. 5.4). Similar spatial pattern can be found for other IWV columns. The most pronounced trend over Fram Strait is in agreement with Rinke et al. (2019) where four different reanalyses agree on a positive trend over this region for the 1979-2016 period. Additionally, $IWV_{surf-TOA}$ for separate periods shows stronger positive trends of 0.25 kg/m^2 dec^{-1} and 0.4 kg/m^2 dec^{-1} for first and second period respectively. These trends, as for the whole period,

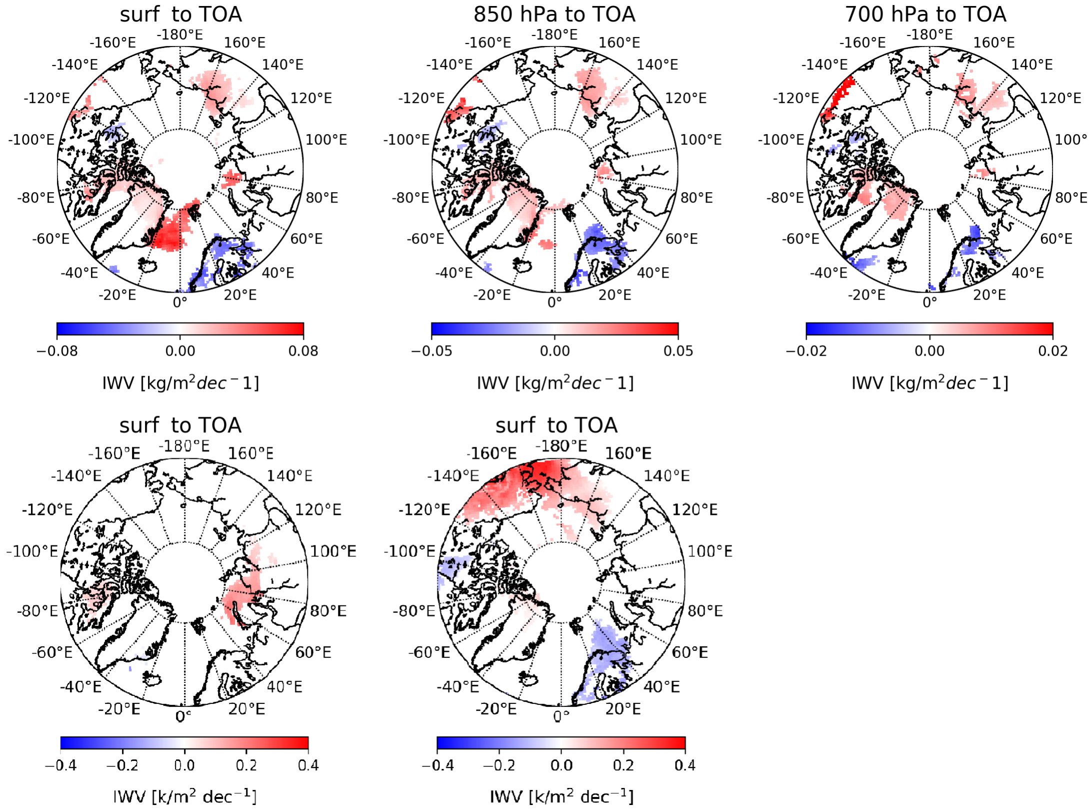

Figure 5.17: *IWV trends for January during 2000-2016 period of* $IWV_{surf-TOA}$ *(top letf),* $IWV_{850hPa-TOA}$ *(top middle) and* $IWV_{700hPa-TOA}$ *(top right). On the bottom part are shown* $IWV_{surf-TOA}$ *for 2000-2009 period and (left) and for 2006-2016 period (right).*

show similar spatial distribution observed in T_b trends for corresponding frequency channels for separate periods. Negative trends for the whole and 2006-2016 period are concentrated over parts of Canadian Archipelago and Norway. This negative IWV trend can not be easily explained at the moment and is most probably related to local effects. Nonetheless, a significant increase of low- and mid-level clouds amount such as Cumulus (Cu) and Cumulonimbus (Cb) over northern parts of Norway and parts of Barents Sea has been reported by Chernokulsky and Esau (2019) for the 1935 - 2012 period. Further, total cloud fraction over norther parts of Norway seem to be increasing, with the trend being significant on 95% confidence level as reported by Jun et al. (2016). In addition an increase in precipitation in form of rain over northern Norway has been found (Pall et al., 2019).
However, Arctic wide climatology of cloud types and their microphysics are still largely uncertain and available only for land stations (Eastman and Warren, 2010, 2013; Chernokulsky and Esau, 2019).
Higher altitude IWV columns, $IWV_{850hPa-TOA}$ and $IWV_{700hPa-TOA}$ show smaller trends, however, due to the altitude this is expected. Found trends for $IWV_{850hPa-TOA}$ are ± 0.05 kg/m^2 dec^{-1} and for $IWV_{700hPa-TOA}$ are in between ± 0.03 kg/m^2 dec^{-1}. However, firm conclusion for negative trends is not possible to reach in this thesis due to the relatively poor representation of clouds in the reanalysis that arise from strongly variable spatial and temporal nature of their formation and dissipation.

Moreover, not only is the clouds representation in difficult but also the retrieval of their properties from satellites over sea-ice and snow covered surfaces such as those in the Arctic are difficult. Notwithstanding, this is an active field of research.

5.3.2 Spring month - May

The same analysis as for January has been performed for May and trends of IWV columns are shown in Fig. 5.18. Trends of IWV$_{850hPa-TOA}$ during May range between -0.1 to 0.1 kg/m^2 dec^{-1}. This increase is larger than the one found for January for IWV$_{surf-TOA}$.

It can be noted that although trends in IWV are larger during May, this does not reflect in stronger trends of T$_b$s, since stronger T$_b$ increase has been observed during January. This effect of stronger and faster warming of the Arctic in January (or winter) is the most pronounced feature of the Arctic amplification. Therefore, to answer this question, besides water vapour other mechanisms, such as moisture transport into the Arctic, albedo effect (sea-ice and clouds) or lapse rates mentioned in the introduction are actively being investigated by the scientific community.

The spatial pattern of IWV$_{850hPa-TOA}$ trends for the whole period matches well with those of T$_b$ for 183.31 ± 7 (190.31) GHz joint product (Fig. 5.4). Moreover, it seems that better matching of spatial patterns between IWV and T$_b$ trends is achieved for May when products from two frequencies are joint than for the separate periods. IWV$_{700hPa-TOA}$ shows changes of ± 0.05 kg/m^2 dec^{-1} and the spatial pattern is in

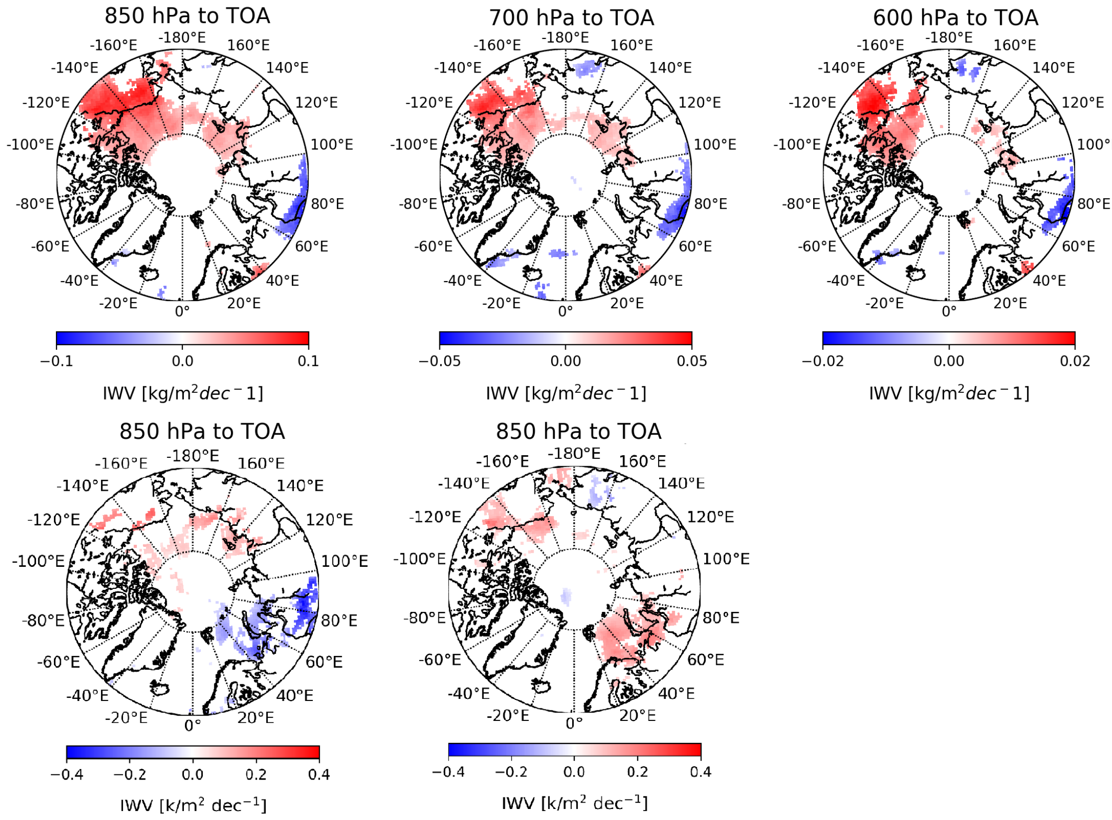
850 hPa to TOA
700 hPa to TOA
600 hPa to TOA
850 hPa to TOA
850 hPa to TOA

Figure 5.18: *As in Fig. 5.17 only for May.*

general agreement with T_b for 183.31 ± 3 GHz frequency channel. Largest discrepancies can be found over the Central Arctic ocean, East Siberian sea, where significant increase in total cloud cover has been reported (Jun et al., 2016), and Alaska. Other regions show the same sign in trends as do trends in T_b for 183.31 ± 3 GHz, however trends of IWV cover smaller areas, i.e. NW Russia. For the higher IWV column, 600 hPa-TOA, it seems that IWV negative trends over Siberia match well with the ones observed in T_b for the 183.31 ± 1 GHz frequency channel. However, positive trends for this IWV column do not reflect in positive trends of corresponding T_b because water vapour signal comes from higher atmospheric region.

The results for both months show that trends of IWV columns follow spatiotemporal variability of corresponding T_b relatively well, with exception of $IWV_{600hpa-TOA}$ in May. Following the weighting functions sensitivity study this is expected for the 183.31 ± 7 GHz and most of the regions for 183.31 ± 3 GHz in January, however results for 183.31 ± 1 GHz, especially in May are inconclusive indicating certain limitations of weighting functions. Before acceptance of the hypothesis one, ASRv2, from which IWV were calculated, should be evaluated in T_b space. This has been performed by running forward simulations for which forward model PAMTRA was employed and is a subject of the following section.

5.4 Conversion of the ASRv2 to observation space by usage of the forward model PAMTRA

In order to convert ASRv2 (from which IWV was calculated) into T_b space, forward simulations for January and May using forward model PAMTRA were performed. PAMTRA was set up in a way to best represent ASRv2 and its two moment scheme. Chapter 4 explains the set up of PAMTRA for calculations of synthetic T_b. In order to make simulations less costly, simulations were performed for every 4th grid point and for 183.31 ± 3 and 183.31 ± 1 GHz frequencies only for the left side of the wing. For these high sounding frequencies, the effect of simulating only left side of the wing should not affect simulated T_bs much since at these altitudes signal generally should not be affected by surface.

After simulations have been completed, every time step has been processed so that it follows the orbit from each of the satellites. Such simulated orbits were then interpolated to the observation angles in order to represent the observed state as close as possible. Since reanalysis (ASRv2), and therefore simulations have 8 time steps in a day, starting at midnight and ending at 21:00 UTC, observations were taken for each of the simulated time steps only and as well for every 4th grid point to allow for equitable comparison. Furthermore, a land mask as a mean of 17 years of observations from all satellites has been produced. Simulations and observations as well were than compared for regions over land and ocean separately.

Figure 5.19 shows the monthly mean of both observations and simulations for January 2008 as maps and theirs comparison is presented separately over land and ocean by histograms. Over land, it can be seen that simulations compare remarkably well with the observations, being correct to third decimal point when averaged.

Similar agreement between observations and simulations is found for ocean region where simulations differ from observation by only 0.03 K when averaged. Over land

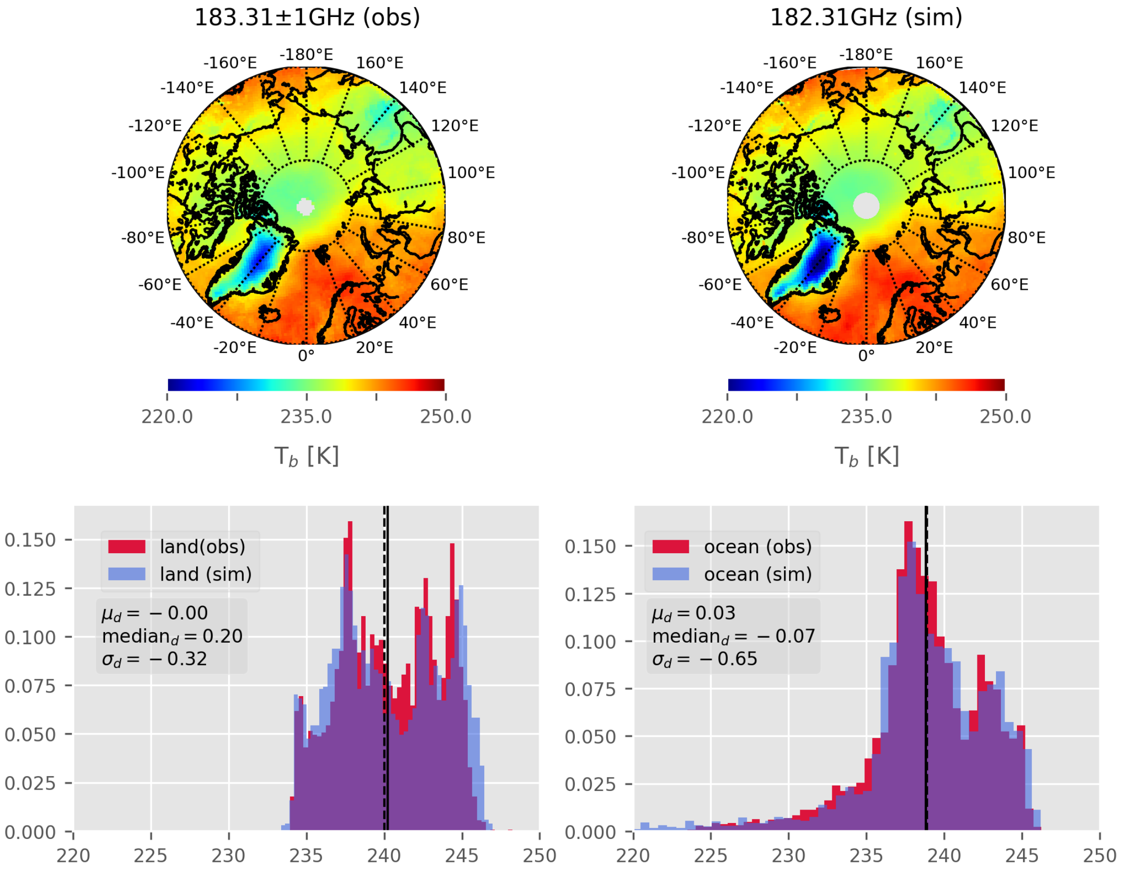

Figure 5.19: *January 2008 monthly mean observations for 183.31 ±f 1 GHz frequency channels from all available satellites (top left) and simulations for 182.31 GHz (top right). Histograms of observations and simulations over land (bottom left) and over ocean (bottom right). Colors denote observations (red) and simulations (blue). Vertical black lines on histograms are means of observations (solid) and simulations (dashed). Additionally differences between observations minus simulations mean (μ_d), median$_d$ and STD (σ_d) in Kelvin are marked in the square on the left.*

a slight difference is evident over central Greenland due to its high orography and complex emissivity. Over ocean, which includes sea ice covered surface as well, a very small difference is observed over the region south-east of Greenland to Island and over Barents and Norwegian Seas where simulations tend to be negligibly warmer.

For the 183.31 ± 3 GHz frequency channel, simulations (180.31 GHz) show a mean difference of 1.42 K over land and of 0.13 K over ocean. The effects of the surface during dry January are slightly reflected in the simulations over land where emissivity is much harder to retrieve. This is evident for the Central Arctic region as can be seen in Fig. 5.9 from the weighting function for 183.31 ± 3 GHz (red line). It needs to be reminded that in PAMTRA, surface emissivity for land was taken from the TELSEM^2 model which retrieves emissivity values from SSM/I, SSMIS and AMSU-B satellites and offers a climatological mean for each month. Simulations for this frequency, as for the above, tend to be slightly warmer over both land and ocean. Nonetheless, a very good agreement is achieved, with difference of only 0.13 K between simulations and observations.

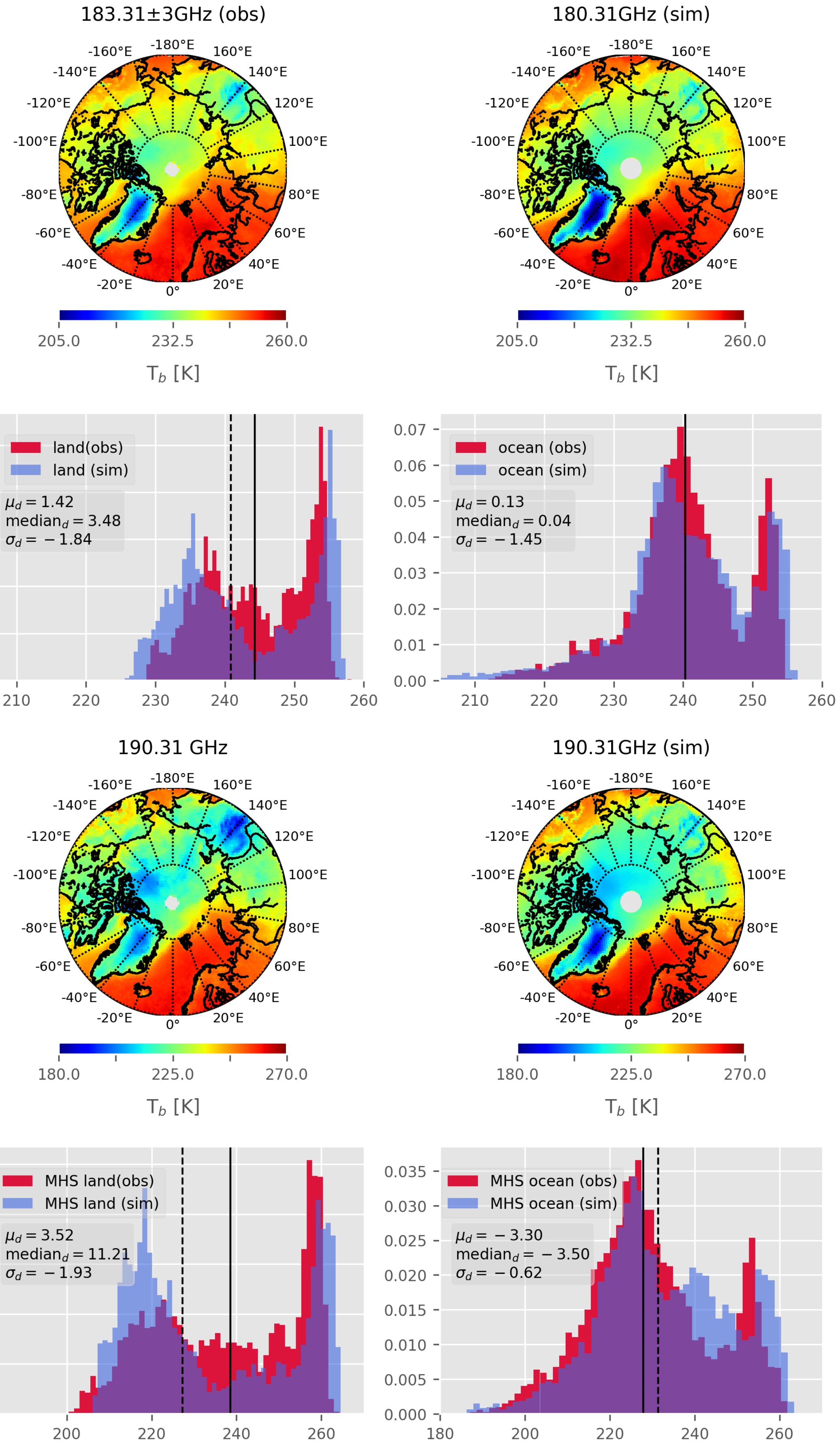

Figure 5.20: *As in Fig. 5.19 only for 183.31 ± 3 (180.31) GHz (first two rows) and for 190.31 GHz (last two rows).*

For the 190.31 GHz frequency channel simulations tend to have larger disagreement with observations. The differences over land can be of 3.5 K and over ocean of 3.3 K. Eve stronger than for the 183.31 ± 3 GHz frequency channel, simulated T_b values are affected by surface emissivity since the signal for this channel is received from even lower altitudes during cold and dry period of the year and often comes from the surface. This effect from the surface can as well be seen in the weighting functions (Fig. 5.10; pink line). The strongest disagreement, besides Greenland, is observed over Hudson Bay, Alaska (Yukon) and Siberia (Verkhoyansk range) region where complex topography is present. Due to complex topography over these regions, large local variability of both T_b and IWV was observed near Mackenzie and Lena rivers. Therefore, the disagreement over these regions can as well result from complex dynamical processes that need to be parameterized in the ASRv2.

A similar comparison of T_b simulations and observations has been performed for May 2009 and is presented in Figs. 5.21 and 5.22. Since years 2008 and 2009 are overlap years of most of the satellites, these have been chosen for the investigation. For May, it can be seen that simulations of T_b for 183.31 ± 1 GHz agree very well with the observations. Small disagreement between simulated and observed T_b of 0.25 K and 0.28 K can be seen over land and ocean, respectively.

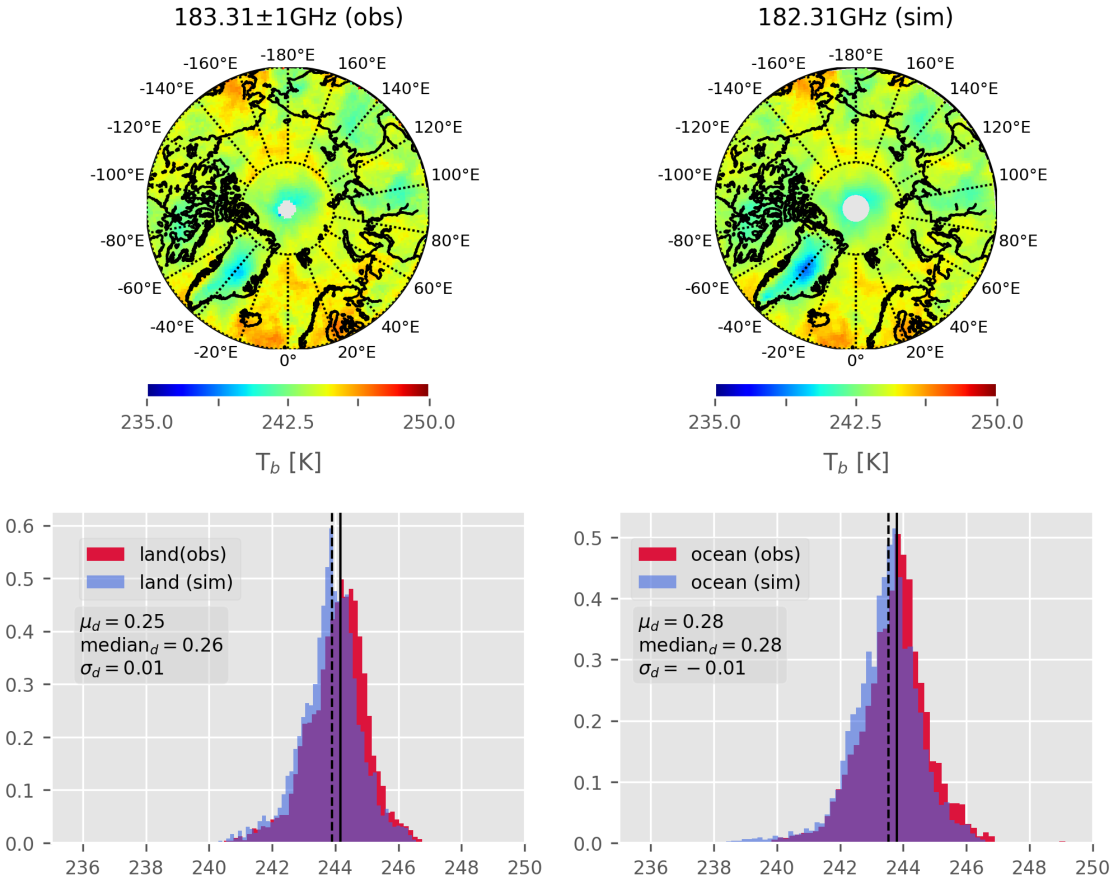

Figure 5.21: As in Fig. 5.19 only for May 2009.

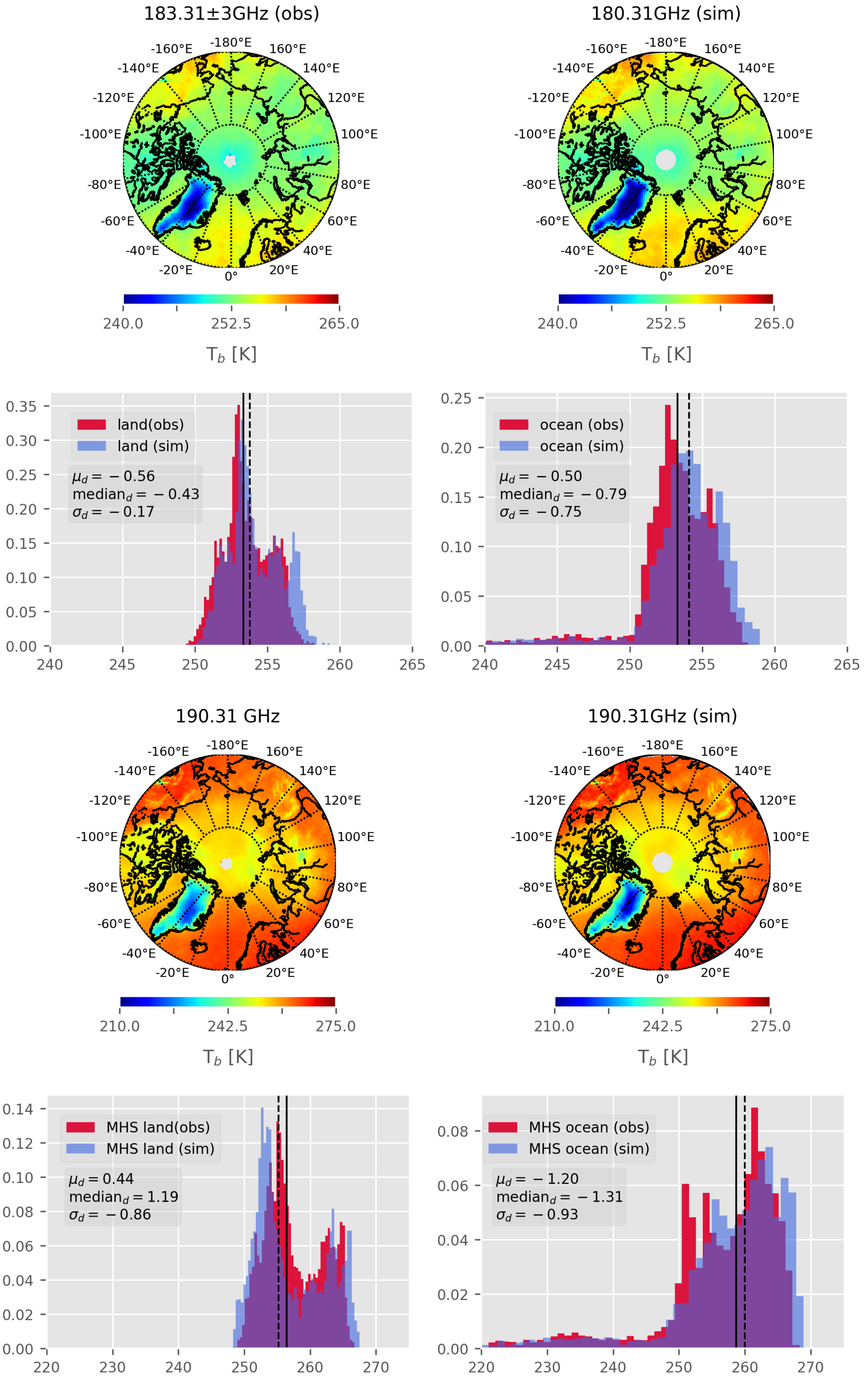

Figure 5.22: *As in Fig. 5.20 only for May 2009.*

Differences between simulations and observations over land are seen over Nordic countries while over ocean, disagreement is noticed over Greenland Sea and from 140°W to 140°E around 75° latitude. Figure 5.22 shows that simulations for 183.31 ± 3 GHz (top) agree very well with the observations with slight differences over land noticed over Alaska region from 120°W to 160°W and from 60°N to 70°N while over ocean differences are noticed over Greenland and Norwegian Seas. However, on average differences are not larger than 0.56 K over land or 0.5 K over ocean surfaces. Moreover, in comparison to January it seems that simulations for this frequency tend to be colder when compared to observations.

T_b simulations for 190.31 GHz frequency channel show very good agreement with observations given the fact that this frequency channel can be strongly affected by surface. Differences over land do not go above 0.44 K or above 1.2 K over ocean. Such good agreement, however, rises from the fact that due to more opaque atmosphere in May in comparison to January, the signal receiving altitude is lifted higher into troposphere. This can be seen in the weighting functions, especially for North Atlantic (Fig. 5.12), NW Russia and Siberia (Fig. B.7) regions. Over the North Atlantic region, 190.31 GHz frequency does not seem to be strongly affected by surface emissivity during neither January nor May. However, it needs to be mentioned that assessment of water vapour for lower sounding frequencies during cold and dry periods is much harder to interpret over sea-ice covered surfaces. This and the fact that different satellites are scanning different local time needs to be kept in mind when using the joint product for trend calculations.

After the comparison between simulated and observed T_b has been presented for monthly means, it is of interest to see how simulations correlate with observations on different time scales. Therefore correlations are calculated for daily, monthly and 17 years period (shown in Figs. 5.23 and 5.24 for January and May, respectively). It can be seen that simulations correlate extremely well with the observations for all time scales ranging from 0.96 to 0.99 and from 0.88 to 0.98 for 183.31 ± 1 GHz T_b for January and May respectively. It can be noted that correlations increase for longer time scales for both months. However, during May when stronger atmospheric variability is observed correlations for daily and monthly time scale for 183.31 ± 1 GHz tend to be slightly smaller than those found for January. This could be due to more stable UTLS region in January compare to May when the stable polar vortex has broken up. Same is found for T_b from 183.31 ± 3 GHz frequency channel.

On monthly time scale for 183.31 ± 3 GHz frequency channel, sightly higher increase in correlation is found for May. The reason could be that during January emissivity from surface can sometimes affect received signal from 183.31 ± 3 GHz channel, not evident in weighting functions calculated using climatological profiles, while during May this was not observed. Similar behavior of correlations for different time scales is observed for both lower scanning frequencies and their respective periods, with correlations ranging from 0.9 to 0.92 for January (Fig. B.9) and 0.91 to 0.98 for May Fig. B.10).

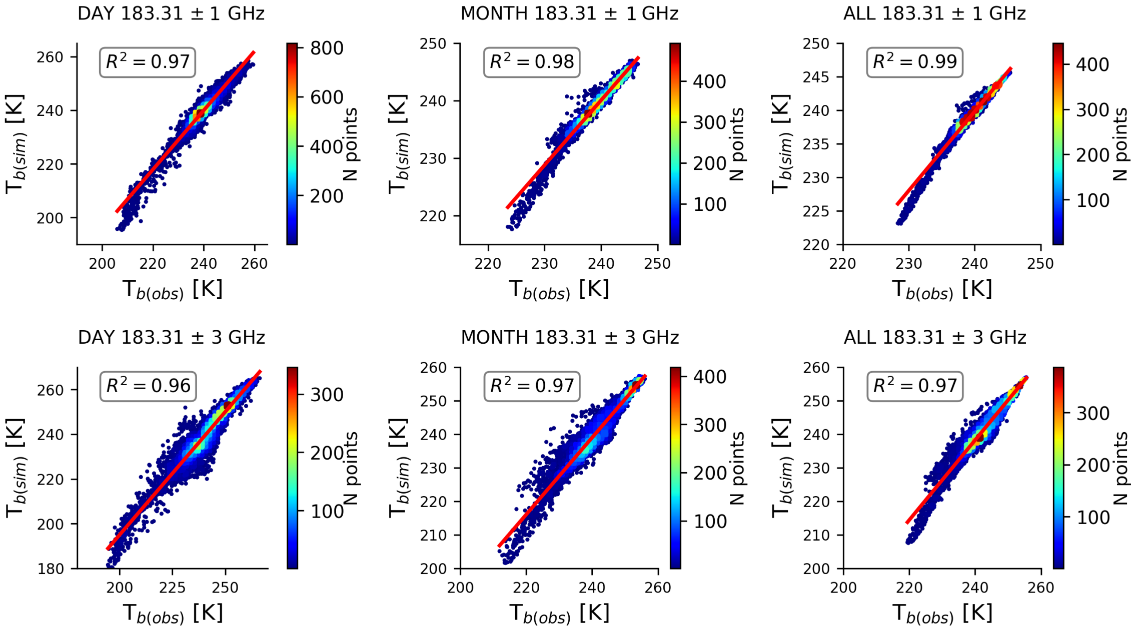

Figure 5.23: *2D histogram of simulated and observed T_b for 183.31 ± 1 GHz (top) and 183.31 GHz ± 3 (bottom) frequencies. Shown are pixels from all satellites for 2 January 2008, monthly means of January 2008 and monthly means for all Januaries during the 2000-2016 period. Red line indicates the best fit.*

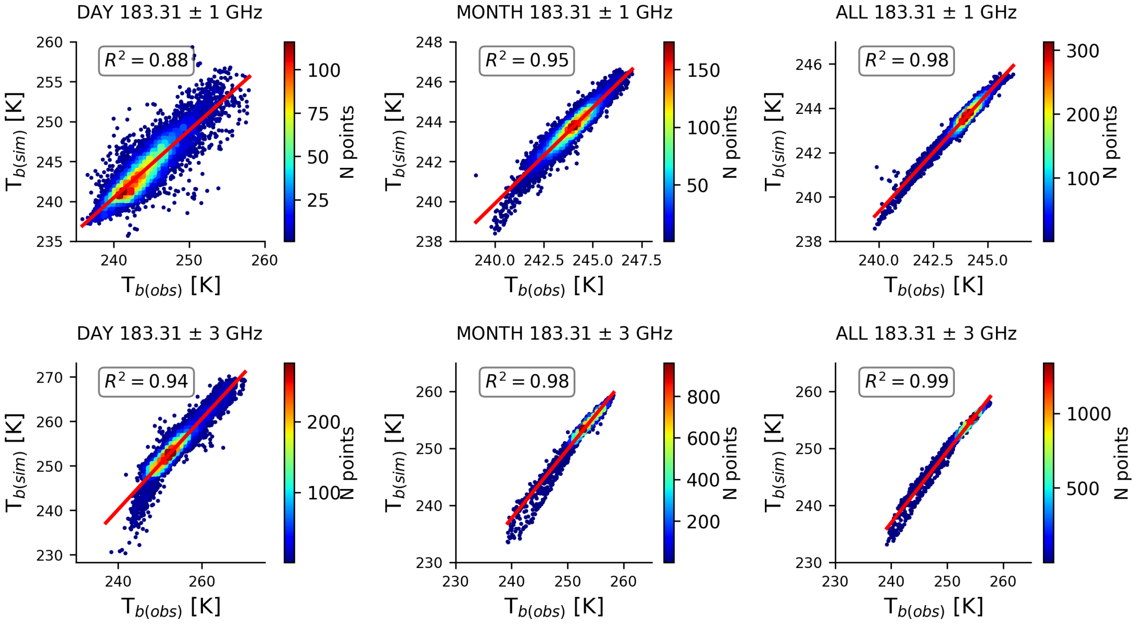

Figure 5.24: *As in Fig. 5.23 only for 2 May 2009, month of May 2009 and all Mays during 2000-2016 period.*

5.5 Can T_b be used as a proxy for IWV in the Arctic?

So far, this chapter presented observed T_b trends calculated from all available satellites overpasses and discussed the sensitivity to water vapour of three frequency channels. From the sensitivity study three IWV columns roughly corresponding to T_bs of weighting function peaks of three frequency channels were calculated and compared with those found in T_b to check for spatial pattern resemblance. In order to make firm conclusions about matching patterns, ASRv2 reanalysis was converted to observation space, in this case to T_b. High correlations were found between the observed and simulated state. This confirms that ASRv2 is a good choice for the assessment of IWV and testing of hypothesis one.

In order to answer the hypothesis, this section focuses on trends from IWV columns that were correlated with simulated and observed T_b. Since ASRv2 is a 3-hourly reanalysis, observed T_b were as well, besides whole overpasses, taken only for model time steps to make comparison between observed and simulated state equitable.

5.5.1 Winter month - January

Figure 5.25 shows trends in IWV columns, simulated and observed T_bs (1- and 3-hourly) for January. It can be seen that spatial patterns of IWV column trends follow simulated and observed T_b trends remarkably well. Moreover, correlations between lower altitude sounding frequencies from AMSU-B and MHS joint product for T_b and $IWV_{surf-TOA}$ show that all positive trends in IWV can be approximated by trends in T_b. This is especially evident over regions such as NE Greenland, Fram Strait and NE Arctic. Although, the same is found over Canadian Archipelago and Kara seas, this is not readily seen. Therefore correlations are separately shown in the appendix (Fig. B.12). Overall, the mean correlation of $IWV_{surf-TOA}$ and corresponding T_b for whole Arctic region is of 0.89 with maximum correlation reaching high value of 0.96. Higher $IWV_{850hPa-TOA}$ column trends as well follow corresponding T_b from 183.31 ± 3 GHz trends and can be approximated by them since high correlations of 0.89 between them was found. The six regions of interest (Fig. 5.8) as for previous pair of IWV and T_b, with slightly less coverage are observed for $IWV_{850hPa-TOA}$ column and corresponding T_b. Most evident difference between $IWV_{surf-TOA}$ and $IWV_{850hPa-TOA}$ column is observed over Fram Strait which for higher column does not show significant increase in contrast to lower IWV column and which moreover, is most pronounced for the previous pair. Over southern Norway a smaller area with significant negative trends is observed. Furthermore, over northern part of Norway and parts of Barents sea, stronger decrease in $IWV_{850hPa-TOA}$ is observed which does not seem to be positively correlated with 183.31 ± 3 GHz T_b but in contrast T_b shows slight increase. This is in agreement with weighting function test over land covered area where increase in humidity shows a decrease in T_b, especially for the 183.31 ± 1 GHz frequency channel (Figs. 5.9, 5.10 and B.2).

In order to further investigate this negative trend in IWV over Northern Norway, integrated CLW and snow content from the ASRv2 were also investigated, however only for surf-TOA column. It was found that both integrated CLW and snow content are decreasing. Although this is in a way expected due to the fact that decrease in the IWV, and therefore less available humidity, would subsequently lead to less con-

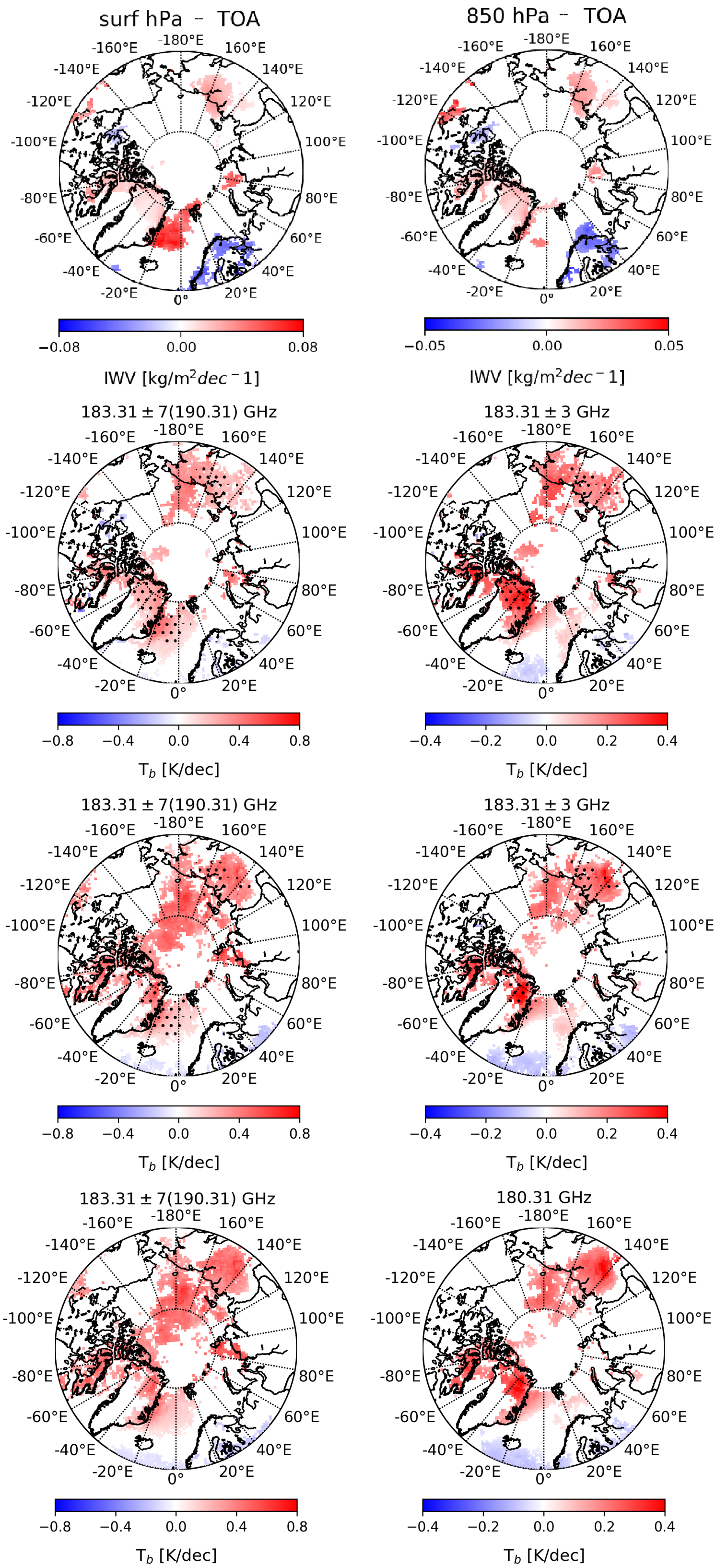

Figure 5.25: *January changes in three IWV columns as noted in figure (first row), T_b simulated from ASR (2nd row), T_b observed at ASR time (3rd row) T_b observed at hourly resolution (last row). T_b for 183.31 ± 7 and 190.31 GHz are shown as joint product. Shown are only significant changes for 90% confidence with stippled regions (second and third row) indicating positive correlation between IWV and T_b.*

-densation, cloud formation and precipitation there are other phenomena to consider. However, it is important to mention that representation of CLW in models is difficult due to various process such as cloud glaciation and precipitating icy crystals from supercooled liquid water (Bergeron, 1928; Rauber and Tokay, 1991; Shupe et al., 2008; Pithan et al., 2018) that need to be parameterized. This is especially true for the mixed-phase clouds and their transition from one phase to another which is still very challenging, and thus models struggle to represented such clouds well (Korolev et al. (2017) and references therein). Overall due to the absence of increase in integrated CLW or snow, it seems that this region has experienced increase in T_b accompanied by drying over approximately past two decades. Moreover, investigation of T at close pressure level of 700 hPa-TOA from ASR show no significant trend over this region.

$IWV_{700hPa-TOA}$ trends as those from lower IWV columns seem to follow trends in both simulated and observed corresponding T_b with the spatial pattern over Norway being more similar to $IWV_{850hPa-TOA}$. A high correlation for positive trends between $IWV_{700hPa-TOA}$ and corresponding T_b has been found for this level as well. Besides the above, it is worth to check for agreement of T_b simulations (2nd row) and 3-hourly (3rd row) observations with 1-hourly observations (4th row) shown in Fig. 5.25. It can be seen that at the lower sounding frequencies (183.31 ± 7 and ± 3 GHz) 3-hourly values agree well with 1-hourly T_bs and show high robustness over all regions of significance. However, it can also be noted that taking only 3-hourly T_b values for 183.31 ± 1 GHz suffer from lower robustness over certain regions. Larger disagreement between both temporal resolutions is noted at 183.31 ± 1 GHz frequency over the North Atlantic, northern Norway and NW Russia. This could be explained by lower observational coverage over these regions for model time steps (Fig. B.15).

Overall, a conclusion regarding hypothesis for January can be drawn which is: T_b for corresponding IWV columns can be used as a proxy since high correlations has been found for all pairs of IWV columns and T_b especially for positive trends that show high correlation reaching 0.96. Nonetheless, it seems that negative trends in IWV are not as easily explained by T_b only although weighting functions tests over land surfaces indeed show negative correlation, this correlation is not significant. Moreover, this disagreement in trends sign could as well steam from poorer satellites coverage over these regions for model time steps.

5.5.2 Spring month - May

The same analysis as for January has been performed for May, shown in Fig. 5.26. Herein as for January, lower IWV column, i.e. here $IWV_{850hPa-TOA}$, due to drier atmosphere (Table 4), follows the trend in corresponding T_b of joint product (183.31 ± 7 and 190.31 GHz). The highest correlations have been found over the Alaska region with Beaufort sea and East Siberian sea reaching values of 0.98. However, observed negative trends in IWV between 80°E and 100°E do not seem to correlate completely with the simulated T_b but follow observed T_b trends relatively well. Moreover, over small parts of NW Russia around 60°E, these two variables show small negative correlation of -0.25 (Fig. B.12).

As for January, CLW and snow content has been analysed (Fig. B.11). It is found that a decrease in CLW and snow follows a decrease in IWV for the NW Russia region.

Overall significant trends in $IWV_{850hpa-TOA}$ can be approximated with corresponding T_b with the exception of small negative trends observed around 60°E. Regarding only T_b from the joint product, a much larger area of positive trends is observed in simulated T_b over parts of Russia, Barents and Kara seas in comparison to observed trends of both, 3-hourly and 1-hourly composites.

Similar result of the trend and correlation analysis to the above pair is found for upper atmospheric IWV column, namely $IWV_{700hPa-TOA}$ and T_b at 183.31 ± 3 GHz. However, here much smaller area is showing positive correlation over Alaska, while trends over parts of East Siberian Sea are not observed in neither temporal resolution nor simulations of T_b trends. For the last pair, $IWV_{600hPa-TOA}$ and T_b at 183.31 ± 1 GHz no significant positive but instead only a negative correlation as for lower sounding frequency over small region around 60°E has been found. However, for higher sounding frequency channel at 183.31 ± 1 GHz, which receives the strongest signal from $\sim$ 10-12 km and it was shown by other studies that increase in stratospheric humidity leads to cooling at those altitudes (Manabe and Strickler, 1964; Manabe and Wetherald, 1975; Gillett et al., 2003; Maycock et al., 2011). higher sounding frequency 183.31 ± 1 GHz

In order to verify that T_b at higher sounding frequencies decreases due to increase in humidity, higher scanning frequencies were tested for an increase in specific humidity of 10%, 15%, 20%, 25% and 30%. For this the forward model PAMTRA was employed. It is indeed found that over these regions an increase in humidity would lead to a decrease in T_b (Fig. B.13). Therefore, higher IWV column for 300 hPa-TOA has as well been investigated. It was found that IWV indeed was increasing over regions where T_b showed a negative trend. However, a significant negative trend in $IWV_{300hpa-TOA}$ is found only for NW Russian region while positive trend is found over parts of East Siberian sea (Fig. B.13). For this reason trends in T at two different levels, namely 700 and 500 hPa where as well investigated (Fig. B.14). It was found that trends of T at 700 hPa match well with the simulated and one hourly resolution T_b trends at 183.31 ± 3 GHz joint product. For trends in T at 500 hPa it was found that T trends match well with the ones found for the one hourly resolution T_b at 183.31 ± 1 GHz, however, excluding Alaska and Beaufort Sea region. Moreover, positive trend in T over East Siberian Sea has been found for both, T at 700 and 500 hPa. This implies that Clausius-Clapeyron relation possibly is not valid locally due to importance of transport and that Clausius-Clapeyron scaling could possibly have some departures. This could partially be explained by residence time effect of water vapour in UTLS region after entering the stratosphere, which is a consequence of the spatiotemporal variance in the temperature field. However, a departure from Clausius-Clapeyron scaling has not been, up to now, investigated for the complex Arctic stratosphere region that in respect to above and more importantly Arctic Amplification, deserves more attention. In addition, it is important to mention that for high altitudes, water vapor is found only in trace amounts and other factors influence variability of the temperature field and subsequently observed trends, such as ozone, chlorine, CH_4 and their mixing influenced by large-scale planetary waves (Newman et al., 2001; McConnell and Jin, 2008).

As for January, the influence of temporal availability of observations on the disagreement between simulated and observed T_b was investigated. It was found that for

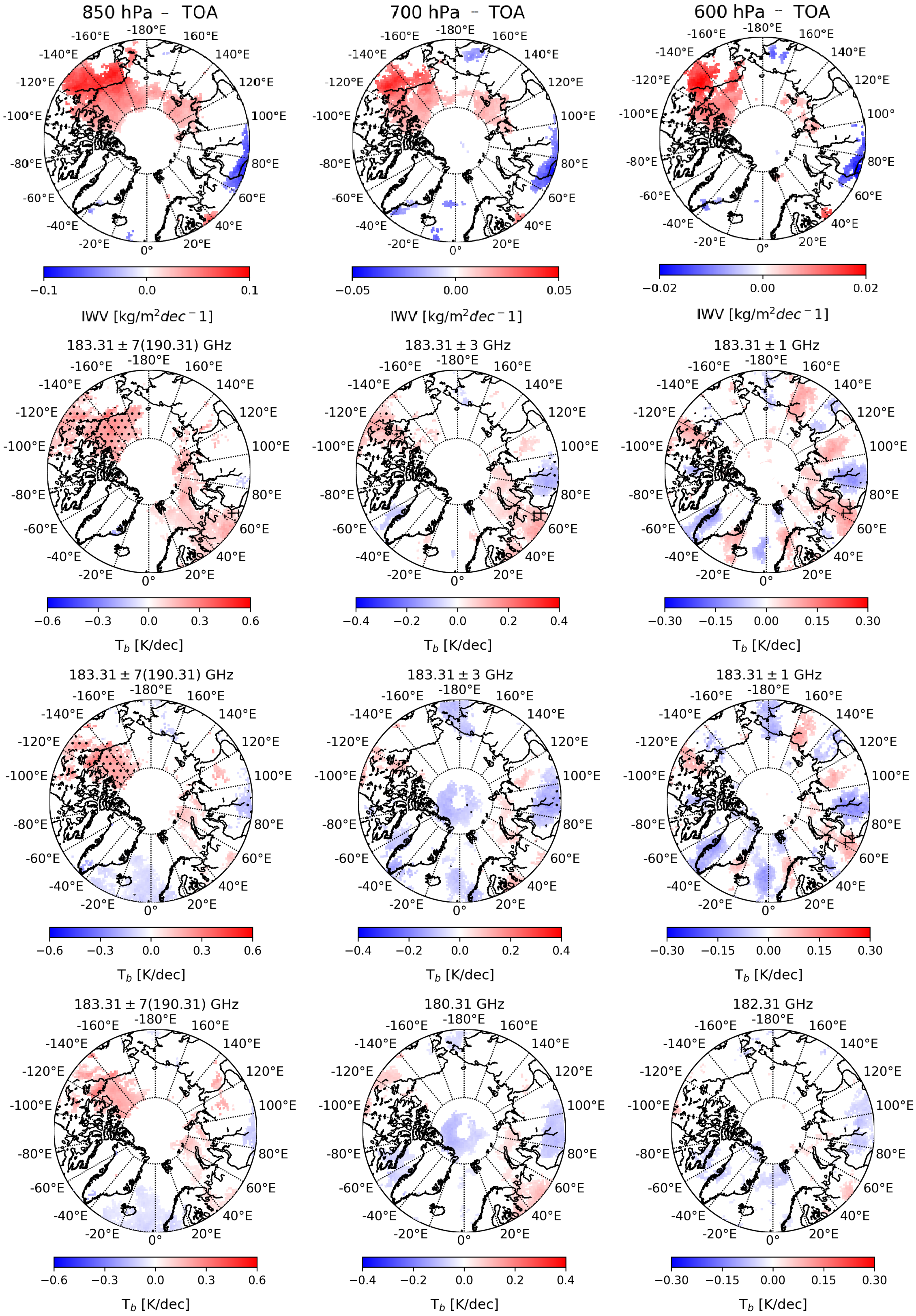

Figure 5.26: *As in Fig. 5.25 only for May.*

all regions of disagreement, especially North Atlantic and Siberia, observations for model time steps were much lower than for 1-hourly steps (Fig. B.16 and Fig. B.17). Hypothesis one for May, for lower IWV columns to a limited degree can be confirmed since correlations between corresponding T_b tend to be relatively high and positive but excluding the North Atlantic region. However, smaller region of positive $IWV_{700hPa-TOA}$ trends over Beaufort and East Siberian sea was not observed in corresponding T_b of 183.31 ± 3 GHz frequency channel. The only exception for which hypothesis one can not be confirmed for any region is found for higher $IWV_{600hPa-TOA}$ column. This IWV column seems harder to be explained by T_b trend only. Moreover, for the regions where correlations have been found, they tend to be negative. A sensitivity study and the weighting functions have shown that T_b for 183.31 ± 1 GHz indeed decreases as the water vapor increases. This was further confirmed by investigating $IWV_{300hPa-TOA}$. To be able to better explain the detected trends this pair of IWV and T_b, further investigation of the complex UTLS temperature and water vapour field is needed. An additional reason for this disagreement could steer from effects of pressure broadening of 183 GHz absorption line on T_b as well as the water vapour line modelling in absorption model implemented into PAMTRA. So far different laboratory experiments considering water vapour absortion line have been made (Bauer et al., 1989; Gamache and Vispoel, 2018; Stolarczyk et al., 2020) and this topic is still an active field of research. It would be of interest to investigate possible implications of different absorption models on the Arctic atmosphere. However, this is not covered in this thesis and is left to be answered.

6 Arctic phenomena: Polar lows

The content of the following chapter has been published by Radovan et al. (2019). The research focus is on the second hypothesis:

> **Hypothesis 2**: Through investigation of multiple important environmental conditions of polar lows during genesis stage, it is possible to find the most important one/or the combination of that enables/enable further persistence of the polar low to its maturity stage and determines its severity in terms of the wind speed.

This research investigated six different environmental conditions and revealed the importance of interplay between temperature gradient at the surface and the 500 hPa level and low-level convectional instability indicated by strong lapse rates. Moreover it was found that RH during genesis stage has a great impact on maturity stage wind speed intensity.

The author of this thesis conceptualized the study together with advises from Susanne Crewell, Annette Rinke and Erlend M. Knudsen. The preparation and the analysis of data set was done by the main author while preparation for the publication was done with support from all co-authors.

Environmental conditions for polar low formation and development over the Nordic Seas: study of January cases based on the Arctic System Reanalysis

Ana Radovan[1] Susanne Crewell[1] Erlend Moster Knudsen[1*] Annette Rinke[2]

[1]Institute of Geophysics and Meteorology, University of Cologne, Cologne, Germany
[2] Alfred Wegener Institute, Helmholtz Centre for Polar and Marine Research, Potsdam, Germany

Abstract

The sparse observational network over the Arctic region makes severe storms such as polar lows (PLs) still hard to predict. To improve their forecasting and detection, it is of great importance to gain better understanding of their formation and development. Therefore we have analyzed the environment of PLs at their genesis and mature stages using a set of parameters: the difference between sea surface and 500 hPa temperature (or at 2 m height), lapse rate (LR) and relative humidity below 850 hPa (RH), near-surface wind speed and geopotential height anomaly. We evaluate which of these conditions (or which combination) is(are) the most favorable for PL formation and persistence. The analysis was performed on 33 January cases over 12 years (2000 - 2011) using the Arctic System Reanalysis. The results showed that, for the cases with lower thermal instability during formation stage, LRs throughout the boundary layer were stronger and steeper; therefore, these PLs were fostering convective development. However, for few cases it was noted that when convection decreased simultaneously with increased thermal stability, RH most of the times was above 90 % . It was also noted that the higher amount of RH at lower levels during genesis stage promoted stronger winds at the maturity stage.

6.1 Introduction

Throughout history, in the Arctic region, severe sudden storms that pose a great threat were well known to the coastal community. A sudden change of weather with a storm that brings heavy precipitation and strong winds causes substantial infrastructural damage, wreaks havoc on ships and disrupts shipping routes. Today, in a rapidly changing climate where the increase in near-surface air temperature in the Arctic region is twice the global value; term know as the Arctic amplification (Serreze and Francis, 2006b), thinner sea ice is becoming more vulnerable to storms (Zabolotskikh et al., 2015). To understand the major feedback mechanisms of Arctic amplification, major efforts are being made to identify, investigate and evaluate the key processes that contribute to it (Wendisch et al., 2017). A study by Condron and Renfrew (2013) found that the most intense cyclones extract huge amounts of heat from the ocean (≥ 1000 Wm^{-2}) and thus affect open-ocean deep convection and subsequently the Atlantic meridional overturning circulation (AMOC). Therefore, how these cyclones will occur and strengthen in the future climate is highly important, especially in the region of the Nordic Seas, which is already experiencing drastic changes (Lind et al., 2018; Carmack et al., 1997; Morison et al., 2012). The first attempt to explain the formation of these severe storms was given by Dannevig (1954), where he referred to them as "Arctic instability lows". He noted that such a storm can develop due to instability within a cold air outbreak (CAO) that flows over the warmer sea. These severe storms were termed polar lows (PLs) (Harley, 1960) since they appear only over polar regions. The commonly used definition for this term has been proposed by Rasmussen and Turner (2003):

> *"Polar low is a small, but fairly intense maritime cyclone that forms poleward of the main baroclinic zone (the polar front or other major baroclinic zone). The horizontal scale of polar low is approximately between 200 and 1000 km and surface winds near or above gale force."*

However, as the observational network over the Arctic Ocean is sparse and polar lows are relatively small and short-lived maritime cyclones (can last only 4 h (Blechschmidt, 2008)), their prediction still presents a challenge. Improving their treatment in numerical models requires a deeper knowledge of the environmental conditions in which they form and develop.

Among the first theories that tried to explain the formation of a PL was the thermal instability theory, which proposes instability inside a CAO flowing over the warmer sea as the main mechanism (Dannevig, 1954). Although thermal instability partly explains the formation of PLs, this theory lacks the explaining mechanism for vorticity formation. The baroclinic instability theory proposed by Harold and Browning (1969) showed that a low-level baroclinic field is necessary but is not sufficient for PL formation. Due to PLs' resemblance to tropical hurricanes on the satellite images, such as the frequently visible eye and the presence of spiral of cumulus clouds around it, convection was believed to explain their formation. Therefore, the conditional instability of the second kind (CISK) was proposed to account for PL genesis (Rasmussen (1979)). However, that mechanism was only able to explain the intensification of an already developed circulation (Sardie and Warner, 1983; Charney and Eliassen, 1964), and the calculated growth rates were too small. Another theory originating from the resemblance of PLs to tropical hurricanes is the Air-Sea Interaction Instability (ASII) theory given by Emanuel (1986) and later renamed as the Wind Induced Surface Heat Exchange (WISHE) theory (Emanuel and Rotunno, 1989). According to that theory, a PL acquires energy from the sea surface fluxes and moist enthalpy, as also shown by Rasmussen (1979). However, the theory neglects environmental baroclinicity and is not able to produce the PL growth rate (Montgomery and Farrell, 1992). Sardie and Warner (1983) also showed that some PLs tend to be mainly baroclinic while others show strong convective features. Despite the multitude of these theories about PL development, and despite several research aircraft campaigns into the topic (Shapiro et al., 1987; Douglas et al., 1995; Føre et al., 2011), the phenomena of PLs remain too complex to be explained by only one of the theories. This difficulty has led to the acceptance of several mechanisms acting simultaneously in triggering and intensifying a PL and a spectrum between the extremely baroclinic and convective cases (Bracegirdle and Gray, 2008).

Our study improves understanding of PL formation and development by investigating a comprehensive set of parameters suggested in the literature for characterizing the environmental conditions. The study looked at different thresholds in these parameters to identify the most relevant one(s) or the most relevant combination. Furthermore, the parameters for both the genesis and maturity stage of PLs were investigated to potentially derive information on their development and persistence. For this analysis, we used both versions of the Arctic System Reanalysis (ASR), which improves the depiction of mesoscale processes in the Arctic region (Bromwich et al., 2010, 2016). We focused on PL cases for January between 2000 - 2011 over the North Atlantic region. Generally, January is the month with highest PL occurrence (Noer et al., 2011) and also the coldest month of the PL season (October - May). The detailed description of the analysis technique and the set of parameters including their thresholds (from now on called conditions) are explained in Section 2. In Section 3, we present our results with two main focuses: first, the analysis of the parameters and their change from the genesis to maturity stage; second the climatological perspective, where we compared the large-scale environment during PL genesis with the overall January climatology. In Section 4, we briefly discuss and conclude our results.

6.2 Data and Methods

6.2.1 PL cases

The investigated January PL cases are based on the Noer and Lien (2010) list (hereinafter referred to as NL list). The NL list contains the date, time and coordinates of each PL case at its maturity stage. The stage of maturity is defined by inspecting Advanced Very High Resolution Radiometer (AVHRR) images, where a PL is noted as fully developed when the cloud band structure and a partially clear eye of the low is visible. In addition, whenever possible, wind speed, and gust information from the Advanced Scatterometer (ASCAT) were registered. Using sea level pressure analysis from the numerical weather prediction model High Resolution Limited Area Model (HIRLAM) at 4 km resolution, minimum mean sea level pressure (MSLP) was also recorded. For the 2000 - 2011 period, in total, 33 January cases were reported (Figure 6.1).

6.2.2 ASR

The first version of ASR (ASRv1) is a 3-hourly regional reanalysis with a horizontal resolution of $\sim$ 30 km and 29 pressure levels available for the 2000-2012 period. It is produced using the state-of-the-art Weather Research and Forecasting Model (WRF) tuned for polar regions (Bromwich et al., 2010). When compared to observations, the WRF showed good performance for surface variables with MSLP having the best prediction, while poorest performance is shown for near surface wind speed due to inadequate modeling of local wind effects and obstructions (Bromwich et al., 2010). When compared to ECMWF Re-Analysis Interim (ERA-I), which has coarser temporal (6 hourly) and horizontal resolutions ($\sim$ 79 km), ASRv1 has improved modeling of near-surface wind fields and moisture while the remaining variables showed similar behavior (Wilson et al., 2011, 2012).

In addition, we also used the second version of ASR (ASRv2), which in comparison to ASRv1 has twice the horizontal resolution (15 km) and five more vertical levels (in

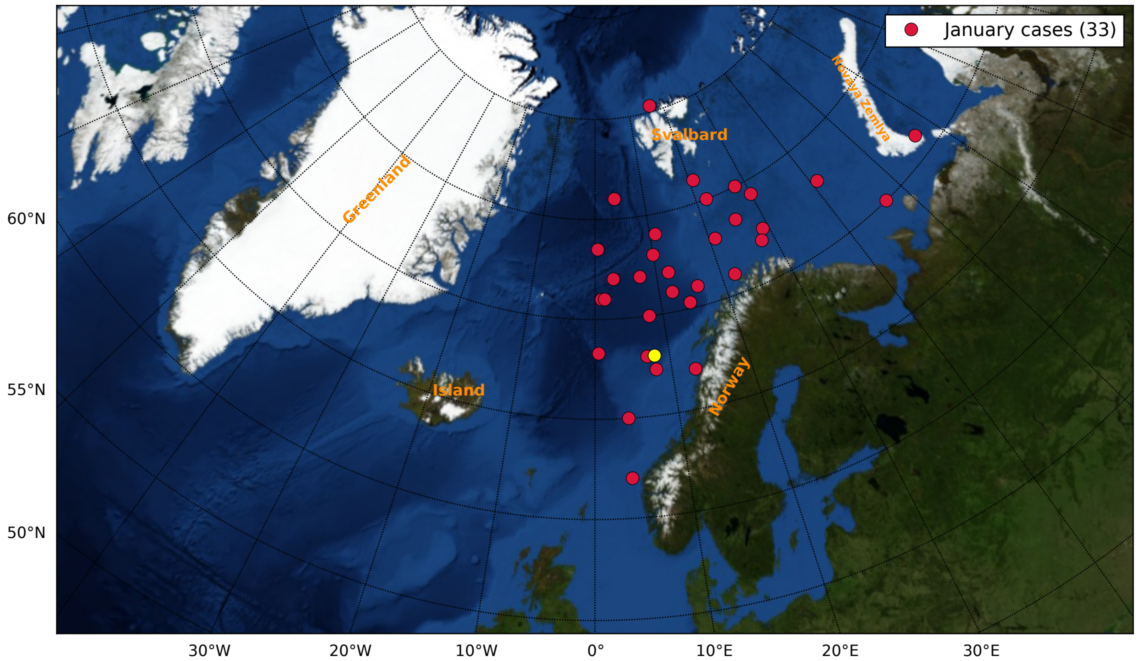

Figure 6.1: *January polar lows between 2000 and 2011. Each of the 33 cases is represented at the location reported in the Noer and Lien (2010) list (red dots). The case marked with yellow is the one presented in Figure 6.2.*

total 34 levels). Besides resolution, it also has improvements in the model physics, including sub-grid scale cloud fraction interaction with radiation, and in the data assimilation scheme. This new version also shows improvements in reproduction of near-surface and tropospheric variables (Bromwich et al., 2017). Although ASRv2 is offered for a longer time span, 2000 - 2016, to compare our results to ASRv1, we have used data for the same period for which the ASRv1 was released. Moreover, 2012 was excluded from the analysis since there were no PLs in January that year. Since PLs are 'extreme' maritime cyclones, it is of significance to check for ASR performance in respect to its general cyclones representation first. This has been done by Tilinina et al. (2014). They showed that the ASRv1, during winter, detects 28 % more cyclones than ERA-I. A similar result was shown in Akperov et al. (2018), where it was found that ASRv2 resolves more small and shallow cyclones. Compared to the Noer et al. (2011) PL climatology, ASRv1 was able to resolve 89% of the PLs compared to 48 % resolved in the ERA-I. ASRv1 also showed more realistic wind speed information that is closer to satellite observations (Smirnova and Golubking, 2017). In studies using ERA-I, Michel et al. (2018) and Zappa et al. (2014), the PL detections were 60% and 55% of those reported in the Sea Surface Temperature and Altimeter Synergy for Improved Forecasting of Polar Lows (STARS) data base (Ø.Sætra et al., 2010), respectively. Since ASRv1 proved to be more reliable in those studies, the choice of using ASR over ERA-I is justified.

6.2.3 PL genesis and maturity states

Investigating the environmental conditions (detailed in Section 6.2.4) at two different stages requires a time reference of a PL event. The maturity information was taken from the NL list, which notes the time of the maturity. Accordingly, we extracted the parameters from the ASR at the time step closest to maturity time. To analyze the same environmental conditions at the genesis stage, we followed the procedure by Terpstra et al. (2016) and took the genesis time to be 6-9 h prior to the maturity time. This time interval was chosen to take into account the time needed for PL development and the 3-hourly resolution of the ASR.

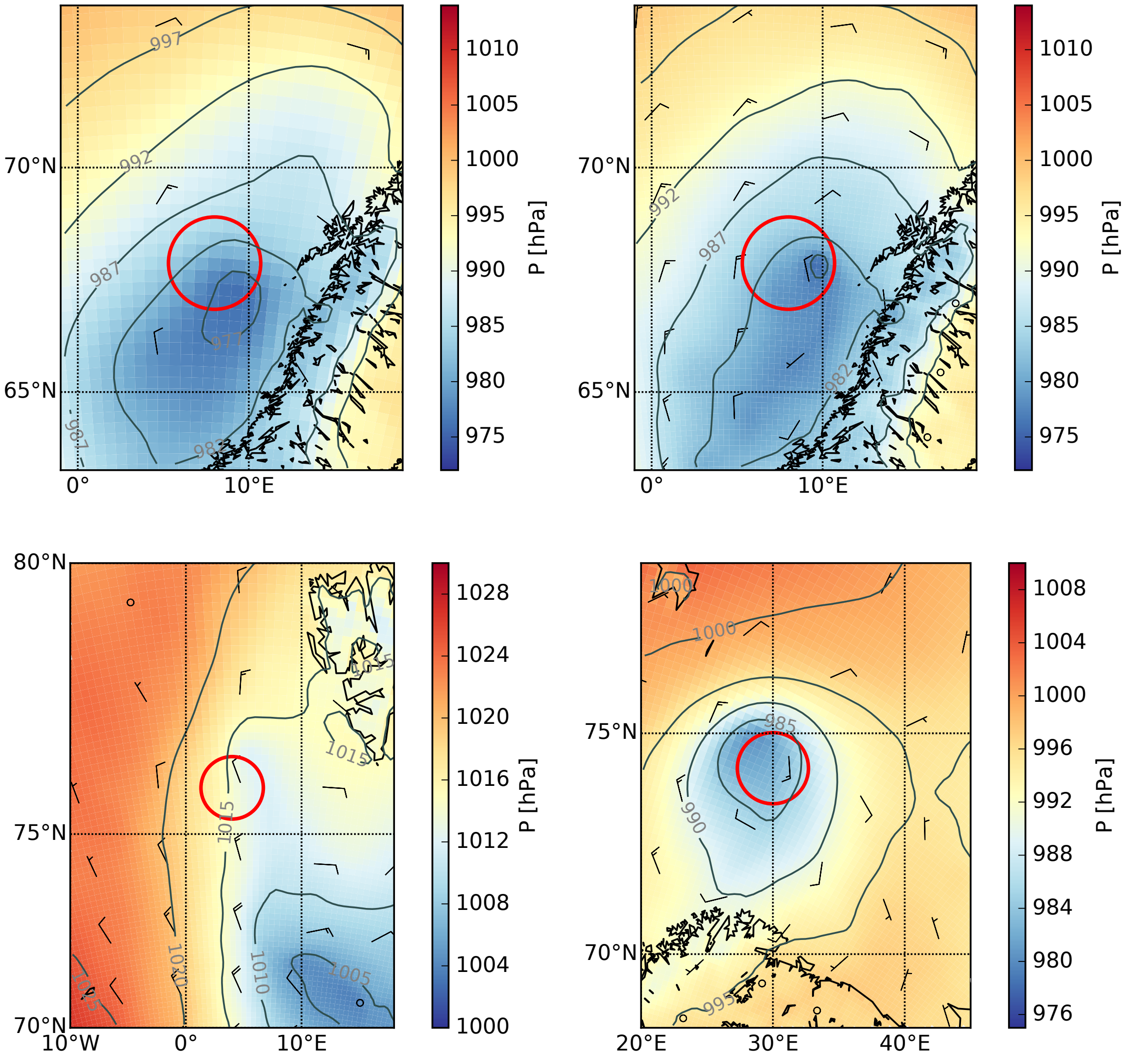

Figure 6.2: *MSLP (color shading and gray counters every 5 hPa) and wind speed and direction (wind barbs) for polar low cases on 29th Jan 2010 from ASRv1 (upper left) and ASRv2 (upper right) and for 22nd Jan 2007 (lower left) and 30th Jan 2011 (lower right). Both cases in the bottom row were plotted using the ASRv2 data. The red circle indicates a 200 km radius around the location from NL list*

At the genesis time, for each case, an area in the 200 km radius around the genesis point was used for the analysis. The small scale of PLs and the fact that only 2 % of the polar mesocyclones identified on satellite imagery have a diameter less than 200 km supports usage of that area as representative of the pre-PL environment (Condron et al., 2006). Due to this assumption, there could be larger spread of values in conditions in between cases. This can also, at times, attribute to different

Table 5: *PL conditions (denoted by C1,C2,...C6; see Section 6.2.4) and their values taken from various studies (second and third column, respectively). The last two columns give the 75 percentile means of C1, C2, C3, C4(i), C4(ii), maximum of C5 and mean of C6 for all the 33 cases during the genesis stage found using the ASR versions 1 and 2.*

	Condition	Value	Source	ASRv1	ASRv2
C1	SST - T(500 hPa)	$\geq$ 43 K	Noer and Ovhed (2003)	46 K	45 K
C2	SST - T(2m)	$\sim$ 6 K	Terpstra et al. (2016)	6 K	8 K
C3	LR	cond. unstable below 850 hPa	Terpstra et al. (2016)	1.4 K/km	2.6 K/km
C4	(i) RH(surf.-950 hPa)	$\sim$ 75%	Terpstra et al. (2016)	80 %	87 %
	(ii) RH(950-850 hPa)	$\sim$ 82%	Terpstra et al. (2016)	91 %	90 %
C5	NSWS	$\geq$ 15 m s^{-1}	Rasmussen and Turner (2003)	16.2 m/s	17.6 m/s
C6	GPH anomaly	160 gpm	Forbes and Lottes (1985)	182 gpm	140 gpm

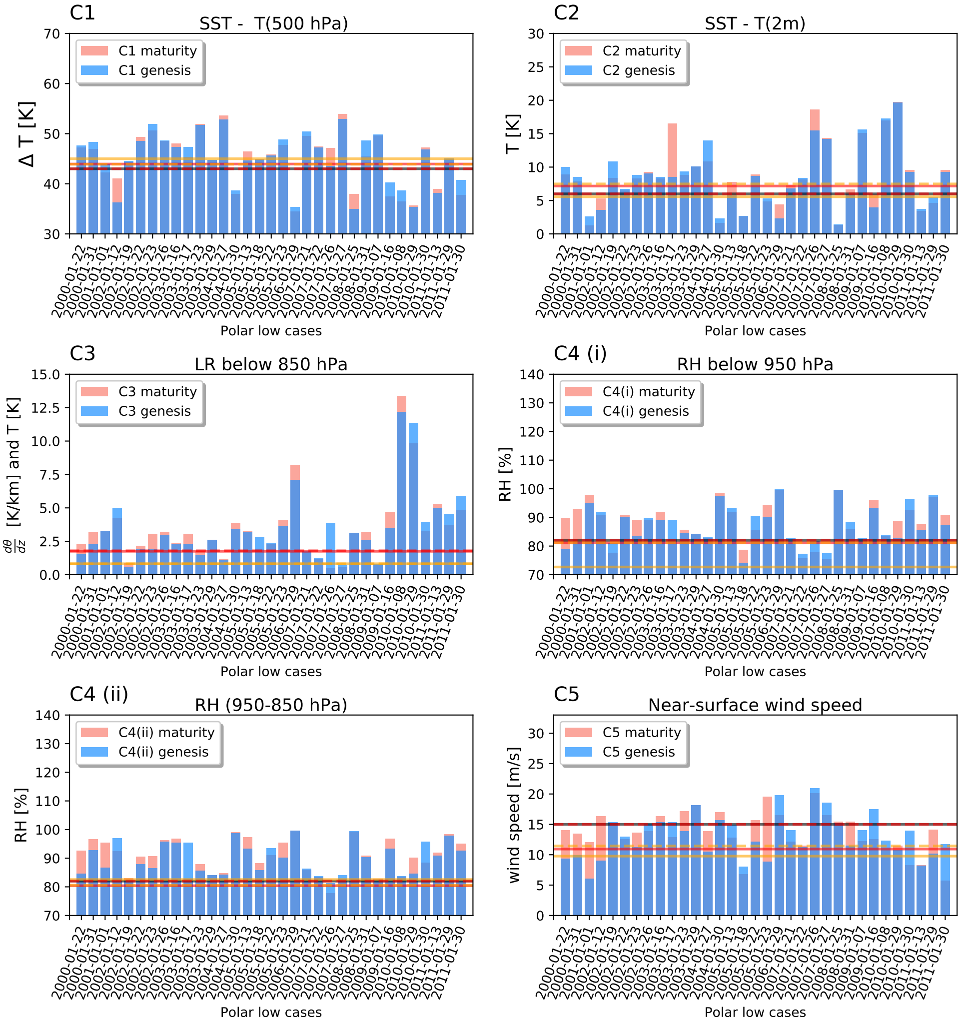

Figure 6.3: *Bars represent the values for the different conditions based on ASRv2 grid points within a 200 km radius around the genesis (blue) and maturity (orange) point for each of the January cases between 2000 and 2011. C1 (upper left), C2 (upper right), C3 (middle left), C4(i) (middle right), C4(ii) (bottom left) and C5 (bottom right). Horizontal lines represent: the literature threshold from Table 5 (black), ASRv2 mean (red) and ASRv1 mean (yellow) for genesis (maturity) stage denoted with full (dashed) line.*

values of conditions in between reanalyses versions (Figure 6.2 (top)). Moreover, the final value can also be affected by the lower precision of the PL location found in ASR when compared to the one noted in the NL list (Figure 6.2 (bottom)) as well as due to a potential movement of the developed PL.

For the maturity stage, we checked which conditions were above the threshold of interest, when the PL was listed in NL, although the C1 condition (commonly used for detection) was not fulfilled. We aim to clarify by this the importance of the other conditions at the maturity state.

6.2.4 Conditions for PL development

In the literature, different conditions were used to identify and characterize PLs. These are listed bellow while often found values are given in Table 5.

1. **Condition 1: SST - T(500hPa)**

   From the thermal instability theory, which tried to explain the formation of PL through the instability inside of a CAO flowing over warmer sea, follows the logic of looking at the difference between the sea surface temperature (SST) and temperature at 500 hPa (T(500 hPa)). This temperature difference gives information on the static stability and is the most frequently used parameter for PL development and tracking (Noer and Ovhed, 2003; Zahn and von Storch, 2008).

   A common threshold is $\geq$ 43 K, but some studies argue that, in choosing a strict threshold, some PL with lower SST-T(500hPa) values (e.g., 36 K) can be missed (Blechschmidt et al., 2009; Terpstra et al., 2016). Nonetheless, we chose the stricter criteria of 43 K since the likelihood of a strong cyclone to be identified as a PL was reduced.

2. **Condition 2: SST - T(2m)**

   From WISHE theory, a PL is intensified by air-sea instability interaction as the PL is sustained by latent and sensible heat from the ocean, which are enhanced by wind. Seatra et al. (2008) and Linders et al. (2011) showed that strong winds can mix the subsurface sea water and increase the SST up to 3 °C, which then feeds back to the PL itself and intensifies it. This means that for a higher difference between SST and temperature at 2 m height, greater thermal instability and more sensible heat at the lowest parts will be present which provide a favorable environment for PL formation. Therefore, in addition to checking for the wind threshold, SST and the difference between SST and temperature at 2 m have been analyzed in more recent studies. For some cases, this difference can be as high as 6 - 7 K (Terpstra et al., 2016).

3. **Condition 3: Potential temperature lapse rate (LR) below 850 hPa**

   While Condition 1 gives the broad picture on static stability, Condition 3 investigates the potential for convection in the boundary layer, here defined as below 850 hPa. When the potential temperature θ is constant with height, i.e. LR $= d\theta/dz$ is zero, dry adiabatic conditions indicating well-mixed conditions prevail.

Table 6: *Overview of conditions for each PL case at genesis stage with their dates and location. Values in the table are means for a 200 km radius around the genesis point.*

	case	Coord.	C1 (K)	C2 (K)	C3 (K/km)	C4(ii) (%)	C5 (m/s)	C6 (m)	shear
1.	2000-01-22	72.5°N 29°E	47.6 ↓	10 ↓	0.62 ↑	85 ↑	11.97 ↑	- 144 ↓	R
2.	2000-01-31	65°N 4°E	48.3 ↓	8.5 ↓	1.47 ↑	93 ↑	17.2 ↑	- 282 ↑	R
3.	2001-01-01	75°N 22°E	43.9 ↓	2.6 ↓	2.93 ↑	87 ↑	12.8 ↑	- 44 ↑	R
4.	2002-01-12	73°N 21°E	36.2 ↑	3.6 ↑	3.51 ↓	97 ↓	16 ↑	- 56 ↓	-
5.	2002-01-19	70°N 47°E	44.5 ↓	10.8 ↓	0.48 ↑	82 ↑	18.7 ↓	- 292 ↑	-
6.	2002-01-22	75°N 28°E	48.5 ↑	6.7 ↓	1.76 ↑	88 ↑	22.6 ↓	- 207 ↑	R
7.	2002-01-23	71°N 16°E	51.9 ↓	8.8 ↓	1.78 ↑	86 ↑	19.4 ↑	- 281 ↓	R
8.	2002-01-26	72°N 12°E	48.6 ↓	9 ↑	1.91 ↓	96 ↑	19.7 ↓	- 187 ↓	R
9.	2003-01-16	72°N 7.3°E	47.3 ↑	8.5 ↓	2.08 ↑	95 ↑	22.2 ↑	- 259 ↑	R
10.	2003-01-17	73.5°N 25.5°E	47.3 ↓	8.5 ↑	1.22 ↓	95 ↓	22.2 ↓	- 259 ↓	R
11.	2003-01-23	73°N 10°E	51.7 ↑	9.3 ↓	2.08 ↑	86 ↑	18.5 ↑	- 262 ↑	R
12.	2003-01-29	73.5°N 0.5°E	44.7 -	10.1 -	1.23 -	84 -	19.8 -	- 98 -	-
13.	2004-01-27	71°N 12°E	52.9 ↑	14 ↓	1 ↑	84 ↑	17.3 ↑	- 271 ↑	R
14.	2004-01-30	70°N 8°W	38.6 ↓	2.3 ↓	3.5 ↑	99 ↑	17.7 ↑	- 201 ↑	R
15.	2005-01-13	68°N 7°E	44.6 ↑	5.7 ↑	3.01 ↓	93 ↑	19.4 ↓	- 50 ↑	-
16.	2005-01-18	72°N 3°W	44.8 ↑	2.6 ↓	0.22 ↑	86 ↑	11.4 ↓	- 203 ↑	R
17.	2005-01-22	66°N 6.3°E	45.6 ↑	8.6 ↑	2.16 ↓	93 ↓	15.7 ↑	- 90 ↑	-
18.	2005-01-23	67°N 13°E	48.8 ↓	5.3 ↓	3.24 ↑	90 ↑	20 ↑	- 120 ↑	-
19.	2006-01-29	Hopen	35.3 ↓	2.3 ↑	6.44 ↑	100 -	22.1 ↓	165 ↑	R
20	2007-01-21	73°N 41°E	50.4 ↓	6.7 ↑	1.74 ↓	86 ↓	16.4 ↓	- 149 ↑	R
21.	2007-01-22	76°N 4°E	47.2 ↑	8.3 ↓	0.91 ↓	84 ↓	15.2 ↑	- 184 ↑	R
22.	2007-01-26	70.3°N 14.3°E	43.6 ↑	15.4 ↑	0.51 ↓	81 ↓	22.1 ↓	- 256 ↓	-
23.	2007-01-27	71°N 22°E	52.9 ↑	14.2 ↑	0.63 ↓	84 ↓	20.1 ↓	- 304 ↓	R
24.	2008-01-25	67.3°N 8°E	48.6 ↑	1.4 ↓	2.55 ↑	99 ↓	17.9 ↑	- 67 ↓	-
25.	2008-01-31	74°N 11°E	35 ↓	6 ↑	2.48 ↑	90 ↑	13.9 ↑	- 137 ↓	R
26.	2009-01-07	72°N 28°E	49.8 ↓	15.6 ↓	0.6 ↓	83 ↑	19.5 ↓	- 232 ↑	-
27.	2009-01-16	71°N 57°E	40.2 ↓	3.9 ↑	3.1 ↑	93 ↑	19.7 ↓	88 ↑	-
28.	2010-01-08	80.3°N 16.3°E	38.6 ↓	17.3 ↓	9.7 ↑	84 ↓	15.4 ↓	82 ↑	R
29.	2010-01-29	68°N 8°E	35.4 ↑	19.6 ↑	10.66 ↓	85 ↑	14.9 ↑	74 ↓	R
30.	2010-01-30	62°N 4°E	46.8 ↑	9.2 ↑	2.97 ↓	96 ↓	16.6 ↓	- 191 ↑	F
31.	2011-01-13	71°N 1°W	38.2 ↑	3.7 ↓	4.64 ↑	91 ↑	15.5 ↑	- 56 ↑	-
32.	2011-01-29	71°N 1°W	45.1 ↓	5.4 ↓	3.84 ↓	98↑	14.5 ↑	- 99 ↓	-
33.	2011-01-30	74.3°N 30°E	40.7 ↓	9.2 ↑	2.05 ↑	93 ↑	14.7 ↓	- 70 ↑	-
ASRv2		**Mean**	45	8.2	2.64	89	17.6	- 141	
		Std	5.2	4.5	2.33	5	3.0	120	
ASRv1		**Mean**	46.2	6.5	1.47	91	16.3	-182	
		std	3.6	3.6	1.21	5	4.0	85	

Thresholds are marked in colors and, for the conditions C1-C5, have the following meaning: red - condition has not been fulfilled, yellow - condition is neutral (between one STD and the mean (or the threshold)) and green - condition is fulfilled. For C6, the colors indicate the following: red - conditions is above zero, yellow - condition is between zero and -160 gpm and green - condition is fulfilled. For the thresholds, refer to Table 5. The last two rows give the mean and STD of the condition of the respective column. The arrow next to each value represents an increase (decrease) at the maturity stage.

Any negative LR reveals absolute instability, which would quickly be removed by convection. Terpstra et al. (2016) could show that, for reverse shear PL, a strong boundary layer inversion between 950 and 850 hPa occurs with LR increasing from slightly above zero in the lowest part of the boundary layer to roughly moist adiabatic conditions (LR about 3 K/km) in the free troposphere.

4. **Condition 4 (i): RH(surface-950 hPa) and (ii): RH(950-850 hPa)**

   Since a PL gains its energy and continues its growth largely from the latent heat release, and therefore rapidly decays once over land, humidity is among the most important factors for PL formation and development. This is most prominent for the type C cyclones whose cyclogenetic dynamic is dominated by the action of strong midlevel latent heating (Plant et al., 2003). High amount of moisture and therefore more latent heat act as s substitute for smaller low-level temperature gradients (Bracegirdle and Gray, 2008). The more moisture a PL acquires during its growth, the more energy is available to continue intensification. Therefore, RH is another important parameter. Terpstra et al. (2016) found values of $\sim 75\%$ for C4(i) and $\sim 82\%$ for C4(ii).

5. **Condition 5: Near surface wind speed (NSWS)**

   Probably one of the most notable features of a PL is the strong near-surface wind (can be above 25 m/s) with a threshold often used in literature of at least 15 m/s (Rasmussen and Turner, 2003). Strong NSWS enhances turbulent fluxes from the sea surface into the atmosphere. Updrafts in the boundary layer transport moisture into colder environment in which moisture starts to condense releasing energy in the form of latent heat, important for PL development. Aside from this, NSWS is usually used to determine the intensity of a storm. It is well documented that PLs are warm core mesocyclones and therefore have reverse wind shears (Kolstad, 2006; Rasmussen and Turner, 2003). However, according the CISK theory, during its genesis stage when growth of an initial disturbance starts from interaction of small-scale organized convective cells with large scale circulation, a PL can have a forward shear and a cold core (resemblance to extratropical cyclones). This kind of pre-polar low environment was studied in Terpstra et al. (2016), and a method for calculation of a shear is presented below.

   To calculate wind shear requires taking the angle between the mean and thermal wind flows (Duncan, 1978; Forbes and Lottes, 1985; Kolstad, 2006; Terpstra et al., 2016). The wind is said to have a reverse shear if the baroclinic waves propagate in the opposite direction to the thermal wind and a forward shear if propagation of baroclinic waves is in the direction of the thermal wind. The angle is calculated between 925 and 700 hPa using:

$$\alpha = -\frac{1}{f}\left(\frac{\mathsf{v}_T \cdot \bar{\mathsf{v}}}{\|\mathsf{v}_T\|\|\bar{\mathsf{v}}\|}\right), \tag{6.1}$$

   where

$$\mathsf{v}_T = \left(-\frac{1}{f}\frac{\partial(\phi_{700}-\phi_{925})}{a\partial\varphi}, \frac{1}{f}\frac{\partial(\phi_{700}-\phi_{925})}{a\cos\varphi\partial\lambda}\right) \tag{6.2}$$

and

$$\overline{\mathrm{v}} = \left(-\frac{1}{2f}\left(\frac{\partial\phi_{700}}{a\partial\varphi}+\frac{\partial\phi_{925}}{a\partial\varphi}\right), \frac{1}{2f}\left(\frac{\partial\phi_{700}}{a\cos\varphi\partial\lambda}+\frac{\partial\phi_{920}}{a\cos\varphi\partial\lambda}\right)\right), \tag{6.3}$$

are thermal and mean vertically averaged wind components and ϕ_{700} and ϕ_{925} represents the geopotential at the 700 hPa and 925 hPa levels, respectively. f denotes the Coriolis parameter, a the Earth's radius, φ the latitude and λ the longitude.

The angle is calculated for each grid cell in the radius of 200 km and then averaged to find the mean shear during the PL genesis stage. Using the α angle from above, it is possible to clearly distinguish between two types of the shear where the flow is said to be reverse if the angle is between $135° \leq \alpha \leq 180°$ and foreward if the angle is between $0° \leq \alpha \leq 45°$. For details, see Kolstad (2006).

6. **Condition 6: Geopotential height (GPH) anomaly at 500 hPa**

   A PL is usually well embedded into a CAO with a cold air mass flowing from the sea ice toward the warmer open ocean. A trough in the GPH field at the 500 hPa level indicates a cold air mass flow. Thus, during a PL, a 500 hPa GPH value is found to be lower than the climatological mean Blechschmidt et al. (2009). In the study by Forbes and Lottes (1985), where mesoscale vortices were investigated from December 1981 - January 1982, the mean GPH anomaly was negative and close to 160 m. That is the value taken here.

Hereinafter, instead of using the long names of the conditions outside of this section, we refer to C1, C2, and so on up to C6. Because MSLP is another parameter often used for PL and cyclone tracking and detection (Zahn and von Storch, 2008; Stoll et al., 2018), we inspected, in addition to the six conditions mentioned above, the mean sea level pressure difference between the genesis and maturity stage.

6.3 Polar low environment

The results of the 33 January PL cases are presented in the following three subsections with the investigated criteria as listed in Table 5. We discuss those based on ASRv2 and include the comparison with ASRv1. First, we present the behavior of conditions at the genesis stage and compare them with the mature stage. Second, we analyze the large-scale environments at the genesis stage and compare them with 12 years of January climatology.

6.3.1 Genesis stage

Figure 6.3 (upper left) shows the SST - T(500 hPa), C1, at the genesis(maturity) stage for all 33 cases. Each bar contains 75 percentile value derived from all the pixels values of 200 km radius around the genesis(maturity) space-time point. Due to the inherent uncertainty in the ASR's positioning of the PLs (Figure 6.2), the 75 percentile value provides more robust results. The results presented below are based

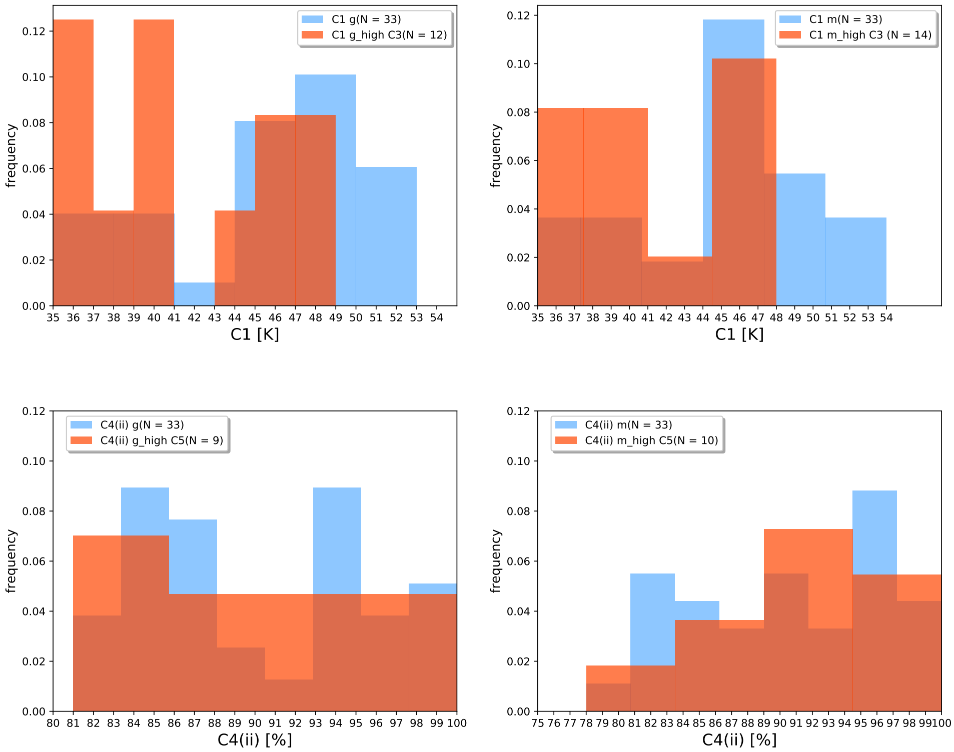

Figure 6.4: *Frequency of occurrence of condition C1 for all 33 cases (blue) and for cases with C3 above mean 75 percentile value of ASRv2 (orange) at genesis (g) (upper left) and maturity (m) (upper right) stages. Similar is shown for conditions C4(ii) with high C5 (above threshold) (bottom).*

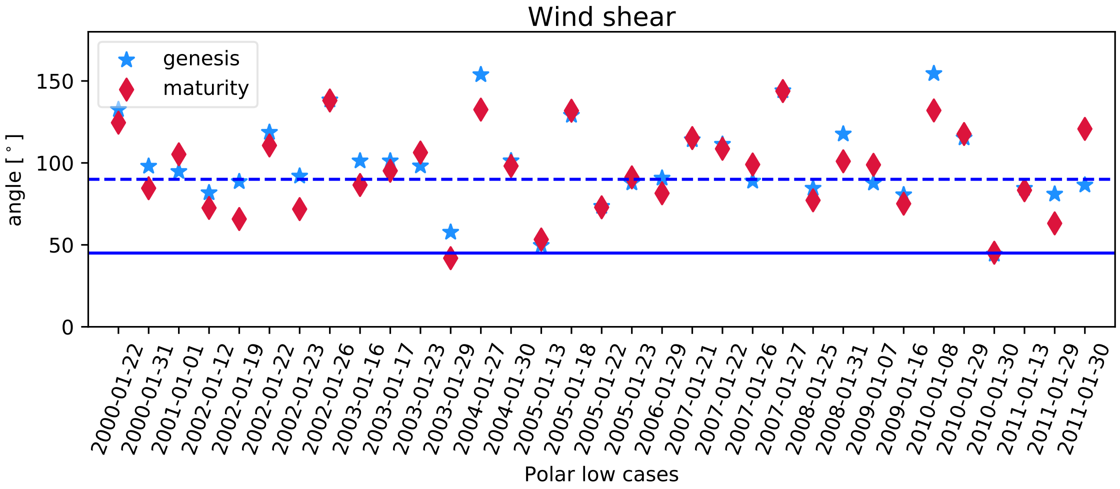

Figure 6.5: *Wind shear at genesis (blue stars) and maturity (red diamonds) stages. Blue lines separate forward (below blue thick line; 45°) and reverse (above blue dashed line; 90°) shear.*

on the ASRv2 while ASRv1 is used to compare PLs' representatives between the two ASR versions. More detailed figures with whisker plots for each stage separately are shown in the supplement. The results show that the mean value of C1 for nine cases did not reach the 43 K temperature difference threshold. However, the mean 75 percentile value for all cases was 45 K ± 5 K, which is 2 K above the threshold. Five cases, namely 23rd Jan 2002, 23rd Jan 2003, 27th Jan 2004, 21st Jan 2007 and 27th Jan 2007 had especially high C1, being above 50 K. By comparison, those cases show weaker lapse rates (cf. C3; Figure 6.3). The region over which these kinds of PLs mostly occur was found to be east of 8 ° E and north of 70° N (Table 6).

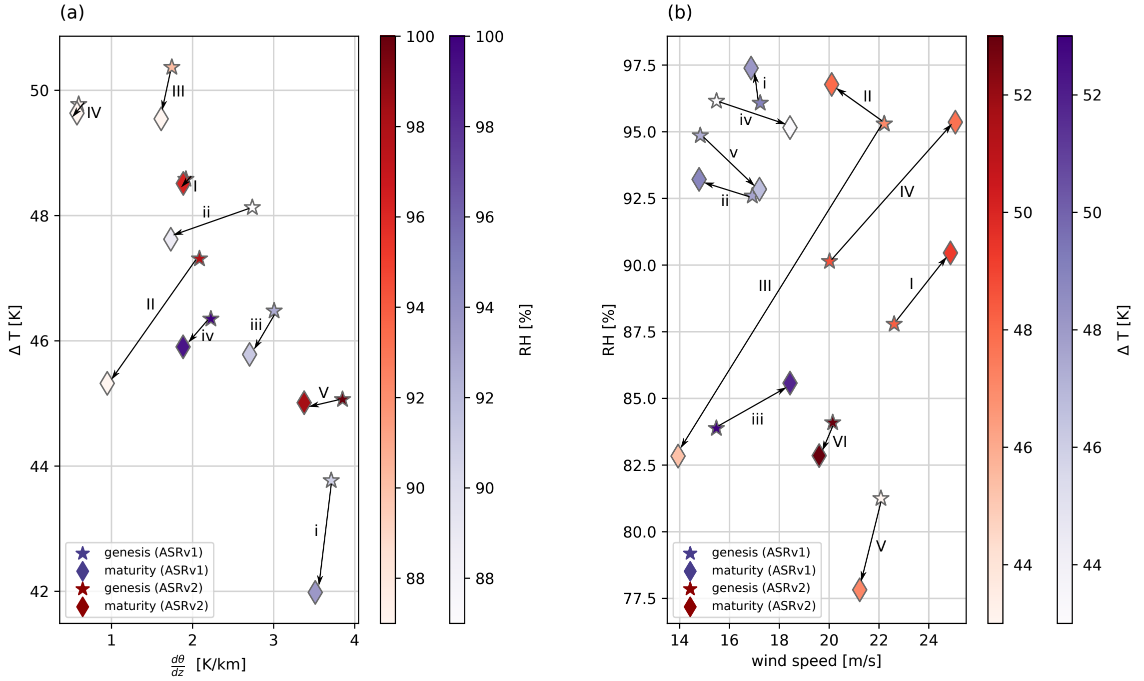

Figure 6.6: *(a) Mean 75 percentile values of C3: $\frac{d\theta}{dz}$ (x-axis), C1: ΔT (y-axis) and C4(ii): RH(850-950 hPa) (color shading) for 4 cases of the ASRv1 (1st Jan 2001, 23rd Jan 2005, 25th Jan 2008 and 29th Jan 2010) (purple) at genesis (stars) and maturity (diamonds) stages and 5 cases of the ASRv2 (26th Jan 2002, 17th Jan 2003, 21st Jan 2007, 7th Jan 2009 and 29th Jan 2011) (red). Lower (upper) case roman numbers above arrows indicate the same case at different stages from ASRv1 (ASRv2). (b) C5: near-surface wind speed (x-axis), C4(ii): RH(850-950 hPa) (y-axis) and C1: ΔT (color shading) for cases with strong C5 in ASRv1 (26th Jan 2002, 22nd Jan 2005, 31st Jan 2008, 7th Jan 2009 and 30th Jan 2010) (purple) and ASRv2 (22nd Jan 2002, 16th Jan 2003, 17th Jan 2003, 23rd Jan 2005, 26th Jan 2007 and 27th Jan 2007) (red).*

Generally, it seems that, whenever a strong C1 (above ASRv2 mean) was present (55 % of the cases), C3 was almost always below the mean, indicating that temperature instability (C1) acted as the main forcing mechanism for PL growth (Figure 6.4). Similarly, when a weak C1 was present (27 % of the cases), C3 often times was above the mean, showing that convection acted as the main triggering mechanism for PL growth (Figure 6.4). The cases with strong C3, above 3 K/km, were forming mostly over the Barents Sea, with one case forming far east in the south western part of the Kara Sea in close proximity to Novaya Zemlya (Table 6). The comparison between ASRv1 and ASRv2 shows smaller values of C1 in ASRv2 due to higher values of SST but the high standard deviation let the statistical significance unclear. Besides higher resolution, this difference could also be attributed to updated WRF's physics, which includes sub-grid scale cloud fraction interaction with the radiation and more accurate data assimilation (Bromwich et al., 2017).

The lowest part of the boundary layer shows that the mean values of the 75 percentile of the SST-T(2m) difference, C2, was 8.2 K with a standard deviation (STD) of 4.5 K. The majority of the cases reached the threshold of 6 K (ASRv1) or 8 K (ASRv2) (Table 5), with a few cases showing values above 15 K (Figure 6.3). The cases with the highest values were mostly forming closer to the sea ice border, where the difference between the near-surface temperature and SST is larger. The cases with higher C2 appear to prefer the region between ∼ 70 and 81 ° N (Table 6). Since the near surface cold air had time to warm up while flowing towards the south, C2 for other cases is lower.

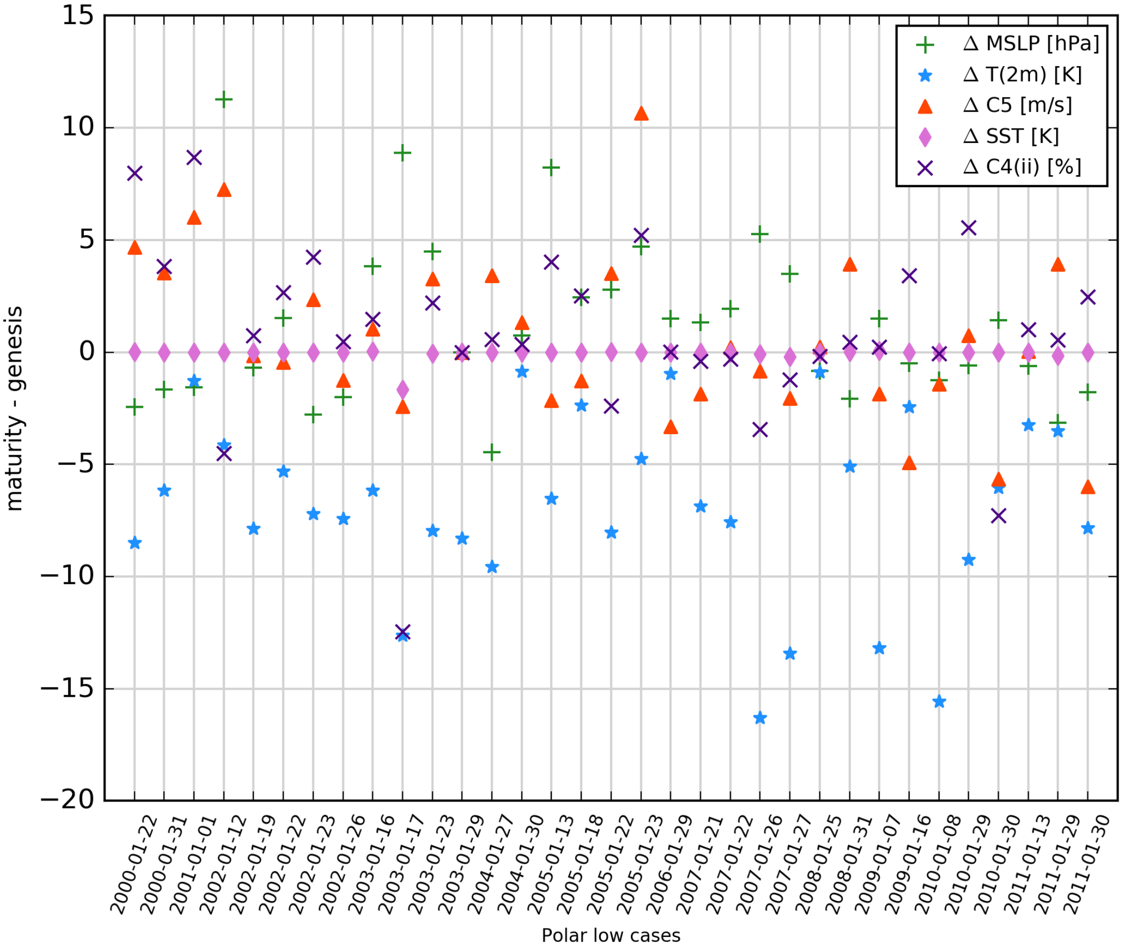

Figure 6.7: *Difference of environmental conditions between the genesis and the maturity stage. Shown are: MSLP difference (green pluses), temperature at 2 m (blue stars), near-surface wind speed (C5), SST, and RH in the layer between 850 hPa and 950 hPa, C4(ii) (indigo crosses).*

For humidity at lower levels, RH ranged from ∼ 81 % below 950 hPa, C4 (i), to slightly above 80 % between 850 hPa and 950 hPa, C4 (ii) (Figure 6.3). In comparison to ASRv1, ASRv2 (Supplementary Figure S2) had an increase in RH for C4(i). However, at a higher level, there were only minor differences between the ASR versions in C4(ii). A near-surface wind speed, C5 (Figure 6.3), was below the 15 m/s threshold while the mean 75 percentile value was ∼ 18 m/s with a STD of 3 m/s. For only 7 out of the 33 cases, maximum wind speed did not reach the 15 m/s threshold (Table 6). In comparison to ASRv1, there was a notable increase in the value of the considered condition (Supplementary Figure S3). With regard to the wind shear, January PLs seem to prefer reverse shear for their development, with only one case forming in the forward shear (Figure 6.5).

6.3.2 Comparison of genesis and maturity stages

In this section we compare conditions (explained in Section 2.4) at two different stages to find out which one (or the combination of) was contributing to the PL's persistence.

The maturity stage of the C1 condition in Figure 6.3 is derived using the same radius as in the genesis stage but at the time of maturity. With a 75 percentile of 44.8 K, C1 was slightly lower than at the genesis stage. Moreover, its STD of 5.1 K was higher, and the same nine cases that did not reach the threshold of 43 K at the genesis stage did not reach it at the maturity stage either. For C1 at maturity stage, a greater difference between the two versions of reanalysis was detected. In ASRv1, the 75 percentile of C1 was 46.6 K ± 2.8 K (which was slightly higher than at the genesis stage and with only 2 cases below the 43 K threshold).

Referring to the theory where C1 and C3 (Figure 6.3) conditions relate to baroclinic instability and CISK, we checked for the change in these conditions to find out which of these conditions contributed to PL persistence from genesis to maturity. Looking at these two conditions, namely C1 and C3, we note similar behavior at the genesis and maturity stages: Low C1 values (below threshold) are compensated with strong C3 (above threshold) (Figure 6.4).

However, Figure 6.3 shows that almost two thirds of the cases had weaker vertical stability, C3, during the genesis stage than in the maturity stage. 12 of those cases showed an increase in wind speed at maturity stage, which may indicate that this C5 condition is important for PL persistence. Five cases continued to persist and showed an increase in either C1 or C2, i.e. decreasing thermal stability at maturity stage. The remaining two cases had no increase in any of the conditions that promote PL strengthening or development, namely conditions between C1 to C5 or decrease in C6. For the PLs with stronger C3 during the genesis stage, eight of the cases showed an increase in C1 while the remaining five even showed a decrease in terms of both, C1 and C3. For those five, it was noted that RH was almost always above 90 % (Figure 6.6 (a)) which may suggest that their persistence was triggered by energy gained through moisture.

Moreover, for the majority of intense PLs, in terms of near surface wind speed, C5, the C4 (ii) was often above 90 % (Figure 6.3), meaning that latent heat release was important as a driving mechanism for those PLs. Cases that resolve this relation are represented in Figure 6.6 (b). Compared to ASRv1, ASRv2 shows higher values of C5, being above 20 m/s for those cases.

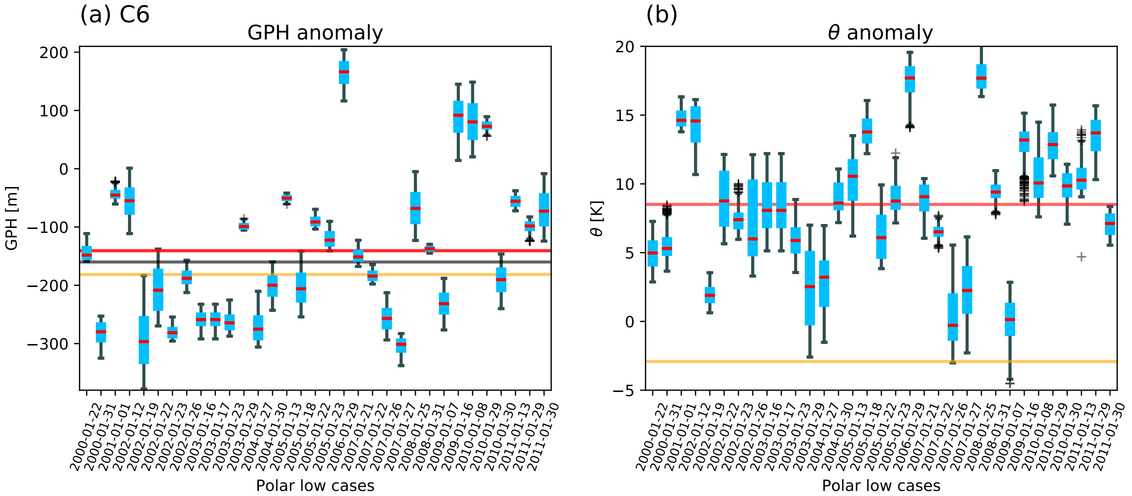

Figure 6.8: *Box plots for ASRv2 grid points within a 200 km radius around the genesis point for each of the January cases between 2000 and 2011. Anomaly of the GPH at 500 hPa level (a) and potential temperature at the 850 hPa level (b). Lines correspond to those in Figure 6.3. Blue boxes indicate interquartile range (IQR) and black whiskers the 1.5IQR. Individual outliers are presented as the black crosses.*

For the C2 condition, the mean value of the 75 percentile was the same as at the genesis stage, 6.4 K, with a STD of 3.4 K. C2 shows no significant positive correlation with any other condition. Nonetheless, a negative correlation of 0.6 was found with C4(ii) at both stages (not shown). Linders et al. (2011) have shown that higher SST produces slightly more intense cyclones in terms of azimuthal wind speed and deeper sea level pressure depression. However, our inspection of differences in the 75 percentile values between the genesis and maturity stages did not reveal a direct connection between SST and wind speed. Two cases with especially high values of C4 (ii) during the genesis stage showed a direct effect on an increased PLs intensity, in terms of the maximum wind speed at maturity stage (12th Jan 2002 and 22nd Jan 2005). Those cases seemed to use energy stored in moisture.

Moreover, increase in wind speed at the maturity stage was also found for the cases that also showed an increase in C4 (ii) (Figure 6.4). Those cases intensified in wind speed by gaining energy from other sources.

Nonetheless, it seems that the change in temperature at 2 m is a better indicator of the change in wind speed intensity in general than it is the SST change (Figure 6.7). The reason for this could be the faster variability of the temperature at 2 m, which is atmospheric component, compared to the SST which at maturity stage, did not increased more than 0.2 K. This explanation is reasonable since water warms much slower than air. Furthermore, it was also noted that temperature at 2 m always decreased at the maturity stage. Data from the STARS data base also showed that, generally, the cases with higher C4 (ii) were more persistent and lasted more than 13 h. Moreover, it seems that the near-surface humidity, C4 (i), behaves similarly to that of C4 (ii) (not shown).

To investigate pressure, we calculated the MSLP difference between the genesis and maturity stages. The results for that calculation show that the MSLP acts opposite to C4 (ii) during genesis and maturity stage. For majority of the cases that had lower pressure during the maturity stage, C4 (ii) was found to be higher during the genesis stage (Figure 6.7). Generally, the opposite also holds true: if C4 (ii) was lower during the genesis stage, the MSLP was higher at the maturity stage. Although the correlation between these two conditions was negative, its strength of only 0.2 was too small to be significant.

To check for the difference between the climatology and the PL events, we calculated the 500 hPa GPH anomalies, C6. Those ranged from -400 gpm to 200 gpm, with a mean value of $\sim$ 154 gpm below the climatological mean (Figure 6.8, (a)). This value is close to mean value found in Forbes and Lottes (1985), where GPH anomaly was 160 gpm. Nonetheless, one should compare values found in this study to those from Forbes and Lottes (1985) with caution since the period of investigation in that study was only one month. Moreover, a comparison between ASRv1 and ASRv2 reveals a notable difference for this condition. While ASRv1 shows a mean value of -182 gpm, which is below that cited in the literature, ASRv2's mean value of -140 gpm is slightly higher and therefore above that of the threshold cited in the literature. Furthermore, the most striking difference between the two ASR versions is evident in the potential temperature, θ, anomaly at 850 hPa, where the mean value in ASRv1 is -3 K and in ASRv2 is $\sim$ 8 K.

6.3.3 Genesis environmental conditions compared to climatology

To obtain a better understanding of the PL environment, we looked at the spatial patterns of MSLP, GPH at 500 hPa and θ at 850 hPa and therefore show their composites at the genesis stage as a mean of all the PL cases and compare them to the January climatology.

The comparison between the PL composites and the January climatology of the MSLP shows that, generally, a central pressure depression is present at the border between the Norwegian and Greenland seas, while, during the PL events, it shifts towards the Norwegian coast (Figure 6.9, (a) and (c)). A deeper investigation of the anomaly shows that, during the PL events, the MSLP establishes a sharp boundary close to the 0 ° meridian and follows the Norwegian coast, touching the tip of the eastern part of Svalbard (Figure 6.9, (e)).

The previously discussed lower anomalous GPH for 54% of the cases found in our study compared to Forbes and Lottes (1985) seems to be explained by troughs of GPH that extend further south and are deeper for those cases. Figure 6.9 (d) shows that the trough in GPH at 500 hPa during the PL dates extends to the southern part of Norway.

The potential temperature anomaly can be as low as - 6 K (Figure 6.9) (f). This difference is slightly more pronounced between the northwestern side of the Norway and Svalbard. The analysis of C1 and C6 together brought to light that the cases with smaller C1 values have higher values of the GPH anomaly, indicating that the troughs were shallower and therefore temperature instability was also smaller. The summary of the results discussed above can be found in Table 6.

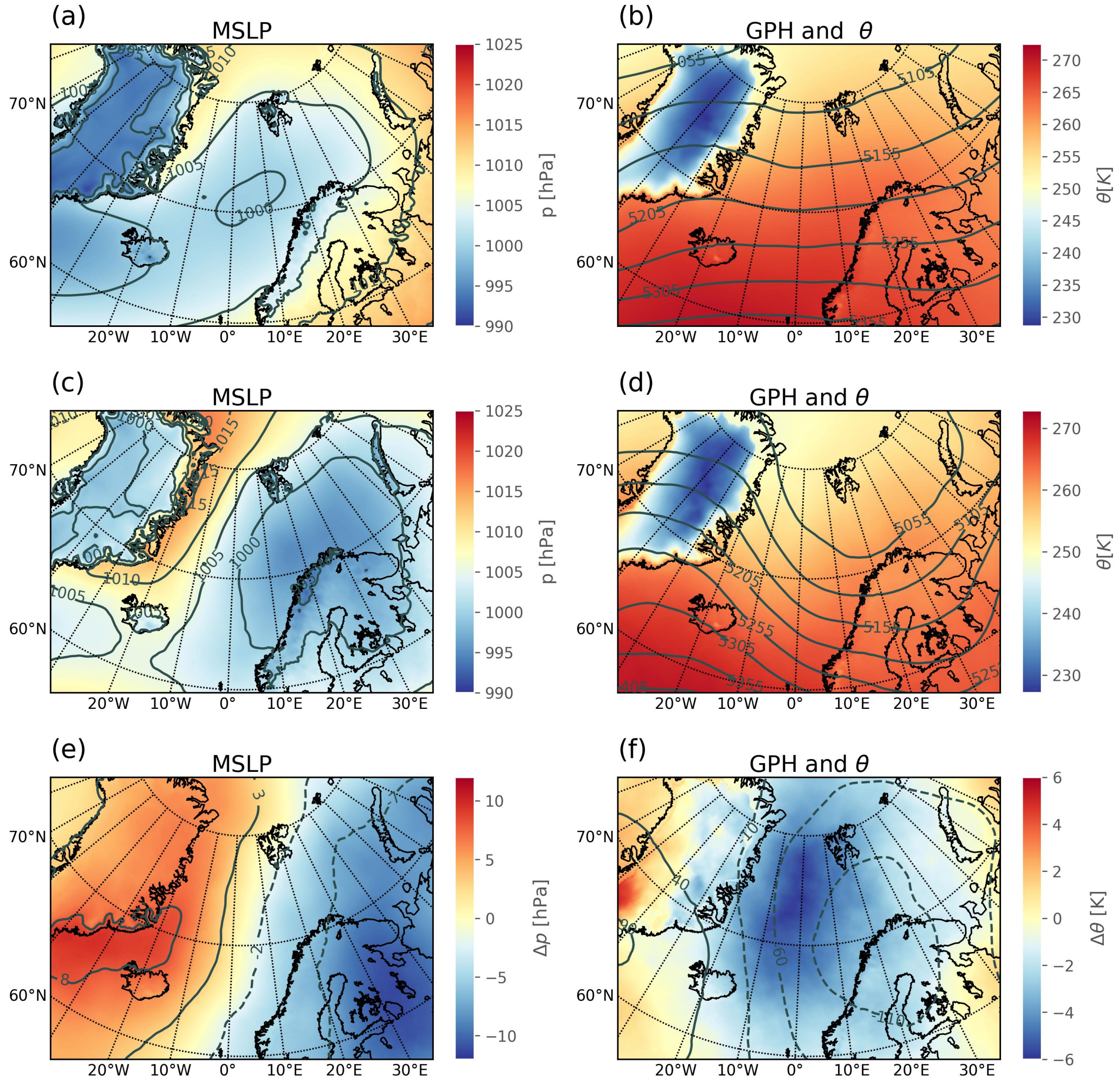

__Figure 6.9:__ Climatology of: (a) all 372 January days for MSLP (color shading and gray labeled counters, every 5 hPa) and (b) GPH at 500 hPa (gray labeled contours, every 50 gpm) and potential temperature at 850 hPa (color shading); (middle) As in the first row but for polar low dates; (bottom) anomalies for both, MSLP (gray labeled contours, every 5 hPa) (e) and GPH at 500 hPa level (gray labeled contours, every 50 gpm) and potential temperature (color shading) (f).

6.4 Summary and Conclusions

In this study, we have used the ASR reanalyses to systematically investigate a set of often used criteria for PL detection and thus to identify the most important one(s) or the most important combination (Table 5). Since January is generally the month with the highest frequency of PLs, we chose that month for investigation. In total 33 cases were reported (Noer and Lien, 2010). PLs were studied within a radius of 200 km around the genesis point since Condron et al. (2006) found that only 2% of the the polar mesocyclones identified on satellite imagery have a diameter lower than that value.

First, we analyzed the C1 condition and the mean ASRv2 value of 45 K was found to be 2 K higher than the commonly reported threshold discussed e.g. in Terpstra et al. (2016). They noted that, for PLs forming in forward shear, a C1 threshold of 43 K was not reached. However, in our study, using only January PLs, we found only one case that developed in forward shear. This case had a C1 of 45 K. Moreover, lower C1 values, at least for January cases, do not have to be characteristic of PL forming in forward shear since nine of the cases that did not reach the C1 threshold were forming mostly in reverse shear. Therefore, it would be of interest to compare this finding with the other months of the PL season in a future analysis. Another reason for a higher C1 value could arise from our application of the ASR reanalysis, which has better resolution and uses a polar-optimized version of WRF, compared to ERA-I, which was used in the earlier study.

Nonetheless, in a few (seven) cases, PLs formed with C1 below 40 K. Since these cases with unfulfilled C1 condition have also been reported as PLs, we checked the combination of C1 with other conditions. We found that the majority of those cases fulfilled the C3 condition (even commonly showed stronger lapse rates) indicating that convection was probably the key driving mechanism for their growth.

The analysis of the area of origin showed that the cases with especially high values of C1 formed mostly east of 8 ° E and north of 70 ° N while the cases with stronger C3 originated mostly over the Barents Sea.

Analyzing C2, we noted that the PLs with extremely high values were forming closer to the sea-ice edge, where the temperature difference between the warmer open ocean and the near-surface air advected from the ice was much higher. The PL cases with higher C2 values prefer a more eastern region for their development, between 10 and 28° E and 70 and 81° N. It was also found that PL cases that possessed higher values of C4 (ii), and therefore had more latent heat energy available for their growth, had a more direct connection to the wind speed intensity at the mature stage than the SST, which at the maturity stage had rarely increased more than 0.2 K. This result differs from the one found in Linders et al. (2011), where a non-hydrostatic numerical model showed that an increase in SST promotes slightly stronger winds and deeper sea level pressure of a PL.

The analysis of the MSLP in combination with C4 (ii) at the two different stages of PL development showed that these two variables have opposite behaviour. This difference means that, at the genesis stage, when the MSLP is higher, C4 (ii) is lower, and vice versa.

While analyzing the GPH anomalies, we found a larger difference between the two ASR versions, where ASRv1 (ASRv2) showed values that were lower (higher) than those in a previous study (Forbes and Lottes, 1985). However, both versions showed that the minimum value can be lower than -400 gpm.

Furthermore, for PLs with a lower C1, we found that C6 values were greater than the threshold reported in the literature. This means that, for these cases, cold air masses were shallower and therefore the temperature instability was weaker.

The investigation into the climatology of MSLP, potential temperature fields (850 hPa) and GPH (500 hPa) revealed that the MSLP field shows a central low over the region between the Norwegian and Greenland seas while, during the PL dates, this central low was shifted over the northeastern part of the coastal Norway. Here, no

significant difference between the two versions of ASR was found.
Overall, the results of this study indicate that there is not one condition that is the most relevant for PL formation or growth. It seems that more information on PL behaviour at the maturity stage can be gained by a combination of conditions. For a few cases, higher amounts of RH at the genesis stage appear to be able to produce more intense PLs at the maturity stage. Therefore, it would be of relevance to investigate this relationship more deeply in the future. For our concerted analysis of environmental PL conditions, we limited our study to PLs in January, the month with highest PL occurrence and the coldest month of the PL season (October - May). We are aware that this leaves us with a limited number of cases, namely 33 PL cases in total, which limits the significance of our statements. However, we confirm that the differences between the two ASR versions are robust for all conditions (C1 - C5). Therefore, a possible next step would be to analyze the whole PL season. Another interesting future study could be the analysis of PL formation and development under various climate change conditions.

Supplementary data

Supplemental data for this article can be accessed here

Acknowledgment

This research has been supported by the Deutsche Forschungsgemeinschaft (DFG, German Research Foundation) - Project number 268020496 - TRR 172, within the Transregional Collaborative Research Center "ArctiC Amplification: Climate Relevant Atmospheric and SurfaCe Processes, and Feedback Mechanisms $(AC)^3$". We are thankful to Polar Meteorology Group at Byrd Polar and Climate Research Center, the Ohio State University, for production of ASR that can be downloaded from https://rda.ucar.edu/datasets/ds631.0/.

Funding

This research has been supported by the Deutsche Forschungsgemeinschaft (DFG, German Research Foundation) – Project number 268020496 – TRR 172, within the Transregional Collaborative Research Center 'ArctiC Amplification: Climate Relevant Atmospheric and SurfaCe Processes, and Feedback Mechanisms $(AC)^3$'.

Supplementary material

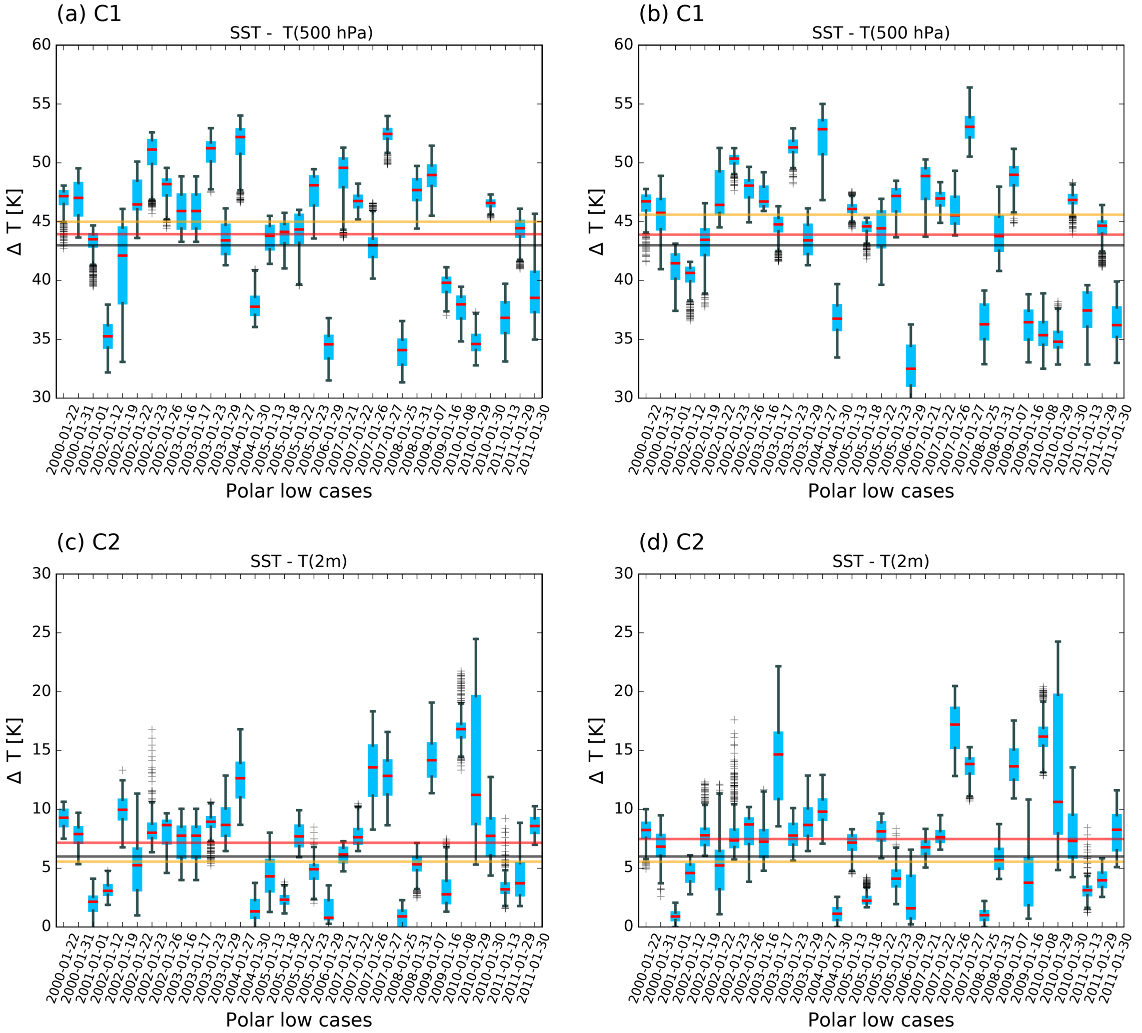

Figure 6.10: *Box plots for ASRv2 grid points within a 200 km radius around the genesis point for each of the January cases between 2000 and 2011. C1 and C2 during the genesis (left) and maturity (right) stage. Horizontal lines represent: the literature threshold from Table 1 (black), ASRv2 mean (red) and ASRv1 mean (yellow). Blue boxes indicate interquartile range (IQR) and black whiskers the 1.5IQR. Individual outliers are presented as the black crosses.*

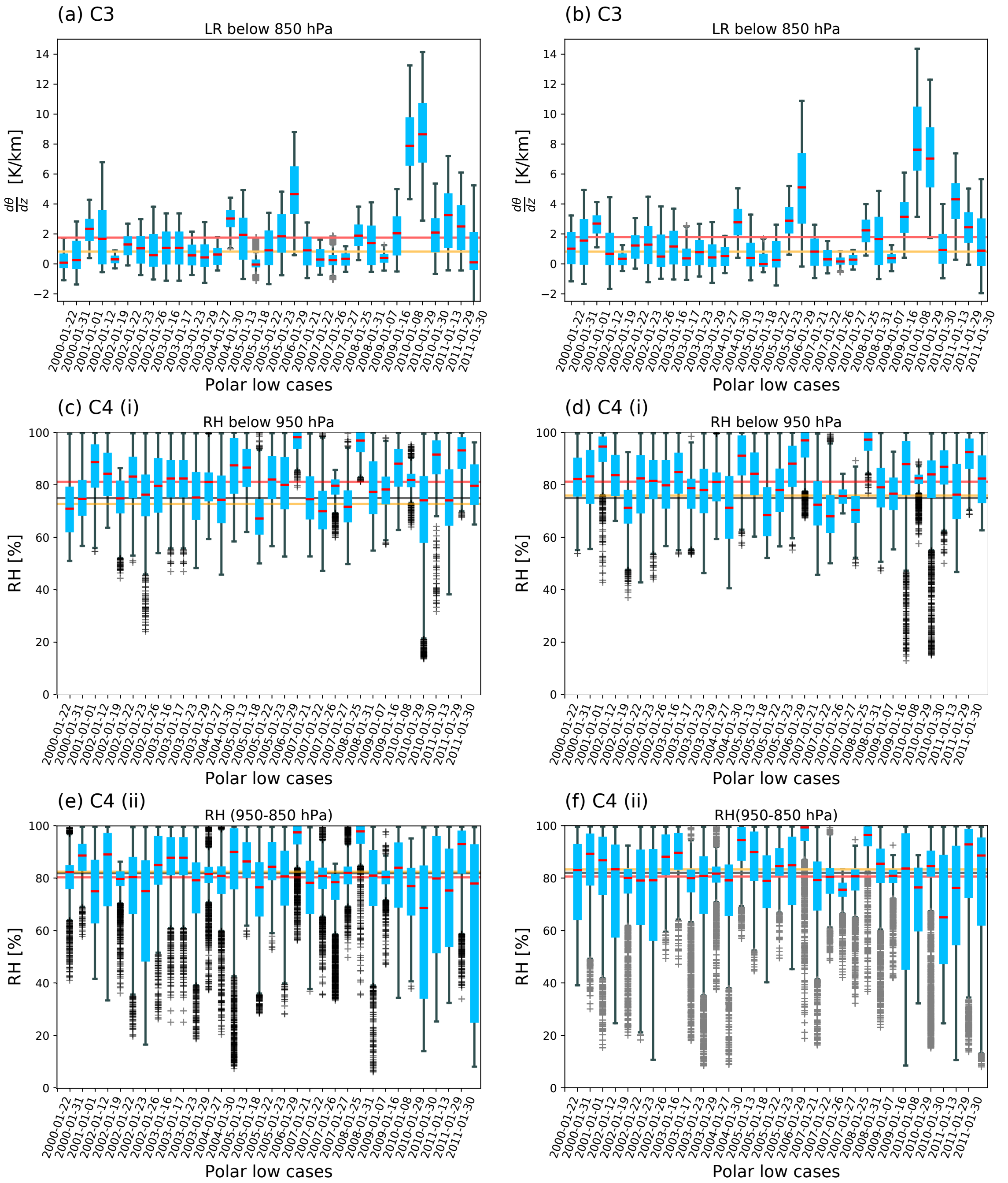

Figure 6.11: *Similar to Figure 6.10 but for C3 (upper), C4(i) (middle) and C4(ii) (bottom). On the left (right) side are shown conditions during the genesis (maturity) stage.*

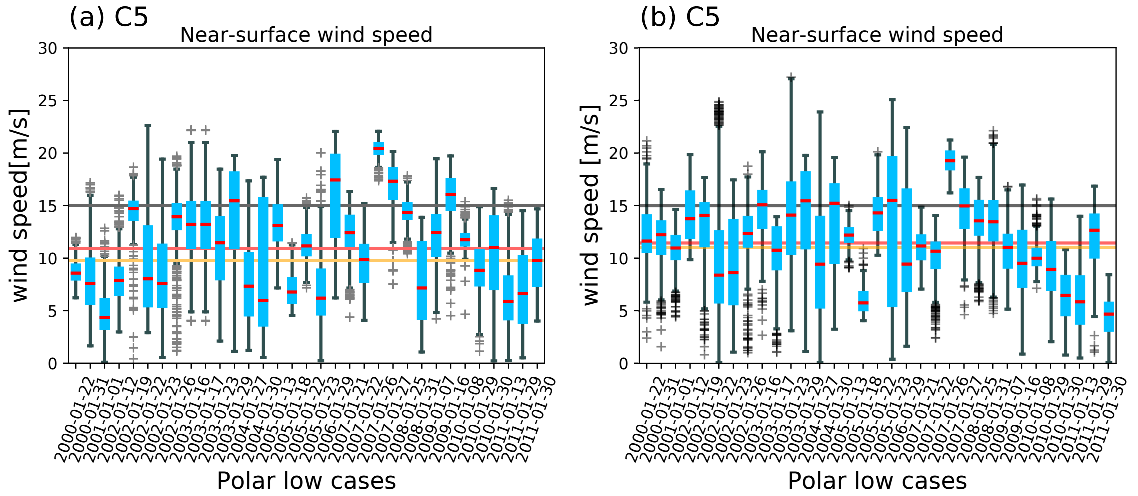

Figure 6.12: *(top) Near-surface wind speed during genesis (a) and maturity (b) stages.*

7 Atmospheric rivers in connection to Polar lows

Increased warming in the Arctic during winter is one of the most pronounced features of the Arctic amplification. Besides local evaporation, latent heat release by condensation of water vapour brought by short-lived cyclones is an important factor in sea-ice melt in the following months (Graham et al., 2019) and subsequently further increase of water vapour. Aforesaid way of enhancing water vapour creates a positive water vapour feedback loop. It was found that the frequency of intense cyclones since 1979 has increased by 6 events per winter (Rinke et al., 2017) and in warming climate these intense cyclones are project to increase further (Trenberth et al., 2003; Kusunoki et al., 2015)

The intense cyclones can be fueled with large amounts of water vapour from filaments known as atmospheric rivers (ARs) (Zhu and Newell, 1994) that reside in the extratropical cyclones warm conveyor belt (Bao et al., 2006). The ARs termed "tropospheric rivers" by Newell et al. (1992) are defined as *"long (about 2000 km), narrow (about 300–500 km wide) bands of enhanced water vapor flux"* where IWV can exceed 2 cm for 40°N to 50°N (Ralph et al., 2004). Newell et al. (1992) termed it rivers since they transport volumetric water equitable to those of the world's largest rivers (Gimeno et al., 2014). Today the American Meteorological Society defines them as a long, narrow, and transient corridor of strong horizontal water vapor transport that is typically associated with a low-level jet stream ahead of the cold front of an extratropical cyclone. Moreover, in the Fourth National Climate Assessment, ARs are included as a type of extreme storm (Ralph et al., 2019). Moreover, although ARs take up only 10% of zonal circumference (total longitudinal length) at midlatitudes they are responsible for 90% of the total mid-latitude vertically integrated water vapour transport (IVT) (Zhu and Newell, 1998; Guan and Waliser, 2017).

ARs can bring large amounts of precipitation (Dettinger, 2011; Gorodetskaya et al., 2014) causing damaging floods in certain regions such as California, Great Britain and Japan (Lavers et al., 2011, 2012; Lavers and Villarini, 2013; Ralph et al., 2004; Hirota et al., 2016) but they are also beneficial to some very dry regions by adding the water to the water reservoirs. Therefore better definition of ARs based on their damaging or beneficial characteristics was needed. Recently, Ralph et al. (2019) proposed a scale for ARs based on their intensity defined by the total vertically integrated horizontal water vapour transport (IVT) ranging from weak ($\geq$ 250–500 kg m^{-1} s^{-1}) and beneficial to exceptional and hazardous ($\geq$ 1,250 kg m^{-1} s^{-1}).

For the Arctic region however, even a weak AR can be hazardous due to the increased moisture and subsequently increased longwave radiation. Nonetheless, only recently, the influence of ARs in the Antarctic and Arctic region has gained interest (Gorodetskaya et al., 2014; Woods et al., 2013; Nash et al., 2018).

Role of atmospheric rivers in the Arctic

ARs are responsible for 28% of the total poleward transport of moisture across 70°N in winter as reported by Woods et al. (2013). Moreover, their frequency during winter season is higher in comparison to other seasons (Guan and Waliser, 2015). Due to their importance in the hydrological cycle, their correlation with precipitation has been investigated for different time scales by Nash et al. (2018). Although, they found high correlation for larger time scales (monthly) where ARs can explain about 73% of precipitation variance, it was also found that AR IVT for daily time scales can account for only 35% of the variance across 70°N making local small scale systems more important. While there is no strong linear correlation between between ARs and precipitation ARs might be connected or even trigger extreme events such as polar lows. Therefore, in this thesis, a coupled case of AR and PL and the AR influence on the PL intensity in terms of precipitation will be investigated and compared to the case that featured a PL only.

Polar lows precipitation in connection to atmospheric rivers

During all Januaries between 2000 and 2016, 33 polar low events were reported by Noer and Lien (2010) and were investigated in Radovan et al. (2019). Six of these 33 cases were accompanied by ARs, making their concurrent appearance for $\sim$ 18% of time of all January PLs events. The AR occurrence dates were provided through personal communication by I. Gorodetskaya and C. Viceto. ARs in this thesis were presented by calculating IVT using the definition from Lavers et al. (2012) and Ramos et al. (2016):

$$IVT = \sqrt{IVT_u{}^2 + IVT_v{}^2}. \tag{7.1}$$

Herein, IVT$_u$ and IVT$_v$ are vertical integrals of zonal and meridional water vapour transport components defined by:

$$IVT_u = \frac{1}{g}\int_{p_s}^{p_t} qu\,dp \tag{7.2}$$

and

$$IVT_v = \frac{1}{g}\int_{p_s}^{p_t} qv\,dp. \tag{7.3}$$

where g is the gravitational force, q the specific humidity, u and v are the zonal and meridional pressure layer averaged wind components and dp is the pressure difference between two adjacent vertical pressure layers. Because precipitation brought by PLs is mostly in the form of snow in this chapter besides IWV content, integrated snow amount has been analyzed as well.

The analysis has been performed by using PL tracks downloaded from the STARS data base (Ø.Sætra et al., 2010) which contains coordinates that define the center of PL system (the eye) through its lifetime. Similar to Radovan et al. (2019), the area of 200 km around the maturity point provided by Noer and Lien (2010) has been taken for each of the ASRv2 time steps and followed until PL landfall.

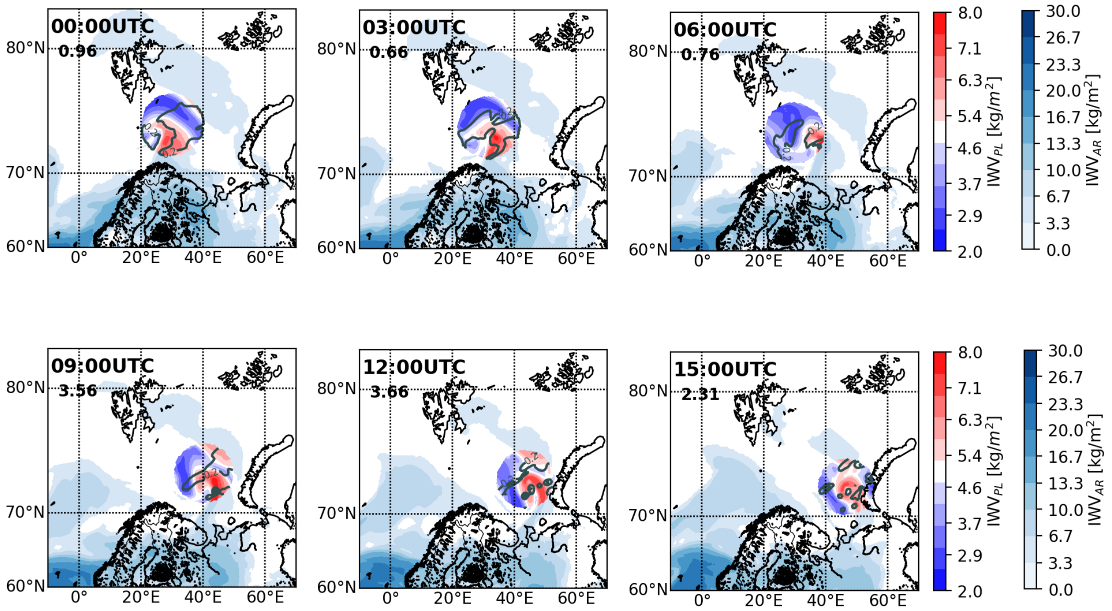

Figure 7.1: *IWV field for a case study with the simultaneous occurrence of atmospheric river (blue shading) and polar low IWV on 12 January, 2002. Snow amount are presented as gray counters inside 200 km of a PL with maximum in kg/m^2 in upper left corners (second row). Shown are time steps from PL genesis until landfall.*

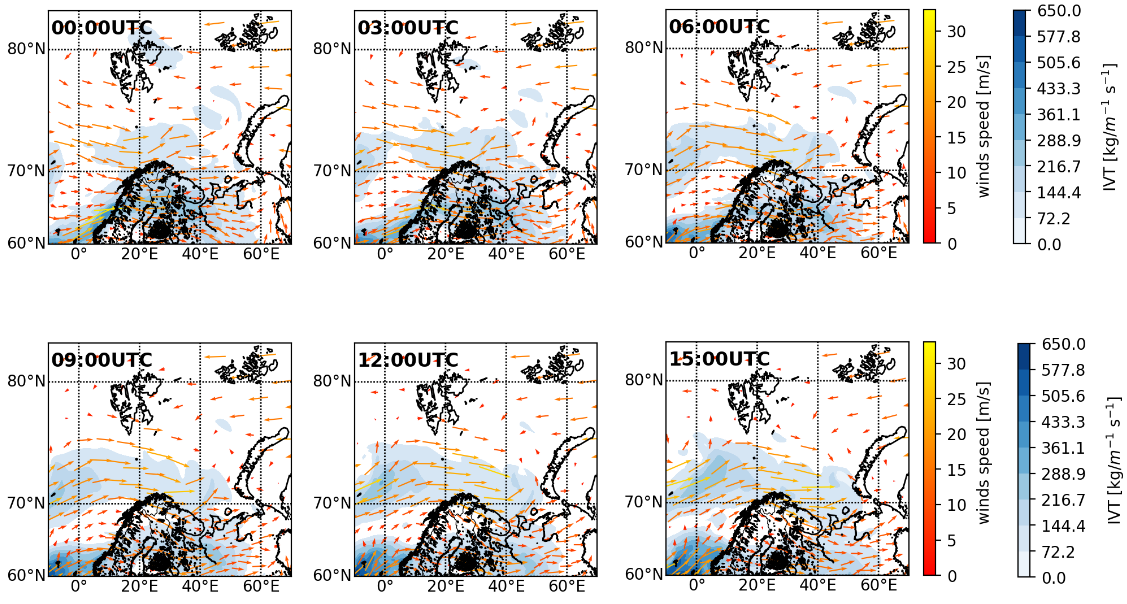

Figure 7.2: *IVT (shading) and wind vector for atmospheric river and polar low coupled case on 12 January, 2002. Shown are time steps from PL genesis until landfall as in Fig. 7.1.*

In addition to IWV and integrated snow content for the PL region of 200 km, the IVT has been calculated for each of the time steps and related to 850 hPa wind speed and direction for larger area (between 10°W - 70°E and 60°N - 82°N) in order to investigate the influence of the AR's on the PL.

Since water vapour brought by ARs to the Arctic region will condense fast in cold air, the amount of IWV reaching the Arctic often will not reach values of 2 cm (20 $\mathrm{kg/m^2}$) defined by Ralph et al. (2019) for ARs over extratropical regions. In Gorodetskaya et al. (2014) it was observed that IWV amounts for an AR can drop to below 1 cm (10 kg/m^2) when approaching dry and cold regions such as Antarctica. Considering that the Arctic is rather similar, here the AR is identified if the values of IWV and IVT exceed 1 cm and 200 $\mathrm{kg/m^{-1}s^{-1}}$, respectively.

The PL case on 12 January, 2002 that simultaneously occurs with an AR is presented in Figs. 7.1 and 7.2. It can bee seen that at the initial stage (00:00 UTC) of the PL, the IWV reached values of 8 $\mathrm{kg/m^2}$ with snow amounts of ~ 1 $\mathrm{kg/m^2}$ where the front edge of the AR connects with the PL system above the northern part of Norway. The AR brought large amounts of IWV reaching values of 13 $\mathrm{kg/m^2}$ (1.3 cm). It can be seen that the PL progresses in eastward direction along with the AR (Fig. 7.2) which supplies the PL with additional moisture for its intensification. At the points where PL and AR are connected, highest values of IWV and snow amount are found with snow amount reaching values of almost 4 $\mathrm{kg/m^2}$ at 12:00 UTC. The IVT values around the PL system suggest a fast transportation of large amounts of moisture of 280 $\mathrm{kg/m^{-1}\ s^{-1}}$ with winds speed reaching extremely high values of ~ 30 m/s along the PL track. As the surface below the PL switches from ocean to land (Novaya Zemlya), the amounts of snowfall starts to decrease forming more clusters as indicated by the gray counters inside a PL radius of 200 km (Fig. 7.1).

In order to to investigate for an additional case the influence of AR on the PL precipitation, the analysis of a PL case without an AR (26 January, 2002) has been

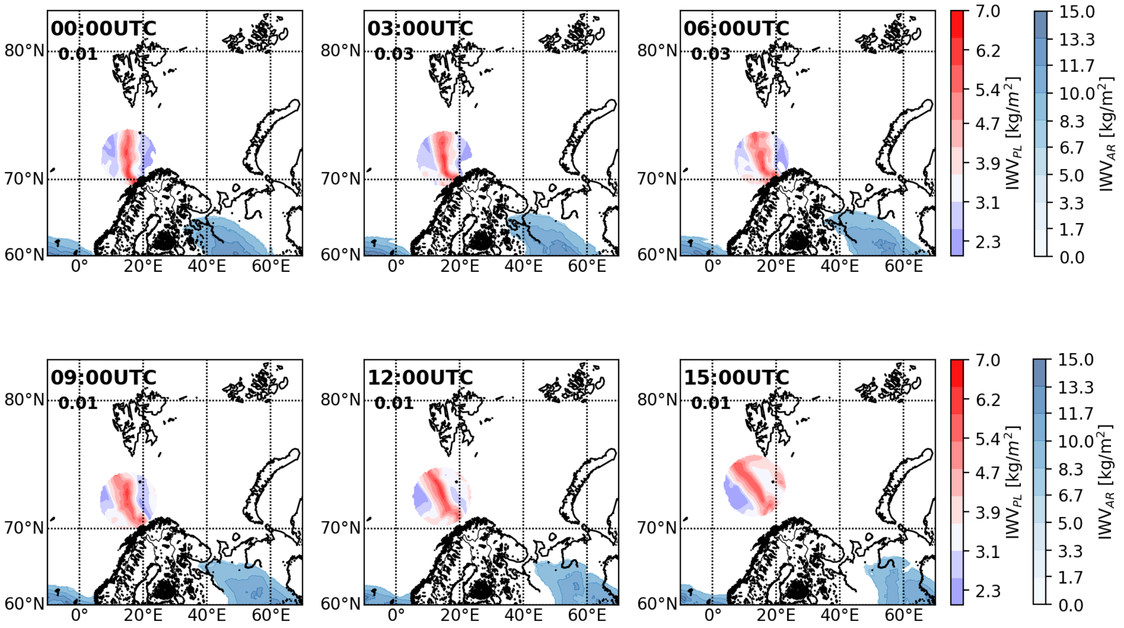

Figure 7.3: *As in Fig. 7.1 only for PL case without the presence of an AR on 26 January, 2002.*

performed in a similar fashion and is shown on Figs. 7.3 and 7.4. This PL only case was chosen since it developed over approximately the same region and only 14 days after the concurrent PL/AR case on 12 January, 2002. It can be noted that the IWV inside the PL region of 200 km around the center reached relatively high values of 7 kg/m^2 even though an AR was not identified for this case. However, weaker transport from south-west Siberia bringing water vapour with amounts of $\sim$ 100 kg/m^{-1} s^{-1} as indicated by IVT was present. These amounts however were too small to be identified as the AR (Fig. 7.4). The formation of this PL case was probably originating from the collision of two air masses moving in the opposite direction with one coming from the north Atlantic moving towards the north and the other from Siberia moving towards south-west. With their encounter at 70°N latitude off the coast of Norway, the winds started to weaken and gain more eastward direction (Fig. 7.4).

Compared to the PL connected with to the AR, the PL on 26 January, 2002 seems to be more static with weaker wind speed of $\sim$ 20 m/s. In terms of snow amount, this PL case showed extremely small values barley reaching 0.03 kg/m^2. It seems that for the concurrent case, the AR and the large IVT have a great influence on the PL precipitation amount bringing more remote supply of moisture to the PL while the PL only case was mostly supplied by evaporation from local sources.

While these two case studies point at an influence of ARs on the strength of PLs more research including long-term climatology is needed to draw firm conclusions.

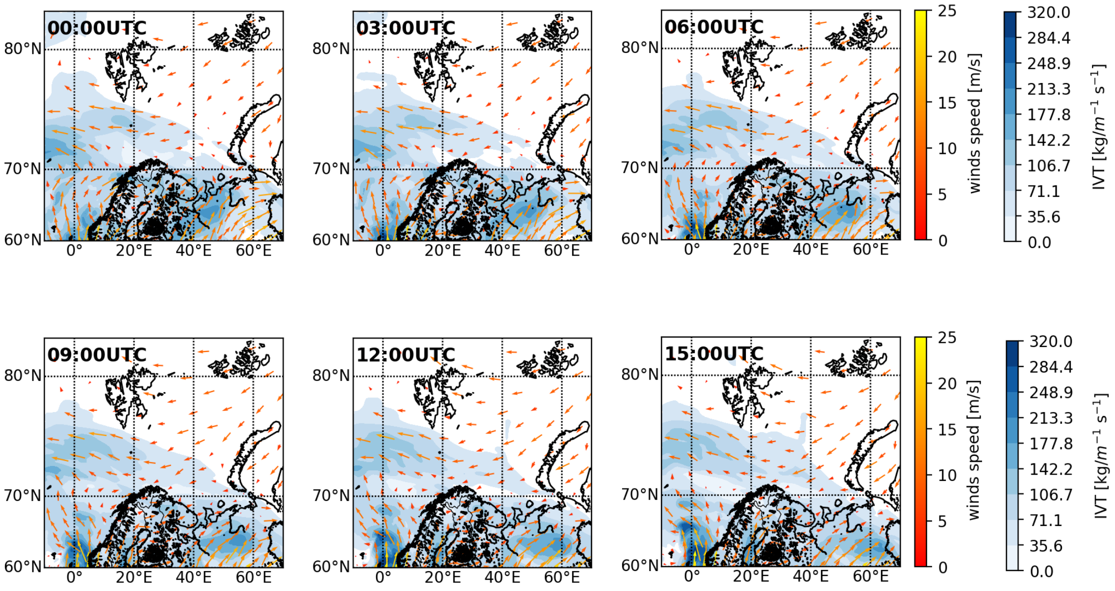

Figure 7.4: *As in Fig. 7.2 only for PL case decoupled from AR on 26 January, 2002.*

8 Summary and Perspectives

The importance of the accurate assessment of water vapour and its influence on small- and large-scale processes is of great importance, especially in changing climate. However, in the remote and harsh environment such as the Arctic, ground-based observations are confined mostly to the land surfaces, creating a large spatial gap over the Arctic ocean. Therefore, the usage of satellites in water vapour assessment is of crucial importance. Although water vapour absorbs mostly in the near IR spectral region, satellites measuring in this frequency range can asses water vapour only above cloud tops while levels below are obscured by clouds. Moreover, satellites measuring in the IR spectral region rely on sun glints making the retrievals of IWV over polar night extremely hard if not impossible. Therefore it is imperative to resort to passive microwave radiometers using water vapour sounding frequencies which are independent of sun light and are having the ability to penetrate even the thickest of the clouds. Although IWV retrieved form passive microwave observations are available, these are often prone to dry or moist biases when compared to in situ measurements. These biases stem from the various assumptions and the *a priori* data that need to be included in the retrieval algorithms.

Therefore, in this thesis, the T_bs from two passive microwave radiometers, AMSU-B and MHS have been used to approximate IWV calculated from the ASR over the Arctic region. The T_bs from the sounding frequencies were used as a proxy for IWV column by correlating the T_bs of each frequency channel with corresponding IWV column based on weighted AH peak level to TOA. Prior to the correlation analysis, a water vapour sensitivity analysis of the five frequency channels of AMSU-B and MHS has been performed for two months of interest, namely January and May. These months were chosen since they were assumed to be representatives for the winter and spring seasons. In order to correlate the observed T_bs to the ASR IWV, the ASR was evaluated in T_b space by calculating synthetic T_bs for which the forward operator PAMTRA was employed. PAMTRA was choosen for calculation of synthetic T_bs due to its flexibility in definition of complex microphysical properties of hydrometeors for various Cloud Resolving Models outputs.

High correlation have been found between observed and synthetic T_b for all channels, reaching values of 0.99 for 183.31 ± 1 GHz and 183.31 ± 3 GHz for January and May, respectively. Additionally, high correlation has been found for lower scanning frequency channels, 183.31 ± 7 (190.31) GHz, even though this channel is largely affected by surface emissivity, especially in winter over Central Arctic region where the atmosphere is extremely cold and dry. A summary of correlations can be found in table 7.

After high correlations between observed and synthetic T_bs have been found for all frequency channels, the ASR was evaluated as a good choice for the IWV analysis. This gave confidence for testing of the hypothesis one:

> **Hypothesis 1**: Long-term brightness temperatures (T_bs) can be used as a proxy for water vapour spatiotemporal trends in the Arctic.

by correlating T_b to corresponding IWV columns. Synthetic T_bs from three frequency channels as well as observations showed high correlation between corresponding IWV columns. This is especially true for January, for the frequency channels being sensitive to water vapour amounts in the lower troposphere. While the frequency channel being sensitive to water vapour in UTLS region correlates very well with corresponding IWV column ($IWV_{700hPa-TOA}$) during January, its correlation with $IWV_{600hPa-TOA}$ column seems to show lower and even negative correlations during May.

Table 7: *Correlations of simulated and observed T_b for three AMSU-B and MHS frequency channels for three different time scales, daily, monthly and whole period for certain frequency.*

Frequency [GHz]	**period**	**r**	
		JAN	**MAY**
183.31 ± 7	day	0.92	0.96
	month	0.91	0.97
	all time	0.90	0.98
190.31	day	0.90	0.91
	month	0.92	0.96
	all time	0.91	0.98
183.31 ± 3	day	0.96	0.94
	month	0.97	0.98
	all time	0.97	0.99
183.31 ± 1	day	0.97	0.88
	month	0.98	0.95
	all time	0.99	0.98

The reason for such a difference could stem from the fact that during polar night, the atmosphere is relatively calm and stable due to the absence of sunlight and a well defined strong polar vortex, while during May, the UTLS region becomes more chemically active due to sun return. This indicates the importance of other GHGs in the UTLS region during spring but as well more complex dynamics of weak spring polar vortex and planetary Rossby waves breaking that are modulating stronger variability of both, water vapour and temperature.

From the above it can be concluded that the T_bs can be used as a proxy for IWV, however, excluding the UTLS region during May. A possible improvement of the above mentioned method can be achieved by performing two additional steps, 1) including layer-averaged IWV below weighted AH peaks and 2) by setting certain thresholds for the humidity weighting function for the frequencies which are affected by surface emissivity. In this way, the whole broadened part of weighing functions are taken in consideration while the influence from highly variable surface emissivity is reduced to minimum. Moreover, in this way an improvement for the IWV retrieval from frequency channels sensitive to lower parts of the atmosphere would be achieved.

In future, it would be possible to expand this method to improve IWV retrieval by the synergy of microwave and IR frequencies. In this way, profiles of water vapour contaminated by precipitation from convective clouds could be screened out in a more efficient way. A possible combination of passive microwave instruments, e.g., the Advanced Technology Microwave Sounder (ATMS) (launched in 2011 - onboard Suomi National Polar-orbiting Partnership (Suomi NPP) and 2017 - onboard NOAA-20 as a part of Joint Polar Satellite System (JPSS)) with the Infrared Atmospheric Sounding Interferometer (IASI) (onboard MetOp-A and MetOp-B as a part of EUMETSAT Polar System) could be done.

Moreover, these satellites are flying in a sun-syncronous orbit as do AMSU-B and MHS. In addition,as part of the JPSS and EUMETSAT Polar System successive launches of the above mentioned instruments are planned: by 2038 ATMS onboard JPSS-1, -2, -3 and -4 in intervals of ∼ 5 years and by 2027 IASI onboard MetOp-C or by 2044 IASI-New Generation (IASI-NG) on MetOp Second Generation A3 (MetOp SG A3), respectively. Therefore it would be of interest to further test the method presented in this thesis.

Since water vapour is largely released by convectional condensation from cyclones, the most intense Arctic storms, know as polar lows have been investigated. PLs occur most frequently in January. Thus, this is the month which has been analysed in this work. For the 2000-2011 Januaries, altogether there are identified 33 mature cases as recorded by Noer and Lien (2010). Since their formation and persistence to maturity stage is not yet fully understood, a number of environmental conditions and their combination have been chosen for the analysis of PL dynamics. The area of a PL has been defined as the region of 200 km around the maturity location since this is the radius mostly observed for these storms on satellites images.

Among six different conditions analysed during PL genesis and maturity stage it seems that there is an interplay between the temperature gradient at the surface and the 500 hPa level and low-level convectional instability indicated by strong lapse rates. When lower thermal instability during formation stage was present, LRs throughout the boundary layer were stronger, and therefore steeper, showing that these PLs were fostering convective development. For few other cases, when both mentioned conditions decreased simultaneously, RH was mostly above 90%. It was also noted that the higher amount of RH at lower levels during genesis stage promoted stronger winds at the maturity stage.

The analysis revealed the most relevant parameters that should be taken into consideration when forecasting PL persistence with indication of high RH during genesis stage promoting more intense PL in terms of the wind speed.

Since one of the features of PLs are large amounts of precipitation, mostly in the form of snow, and since atmospheric rivers, besides local evaporation from ocean and sea-ice melt, are large suppliers of water vapour in the Arctic, their influence on PLs snow amount has been analysed for a case study and compared to a PL case not connected to an AR. Both, the concurrent case of PL and AR and PL only case, formed approximately in the same region with only two weeks apart.

Although both PLs featured especially large amounts of IWV (for January), it was found that the region of the AR attached to the PL system experienced much larger amounts of snow, reaching values of almost 4 kg/m^2 through its lifetime. However, the PL only case showed negligible amounts of the snow. The PL only case was supplied more by locally evaporated moisture while the concurrent case of AR and PL was mostly supplied by large amounts of moisture from the AR. Moreover, the coupled PL/AR case was more intense in terms of wind speed, reaching values of almost 30 m/s compared to wind speeds of 20 m/s of PL only case. In addition, due to large amounts of water vapour supply, a PL coupled to AR had traveled larger distance, most probably due to faster conversion of potential energy of moisture into kinetic energy of wind speed in comparisons to PL only case.

These findings indicate the importance that ARs can have on the convective systems such as PLs. To make these findings more firm and robust, a larger number of the concurrent PLs and ARs cases should be investigated by including other seasons in conjunction with model simulations.

Acknowledgments

I would like to thank my supervisors Prof. Susanne Crewell and Annete Rinke (AWI Potsdam) for their guidance, encouragement, advice and interest during the course of this research. I would also like to thank, Mario Mech and Erlend M. Knudsen for their help and valuable discussion throughout the process of writing my first publication and finishing my thesis. I gratefully acknowledge Mario's effort with explaining radiative transfer model PAMTRA and helping with other technical issues. I thank Marek Jacob for his help in programming and his patience whenever I had some question about it. I would like to thank Kerstin Ebell, Jan Chylik and Christoph Böhm for reading some of this thesis chapter drafts and their comments in helping to improve it.

I thank Gunnar Noer and Claud Chantal for their interest and discussion about polar lows dynamics. I thank Irina Gorodetskaya and Carolina Viceto for providing information on atmospheric rivers for polar low cases. I also thank Dave Bromwich and Shi Li for providing the ASRv2 data and answering my questions about its production.

I would like to express my gratitude for the funding by the Deutsche Forschungsgemeinschaft (DFG, German Research Foundation) – Projektnummer 268020496-TRR172, within the Transregional Collaborative Research Center "ArctiC Amplification: Climate Relevant Atmospheric and SurfaCe Processes, and Feedback Mechanisms $(AC)^3$ project under which work for this dissertation was performed.

I am grateful for having the opportunity to do aviation weather forecasting and research flight during Arctic CLoud Observations Using airborne measurements during polar Day (ACLOUD) campaign in Svalbard.

Big thank you goes to my uncles who were always there when I needed them.

Last but most important, I thank my beloved father for waking my interest in physics that led me to be an enthusiast in meteorology and for teaching me to never quit and always look for answers myself. I would express my deepest gratitude to my mother, my grandma and sisters for always being a support and source of prayers that are encouraging me.

Appendix A

A.1 Conversion of counts to T_b

Generally, measuring radiation for a certain frequency can be achieved by usage of certain filters that will block passage of all the radiation outside of the frequency spectrum that needs to be measured. For AMSU-B's channel i what is being measured is actually the antenna temperature (in units $[\mu W/(cm^{-1} sterm^2)]$) of the instrument expressed with:

$$T_a(i) = G(i) \times (C_E(i) - C_0(i)) \tag{A.1}$$

where $C_E(i)$ the is the measured count for channel i whilst viewing the Earth scene and $C_0(i)$ is the zero radiance offset related to the receiver noise and the DC offset applied to the video amplifier and G is the gain of the instruments expressed with:

$$G(i) = \frac{B(\nu, T_b) - B(\nu, T_{SP})}{\overline{C}_{BB}(i) - \overline{C}_{SP}(i))} \tag{A.2}$$

where $B(\nu, T_b)$ is the Planck function for a frequency ν and temperature T, T_{BB} and T_{SP} are mean temperature of space target (deep space view (DSV)) and internal target (black body (BB)), respectively. $\overline{C}_{BB}$ and $\overline{C}_{SP}$ are the mean number of counts for DSV and internal target view.

A.2 Solving Planck sum

In the Planck's sum (3.12) the average energy per mode of blackbody radiation is:

$$\langle E \rangle = \frac{\sum\limits_{i=0}^{\infty} nh\nu \exp\left(-\frac{nh\nu}{kT}\right)}{\sum\limits_{i=0}^{\infty} \exp\left(-\frac{nh\nu}{kT}\right)} \tag{A.3}$$

It is convenient to introduce the variable $\alpha \equiv \frac{1}{kT}$, so:

$$\langle E \rangle = \frac{\sum\limits_{i=0}^{\infty} nh\nu \exp(-\alpha nh\nu)}{\sum\limits_{i=0}^{\infty} \exp(-\alpha nh\nu)} \tag{A.4}$$

Taking the derivative over alpha in the upper sum and using the chain rule yields:

$$-\frac{d}{d\alpha}\left[\ln \sum_{i=0}^{\infty} nh\nu \, exp\,(-\alpha nh\nu)\right] = \tag{A.5}$$

$$= -\left[\sum_{i=0}^{\infty} nh\nu \, exp\,(-\alpha nh\nu)\right]^{-1} \frac{d}{d\alpha}\left[\sum_{i=0}^{\infty} nh\nu \, exp\,(-\alpha nh\nu)\right] \tag{A.6}$$

$$= \frac{\sum\limits_{i=0}^{\infty} nh\nu \, exp\,(-\alpha nh\nu)}{\sum\limits_{i=0}^{\infty} exp\ (-\alpha nh\nu)} \tag{A.7}$$

Therefore,

$$\langle E\rangle = -\frac{d}{d\alpha}\left[\ln\sum_{i=0}^{\infty} nh\nu exp\left(-\alpha nh\nu\right)\right] \tag{A.8}$$

and the expansion of the sum into series:

$$\sum_{i=0}^{\infty}\exp\left(-\alpha nh\nu\right) = 1 + \left[\exp\left(-\alpha h\nu\right)\right]^1 + \left[\exp\left(-\alpha h\nu\right)\right]^2 + ... \tag{A.9}$$

The above series can be written in the form $(1-\left[exp\left(-\alpha nh\nu\right)\right])^{-1}$ and we than have:

$$\begin{aligned}\langle E\rangle &= -\frac{d\ln\left[1-\exp\left(-\alpha h\nu\right)\right]^{-1}}{d\alpha}\\ &= -\left[1-exp\left(-\alpha h\nu\right)\right])(-1)\left[1-exp\left(-\alpha h\nu\right)\right]^{-2} h\nu exp\left(-\alpha h\nu\right)\\ &= \frac{h\nu\, exp\left(-\alpha h\nu\right)}{1-exp\ \left(-\alpha h\nu\right)} = \frac{h\nu}{exp\left(\alpha h\nu\right)-1} = \frac{h\nu}{exp\left(\frac{h\nu}{kT}\right)-1}.\end{aligned}$$

A.3 Rayleigh scattering

The phase function P(cosθ) = 1/2 also can be expressed as an infinite series of orthogonal basis functions, such as the Legendre polynomials, $P_l(cos\theta)$:

$$P(cos\theta) = \sum_{i=0}^{N-1}\beta_l P_l \xRightarrow[\text{the first 3 orders}]{\text{solution for}} \begin{cases} P_0 = 1,\\ P_1 = cos\theta,\\ P_2 = \frac{1}{2}(3cos^2\theta - 1).\end{cases} \tag{A.10}$$

where β_l are the moments of the phase function:

$$\beta_l = \frac{2l+1}{2}\int_{-1}^{1} P_l(cos\theta)p(cos\theta)dcos\theta \tag{A.11}$$

and are related to the asymmetry parameter, g:

$$g \equiv \langle cos\theta\rangle = \int_{-1}^{+1} p(cos\theta)cost\theta d\theta \tag{A.12}$$

This parameter can be:

$$g\begin{cases} >0, & \text{foreward scattering } (\theta > \pi/2),\\ =0, & \text{Rayleigh scattering},\\ <0, & \text{backward scattering } (\theta < \pi/2).\end{cases} \tag{A.13}$$

Therefore in the Rayleigh approximation a phase function is equal to:

$$P(cos\theta) = \frac{3}{4}(1 + cos^2\theta) \tag{A.14}$$

For an unpolarized incident light, I, on a sphere of real permittivity ε and radius r the differential cross-section is:

$$\frac{d\sigma(d\theta)}{d\Omega} = \frac{1}{2}\left(\frac{2\pi n_0}{\lambda}\right)^4 r^6\left(\frac{\varepsilon-\varepsilon_0}{\varepsilon+2\varepsilon_0}\right)^2(1+cos^2\theta) \tag{A.15}$$

where n_0 is the refractive index of the medium surrounding the sphere of refractive index n. Integrating this equation over the entire solid angle yields the total cross section:

$$\sigma_R = \frac{8\pi}{3}\left(\frac{2\pi n_0}{\lambda}\right)^4 r^6 \left(\frac{\varepsilon - \varepsilon_0}{\varepsilon + 2\varepsilon_0}\right)^2 \tag{A.16}$$

Where R stands for Rayleigh. And the intensity is given with:

$$I_R = I\frac{2\pi n_0}{\lambda}^4 \frac{r^6}{2D^2}\left(\frac{\varepsilon - \varepsilon_0}{\varepsilon + 2\varepsilon_0}\right)^2 (1 + cos^2\theta) \tag{A.17}$$

where D is the distance between the particle and the observer (Lockwood, 2016).

A.4 Lorentz-Mie theory

Similar to Rayleigh, we again consider a sphere of radius r with a complex index of refraction, m, on which is incident a plane EM wave with the wavelength λ. This interaction causes a sphere to radiate itself due to excitation and the radiated EM waves from this process are not isotropic in general. These EM radiant waves can be expanded using generating scalar function, ψ, for the vector harmonics. Since we are dealing with the spherical function, a function ψ has to satisfy the wave equation in spherical polar coordinates, which in scalar form is defined as:

$$\frac{\partial}{\partial r^2}\left(r^2\frac{\partial\psi}{\partial r}\right) + \frac{1}{r^2 sin\theta}\frac{\partial}{\partial\theta}\left(sin\theta\frac{\partial\psi}{\partial\theta}\right) + \frac{1}{r^2 sin\theta}\partial^2\psi\partial\phi^2 + k^2\psi = 0. \tag{A.18}$$

The solution of the above equation is in the form: $\psi(r,\theta,\phi) \approx R(r)\Theta(\theta), \Psi(\psi)$. Substituting this into equation (A.18) we get set of three differential equations:

$$\frac{d^2\Theta}{d\phi^2} + m^2\Theta = 0; \tag{A.19}$$

$$\frac{d}{sin\theta d\theta}\left(sin\theta\frac{d\Theta}{d\theta}\right) + \left[n(n+1) - \frac{m^2}{sin^2\theta}\right]\Theta = 0; \tag{A.20}$$

$$\frac{d}{dr}\left(r^2\frac{dR}{dr}\right) + \left[k^2r^2 - n(n+1)\right]R = 0; \tag{A.21}$$

for which linearly independent solution have to be found. For (A.19) linearity is achieved if $\phi_e = cos\, m\phi$ and $\phi_o = sin\, m\phi$ where e and o note even and odd numbers. For the last two, linearity is achieved by usage of the orthogonal Legendre functions of the first kind (that have limit at $\theta = 0$ and $\theta = \pi$ and for $m = 0$ they become Legendre polynomials) and spherical Bessel functions of the third kind. The expansion of these functions (for a sphere emitted wave) contain coefficients that are called scattering coefficient and after the expansion of a incident plane wave is also done, we have two additional coefficients. These four coefficient have to be combined and after lengthy derivation it can be found that scattering coefficients are equal to:

$$a_n = \frac{m\psi_n(m\chi)\psi'_n(\chi) - \psi'_n(\chi)\psi'(m\chi)}{m\psi_n(m\chi)\xi'_n(\chi) - \xi_n(\chi)\psi'_n(m\psi)} \tag{A.22}$$

$$\tag{A.23}$$

$$b_n = \frac{\psi_n(m\chi)\psi'_n(\chi) - m\psi_n(\chi)\psi'_n(m\chi)}{\psi_n(m\chi)\xi'_n(\chi) - m\xi_n(\chi)\psi'_n(m\chi)} \tag{A.24}$$

where ψ and ξ are Ricati-Bessel functions. After expansion of the outgoing wave is know, a cross section can be calculated and it can be found:

$$\sigma_{scat} = \frac{2\pi}{k^2}\sum_{n=1}^{\infty}(2n+1)\left(\left|a_n\right|^2 + \left|b_n\right|^2\right) \tag{A.25}$$

where $k = 2\pi/\lambda$ is the wave number of incident wave. The full extinction coefficient is:

$$\sigma_{ext} = \frac{2\pi}{k^2}\sum_{n=1}^{\infty}(2n+1)Re\{a_n + b_n\} \tag{A.26}$$

For large particles ($\chi \gg 1$), a calculation of the sum can take a long time.

Appendix B

B.1 Yearly cycle of T_b from 183.31 ± 1 and 183.31 ± 7 (190.31) GHz

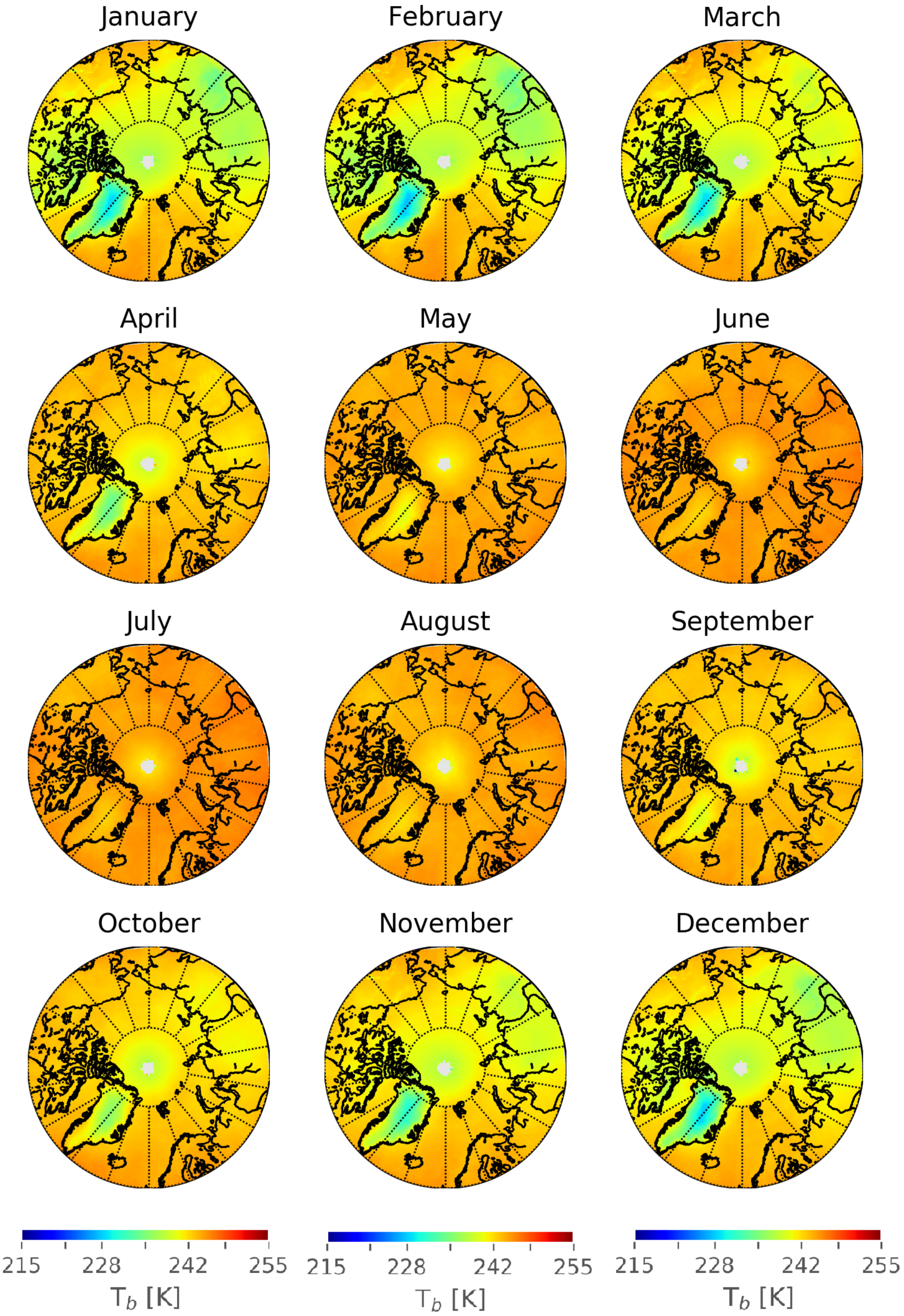

Figure B.1: *Mean monthly T_b composites from all available satellites for 183.31 ± 3 GHz during 2000-2016 period.*

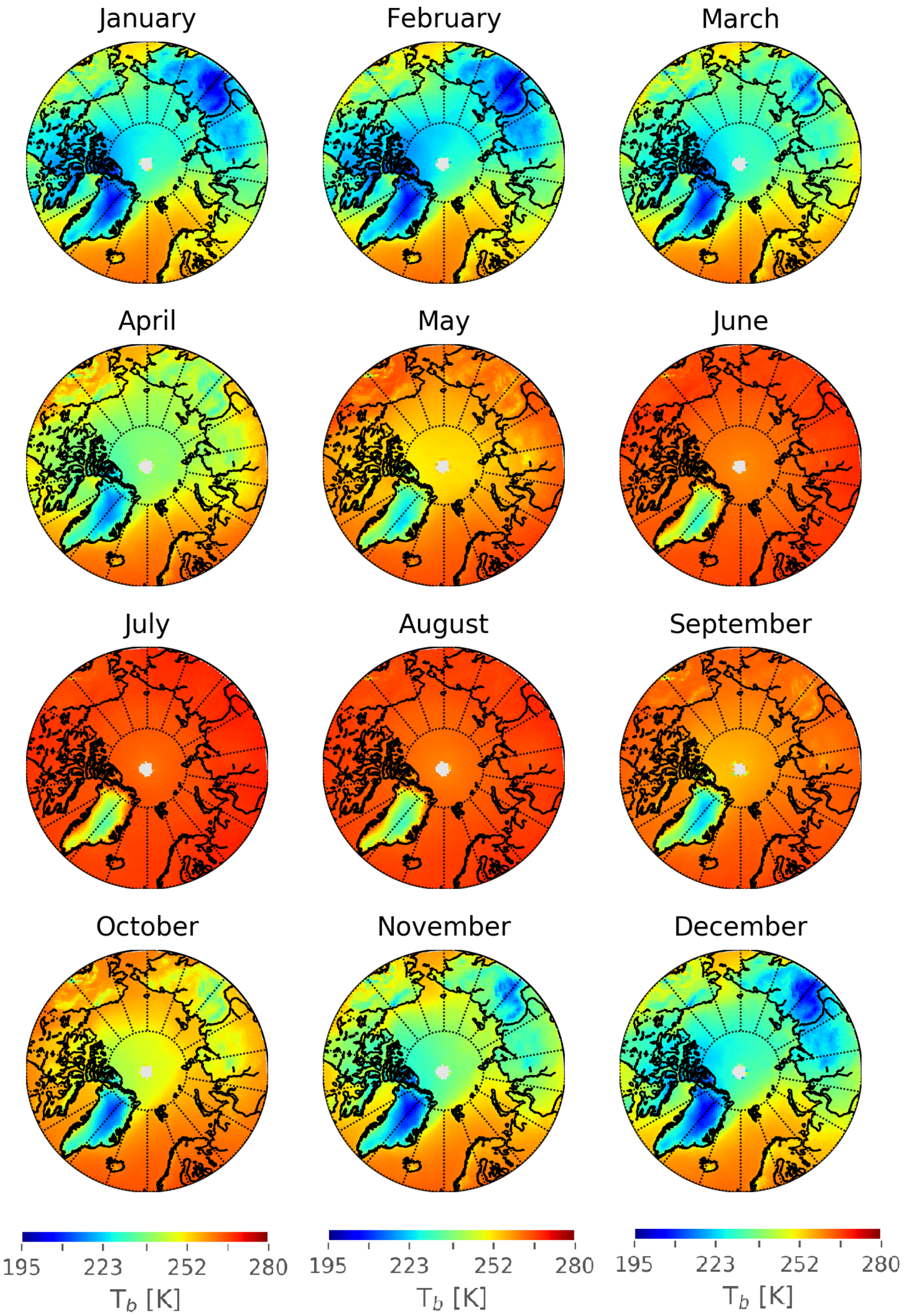

Figure B.2: *As in B.1 only for joined product from AMSU-B's 183.31 ± 7 GHz and MHS's 190.31 GHz frequencies channels.*

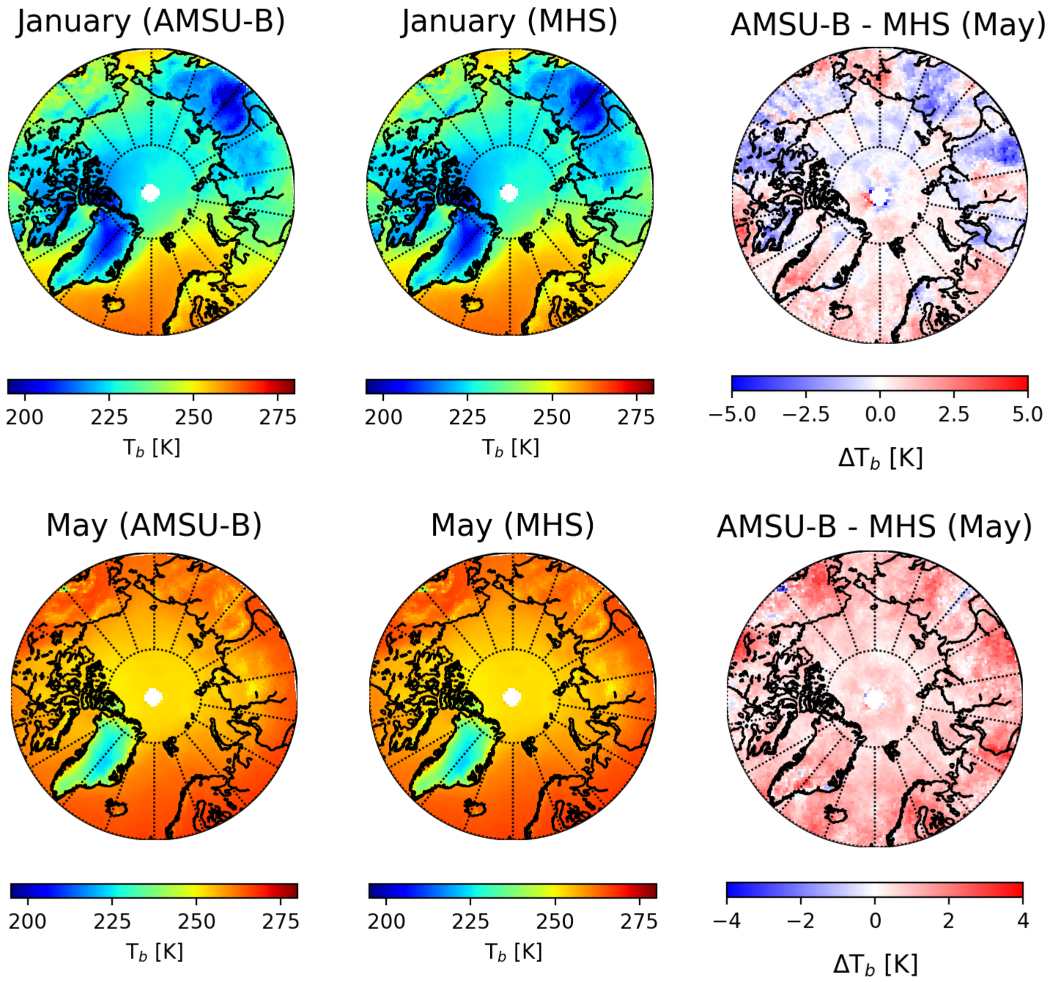

Figure B.3: *Mean T_b from AMSU-B's 183.31 ± 7 GHz frequency during 2000-2009 period (left) and MHS's 190.31 GHz frequency during 2006-2016 period (middle) for January (top) and May (bottom). Differences between AMSU-B's and MHS's overlap period (2006-2009) are shown on the right side of the figure for January (top) and May (bottom).*

B.2 Weighting functions and water vapour sensitivity

January

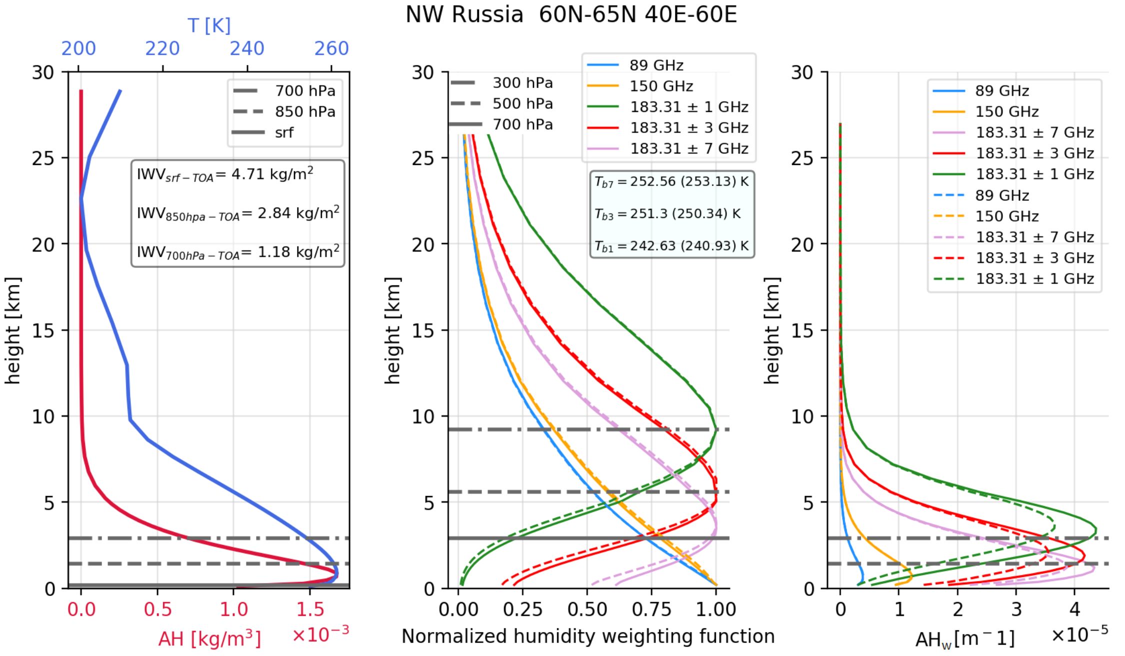
NW Russia 60N-65N 40E-60E

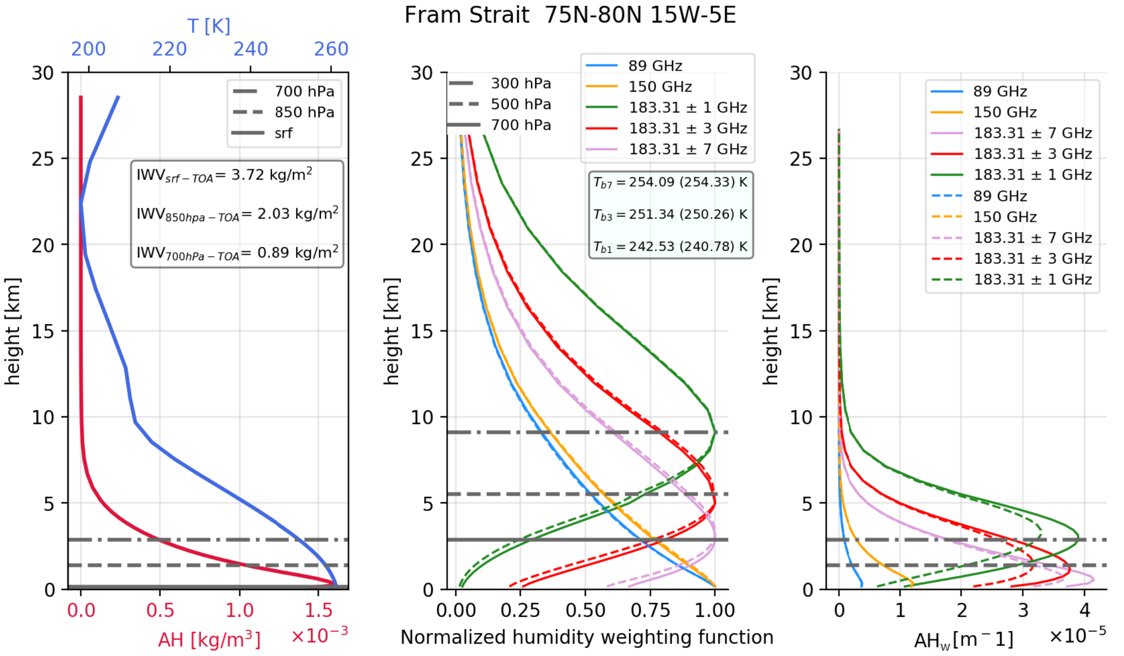
Fram Strait 75N-80N 15W-5E

Figure B.4: *17-year mean input profiles of T and absolute humidity (AH) with IWV values for 3 different column heights (left), normalized weighting function for 5 AMSU-B frequencies for mean profiles and for 20 % increased specific humidity (middle) and AH weighted by weighting function (right). Plots are shown for NW Russia and Fram Strait regions.*

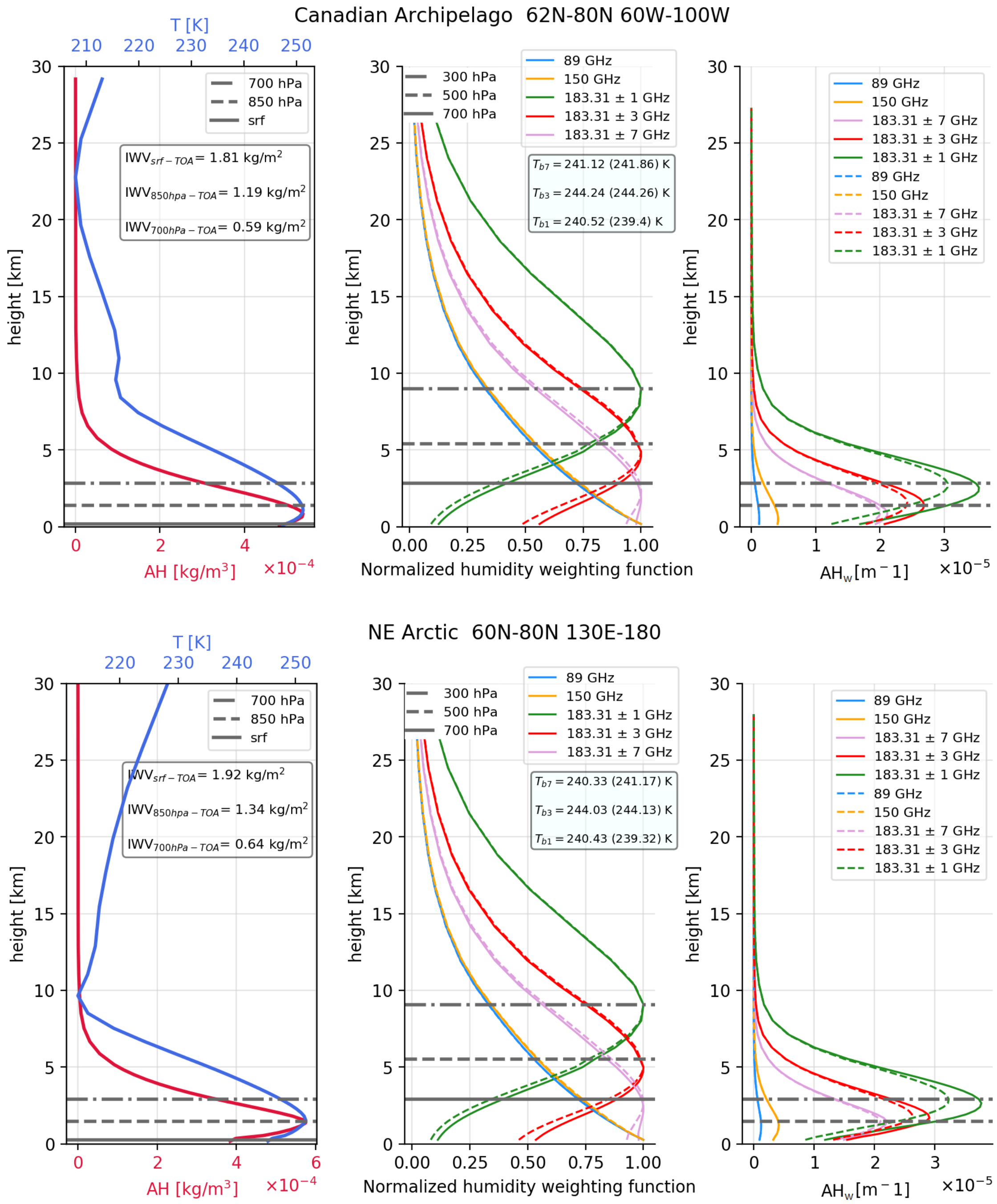

Figure B.5: *As in B.4 only for Canadian Archipelago and NE Arctic regions.*

May

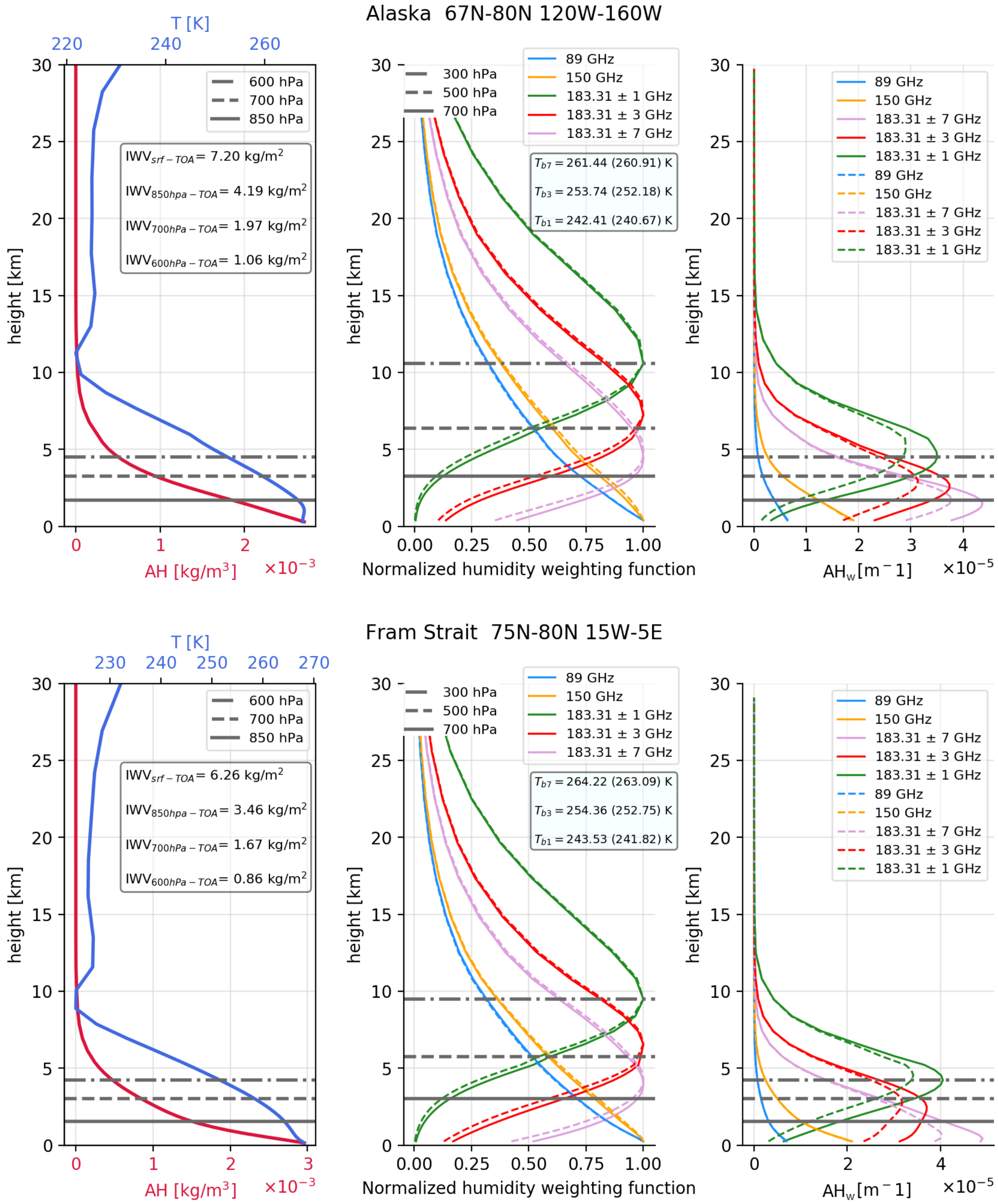

Figure B.6: *As in B.4 only for Alaska and Fram Strait regions in May.*

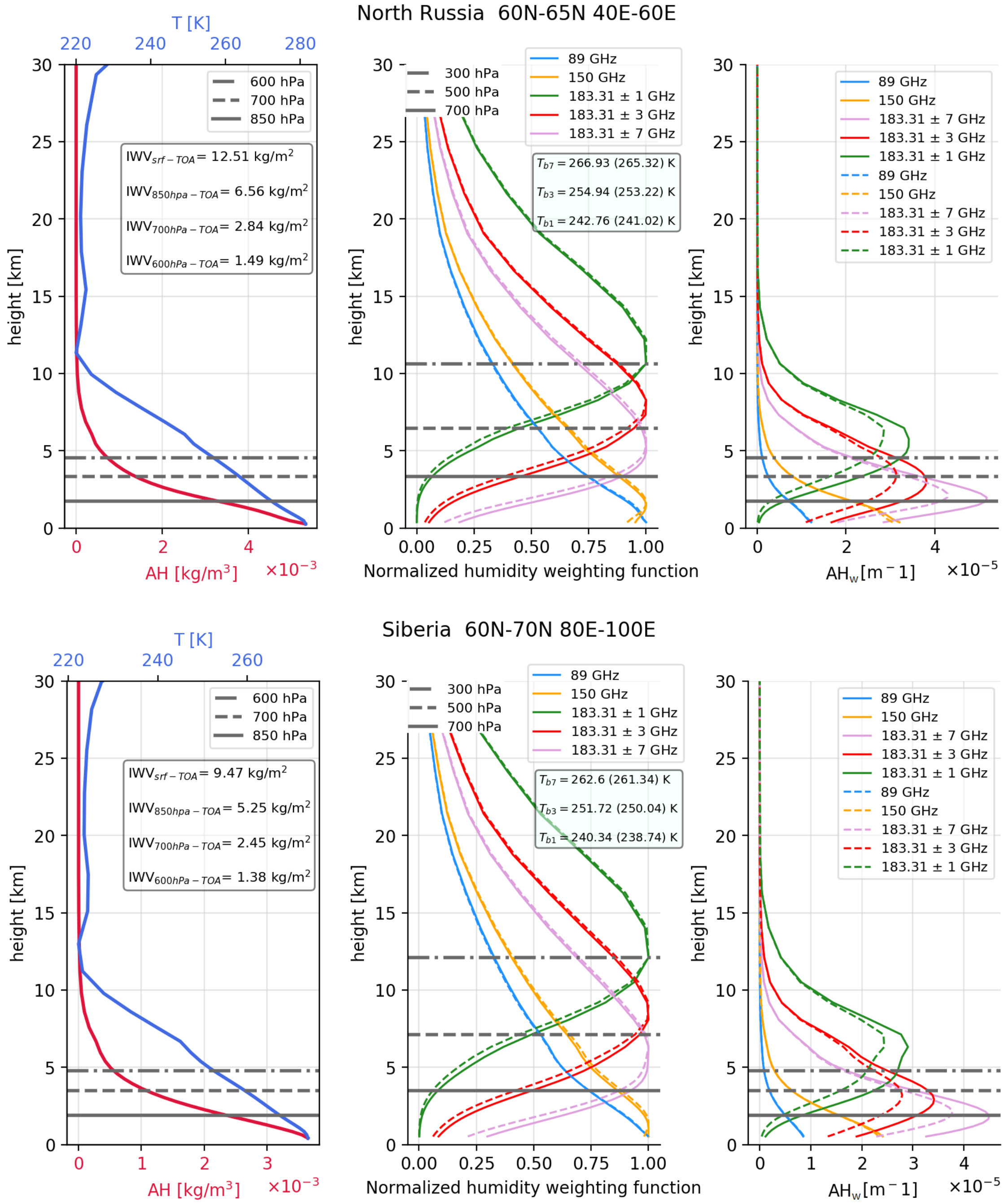

Figure B.7: *As in B.6 only for NW Russia and Siberia regions.*

B.3 Correlations between simulated and observed T_bs

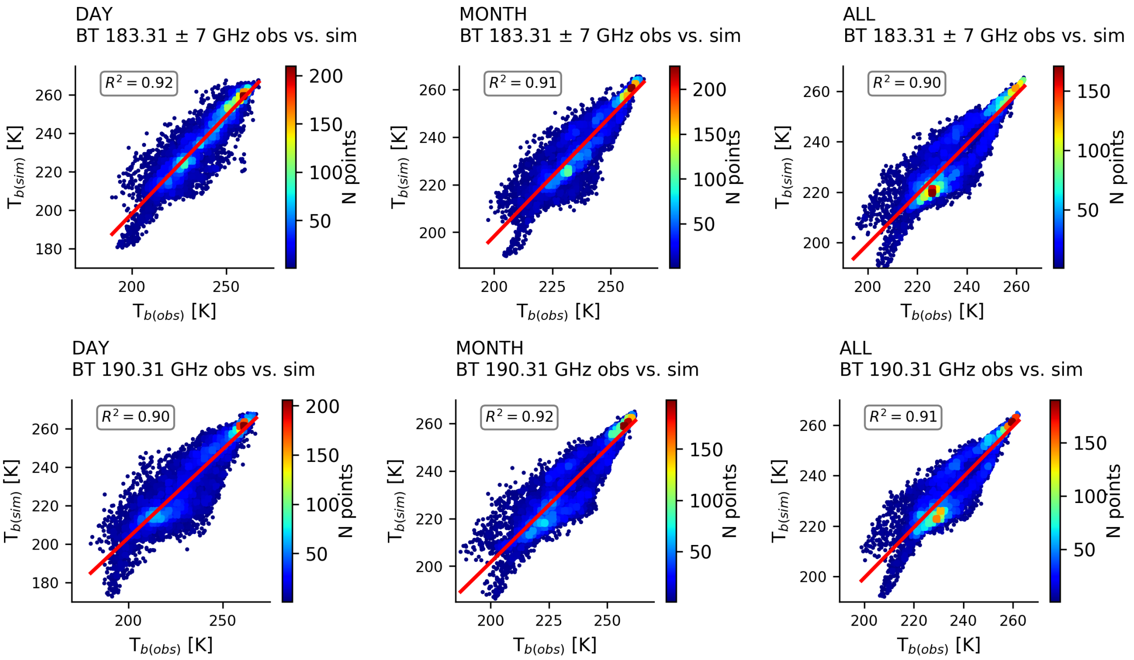

Figure B.9: *January 2D scatter histograms of T_b for 183.31 ± 7 GHz (top) and 190.31 GHz (bottom) frequency channels during 2000-2009 period and 2006-2016 period, respectively. Plots are shown in order, daily values, one month and whole respective period.*

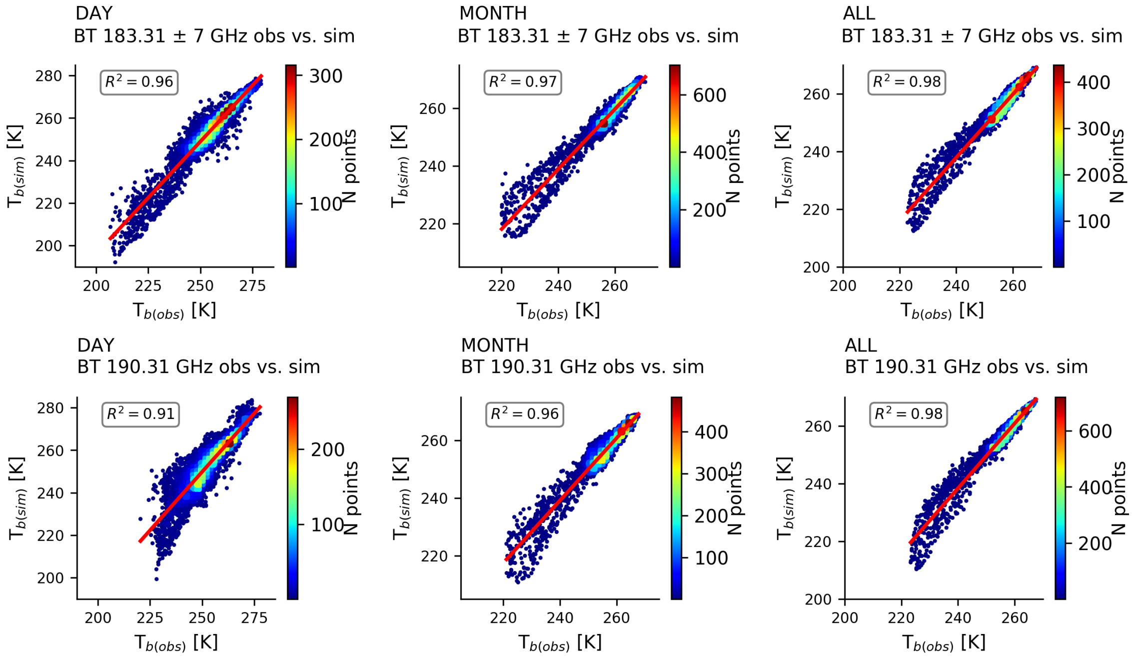

Figure B.10: *As in B.9 only for May.*

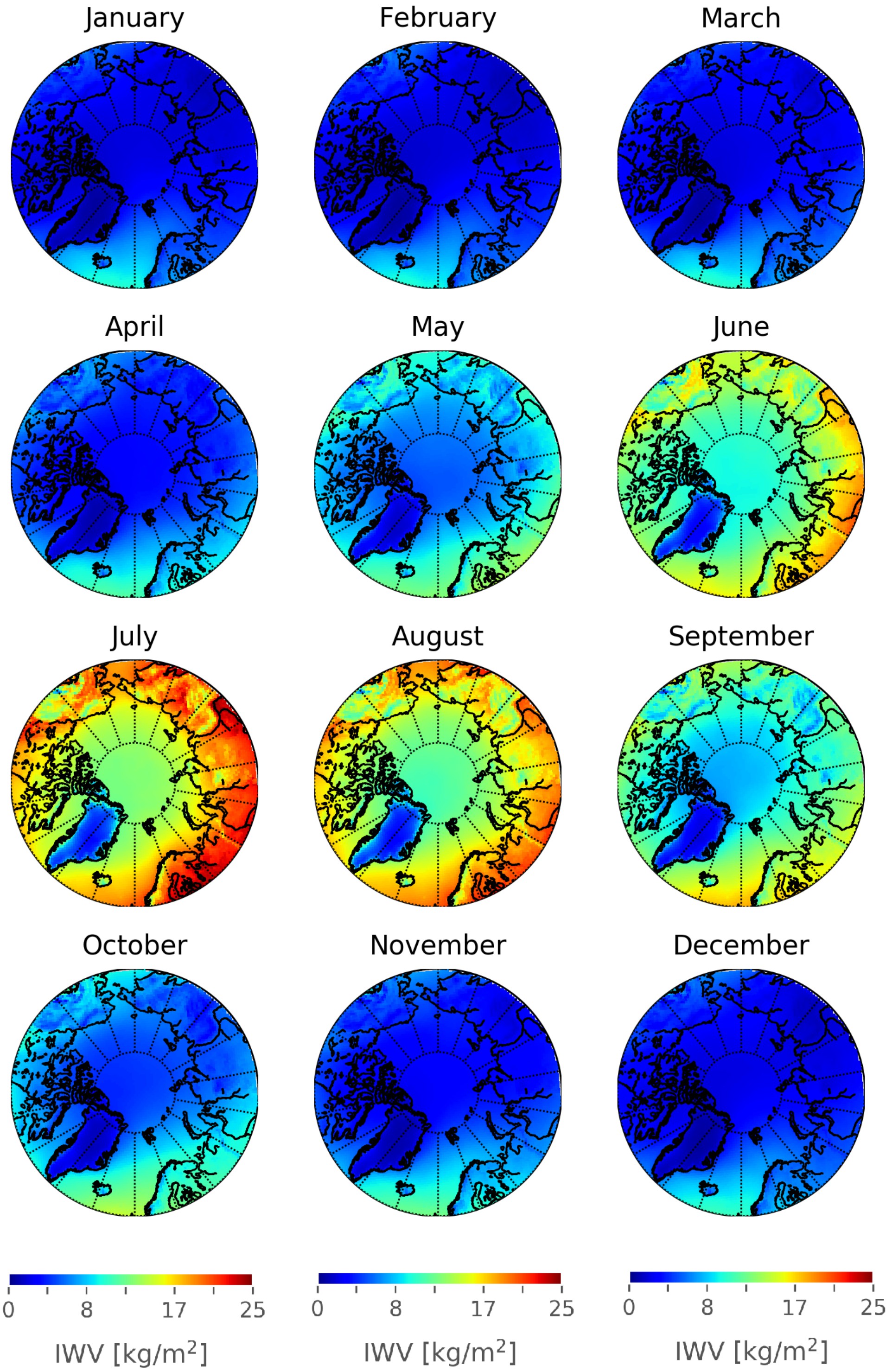

Figure B.8: *Yearly cycle of ASRv2* $IWV_{surf-TOA}$. *Each month shows 17-year mean.*

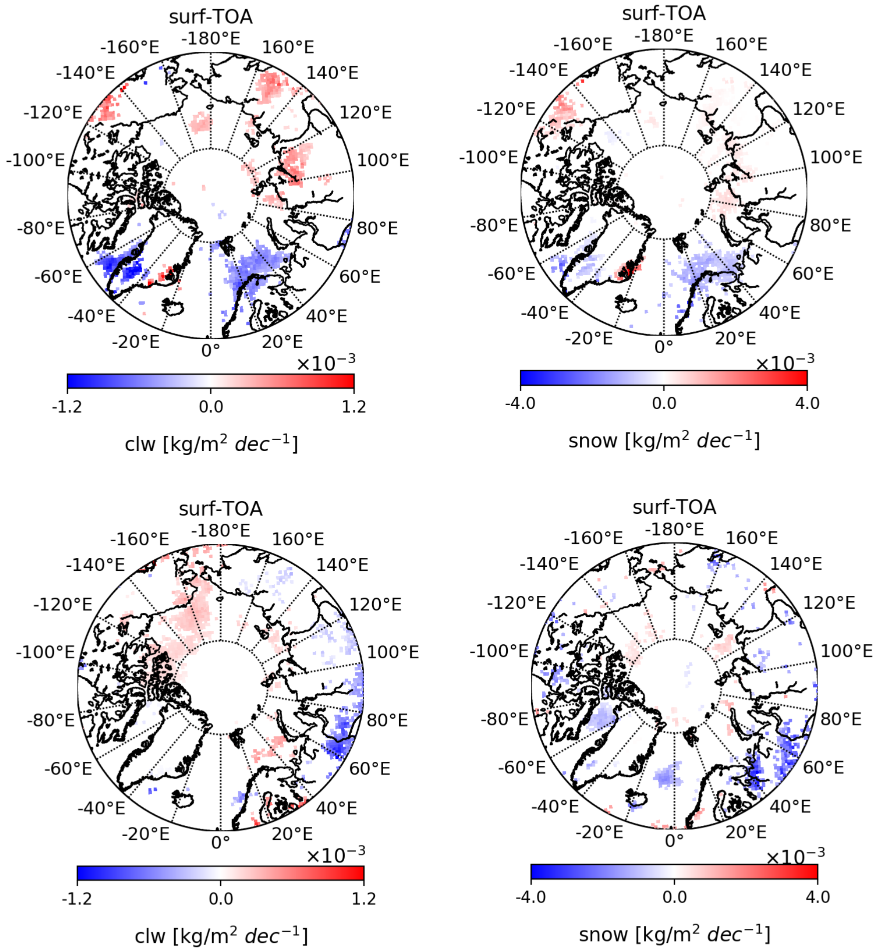

__Figure B.11:__ Integrated CLW (left) and snow (right) content trends for surf-TOA column for January (top) and May (bottom).

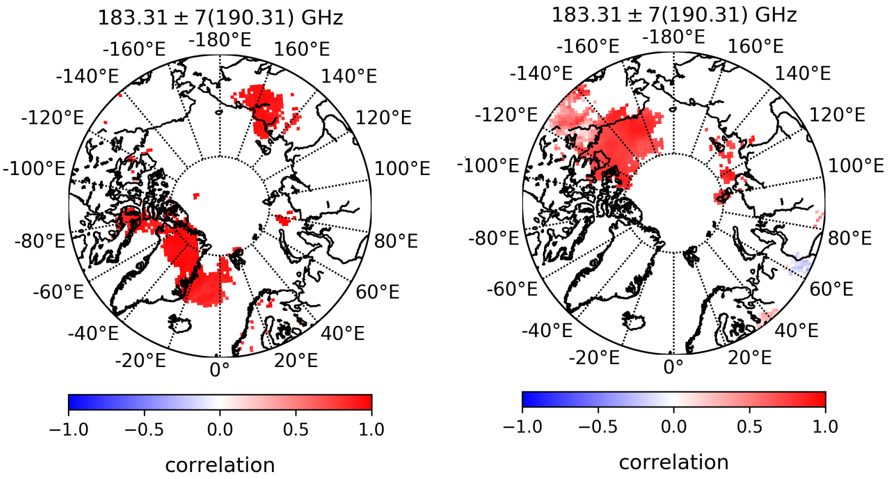

Figure B.12: *Correlations between $IWV_{surf-TOA}$ and 183.31 ± 7 (190.31) GHz T_b for January (left) and between $IWV_{850hPa-TOA}$ and 183.31 ± 7 (190.31) GHz T_b for May (right).*

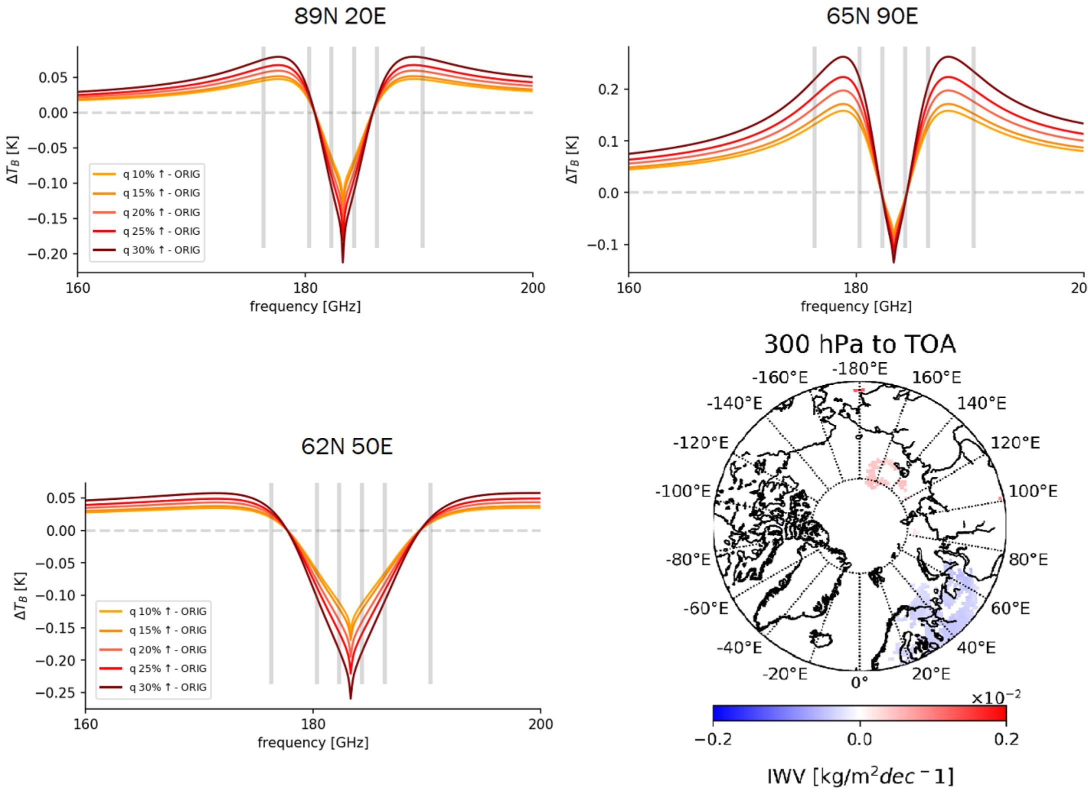

Figure B.13: *Sensitivity of sounding frequencies T_bs for increase in humidity for one point over Central Arctic (top left), Siberia (top right) and NW Russia (bottom left) regions. $IWV_{300hPa-TOA}$ column trend for 2000-2016 period (bottom right).*

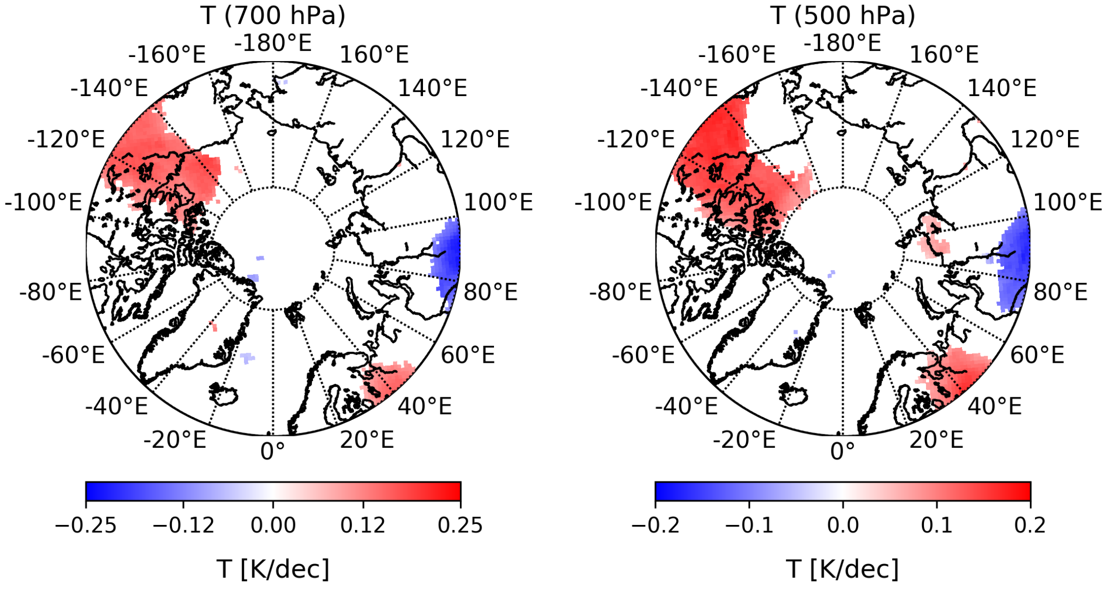

Figure B.14: *Temperature trends from ASR at 700 hPa (left) and 500 hPa (right) for May.*

B.4 Satellites hourly coverage

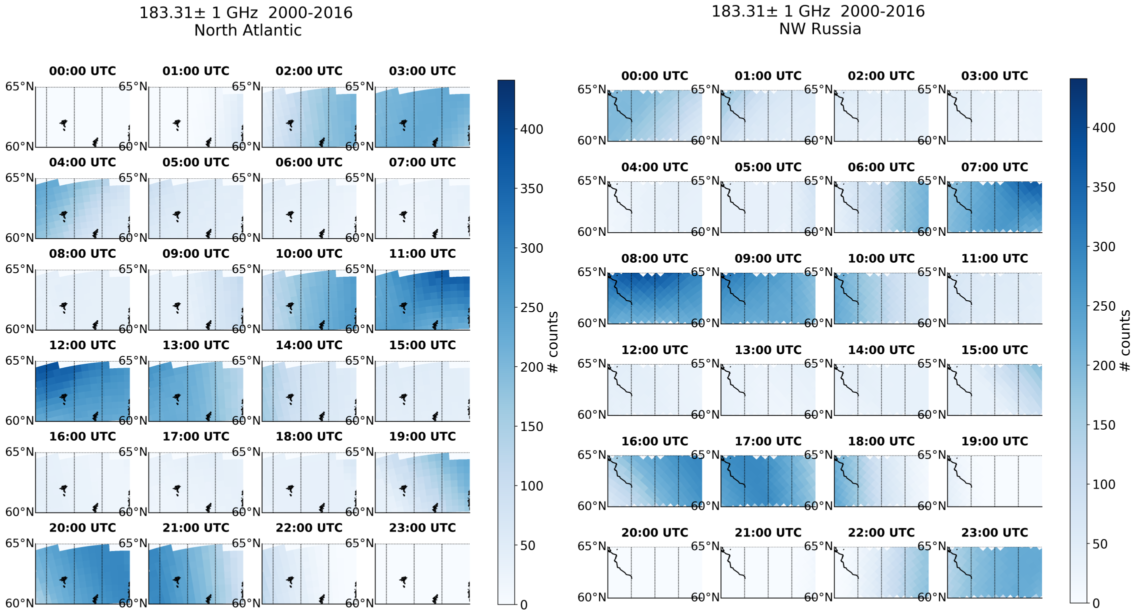

Figure B.15: *January hourly T_b coverage from all satellites during 2000-2016 period for north Atlantic and NW Russia region.*

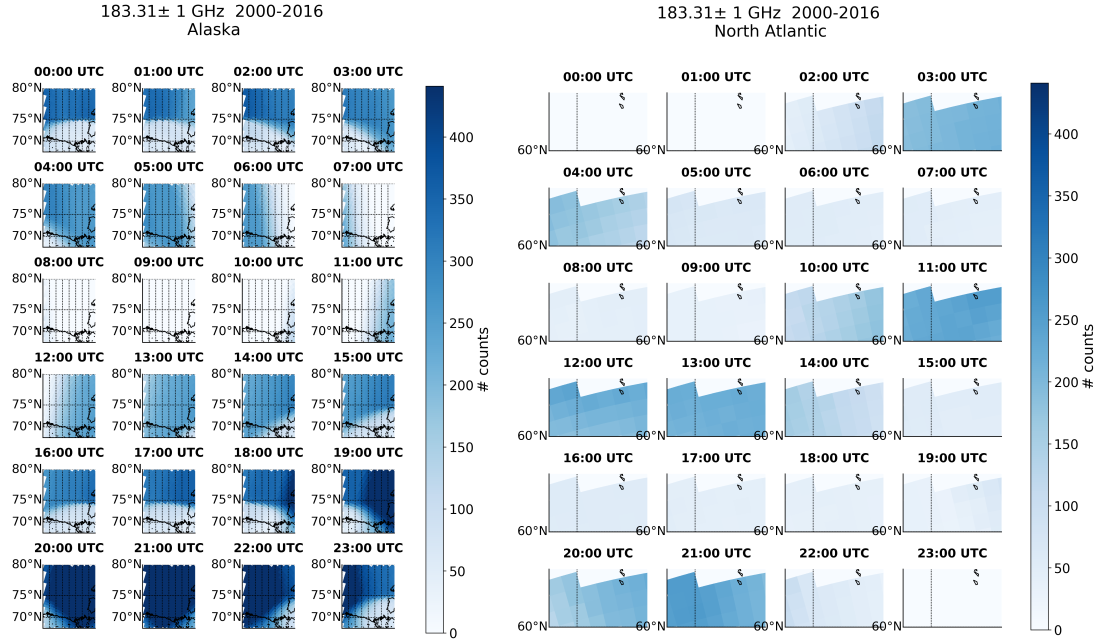

Figure B.16: *As in B.15 only for Alaska and North Atlantic, regions in May.*

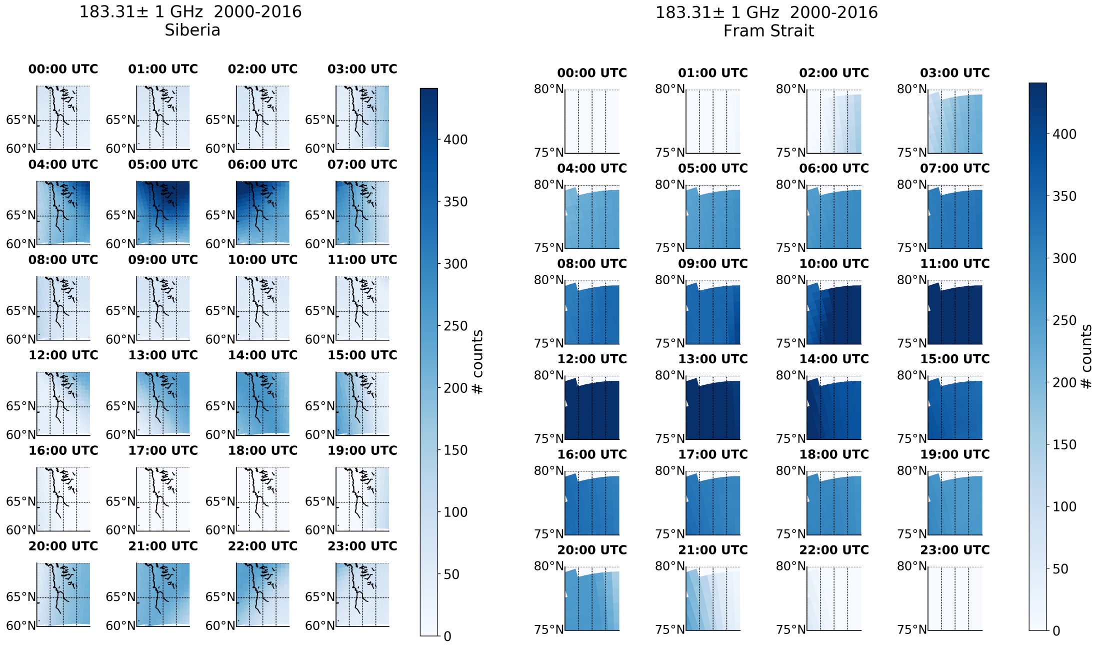

Figure B.17: *As in B.16 only for Siberia and Fram Strait regions.*

Bibliography

V. P. Afanas'ev, A. Yu. Basov, V. P. Budak, D. S. Efremenko, and A. A. Kokhanovsky. Analysis of the discrete theory of radiative transfer in the coupled "ocean–atmosphere" system: Current status, problems and development prospects. *Journal of Marine Science and Engineering*, 8(3):202, 2020.

F. Aires, M. Paul, C. Prigent, B. Rommen, and M. Bouvet. Measure and exploitation of multisensor and multiwavelength synergy for remote sensing: 2. application to the retrieval of atmospheric temperature and water vapor from MetOp. *Journal of Geophysical Research*, 116(D2), 2011a.

F. Aires, C. Prigent, F. Bernardo, C. Jiménez, R. Saunders, and P. Brunel. A tool to estimate land-surface emissivities at microwave frequencies (TELSEM) for use in numerical weather prediction. *Quarterly Journal of the Royal Meteorological Society*, 137(656):690–699, 2011b.

M. Akperov, A. Rinke, I. I. Mokhov, H. Matthes, V. A. Semenov, M. Adakudlu, J.Cassano, J. H. Christensen, M. A. Dembitskaya, K.Dethloff, X. Fettweis, J.N Glisan, O. Gutjahr, G. Heinemann, T. Koenigk, N. V. Koldunov, R. Laprise, R. Mottram, O. Nikiéma, J. F. Scinocca, D. Sein, S. Sobolowski, K. Winger, and W. Zhang. Cyclone Activity in the Arctic From an Ensemble of Regional Climate Models (Arctic CORDEX). *Journal of Geophysical Research: Atmospheres*, 123: 2537–2554, 2018.

J.C. Alishouse, S.A. Snyder, J. Vongsathorn, and R.R. Ferraro. Determination of oceanic total precipitable water from the SSM/i. *IEEE Transactions on Geoscience and Remote Sensing*, 28(5):811–816, 1990.

D. Alraddawi, P. Keckhut, A. Sarkissian, O. Bock, A. Irbah, S. Bekki, C. Claud, and M. Meftah. Enhanced MODIS atmospheric total water vapour content trends in response to arctic amplification. *Atmosphere*, 8(12):241, 2017.

Erik Andersson, Jan Haseler, Per Undén, Philippe Courtier, Graeme Kelly, Drasko Vasiljevic, Cedo Brankovic, Catherine Gaffard, Anthony Hollingsworth, Christian Jakob, Peter Janssen, Ernst Klinker, Andreas Lanzinger, Martin Miller, Florence Rabier, Adrian Simmons, Bernard Strauss, Pedro Viterbo, Carla Cardinali, and Jean-Noël Thépaut. The ECMWF implementation of three-dimensional variational assimilation (3d-var). III: Experimental results. *Quarterly Journal of the Royal Meteorological Society*, 124(550):1831–1860, 1998.

N.C. Atkinson. Calibration, monitoring and validation of AMSU-b. *Advances in Space Research*, 28(1):117–126, 2001.

L. W. Avery and L. L. House. An investigation of resonance-line scattering by the monte carlo technique. *The Astrophysical Journal*, 152:493, 1968.

J. Bailey, L. Kedziora-Chudczer, and K. Bott. Polarized radiative transfer in planetary atmospheres and the polarization of exoplanets. *MNRAS*, in preparation.

J-W. Bao, S. A. Michelson, P. J. Neiman, F. M. Ralph, and J. M. Wilczak. Interpretation of enhanced integrated water vapor bands associated with extratropical cyclones: Their formation and connection to tropical moisture. *Monthly Weather Review*, 134(4):1063–1080, 2006.

F. T. Barath, A. H. Barreth, J. Copeland, D. E. Jones, and A. E. Lilly. Mariner 2 microwave radiometer experiment and results. *Astronomical Journal*, 69, 1964.

M. Barlage, F. Chen, M. Tewari, K. Ikeda, D. Gochis, J. Dudhia, R. Rasmussen, B. Livneh, M. Ek, and K. Mitchell. Noah land surface model modifications to improve snowpack prediction in the Colorado Rocky Mountains. *Journal of Geophysical Research*, 115(D22), 2010.

P. Basili, S. Bonafoni, V. Mattioli, F. Pelliccia, P. Ciotti, G. Carlesimo, N. Pierdicca, G. Venuti, and A. Mazzoni. Neural-network retrieval of integrated precipitable water vapor over land from satellite microwave radiometer. In *2010 11th Specialist Meeting on Microwave Radiometry and Remote Sensing of the Environment*. IEEE, 2010.

A. Bauer, M. Godon, M. Kheddar, and J.M. Hartmann. Temperature and perturber dependences of water vapor line-broadening. experiments at 183 GHz; calculations below 1000 GHz. *Journal of Quantitative Spectroscopy and Radiative Transfer*, 41 (1):49–54, 1989.

R. Bennartz. Optimal convolution of amsu-b to amsu-a. *Journal of Atmospheric and Oceanic Technology*, 17:1215–1225, 2000.

R. Bennartz and P. Bauer. Sensitivity of microwave radiances at 85-183 GHz to precipitating ice particles. *Radio Science*, 38(4), 2003.

W. Berg, J. J. Bates, and D. L. Jackson. Analysis of upper-tropospheric water vapor brightness temperatures from SSM/T2, HIRS, and GMS-5 VISSR. *Journal of Applied Meteorology*, 38:589–595, 1999.

W. R. Berg, M. P. Sapiano, J. Horsman, , and C. Kummerow. Improved Geolocation and Earth Incidence Angle Information for a Fundamental Climate Data Record of the SSM/I Sensors. *IEEE Transactions on Geoscience and Remote Sensing*, 51: 1504–1513, 2013.

T. Bergeron. Ueber die dreidimensional verknuepfende wetteranalyse. volume V, page 99. T.il I, Geof. Publ., Oslo, 1928. ISBN 10: 0883187124.

A.-M. Blechschmidt. A 2-year climatology of polar low events over the Nordic Seas from satellite remote sensing. *Geophysical Research Letters*, 35:L09815, 2008.

A. M. Blechschmidt, S. Bakan, and H. Graßl. Large-scale atmospheric circulation patterns during polar low events over the nordic seas. *J. Geophys. Res.*, 114: D06115, 2009.

K. Block, F. A. Schneider, J. Mülmenstädt, M. Salzmann, and J. Quaas. Climate models disagree on the sign of total radiative feedback in the arctic. *Tellus A: Dynamic Meteorology and Oceanography*, 72(1):1–14, 2019.

L. P. Bobylev, E. V. Zabolotskikh, L. M. Mitnik, and M. L. Mitnik. Atmospheric water vapor and cloud liquid water retrieval over the arctic ocean using satellite passive microwave sensing. *Transactions on Geoscience and Remote Sensing*, 2008.

T. Böhme, Stefan Stapelberg, Tom Akkermans, Susanne Crewell, Jürgen Fischer, Thorsten Reinhardt, Axel Seifert, Christoph Selbach, and Nicole Van Lipzig. Long-term evaluation of COSMO forecasting using combined observational data of the GOP period. *Meteorologische Zeitschrift*, 20(2):119–132, 2011.

C. F. Bohren and D. R. Huffman. *Absorption and Scattering of Light by Small Particles*. Wiley, 1998. doi: 10.1002/9783527618156.

M. G. Bosilovich, F. R. Robertson, L. Takacs, A. Molod, and D. Mocko. Atmospheric water balance and variability in the MERRA-2 reanalysis. *Journal of Climate*, 30 (4):1177–1196, 2017.

T. J. Bracegirdle and S. L. Gray. An objective climatology of the dynamical forcing of a polar lows in the Nordic seas. *Int. J. Climatol.*, 28:1903–1919, 2008.

W.S. Broecker. Are we on the brink of a pronounced global warming? *Science*, (4201), 1975.

D. H. Bromwich, K. M. Hines, and L-S. Bai. Development and testing of polar weather research and forecasting model: 2. arctic ocean. *J. Geophy. Res. Lett.*, 114:D08122, 2010.

D. H. Bromwich, A. B. Wilson, L-S. Bai, G. W. K. Moore, and P. Bauer. A comparison of the regional Arctic System Reanalysis and the global ERA-Interim reanalysis for the arctic. *Q. J. R. Meteorol. Soc.*, 142:644–658, 2016.

D. H. Bromwich, A. B. Wilson, L. Bai, Z. Liu, M. Barlage, C. F. Shih, S. Maldonado, K. M. Hines, S. H. Wang, J. Woollen, B. Kuo, H. C. LIn, T. K. Wee, M. C. Serreze, and J. E. Walsh. The Arctic System Reanalysis Version 2. *Bull. Amer. Meteor. Soc.*, 99:805–828, 2017.

D. H. Bromwich, A. B. Wilson, L. Bai, Z. Liu, M. Barlage, C.-F. Shih, S. Maldonado, K. M. Hines, S.-H. Wang, J. Woollen, B. Kuo, H.-C. Lin, T.-K. Wee, M. C. Serreze, and J. E. Walsh. The arctic system reanalysis, version 2. *Bulletin of the American Meteorological Society*, 99(4):805–828, 2018.

S. A. Buehler. A simple method to relate microwave radiances to upper tropospheric humidity. *Journal of Geophysical Research*, 110(D2), 2005.

S. A. Buehler, P. Eriksson, T. Kuhn, A. von Engeln, and C. Verdes. ARTS, the atmospheric radiative transfer simulator. *Journal of Quantitative Spectroscopy and Radiative Transfer*, 91(1):65–93, 2005a.

S. A. Buehler, M. Kuvatov, and V. O. John. Scan asymmetries in AMSU-b data. *Geophysical Research Letters*, 32(24), 2005b.

S. A. Buehler, J. Mendrok, P. Eriksson, A. Perrin, R. Larsson, and O. Lemke. ARTS, the Atmospheric Radiative Transfer Simulator – version 2.2, the planetary toolbox edition. *Geoscientific Model Development*, 11(4):1537–1556, 2018.

K. D. Burke, J. W. Williams, M. A. Chandler, A. M. Haywood, D. J. Lunt, and L. B. Otto-Bliesner. Data from: Pliocene and eocene provide best analogs for near-future climates. *PNAS*, 2018.

B.A. Burns, X. Wu, and G.R. Diak. Effects of precipitation and cloud ice on brightness temperatures in AMSU moisture channels. *IEEE Transactions on Geoscience and Remote Sensing*, 35(6):1429–1437, 1997.

Z. Cao, R. E. Stewart, and W. D. Hogg. Extreme winter warming over the mackenzie basin: Observations and causes. In M. Woo, editor, *Cold Region Atmospheric and Hydrologic Studies.The Mackenzie GEWEX Experience*. Springer, Berlin, Heidelberg, 2008. ISBN ISBN 978-3-540-73936-4. doi: doi.org/10.1007/978-3-540-73936-4_5.

E. Carmack, K. Aagaard, J. H. Swift, R. W. Macdonald, F. A. Mclaughlin, E. P. Jones, R. G. Perkin, J. N. Smith, K. M. Ellis, and L. R. Killius. Changes in the temperature and tracer distributions within the Arctic Ocean: results from the 1994 Arctic Ocean section. *Deep Sea Research II*, 44(8):1487–1502, 1997.

P. Ceppi, F. Brient, Mark D. Zelinka, and D. L. Hartmann. Cloud feedback mechanisms and their representation in global climate models. *Wiley Interdisciplinary Reviews: Climate Change*, 8(4):e465, 2017.

S. Chandrasekhar. On the radiative equilibrium of a stellar atmosphere. x. *The Astrophysical Journal*, 103:351, 1946.

Q. Chao and A. Feng. Scientific basis of climate change and its response. *Global Energy Interconnection*, (8), 2018.

J. G. Charney. Planetary fluid dynamics. In *Dynamic Meteorology*, pages 97–351. Springer Netherlands, 1973.

J. G. Charney and A. Eliassen. On the growth of the hurricane depression. *J. Atmos. Sci.*, 21:68–75, 1964.

R. Chemke, L. Zanna, and L. M. Polvani. Identifying a human signal in the north atlantic warming hole. *Nature Communications*, 11(1), 2020.

B. Chen and Z. Liu. Global water vapor variability and tren from the latest 36year (1979 to 2014) data of ecmwf and ncep reanalyses, radiosonde, gps, and microwave satellite. *Journal of Geophysical Research: Atmospheres*, 443(11), 2016.

R. Chen and R. Bennartz. Sensitivity of 89–190-GHz microwave observations to ice particle scattering. *Journal of Applied Meteorology and Climatology*, 59(7): 1195–1215, 2020.

A. Chernokulsky and I. Esau. Cloud cover and cloud types in the eurasian arctic in 1936–2012. *International Journal of Climatology*, 39(15):5771–5790, 2019.

A. Chernokulsky and I. Mokhov. Climatology of Total Cloudiness in the Arctic: An Intercomparison of Observations and Reanalyses. *Advances in Meteorology*, pages 1–15, 2012.

T. Chshyolkova, A. H. Manson, C. E. Meek, T. Aso, S. K. Avery, C. M. Hall, W. Hocking, K. Igarashi, C. Jacobi, N. Makarov, N. Mitchell, Y. Murayama, W. Singer, D. Thorsen, and M. Tsutsumi. Polar vortex evolution during northern hemispheric winter 2004/05. *Annales Geophysicae*, 25(6):1279–1298, 2007.

E.-S. Chung, B. Soden, B. J. Sohn, and L. Shi. Upper-tropospheric moistening in response to anthropogenic warming. *Proceedings of the National Academy of Sciences*, 111(32):11636–11641, 2014.

D. Cimini, N. Pierdicca, E. Pichelli, R. Ferretti, V. Mattioli, S. Bonafoni, M. Montopoli, and D. Perissin. On the accuracy of integrated water vapor observations and the potential for mitigating electromagnetic path delay error in InSAR. *Atmospheric Measurement Techniques*, (5):1015–1030, 2012.

J. A. Coakley Jr. and Petr Chýlek. Two Stream Approximation in Radiative Transfer: Including the Angle of the Incident radiation. *Journal of the Atmospheric Sciences*, 32:409–418, 1974.

J. Cohen, J. A. Screen, J. C. Furtado, M.Barlow, D. Whittleston, D. Coumou, J. Francis, K. Dethloff, D. Entekhabi, J. Overland, and J. Jones. Recent arctic amplification and extreme mid-latitude weather. *Nature Geoscience*, 7(9):627–637, 2014.

J. C. Comiso and D. K. Hall. Climate trends in the arctic as observed from space. *Wiley Interdisciplinary Reviews: Climate Change*, 5(3):389–409, 2014.

A. Condron and I. A. Renfrew. The impact of polar mesoscale storms on northeast Atlantic Ocean Circulation. *Nature*, 6:34–37, 2013.

A. Condron, G. Bigg, and I. A. Renfrew. Polar Mesoscale Cyclones in the Northeast Atlantic: Comparing Climatologies from ERA-40 and Satellite Imagery. *Mon. Wea. Rev.*, 134:1518–1533, 2006.

D. Coumou, G. Di Capua, S. Vavrus, L. Wang, and S. Wang. The influence of arctic amplification on mid-latitude summer circulation. *Nature Communications*, 2018.

N. Courcoux and M. Schröder. The CM SAF ATOVS data record: overview of methodology and evaluation of total column water and profiles of tropospheric humidity. *Earth System Science Data*, 7(2):397–414, 2015.

A. D. Crawford and M. C. Serreze. Projected changes in the arctic frontal zone and summer arctic cyclone activity in the CESM large ensemble. *Journal of Climate*, 30(24):9847–9869, 2017.

D. J. Cavalieri J. Crawford, M. Drinkwater, W. J. Emery, D. T. Eppler, L. D. Farmer, M. Goodberlet, R. Jentz, C. Morris A. Milman, R. Onstott, A. Schweiger, R. Shuchman, K. Steffen, C. T. Swift, C. Wackerman, and L. Weaver. Nasa sea ice validation program for the dmsp ssm/i: final report. NASA Technical Memorandum 104559. 126 pp., 1992.

S. Crewell. Hydrological applications of remote sensing: Atmospheric states and fluxes: Water vapor and clouds (passive/active) techniques. In M. G. Anderson and J. J. McDonnell, editors, *Encyclopedia of Hydrological Sciences*, chapter 56, pages 266–290. John Wiley & Sons, Ltd, 2006.

P. Dannevig. *Meterologi for Flygere*. Aschehoug, Oslo, 1954.

P. Debye. Der lichtdruck auf kugeln von beliebigem material. *Annalen der Physik*, 335(11):57–136, 1909.

D. P. Dee, S. M. Uppala, A. J. Simmons, P. Berrisford, P. Poli, S. Kobayashi, U. Andrae, M. A. Balmaseda, G. Balsamo, P. Bauer, P. Bechtold, A. C. M. Beljaars, L. van de Berg, J. Bidlot, N. Bormann, C. Delsol, R. Dragani, M. Fuentes, A. J. Geer, L. Haimberger, S. B. Healy, H. Hersbach, E. V. Hólm, L. Isaksen, P. Kållberg, M. Köhler, M. Matricardi, A. P. McNally, B. M. Monge-Sanz, J.-J. Morcrette, B.-K. Park, C. Peubey, P. de Rosnay, C. Tavolato, J.-N. Thépaut, and F. Vitart. The ERA-interim reanalysis: configuration and performance of the data assimilation system. *Quarterly Journal of the Royal Meteorological Society*, 137(656):553–597, 2011.

D. Deimendjian. Complete Microwave Scattering and Extinction Properties of Polydispersed Cloud and Rain Elements. Technical report, A report prepared for United States Air Force Project Rand, Santa Monica, California, 1963.

M. Dettinger. Climate change, atmospheric rivers, and floods in california - a multimodel analysis of storm frequency and magnitude changes1. *JAWRA Journal of the American Water Resources Association*, 47(3):514–523, 2011.

A. Devasthale, J. Sedlar, T. Koenigk, and E. J. Fetzer. The thermodynamic state of the arctic atmosphere observed by AIRS: comparisons during the record minimum sea ice extents of 2007 and 2012. *Atmospheric Chemistry and Physics*, 13(15): 7441–7450, 2013.

Q. Ding, A. Schweiger, M. L'Heureux, E. J. Steig, D. S. Battisti, N. C. Johnson, E. Blanchard-Wrigglesworth, S. Po-Chedley, Q. Zhang, K. Harnos, M. Bushuk, B. Markle, and I. Baxter. Fingerprints of internal drivers of arctic sea ice loss in observations and model simulations. *Nature Geoscience*, 12(1):28–33, 2018.

S. Ding, P. Yang, F. Weng, Q. Liu, Y. Han, P. van Delst, J. Li, and B. Baum. Validation of the community radiative transfer model. *Journal of Quantitative Spectroscopy and Radiative Transfer*, 112(6):1050–1064, 2011.

M. W. Douglas, M. A. Shapiro, L. S. Fedor, and L. Saukonnen. Research Aircraft Observations of a Polar Low at the East Greenland Ice Edge. *Mon. Wea. Rev*, 123: 5–15, 1995.

B. T. Draine and P. J. Flatau. Discrete-dipole approximation for scattering calculations. *Journal of the Optical Society of America A*, 11(4):1491, 1994.

M. Drusch and S. Crewell. Hydrological applications of remote sensing: Atmospheric states and fluxes: Water vapor and clouds (passive/active) techniques. In M. G. Anderson and J. J. McDonnell, editors, *Encyclopedia of Hydrological Sciences*, chapter 46, pages 266–290. John Wiley & Sons, Ltd, 2006.

C. Duncan. Baroclinic instability in a reverse shear flow. *Meteor. Mag.*, 107:17–23, 1978.

R. Eastman and S. G. Warren. Arctic cloud changes from surface and satellite observations. *Journal of Climate*, 23(15):4233–4242, 2010.

R. Eastman and S. G. Warren. A 39-yr survey of cloud changes from land stations worldwide 1971–2009: Long-term trends, relation to aerosols, and expansion of the tropical belt. *Journal of Climate*, 26(4):1286–1303, 2013.

L. Edel, J.-F. Rysman, C. Claud, C. Palerme, and C. Genthon. Potential of Passive Microwave around 183 GHz for Snowfall Detection in the Arctic. *Remote Sensing*, 11(19):2200, 2019.

W. Ellison. Dielectric properties of natural media. In Christian Mätzler, editor, *Thermal Microwave Radiation: Applications for Remote Sensing*, pages 427–506. The Institution of Engineering and Technology (IET), London, 2006.

K. Emanuel. An air-sea interaction theory for tropical cyclones, part1: Steady-state maintenance. *J. Atmos. Sci.*, 43:585–605, 1986.

K. Emanuel and R. Rotunno. Polar lows as Arctic hurricanes. *Tellus*, 41A:1–17, 1989.

R. J. Engelen and G. L. Stephens. Comparison between TOVS/HIRS and SSM/T-2 derived upper tropospheric humidity. *Bull. Am. Meteorol. Soc.*, 79(12):2748–2751, 1998.

P. Eriksson, S. A. Buehler, C. P. Davis, C. Emde, and O. Lemke. ARTS, the atmospheric radiative transfer simulator, version 2. *Journal of Quantitative Spectroscopy and Radiative Transfer*, 112(10):1551–1558, 2011.

P. Eriksson, M. Jamali, J. Mendrok, and S. A. Buehler. On the microwave optical properties of randomly oriented ice hydrometeors. *Atmospheric Measurement Techniques*, 8(5):1913–1933, 2015.

P. Eriksson, R. Ekelund, J. Mendrok, M. Brath, O. Lemke, and S. A. Buehler. A general database of hydrometeor single scattering properties at microwave and sub-millimetre wavelengths. *Earth System Science Data*, 10(3):1301–1326, 2018.

ESA. European space agency, Nimbus-7, a. `https://directory.eoportal.org/web/eoportal/satellite-missions/n/nimbus-7`, Last accessed on 2020-06-08.

ESA. Sharing earth observation resources - DMSP Block 5D-3 Satellite Series, b. `https://directory.eoportal.org/web/eoportal/satellite-missions/d/dmsp-block-5d`, Last accessed on 2020-06-08.

K. F. Evans and G. L. Stephens. Microwave radiative transfer through clouds composed of realistically shaped ice crystals. part II. remote sensing of ice clouds. *Journal of the Atmospheric Sciences*, 52(11):2058–2072, 1995.

J. R. Eyre. The information content of data from satellite sounding systems: A simulation study. *Quarterly Journal of the Royal Meteorological Society*, 116(492): 401–434, 1990.

V. Eyring, P. M. Cox, G. M. Flato, P. J. Gleckler, G. Abramowitz, P. Caldwell, W. D. Collins, B. K. Gier, A. D. Hall, F. M. Hoffman, G. C. Hurtt, A. Jahn, C. D. Jones, S. A. Klein, J. P. Krasting, L. Kwiatkowski, R. Lorenz, E. Maloney, G. A. Meehl, A. G. Pendergrass, R. Pincus, A. C. Ruane, J. L. Russell, B. M. Sanderson, B. D. Santer, S. C. Sherwood, I. R. Simpson, R. J. Stouffer, and M. S. Williamson. Taking climate model evaluation to the next level. *Nature Climate Change*, 9(2): 102–110, 2019.

T. Feck, J.-U. Grooß, and M. Riese. Sensitivity of arctic ozone loss to stratospheric h2o. *Geophysical Research Letters*, 35(1), 2008.

K. Fennig, M. Schröder, A. Andersson, and R. Hollmann. A fundamental climate data record of SMMR, SSM/i, and SSMIS brightness temperatures. 2019.

R. Ferraro and I. Moradi. The development of advanced microwave sounding unit-b (amsu-b) and microwave humidity sounder (mhs) fundamental climate data records (fcdr) for hydrological applications, c-atbd: Amsu-b/mhs brightness temperature. Number 01B-38b. American Geophysical Union, 2016.

R. Ferraro, F. Weng, N.C. Grody, L. Zhao, H. Meng, C. Kongoli, P. Pellegrino, S. Qiu, and C. Dean. NOAA operational hydrological products derived from the advanced microwave sounding unit. *IEEE Transactions on Geoscience and Remote Sensing*, 43(5):1036–1049, 2005.

R. Ferraro, B.n Nelson, T. Smith, and O. Prat. The AMSU-Based Hydrological Bundle Climate Data Record—Description and Comparison with Other Data Sets. *Remote Sensing*, 10(10):1640, 2018.

E. Fionda, M. Cadeddu, V. Mattioli, and R. Pacione. Intercomparison of integrated water vapor measurements at high latitudes from co-located and near-located instruments. *Remote Sensing*, 11(18), 2019.

J. V. Fiore and N. C. Grody. Classification of snow cover and precipitation using SSM/i measurements: case studies. *International Journal of Remote Sensing*, 13 (17):3349–3361, 1992.

C. Flamant. SSM/i integrated water vapor content measurements in coastal regions: A comparison with shipborne and airborne remote sensing measurements, radiosonde measurements, and NWP model retrievals. *Journal of Geophysical Research*, 108(C3), 2003.

G. Forbes and W. D. Lottes. Classification of mesoscale vortices in polar airstreams and the influence of the large-scale environment on their evolutions. *Tellus*, 37A: 132–155, 1985.

I. Føre, J. E. Kristjánsson, Ø. Seatra, Ø. Breivik, B. Røstig, and M. Shapiro. The full life cycle of a polar low over the Norwegian Sea observed by three research aircraft flights. *Q. J. R. Meteorol. Soc.*, 137:1659–1673, 2011.

J. A. Francis and S. J. Vavrus. Evidence linking arctic amplification to extreme weather in mid-latitudes. *Geophysical Research Letters*, 39(6), 2012.

R. Fu, A. D. Del Genio, and W. B. Rossow. Behavior of Deep Convective Clouds in the Tropical Pacific Deduced from ISCCP Radiance. *Journal of Climate*, 3: 1129–1152, 1990.

B. M. Funatsu, J.-F. Rysman, C. Claud, and J.-P. Chaboureau. Deep convective clouds distribution over the mediterranean region from AMSU-b/MHS observations. *Atmospheric Research*, 207:122–135, 2018.

Robert R. Gamache and Bastien Vispoel. On the temperature dependence of half-widths and line shifts for molecular transitions in the microwave and infrared regions. *Journal of Quantitative Spectroscopy and Radiative Transfer*, 217:440–452, 2018.

N. E. Gaut. Studies of atmospheric water vapor by means of microwave techniques. Number 02139. Massachusetts Institute of Technology, Reasearch laboratory of electronics, 1968.

R. Gelaro, W. McCarty, M. J. Suárez, R. Todling, A. Molod, L. Takacs, C. A. Randles, A. Darmenov, M. G. Bosilovich, R. Reichle, K. Wargan, L. Coy, R. Cullather, C. Draper, S. Akella, V. Buchard, A. Conaty, A. M. da Silva, W. Gu, G.-K. Kim, R. Koster, R. Lucchesi, D. Merkova, J. E. Nielsen, G. Partyka, S. Pawson, W. Putman, M. Rienecker, S. D. Schubert, M. Sienkiewicz, and B. Zhao. The modern-era retrospective analysis for research and applications, version 2 (MERRA-2). *Journal of Climate*, 30(14):5419–5454, 2017.

M. Gervais, J. Shaman, and Y. Kushnir. Impacts of the north atlantic warming hole in future climate projections: Mean atmospheric circulation and the north atlantic jet. *Journal of Climate*, 32(10):2673–2689, 2019.

A. Gettelman and S. C. Sherwood. Processes responsible for cloud feedback. *Current Climate Change Reports*, 2(4):179–189, 2016.

A. Gettelman, M. L. Salby, and F. Sassi. Distribution and influence of convection in the tropical tropopause region. *Journal of Geophysical Research: Atmospheres*, 107(D10):ACL 6–1–ACL 6–12, 2002.

J. Gil. Interpretation of the coherency matrix for three-dimensional polarization states. *Phys. Rev. A*, 90(4):043858, 2014.

N. P. Gillett, M. R. Allen, and K. D. Williams. Modelling the atmospheric response to doubled CO2 and depleted stratospheric ozone using a stratosphere-resolving coupled GCM. *Quarterly Journal of the Royal Meteorological Society*, 129(589): 947–966, 2003.

L. Gimeno, R. Nieto, M. VÃ¡zquez, and David A. Lavers. Atmospheric rivers: a mini-review. *Frontiers in Earth Science*, 2, 2014.

M. D. Goldberg, D. S. Rosby, and L. Zhou. The limb adjustment of amsu-a observations: Methodology and validation. *Journal of Applied Meterology*, 40:70–83, 2001.

T. Gong, S. B. Feldstein, and S. Lee. Rossby wave propagation from the arctic into the midlatitudes: Does it arise from in situ latent heating or a trans-arctic wave train? *Journal of Climate*, 33(9):3619–3633, 2020.

H. Goosse, J. E. Kay, K. C. Armour, A. Bodas-Salcedo, H. Chepfer, D. Docquier, A. Jonko, P. J. Kushner, O.r Lecomte, F. Massonnet, H. Park, F. Pithan, G. Svensson, and M. Vancoppenolle. Quantifying climate feedbacks in polar regions. *Nature Communications*, 9(1), 2018.

I. V. Gorodetskaya, M. Tsukernik, K. Claes, M. F. Ralph, W. D. Neff, and N. P. M. Van Lipzig. The role of atmospheric rivers in anomalous snow accumulation in east antarctica. *Geophysical Research Letters*, 41(17):6199–6206, 2014.

R. M. Graham, P. Itkin, A. Meyer, A. Sundfjord, G. Spreen, L. H. Smedsrud, G. E. Liston, B. Cheng, L. Cohen, D. Divine, I. Fer, A. Fransson, S. Gerland, J. Haapala, S. R. Hudson, A. M. Johansson, J. King, I. Merkouriadi, A. K. Peterson, C. Provost, A. Randelhoff, A. Rinke, A. Rösel, N. Sennéchael, V. P. Walden, P. Duarte, P. Assmy, H. Steen, and M. A. Granskog. Winter storms accelerate the demise of sea ice in the atlantic sector of the arctic ocean. *Scientific Reports*, 9(1), 2019.

J. Grandell and M. Hallikainen. Retrieval of snow and sea ice parameters from SSM/I data. In *Proceedings of IGARSS 94 - 1994 IEEE International Geoscience and Remote Sensing Symposium*. IEEE, 1994.

T. J. Greenwald and S. A. Christopher. ffect of cold clouds on satellite measurements near 183 ghz. *Geophys. Res*, 107, 2002.

T. J. Greenwald, R. Bennartz, M. Lebsock, and J. Teixeira. An uncertainty data set for passive microwave satellite observations of warm cloud liquid water path. *Journal of Geophysical Research: Atmospheres*, 123(7):3668–3687, 2018.

G. Grell, J. Dudhia, and D. Stauffer. A description of the fifth-generation penn state/NCAR Mesoscale Model (mm5). 1994.

B. Guan and D. E. Waliser. Detection of atmospheric rivers: Evaluation and application of an algorithm for global studies. *Journal of Geophysical Research: Atmospheres*, 120(24):12514–12535, 2015.

B. Guan and D. E. Waliser. Atmospheric rivers in 20 year weather and climate simulations: A multimodel, global evaluation. *Journal of Geophysical Research: Atmospheres*, 122(11):5556–5581, 2017.

T. J. Hall and T. H. Vonder Haar. The diurnal cycle of west pacific deep convection and its relation to the spatial and temporal variation of tropical mcss. *Journal of the Atmospheric Sciences*, 56:3402–3415, 1999.

I. Hans, M. Burgdorf, V. O. John, J. Mittaz, and S. A. Buehler. Noise performance of microwave humidity sounders over their lifetime. *Atmospheric Measurement Techniques*, 10(12):4927–4945, 2017.

E. Hansen, S. Gerland, M. A. Granskog, O. Pavlova, A. H. H. Renner, J. Haapala, T. B. Løyning, and M. Tschudi. Thinning of arctic sea ice observed in fram strait: 1990-2011. *Journal of Geophysical Research: Oceans*, 118(10):5202–5221, 2013.

J. E. Hansen and L. D. Travis. Light scattering in planetary atmosphere. *Space Science Reviews*, 16:527–610, 1974.

D. G. Harley. Frontal contour analysis of a "polar low". *Meteor. Mag.*, 89:146–147, 1960.

R. Chawn Harlow. Millimeter Microwave Emissivities and Effective Temperatures of Snow-Covered Surfaces: Evidence for Lambertian Surface Scattering. *IEEE Transactions on Geoscience and Remote Sensing*, 47(7):1957–1970, July 2009.

T. W. Harold and K. A. Browning. The polar low as a baroclinic disturbance. *Quart. J. Roy. Meteor. Soc.*, 95:710–723, 1969.

M. He, Y. Hu, N. Chen, D. Wang, J. Huang, and K. Stamnes. High cloud coverage over melted areas dominates the impact of clouds on the albedo feedback in the arctic. *Scientific Reports*, 9(1), 2019.

H. Hersbach, B. Bell, P. Berrisford, S. Hirahara, A. Horányi, J. Muñoz-Sabater, J. Nicolas, C. Peubey, R. Radu, D. Schepers, A. Simmons, C. Soci, S. Abdalla, X. Abellan, G. Balsamo, P. Bechtold, G. Biavati, J. Bidlot, M. Bonavita, G. Chiara, Per D., D. Dee, M. Diamantakis, R. Dragani, J. Flemming, R. Forbes, M. Fuentes, A. Geer, L. Haimberger, S. Healy, R. J. Hogan, E. Hólm, M. Janisková, S. Keeley, P. Laloyaux, P. Lopez, C. Lupu, G. Radnoti, P. Rosnay, I. Rozum, F. Vamborg, S. Villaume, and J.-N. Thépaut. The ERA5 global reanalysis. *Quarterly Journal of the Royal Meteorological Society*, 146(730):1999–2049, 2020.

T. J. Hewison and R. Saunders. Measurements of the amsu-b antenna pattern. *IEEE TRANSACTIONS ON GEOSCIENCE AND REMOTE SENSING*, 34(2):405–412, 1996.

A. J. Heymsfield and G. M. McFarquhar. High albedos of cirrus in the tropical pacific warm pool: Microphysical interpretations from CEPEX and from kwajalein, marshall islands. *Journal of the Atmospheric Sciences*, 53(17):2424–2451, 1996.

A. J. Heymsfield, C. Schmitt, and A. Bansemer. Ice Cloud Particle Size Distributions and Pressure-Dependent Terminal Velocities from In Situ Observations at Temperatures from 0° to -86° C. *Journal of the Atmospheric Sciences*, 70(12):4123–4154, 2013.

K. M. Hines and D. H. Bromwich. Development and Testing of Polar Weather Research and Forecasting (WRF) Model. Part I: Greenland Ice Sheet Meteorology$*. Monthly\ Weather\ Review, 136(6) : 1971 - -1989, 2008.$

N. Hirota, Y. N. Takayabu, M. Kato, and S. Arakane. Roles of an atmospheric river and a cutoff low in the extreme precipitation event in hiroshima on 19 august 2014. *Monthly Weather Review*, 144(3):1145–1160, 2016.

S.-P. Ho, L. Peng, C. Mears, and R. A. Anthes. Comparison of global observations and trends of total precipitable water derived from microwave radiometers and COSMIC radio occultation from 2006 to 2013. *Atmospheric Chemistry and Physics*, 18(1):259–274, 2018.

R. J. Hogan and C. D. Westbrook. Equation for the Microwave Backscatter Cross Section of Aggregate Snowflakes Using the Self-Similar Rayleigh–Gans Approximation. *Journal of the Atmospheric Sciences*, 71(9):3292–3301, 2014.

R. J. Hogan, R. Honeyager, J. Tyynelä, and S. Kneifel. Calculating the Millimetre –Wave Scattering Phase Function of Snowflakes Using the Self–Similar Rayleigh–Gans Approximation. *Quarterly Journal of the Royal Meteorological Society*, 143(703):834–844, 2017.

J. Hollinger, R. Lo, and G. Poe. Special Sensor Microwave/Imager User's Guide. Navel Research Laboratory, Washington, D.C., 1987.

G. Hong. Detection of tropical deep convective clouds from AMSU-b water vapor channels measurements. *Journal of Geophysical Research*, 110(D5), 2005.

G. Hong, P. Yang, Bryan A. B. A. Baum, Heymsfield, f. Weng, Q. Liu, G. Heygster, and S. A. Buehler. Scattering database in the millimeter and submillimeter wave range of 100-1000 GHz for nonspherical ice particles. *Journal of Geophysical Research Atmospheres*, 114(6):D06201, 2009.

R. E. Huffman and J. C. Larrabe. Effect of absorption by atomic oxygen and atomic nitrogen lines on upper atmosphere composition measurements. *Journal of Geophysical Research, Space Physics*, 73:23, 1968.

E. Jakobson and T. Vihma. Atmospheric moisture budget in the arctic based on the ERA-40 reanalysis. *International Journal of Climatology*, 30(14):2175–2194, 2009.

M. A. Janssen. Atmospheric remote sensing by microwave radiometry. In M. A. Janssen, editor, *Atmospheric Remote Sensing by Microwave Radiometry*, page 572. Wiley, New York, 1993. ISBN 0-471-62891-3.

J. H. Joseph, W. J. Wiscombe, and J. A. Weinman. The Delta-Eddington Approximation for Radiative Flux Transfer. *Journal of the Atmospheric Sciences*, 33: 2452–2459, 1976.

S.-Y. Jun, C.-H. Ho, J.-H. Jeong, Y.-S. Choi, and B.-M. Kim. Recent changes in winter arctic clouds and their relationships with sea ice and atmospheric conditions. *Tellus A: Dynamic Meteorology and Oceanography*, 68(1):29130, 2016.

J. S. Kain. he kain–fritsch convective parameterization: An update. *JOURNAL OF APPLIED METEOROLOGY*, 43:170–181, 2003.

J. S. Kain and J. M. Fritsch. A One-Dimensional Entraining/Detraining Plume Model and Its Application in Convective Parameterization. *Journal of the Atmospheric Sciences*, 47(23):2784–2802, 1990.

J. S. Kain and J. M. Fritsch. Convective Parameterization for Mesoscale Models: The Kain-Fritsch Scheme. In *The Representation of Cumulus Convection in Numerical Models*, chapter 4, pages 165–170. American Meteorological Society, 1993.

M.-L. Kapsch, R. G. Graversen, and M. Tjernström. Springtime atmospheric energy transport and the control of arctic summer sea-ice extent. *Nature Climate Change*, 3(8):744–748, 2013.

M.-L. Kapsch, N. Skific, R. G. Graversen, M. Tjernström, and J. A. Francis. Summers with low arctic sea ice linked to persistence of spring atmospheric circulation patterns. *Climate Dynamics*, 52(3-4):2497–2512, 2018.

F. Karbou, F. Rabier, and C. Prigent. The assimilation of observations from the advanced microwave sounding unit over sea ice in the french global numerical weather prediction system. *Monthly Weather Review*, 142(1):125–140, 2014.

U. Karstens, C. Simmer, and E. Ruprecht. Remote Sensing of Cloud Liquid Water. *Meteorol. Atmos. Phys*, 54:157–171, 1994.

J.r E. Kay, T. L'Ecuyer, H. Chepfer, N. Loeb, A. Morrison, and G. Cesana. Recent advances in arctic cloud and climate research. *Current Climate Change Reports*, 2 (4):159–169, 2016.

M. Kazumori, T. Egawa, and K. Yoshimoto. A retrieval algorithm of atmospheric water vapor and cloud liquid water for AMSR-E. *European Journal of Remote Sensing*, 45(1):63–74, 2012.

Christian Keil, Arnold Tafferner, and Thorsten Reinhardt. Synthetic satellite imagery in the lokal-modell. *Atmospheric Research*, 82(1-2):19–25, 2006.

M. G. Kendall. *Rank Correlation Methods.* Charles Griffin, London, 1975.

S. Kern and G. Heygster. Sea-ice concentration retrieval in the antarctic based on the SSM/I 85.5 GHz polarization. *Annals of Glaciology*, 33, 2001.

M.-J. Kim, J. A. Weinman, W. S. Olson, D.-E. Chang, G. Skofronick-Jackson, and J. R. Wang. A physical model to estimate snowfall over land using AMSU-b observations. *Journal of Geophysical Research*, 113(D9), 2008.

P. Kishore, S. P. Namboothiri, K. Igarashi, Jonathan H. Jiang, Chi O. Ao, and Larry J. Romans. Climatological characteristics of the tropopause parameters derived from GPS/CHAMP and GPS/SAC-c measurements. *Journal of Geophysical Research*, 111(D20), 2006.

S. Kneifel, U. Löhnert, A. Battaglia, S. Crewell, and D. Siebler. Snow scattering signals in ground-based passive microwave radiometer measurements. *Journal of Geophysical Research*, 115(D16), 2010.

E. M. Knudsen, Y. J. Orsolini, T. Furevik, and K. I. Hodges. Observed anomalous atmospheric patterns in summers of unusual arctic sea ice melt. *Journal of Geophysical Research: Atmospheres*, 120(7):2595–2611, 2015.

S. Kobayashi, Y. Ota, Y. Harada, A. Ebita, M. Moriya, H. Onoda, K. Onogi, H. Kamahori, C. Kobayashi, H. Endo, K. Miyaoka, and K. Takahashi. The JRA-55 reanalysis: General specifications and basic characteristics. *Journal of the Meteorological Society of Japan. Ser. II*, 93(1):5–48, 2015.

E. W. Kolstad. A new climatology of favourable conditions for reverse-shear polar lows. *Tellus*, 58A:344–354, 2006.

E. W. Kolstad, T. J. Bracegirdle, and I. A. Seierstad. Marine cold-air outbreaks in the north atlantic: temporal distribution and associations with large-scale atmospheric circulation. *Climate Dynamics*, 33(2-3):187–197, 2008.

K. K. Komatsu, V. A. Alexeev, I.A. Repina, and Y. Tachibana. Poleward upgliding siberian atmospheric rivers over sea ice heat up arctic upper air. *Scientific Reports*, 8(1), 2018.

A. Korolev, G. McFarquhar, P. R. Field, C. Franklin, P. Lawson, Z. Wang, E. Williams, S. J. Abel, D. Axisa, S. Borrmann, J. Crosier, J. Fugal, M. Krämer, U. Lohmann, O. Schlenczek, M. Schnaiter, and M. Wendisch. Mixed-phase clouds: Progress and challenges. *Meteorological Monographs*, 58:5.1–5.50, 2017.

C. Kummerow, W. S . Olson, , and L. Giglio. A simplified scheme for obtaining precipitation and vertical hvdrometeor profiles from passive microwave sensors. *IEEE Transactions on Geoscience and Remote Sensing*, 34(5), 1996.

K. Kunzi, P. Bauer, R. Eresmaa, P. E., S. B. Healy, A. Mugnai, N. Livesey, C. Prigent, E. A. Smith, and G. Stephens. Microwave absorption, emission and scattering: Trace gases and meteorological parameters. In *Physics of Earth and Space Environments*, chapter 4, pages 153–230. Springer Berlin Heidelberg, 2010.

Y.-H. Kuo. Comparison of GPS radio occultation soundings with radiosondes. *Geophysical Research Letters*, 32(5), 2005.

S. Kusunoki, R. Mizuta, and M. Hosaka. Future changes in precipitation intensity over the arctic projected by a global atmospheric model with a 60-km grid size. *Polar Science*, 9(3):277–292, 2015.

A. A. Lacis, J. E. Hansen, G. L. R., V. Oinas, and J. Jonas. The role of long-lived greenhouse gases as principal LW control knob that governs the global surface temperature for past and future climate change. *Tellus B: Chemical and Physical Meteorology*, 65(1):19734, 2013.

J. R. Lanzante and G. E. Ghars. The "Clear-Sky Bias" of TOVS Upper-Tropospheric HNumidity. *Journal of Climate*, 13:4034–4041, 2000.

D. A. Lavers and G. Villarini. The nexus between atmospheric rivers and extreme precipitation across europe. *Geophysical Research Letters*, 40(12):3259–3264, 2013.

D. A. Lavers, R. P. Allan, E. F. Wood, G. Villarini, D. J. Brayshaw, and A. J. Wade. Winter floods in britain are connected to atmospheric rivers. *Geophysical Research Letters*, 38(23), 2011.

D. A. Lavers, G. Villarini, R. P. Allan, E. F. Wood, and A. J. Wade. The detection of atmospheric rivers in atmospheric reanalyses and their links to british winter floods and the large-scale climatic circulation. *Journal of Geophysical Research: Atmospheres*, 117(D20), 2012.

Z. Li, J.-P. Muller, P. Cross, P. Albert, J. Fischer, and R. Bennartz. Assessment of the potential of MERIS near-infrared water vapour products to correct ASAR interferometric measurements. *International Journal of Remote Sensing.*

H. J. Liebe, G. A. Hufford, and M. G. Cotton. Propagation modeling of moist air and suspended Water/Ice particles at frequencies below 1000 GHz. *Atmospheric Propagation Effects through Natural and Man-Made Obscurants for Visible through MM-Wave Radiation*, 1993.

J. C. Liljegren, S. A. Boukabara, C.-P. Karen, and A. S. Cloug. The effect of the half-width of the 22-GHz water vapor line on retrievals of temperature and water vapor profiles with a 12-Channel microwave radiometer. *IEEE Transactions on Geoscience and Remote Sensing*, 43(5):1102–1108, 2005.

B. Lin, B. Wielicki, P. Minnis, and W. Rossow. Estimation of water cloud properties from satellite microwave, infrared and visible measurements in oceanic environments 1. microwave brightness temperature simulations. *Journal of Geophysical Research*, 103(D4):3873–3886, 1998.

B. Lin, B. A. Wielicki, P. Minnis, L. Chambers, K.-M. Xu, and Y. Hu. The Effect of Environmental Conditions on Tropical Deep Convective Systems Observed from the TRMM Satellite. *Journal of Climate*, 19:5749–5761, 2006.

S. Lind, R. B. I., and T. Furevik. Arctic warming hotspot in the northern Barents Sea linked to declining sea-ice import. *Nature Climate Change*, 8(7):634–639, 2018.

T. Linders, Ø.Sætra, and T.J. Bracegirdle. Limited polar lows sensitivity to sea-surface temperature. *Q. J. R. Meteorol. Soc.*, 137:58–69, 2011.

R. Lindstrot, R. Preusker, H. Diedrich, L. Doppler, R. Bennartz, and J. Fischer. 1d-var retrieval of daytime total columnar water vapour from MERIS measurements. *Atmospheric Measurement Techniques*, 5(3):631–646, 2012.

R. Lindstrot, M. Stengel, M. Schröder, J. Fischer, R. Preusker, N. Schneider, T. Steenbergen, and B. R. Bojkov. A global climatology of total columnar water vapour from SSM/i and MERIS. *Earth System Science Data*, 6(1):221–233, 2014.

F. Liu, S. Beirle, Q.Zhang, S. Dörner, K. He, and T. Wagner. NOx lifetimes and emissions of cities and power plants in polluted background estimated by satellite observations. *Atmospheric Chemistry and Physics*, 16(8):5283–5298, 2016.

G. Liu. A database of microwave single-scattering properties for nonspherical ice particles. *Bulletin of the American Meteorological Society*, 89(10):1563–1570, 2008.

G. Liu and E.-K. Seo. Detecting snowfall over land by satellite high-frequency microwave observations: The lack of scattering signature and a statistical approach. *Journal of Geophysical Research: Atmospheres*, 118:1376–1387, 2013.

Q. Liu, F. Weng, and S. J. English. An improved fast microwave water emissivity model. *IEEE Transactions on Geoscience and Remote Sensing*, 49(4):1238–1250, 2011.

D. J. Lockwood. *Rayleigh and Mie Scattering.* Springer, New York, 2016.

S. Manabe and R. Strickler. Thermal Equuilibrium of the Atmosphere with a Convcetive Adjustment. *Jounal of the Atmospheric Sciences*, 21:361–385, 1964.

S. Manabe and R. T. Wetherald. The Effects of Doublinf the CO_2 Concentration on the Climate of the General Circulation Model. *Jounal of the Atmospheric Sciences*, 32(1):3–15, 1975.

S. Manabe and E. Wetherlad. The Equilibrium of Atmosphere with a Given Distribution of Relative Humidity. *Journal of Atmospheric Science*, (3), 1967.

G. L. Manney. The remarkable 2003–2004 winter and other recent warm winters in the arctic stratosphere since the late 1990s. *Journal of Geophysical Research*, 110 (D4), 2005.

J. S Marshall and W. McK. Palmer. The distribution of raindrops with size. *Journal of Meteorology*, 5:165–166, 1948.

A. C. Maycock, K. P. Shine, and M. M. Joshi. The temperature response to stratospheric water vapour changes. *Quarterly Journal of the Royal Meteorological Society*, 137(657):1070–1082, 2011.

A. C. Maycock, M. M. Joshi, K. P. Shine, S. M. Davis, and K. H. Rosenlof. The potential impact of changes in lower stratospheric water vapour on stratospheric temperatures over the past 30 years. *Quarterly Journal of the Royal Meteorological Society*, 140(684):2176–2185, 2014.

A. C. Maycock, G. I. T. Masukwedza, P. Hitchcock, and I. R. Simpson. A regime perspective on the north atlantic eddy-driven jet response to sudden stratospheric warmings. *Journal of Climate*, 33(9):3901–3917, 2020.

J. C. McConnell and J. J. Jin. Stratospheric ozone chemistry. *Atmosphere-Ocean*, 46(1):69–92, 2008.

C. A. Mears, D. K. Smith, L. Ricciardulli, J. Wang, Hannah H., and F. J. Wentz. Construction and uncertainty estimation of a satellite-derived total precipitable water data record over the world's oceans. *Earth and Space Science*, 5(5):197–210, 2018.

M. Mech, M. Maahn, S. Kneifel, D. Ori, E. Orlandi, P. Kollias, V. Schemann, and S. Crewell. PAMTRA 1.0: A Passive and Active Microwave radiative TRAnsfer tool for simulating radiometer and radar measurements of the cloudy atmosphere. *Geoscientific Model Development*, 13(9):4229–4251, 2020.

C. Melsheimer and G. Heygster. Improved retrieval of total water vapor over polar regions from AMSU-B microwave radiometer data. *IEEE Transactions on Geoscience and Remote Sensing*, 46(8):2307–2322, 2008.

C. Melsheimer, T. Frost, and G. Heygster. Detectability of Polar Mesocyclones and Polar Lows in Data From Space-Borne Microwave Humidity Sounders. *IEEE Journal of Selected Topics in Applied Earth Observations and Remote Sensing*, 9 (1):326–335, 2016.

H. Meng, J. Dong, R. Ferraro, B. Yan, L. Zhao, C. Kongoli, N.-Y. Wang, and B. Zavodsky. A 1DVAR-based snowfall rate retrieval algorithm for passive microwave radiometers. *Journal of Geophysical Research: Atmospheres*, 122(12):6520–6540, 2017.

N. Metropolis. The beginning of the Monte Carlo Method. *Los Alamos Science*, Special Issue, 1987.

C. Michel, A. Terpstra, and T. Spengler. Polar Mesoscale Cyclone Climatology for the Nordic Seas Based on ERA-Interim. *Journal of Climate*, 31:2511–2532, 2018.

G. Mie. Beiträge zur optik trüber medien, speziell kolloidaler metallösungen. *Annalen der Physik*, 330(3):377–445, 1908.

S. Mieruch, M. Schröder, S. Noël, and J. Schulz. Comparison of decadal global water vapor changes derived from independent satellite time series. *J. Geophys. Res. Atmos.*, 12:489–499, 2014.

M. I. Mishchenko. Radiative transfer theory: from Maxwell's equations to practical applications. In B. A. van Tiggelen and S. E. Skipetrov, editors, *Wave Scattering in Complex Media: From Theory to Applications*, pages 367–414. Kluwer Academic Publishers, Dordrecht, The Netherlands, 2003.

M. I. Mishchenko, L. D. Travis, and D. W. Mackowski. T-matrix computations of light scattering by nonspherical particles: A review. *Journal of Quantitative Spectroscopy and Radiative Transfer*, 55(5):535–575, 1996.

Michael I. Mishchenko. Maxwell's equations, radiative transfer, and coherent backscattering: a general perspective. *J. Quant. Spectrosc. Radiat. Transfer*, 101 (3):540–555, 2006.

Michael I. Mishchenko, Li Liu, and Gorden Videen. Conditions of applicability of the single-scattering approximation. *Optics Express*, 15(12):7522, 2007.

C. Monckton, W. W.-H. Soon, D. R. Legates, and W. M. Briggs. Why models run hot: results from an irreducibly simple climate model. *Science Bulletin*, 60(1): 122–135, 2015.

M. T. Montgomery and B. Farrell. Polar low dynamics. *J. Atmos. Sci.*, 49:2482–2505, 1992.

S. A. Montzka, E. J. Dlugokencky, and J. H. Butler. Non-CO2 greenhouse gases and climate change. *Nature*, 476(7358), 2011.

G. W. K. Moore. Decadal variability and a recent amplification of the summer beaufort sea high. *Geophysical Research Letters*, 39(10), 2012.

I. Moradi, S. A. Buehler, V. O. John, and S. Eliasson. Comparing upper tropospheric humidity data from microwave satellite instruments and tropical radiosondes. *Journal of Geophysical Research: Atmospheres*, 115(D24), 2010.

I. Moradi, S. A. Buehler, V. O. John, A. Reale, and R. R. Ferraro. Evaluating instrumental inhomogeneities in global radiosonde upper tropospheric humidity data using microwave satellite data. *IEEE Transactions on Geoscience and Remote Sensing*, 51(6):3615–3624, 2013a.

I. Moradi, H. Meng, R. R. Ferraro, and S. Bilanow. Correcting Geolocation Errors for Microwave Instruments Aboard NOAA Satellites. *IEEE Transactions on Geoscience and Remote Sensing*, 51(6):3625–3637, 2013b.

I. Moradi, R. R. Ferraro, B. J. Soden, P. Eriksson, and P. Arkin. Retrieving layer-averaged tropospheric humidity from advanced technology microwave sounder water vapor channels. *IEEE Transactions on Geoscience and Remote Sensing*, 53 (12):6675–6688, 2015.

J. Morison, R. Kwok, C. Peralta-Ferriz, M. Alkire, I. Rigor, R. Andersen, and M. Steele. Changing arctic ocean freshwater pathways. *Nature*, 481:66–70, 2012.

G. V. Mota, S. Song, and K. Stępniak. Assessment of integrated water vapor estimates from the iGMAS and the brazilian network GNSS ground-based receivers in rio de janeiro. *Remote Sensing*, 11(22):2652, 2019.

T. Naakka, T. Nygård, and T. Vihma. Arctic humidity inversions: Climatology and processes. *Journal of Climate*, 31(10):3765–3787, 2018.

D. Nash, D. Waliser, B. Guan, H. Ye, and F. M. Ralph. The role of atmospheric rivers in extratropical and polar hydroclimate. *Journal of Geophysical Research: Atmospheres*, 123(13):6804–6821, 2018.

S. K. Nayar, K. lkeuchi, and T. Kanade. Determining shape and reflectance of lambertian, specular, and hybrid surfaces using extended sources. *International Workshop on Industrial Applications of Machine Intelligence and Vision*, 1989.

L. Nazarenko, G. A. Schmidt, R. L. Miller, N. Tausnev, M. Kelley, R. Ruedy, G. L. Russell, I. Aleinov, M. Bauer, S. Bauer, R. Bleck, V. Canuto, Y. Cheng, T. L. Clune, A. D. Del Genio, G. Faluvegi, J. E. Hansen, R. J. Healy, N. Y. Kiang, D. Koch, A. A. Lacis, A. N. LeGrande, J. Lerner, K. K. Lo, S. Menon, V. Oinas, J. Perlwitz, M. J. Puma, D. Rind, A. Romanou, M. Sato, D. T. Shindell, S. Sun, K. Tsigaridis, N. Unger, A. Voulgarakis, M.-S. Yao, and Jinlun Zhang. Future climate change under RCP emission scenarios with GISS ModelE2. *Journal of Advances in Modeling Earth Systems*, 7(1):244–267, 2015.

R. E. Newell, N. E. Newell, Y. Zhu, and C. Scott. Tropospheric rivers? - a pilot study. *Geophysical Research Letters*, 19(24):2401–2404, 1992.

M. Newman, G. N. Kiladis, K. M. Weickmann, F. M. Ralph, and P. D. Sardeshmukh. Relative contributions of synoptic and low-frequency eddies to time-mean atmospheric moisture transport, including the role of atmospheric rivers. *Journal of Climate*, 25(21):7341–7361, 2012.

P. A. Newman, E. R. Nash, and J. E. Rosenfield. What controls the temperature of the arctic stratosphere during the spring? *Journal of Geophysical Research: Atmospheres*, 106(D17):19999–20010, 2001.

E. S. Nielsen. pyresample Documentation/Release 1.16.0+5.gb84acad.dirty, 2020.

NOAA. Assessing the global climate in 2019. `https://www.ncei.noaa.gov/news/global-climate-201912`, 2019a. Last accessed: 05-08-2020.

NOAA. POES Operational Status. `https://www.ospo.noaa.gov/Operations/POES/status.html`, 2019b. Last accessed: 2020-05-08.

G. Noer and T. Lien. Dates and positions of polar lows over the Nordic seas between 2000 and 2010. page 16/2010. Tech. Rep. met.no report 16/2010, Norwegian Meteorological Institute, 2010. URL `https://www.met.no/publikasjoner/met-report/met-report-2010`.

G. Noer and M. Ovhed. Forecasting of polar lows in the Norwegian and Barents Sea - proc. of the 9th meeting of the EGS Polar Lows Working Grpup, cambridge, uk. 2003.

G. Noer, Ø. Saetra, T. Line, and Y. Gusdal. A climatological study of polar lows in the Nordic Seas. *Q. J. R. Meteorol. Soc.*, 137:1762–1772, 2011.

Y.-J. Noh, G. Liu, A. S. Jones, and T. H. Vonder Haar. Toward snowfall retrieval over land by combining satellite and in situ measurements. *Journal of Geophysical Research*, 114(D24), 2009.

H. Nowell, G. Liu, and R. Honeyager. Modeling the microwave single-scattering properties of aggregate snowflakes. *Journal of Geophysical Research Atmospheres*, 118(14):7873–7885, 2013.

T. Nygård, T. Valkonen, and T. Vihma. Characteristics of arctic low-tropospheric humidity inversions based on radio soundings. *Atmospheric Chemistry and Physics*, 14(4):1959–1971, 2014.

T. Nygård, R. G. Graversen, P. Uotila, T. Naakka, and T. Vihma. Strong dependence of wintertime arctic moisture and cloud distributions on atmospheric large-scale circulation. *Journal of Climate*, 32(24):8771–8790, 2019.

T. Nygård, T. Naakka, and T. Vihma. Horizontal moisture transport dominates the regional moistening patterns in the arctic. *Journal of Climate*, 33(16):6793–6807, 2020.

P. A. O'Gorman and C. J. Muller. How closely do changes in surface and column water vapor follow clausius–clapeyron scaling in climate change simulations? *Environmental Research Letters*, 5(2):025207, 2010.

Ø.Sætra, Y. Gusdal, S. Eastwood, J. Debernard, P. E. Isachesen, H. Schyberg, B. Furevik, and G. Noer. Sea Surface Temperature and Altimeter Synergy for Improved Forecasting of Polar Lows (STARS). page 49 pp. Scientific analysis plan (d3), Tech. Rep., Norwegian Meteorological Institute, 2010. URL http://polarlow.met.no/stars/.

OSCAR. Observing systems capability analysis and review tool. www.wmo-sat.info/oscar/satellites/view/321, Last accessed on 2020-06-08.

J. E. Overland and M. Wang. When will the summer arctic be nearly sea ice free? *Geophysical Research Letters*, 40(10):2097–2101, 2013.

P. Pall, L. M. Tallaksen, and F. Stordal. A climatology of rain-on-snow events for norway. *Journal of Climate*, 32(20):6995–7016, 2019.

M. Palm, C. Melsheimer, S. Nöel, S. Heise, J. Notholt, J. Burrowsand, and O. Schrems. Integrated water vapor above Ny-Ålesund, spitsbergen: a multi-sensor intercomparison. *Atmospheric Chemistry and Physics*, 10:1215–1226, 2010.

J. R. Pardo, J. Cernicharo, and E. Serabyn. Atmospheric Transmission at Microwaves (ATM): An Improved Model for millimetre/submillimeter Applications. *Earth System Science Data*, 49(12):1683–2694, 2001.

W. S. Parker. Reanalyses and observations: What's the difference? *Bulletin of the American Meteorological Society*, 97(9):1565–1572, 2016.

F.-J. W. Parmentier, T. R. Christensen, L. Lotte Sørensen, S. Rysgaard, A. D. McGuire, P. A. Miller, and D. A. Walker. The impact of lower sea-ice extent on arctic greenhouse-gas exchange. *Nature Climate Change*, 3(3):195–202, 2013.

A. E. Payne, M. F. Jansen, and T. W. Cronin. Conceptual model analysis of the influence of temperature feedbacks on polar amplification. *Geophysical Research Letters*, 42(21):9561–9570, 2015.

J. P. Peixoto and A. H. Oort. *Physics of Climate*. American Institute of Physics; 1st edition, New York, 1992. ISBN 10: 0883187124.

D. K. Perovich and J. A. Richter-Menge. Regional variability in sea ice melt in a changing arctic. *Philosophical Transactions of the Royal Society A: Mathematical, Physical and Engineering Sciences*, 373(2045):20140165, 2015.

D. K. Perovich, J. A. Richter-Menge, K. F. Jones, and B. Light. Sunlight, water, and ice: Extreme arctic sea ice melt during the summer of 2007. *Geophysical Research Letters*, 35(11), 2008.

C. Perro, G. Lesins, T. J. Duck, and M. Cadeddu. A microwave satellite water vapour column retrieval for polar winter conditions. *Atmospheric Measurement Techniques*, 9(5):2241–2252, 2016.

B. J. Peterson. Increasing river discharge to the arctic ocean. *Science*, 298(5601): 2171–2173, 2002.

V. Petoukhov and V.A. Semenov. A link between reduced barents-kara sea ice and cold winter extremes over northern continents. *Journal of Geophysical Research*, 115(D21), 2010.

G. W. Petty. *A First Course in Atmospheric Radiation*. Sundog Publishing, second edi edition, 2006. ISBN 978-0-9729033-1-8.

F. Pithan and T. Mauritsen. Arctic amplification dominated by temperature feedbacks in contemporary climate models. *Nature Geoscience*, 7(3):181–184, 2014.

F. Pithan, G. Svensson, R. Caballero, D. Chechin, T. W. Cronin, A. M. L. Ekman, R. Neggers, M. D. Shupe, A. Solomon, M. Tjernström, and M. Wendisch. Role of air-mass transformations in exchange between the arctic and mid-latitudes. *Nature Geoscience*, 11(11):805–812, 2018.

M. Planck. On the law of distribution of energy in the normal spectrum. *Annalen der Physik*, 4, 1901.

R. S. Plant, G. C. Craig, and S. L. Gray. On a threefold classification of extratropical cyclogenesis. *Quarterly Journal of the Royal Meteorological Society*, 129(594):2989–3012, 2003.

G. A. Poe, E. A. Uliana, B. A. Gardiner, T. E. von Rentzell, and D. B. Kunkee. Geolocation error analysis of the special sensor microwave imager/sounder. *IEEE Transactions on Geoscience and Remote Sensing*, 46(4):913–922, 2008.

L. M. Polvani, M. Previdi, M. R. England, G. Chiodo, and K. L. Smith. Substantial twentieth-century arctic warming caused by ozone-depleting substances. *Nature Climate Change*, 10(2):130–133, 2020.

M. J. Prather, C. D. Holmes, and J. Hsu. Reactive greenhouse gas scenarios: Systematic exploration of uncertainties and the role of atmospheric chemistry. *Geophysical Research Letters*, 39(9), 2012.

M. J. Prather, J. Hsu, N. M. DeLuca, C. H. Jackman, L. D. Oman, A. R. Douglass, E. L. Fleming, S. E. Strahan, S. D. Steenrod, O. A. Søvde, I. S. A. Isaksen, L. Froidevaux, and B. Funke. Measuring and modeling the lifetime of nitrous oxide including its variability. *Journal of Geophysical Research: Atmospheres*, 120 (11):5693–5705, 2015.

C. Prigent, F. Aires, D. Wang, S. Fox, and C. Harlow. Sea-surface emissivity parametrization from microwaves to millimetre waves. *Quarterly Journal of the Royal Meteorological Society*, 143(702):596–605, 2016.

E. Pruitt. The office of naval research and geography, 1979.

J. C. Quintanilla. Water, vibrational and rotational transitions. In *Encyclopedia of Astrobiology*, pages 1–4. Springer Berlin Heidelberg, 2014.

A. Radovan, S. Crewell, E. M. Knudsen, and A. Rinke. Environmental conditions for polar low formation and development over the nordic seas: study of january cases based on the arctic system reanalysis. *Tellus A: Dynamic Meteorology and Oceanography*, 71(1):1618131, 2019.

F. M. Ralph, P. J. Neiman, and A. A. Wick. Satellite and CALJET aircraft observations of atmospheric rivers over the eastern north pacific ocean during the winter of 1997/98. *Monthly Weather Review*, 132:1721–1745, 2004.

F. M. Ralph, J.J. Rutz, J. M. Cordeira, M. Dettinger, M. Anderson, D. Raynolds, L. J. Schick, and C. Smallcomb. A scale to characterize the strength and impacts of amtospheric rivers. *American Meteorological Society*, 2019.

A. M. Ramos, R. Nieto, R. Tomé, L. Gimeno, R. M. Trigo, M. L. R. Liberato, and D. A. Lavers. Atmospheric rivers moisture sources from a lagrangian perspective. *Earth System Dynamics*, 7(2):371–384, 2016.

R. Randriamampianina, H. Schyberg, and M. Mile. Observing system experiments with an arctic mesoscale numerical weather prediction model. *Remote Sensing*, 11 (8):981, 2019.

E. Rasmussen. The polar low as an extratropical CISK disturbance. *Quart. J. Roy. Meteor. Soc.*, 105:531–549, 1979.

E. A. Rasmussen and J. Turner. *Polar Lows.* Cambridge University Press, Cambridge, UK, 2003.

R. M. Rauber and A. Tokay. An explanation for the existence of supercooled water at the top of cold clouds. *Journal of the Atmospheric Sciences*, 48(8):1005–1023, 1991.

P. S. Ray. Broadband complex refractive indices of ice and water. *Applied Optics*, 11(8):1836, 1972.

A. H. H. Renner, S. Gerland, C. Haas, G. Spreen, J. F. Beckers, E. Hansen, M. Nicolaus, and H. Goodwin. Evidence of arctic sea ice thinning from direct observations. *Geophysical Research Letters*, 41(14):5029–5036, 2014.

M. Rex, R. J. Salawitch, H. Deckelmann, P. von der Gathen, N. R. P. Harris, M. P. Chipperfield, B. Naujokat, E. Reimer, M. Allaart, S. B. Andersen, R. Bevilacqua, G. O. Braathen, H. Claude, J. Davies, H. De Backer, H. Dier, V. Dorokhov, H. Fast, M. Gerding, S. Godin-Beekmann, K. Hoppel, B. Johnson, E. Kyrö, Z. Litynska, D. Moore, H. Nakane, M. C. Parrondo, A. D. Risley, P. Skrivankova, R. Stübi, P. Viatte, V. Yushkov, and C. Zerefos. Arctic winter 2005: Implications for stratospheric ozone loss and climate change. *Geophysical Research Letters*, 33(23), 2006.

M. Rigby, R. G. Prinn, S. O'Doherty, S. A. Montzka, A. McCulloch, C. M. Harth, J. Mühle, P. K. Salameh, R. F. Weiss, D. Young, P. G. Simmonds, B. D. Hall, G. S. Dutton, D. Nance, D. J. Mondeel, J. W. Elkins, P. B. Krummel, L. P. Steele, and P. J. Fraser. Re-evaluation of the lifetimes of the major CFCs and CH_3CCl_3 using atmospheric trends. *Atmospheric Chemistry and Physics*, 13(5):2691–2702, 2013.

A. Rinke, M. Maturilli, R. M. Graham, H. Matthes, D. Handorf, L. Cohen, S. R. Hudson, and J. C. Moore. Extreme cyclone events in the arctic: Wintertime variability and trends. *Environmental Research Letters*, 12(9):094006, 2017.

A. Rinke, B. Segger, S. Crewell, M. Maturilli, T. Naakka, T. Nygård, T. Vihma, F. Alshawaf, G. Dick, J. Wickert, and J. Keller. Trends of vertically integrated water vapor over the arctic during 1979–2016: Consistent moistening all over? *Journal of Climate*, 32(18):6097–6116, 2019.

C. D. Rodgers. Retrieval of atmospheric temperature and composition from remote measurements of thermal radiation. *Reviews of Geophysics*, 14(4):609, 1976.

C. D. Rodgers. *Inverse Methods for Atmospheric Sounding: Theory and Practice.* World Scientific Publishing, 2000.

W.G. Rodgers. *Physical Principles of Remote Sensing.* Cambridge University Press, New York, 2012.

E. Roeckner, U. Schlese, J. Biercamp, and P. Loewe. Cloud optical depth feedbacks and climate modelling. *Nature*, 329(6135):138–140, 1987.

P. W. Rosenkranz. Water vapor microwave continuum absorption: A comparison of measurements and models. *Radio Science*, 33(4):919–928, 1998.

P. W. Rosenkranz. A model for the complex dielectric constant of supercooled liquid water at microwave frequencies. *IEEE Transactions on Geoscience and Remote Sensing*, 53(3):1387–1393, 2015.

G. B. Rybicki and A. P. Lightman. In *Radiative Processes in Astrophysics*. WILEY-VCH Verlag GmbH and Co. KGaA, Weinheim, Germany, 2004. ISBN ISBN 978-0-471-82759-7.

J.-F. Rysman, C. Claud, and J. Delanoe. Monitoring deep convection and convective overshooting from 60° S to 60° N using MHS: A cloudsat/CALIPSO-based assessment. *IEEE Geoscience and Remote Sensing Letters*, 14(2):159–163, 2017.

S. Saha, S. Moorthi, H.-L. Pan, X. Wu, J. Wang, S. Nadiga, P. Tripp, R. Kistler, J. Woollen, D. Behringer, H. Liu, D. Stokes, R. Grumbine, G. Gayno, J. Wang, Y.-T. Hou, H. Chuang, H.-M. H. Juang, J. Sela, M. Iredell, R. Treadon, D. Kleist, P. Van Delst, D. Keyser, J. Derber, M. Ek, J. Meng, H. Wei, R. Yang, S. Lord, H. van den Dool, A. Kumar, W. Wang, C. Long, M. Chelliah, Y. Xue, B. Huang, J.-K. Schemm, W. Ebisuzaki, R. Lin, P. Xie, M. Chen, S. Zhou, W. Higgins, C.-Z. Zou, Q. Liu, Y. Chen, Y. Han, L. Cucurull, R. W. Reynolds, G. Rutledge, and M. Goldberg. The NCEP climate forecast system reanalysis. *Bulletin of the American Meteorological Society*, 91(8):1015–1058, 2010.

P. Sanò, G. Panegrossi, D. Casella, F. Di Paola, L. Milani, A. Mugnai, M. Petracca, and S. Dietrich. The passive microwave neural network precipitation retrieval (PNPR) algorithm for AMSU/MHS observations: description and application to european case studies. *Atmospheric Measurement Techniques*, 8(2):837–857, 2015.

L. F. Sapucci, D. L. Herdies, and R. W. B. Mendonça. The inclusion of IWV estimates from AIRS/AMSU and SSM/I sensors into the CPTEC/INPE global data assimilation system. *Monthly Weather Review*, 141(1):93–111, 2013.

J. M. Sardie and T. T. Warner. On the Mechanisms for the Development of Polar Lows. *J. Atmos. Sci.*, 40:869–881, 1983.

J. S. Sawyer. Man-made Carbon Dioxide and "Greenhouse" Effect. *Nature*, 1972.

R. C. Scarlat, C. Melsheimer, and G. Heygster. Retrieval of total water vapour in the arctic using microwave humidity sounders. *Atmospheric Measurement Techniques*, 11(4):2067–2084, 2018.

P. Schlüssel and M. Goldberg. Retrieval of atmospheric temperature and water vapour from iasi measurements. *Adv. Space Res.*, 29(11):1703–1706, 2002.

T. Schneider, K. Smith, P. O'Gorman, and C. Walker. A climatology of tropospheric zonal-mean water vapor fields and fluxes in isentropic coordinates. *Journal of Climate*, 19, 2006.

M. Schröder, M. Lockhoff, J. M. Forsythe, H. Q. Cronk, T. H. Vonder Haar, and R. Bennartz. The GEWEX water vapor assessment: Results from intercomparison, trend, and homogeneity analysis of total column water vapor. *Journal of Applied Meteorology and Climatology*, 55(7):1633–1649, 2016.

M. Schröder, M. Lockhoff, F. Fell, J. Forsythe, T. Trent, R. Bennartz, E. Borbas, M. G. Bosilovich, E. Castelli, H. Hersbach, M. Kachi, S. Kobayashi, E. R. Kursinski, D. Loyola, C. Mears, R. Preusker, W. B. Rossow, and S. Saha. The GEWEX water vapor assessment archive of water vapour products from satellite observations and reanalyses. *Earth System Science Data*, 10(2):1093–1117, 2018.

J. A. Schroeder and W. R. Westwater. Guide to microwave weighting function calculations, NOAA Technical Memorandum. Number ERL WPL-225. 1992.

J. Schulz, P. Schlussel, and H. Grassal. Water vapour in the atmospheric boundary layer over oceans from SSM/i measurements. *International Journal of Remote Sensing*, 14(15):2773–2789, 1993.

A. J. Schweiger. Changes in seasonal cloud cover over the arctic seas from satellite and surface observations. *Geophysical Research Letters*, 31(12), 2004.

J. A. Screen and I. Simmonds. The central role of diminishing sea ice in recent arctic temperature amplification. *Nature*, 464(7293):1334–1337, 2010.

J. A. Screen, I. Simmonds, and K. Keay. Dramatic interannual changes of perennial arctic sea ice linked to abnormal summer storm activity. *Journal of Geophysical Research*, 116(D15), 2011.

O. Seatra, T. Linders, and JB. Debernard. Can polar lows lead to a warming of the ocean surface? *Tellus*, 60:141–153, 2008.

A. Semenov, X. Zhang, A. Rinke, W. Dorn, and K. Dethloff. Arctic intense summer storms and their impacts on sea ice—a regional climate modeling study. *Atmosphere*, 10(4):218, 2019.

M. C. Serreze and A. P. Barrett. The summer cyclone maximum over the central arctic ocean. *Journal of Climate*, 21(5):1048–1065, 2008.

M. C. Serreze and J. A. Francis. The arctic amplification debate. *Climatic Change*, 76(3-4):241–264, 2006a.

M. C. Serreze and J. A. Francis. The arctic amplification debate. *Climate Change*, 76:241–264, 2006b.

M. C. Serreze and J. Stroeve. Arctic sea ice trends, variability and implications for seasonal ice forecasting. *Philosophical Transactions of the Royal Society A: Mathematical, Physical and Engineering Sciences*, 373(2045):20140159, 2015.

M.C. Serreze and R. G. Barry. Processes and impacts of arctic amplification: A research synthesis. *Global and Planetary Change*, 77(1-2):85–96, 2011.

M. A. Shapiro, L. S. Fedor, and T. Hampel. Research aircraft measurements of polar low over the Norwegain Sea. *Tellus*, 39A:272–306, 1987.

E. A. Sharkov. *Passive Microwave Remote Sensing of the Earth: Physical Foundations*. Springer, 2003.

D. Shindell and G.Faluvegi. Climate response to regional radiative forcing during the twentieth century. *Nature Geoscience*, 2(4):294–300, 2009.

M. D. Shupe, J. S. Daniel, G. de Boer, E. W. Eloranta, P. Kollias, C. N. Long, E. P. Luke, D. D. Turner, and J. Verlinde. A focus on mixed-phase clouds. *Bulletin of the American Meteorological Society*, 89(10):1549–1562, 2008.

N. Skliris, J. D. Zika, G. Nurser, S. A. Josey, and R. Marsh. Global water cycle amplifying at less than the clausius-clapeyron rate. *Scientific Reports*, 6(1), 2016.

J. Smirnova and P. Golubking. Comparing polar lows in atmospheric reanalyses: Arctic System Reanalysis versus ERA-Interim. *Mon. Wea. Rev.*, 145:2375–2383, 2017.

S. Solomon. Stratospheric ozone depletion: A review of concepts and history. *Reviews of Geophysics*, 37(3):275–316, 1999.

S. Solomon, K. H. Rosenlof, R. W. Portmann, J. S. Daniel, S. M. Davis, T. J. Sanford, and G.-K. Plattner. Contributions of stratospheric water vapor to decadal changes in the rate of global warming. *Science*, 327(5970):1219–1223, 2010.

M. F. Sterzik, S. Bagnulo, C. Emde, and M. Manev. The cloudbow of planet earth observed in polarisation. *Astronomy & Astrophysics*, 639:A89, 2020.

Bjorn Stevens and Sandrine Bony. Water in the atmosphere. *Physics Today*, 66(6): 29–34, 2013.

A. P. Stogryn. The Microwave Dielectric Properties of Sea and Fresh Water. Aerojet Internal Report 23, GenCorp Aerojet, Azusa, CA, 1995.

N. Stolarczyk, F. Thibault, H. Cybulski, H. Jóźwiak, G. Kowzan, B. Vispoel, I.E. Gordon, L.S. Rothman, R.R. Gamache, and P. Wcisło. Evaluation of different parameterizations of temperature dependences of the line-shape parameters based on ab initio calculations: Case study for the HITRAN database. *Journal of Quantitative Spectroscopy and Radiative Transfer*, 240:106676, 2020.

P. Stoll, R. G. Graversen, G. Noer, and K. Hodges. An objective global climatology of polar lows based on reanalysis data. *Quarterly Journal of the Royal Meteorological Society*, in press, 2018. URL `https://doi.org/10.1002/qj.3309`.

J. Stroeve and D. Notz. Changing state of arctic sea ice across all seasons. *Environmental Research Letters*, 13(10):103001, 2018.

W.-K. Tao and J. Simpson. Goddard cumulus ensemble model. part i: Model description. *Terrestrial, Atmospheric and Oceanic Sciences*, 4(1):035, 1993.

W.-K. Tao, J. Simpson, D. Baker, S. Braun, M.-D. Chou, B. Ferrier, D. Johnson, A. Khain, S. Lang, B. Lynn, C.-L. Shie, D. Starr, C.-H. Sui, Y. Wang, and P. Wetzel. Microphysics, radiation and surface processes in the goddard cumulus ensemble (GCE) model. *Meteorology and Atmospheric Physics*, 82(1-4):97–137, 2003.

M. Tedesco, J. Pulliainen, M. Takala, M. Hallikainen, and P. Pampaloni. Artificial neural network-based techniques for the retrieval of SWE and snow depth from SSM/i data. *Remote Sensing of Environment*, 90(1):76–85, 2004.

A. Terpstra, C. Michel, and T. Spengler. Forward and Reverse Shear Environments during Polar Low Genesis over the Northeast Atlantic. *Monthly Weather Review*, 144:1341–1354, 2016.

L. Thölix, L. Backman, R. Kivi, and A. Yu. Karpechko. Variability of water vapour in the arctic stratosphere. *Atmospheric Chemistry and Physics*, 16(7):4307–4321, 2016.

N. Tilinina, S.K. Gulev, and D. H. Bromwich. New view of Arctic cyclone activity from the Arctic system reanalysis. *J. Geophys. Res. Lett*, 41:1766–1772, 2014.

M. Tjernström, M. D. Shupe, I. M. Brooks, P. O. G. Persson, J. Prytherch, D. J. Salisbury, J. Sedlar, P. Achtert, B. J. Brooks, P. E. Johnston, G. Sotiropoulou, and D. Wolfe. Warm-air advection, air mass transformation and fog causes rapid ice melt. *Geophysical Research Letters*, 42(13):5594–5602, 2015.

M. Tjernström, M.D. Shupe, I. M. Brooks, P. Achtert, J. Prytherch, and J. Sedlar. Arctic summer airmass transformation, surface inversions, and the surface energy budget. *Journal of Climate*, 32(3):769–789, 2019.

K. B. Tokarska, M. B. Stolpe, S. Sippel, E. M. Fischer, C.J. Smith, F. Lehner, and R. Knut. Past warming trend constrains future warming in cmip6 models. *Science Advances, Climatology*, 6, 2020.

E. Di Tomaso, F. Romano, and V. Cuomo. Rainfall estimation from satellite passive microwave observations in the range 89 GHz to 190 GHz. *Journal of Geophysical Research*, 114(D18), 2009.

K. E. Trenberth, A. Dai, R. M. Rasmussen, and D. B. Parsons. The changing character of precipitation. *Bulletin of the American Meteorological Society*, 84(9): 1205–1218, 2003.

T. Trent, H. Boesch, P. Somkuti, and N. Scott. Observing water vapour in the planetary boundary layer from the short-wave infrared. *Remote Sensing*, 10(9): 1469, 2018.

G. Tselioudis, W. B. Rossow, and D. Rind. Global Patterns of Cloud Optical Thicness Variation with Temperature. *Journal of Climate*, 5:1484–1495, 1992.

D. D. Turner, M. P. Cadeddu, U. Lohnert, S. Crewell, and A.M. Vogelmann. Modifications to the water vapor continuum in the microwave suggested by ground-based 150-GHz observations. *IEEE Transactions on Geoscience and Remote Sensing*, 47 (10):3326–3337, 2009.

D. D. Turner, S. Kneifel, and M. P. Cadeddu. An improved liquid water absorption model at microwave frequencies for supercooled liquid water clouds. *Journal of Atmospheric and Oceanic Technology*, 33(1):33–44, 2016.

C. W. Ulbrich. Natural variations in the analytical form of the raindrop size distribution. *Journal of Climate and Applied Meteorology*, 22(10):1764–1775, 1983.

J. H. Van Vleck. The absorption of microwaves by uncondensed water vapor. *Physical Review*, 71(7):425–433, 1947a.

J. H. Van Vleck. The absorption of microwaves by oxygen. *Physical Review*, 71(7): 413–424, 1947b.

P. Vangasse, J. Charlton, and M. Jarrett. Characterisation of the advanced microwave sounding unit, amsu-b. *Adv. Space Res.*, 17(1):75–78, 1996.

J. Vaquero-Martínez, M. Antón, J. Pablo Ortiz de G., R. Román, and V. E. Cachorro. Water vapor radiative effects on short-wave radiation in spain. *Atmospheric Research*, 205:18–25, 2018.

M. Vázquez, I. Algarra, J. Eiras-Barca, A. M. Ramos, R. Nieto, and L. Gimeno. Atmospheric rivers over the arctic: Lagrangian characterisation of their moisture sources. *Water*, 11(1):41, 2018.

T. Vihma, J.Screen, M. Tjernström, B. Newton, X. Zhang, V. Popova, C. Deser, M. Holland, and T. Prowse. The atmospheric role in the arctic water cycle: A review on processes, past and future changes, and their impacts. *Journal of Geophysical Research: Biogeosciences*, 121(3):586–620, 2016.

D. Vila, R. Ferraro, and R. Joyce. Evaluation and improvement of AMSU precipitation retrievals. *Journal of Geophysical Research*, 112(D20), 2007.

K. Y. Vinnikov and N. C. Grody. Global warming trend of mean tropospheric temperature observed by satellites. *Science*, 302, 2003.

B. Vogel, T. Feck, and J.-U. Grooß. Impact of stratospheric water vapor enhancements caused by CH4and h2o increase on polar ozone loss. *Journal of Geophysical Research*, 116(D5), 2011.

D. Waliser and B. Guan. Extreme winds and precipitation during landfall of atmospheric rivers. *Nature Geoscience*, 10(3):179–183, 2017.

K. M. Walter, S. A. Zimov, J. P. Chanton, D. Verbyla, and F. S. Chapin. Methane bubbling from siberian thaw lakes as a positive feedback to climate warming. *Nature*, 443(7107):71–75, 2006.

D. Wang, C. Prigent, L. Kilic, S. Fox, C. Harlow, C. Jimenez, F. Aires, C. Grassotti, and F. Karbou. Surface emissivity at microwaves to millimeter waves over polar regions: Parameterization and evaluation with aircraft experiments. *Journal of Atmospheric and Oceanic Technology*, 34(5):1039–1059, 2017.

X. Wang and J. R. Key. Recent Trends in Arctic Surface, Cloud, and Radiation Properties from Space. *Science, Reports*, 299:1725–1728, 2003.

X. Wang and J. R. Key. Arctic Surface, Cloud, and Radiation Properties Based on the AVHRR Polar Pathfinder Dataset. Part I: Spatial and Temporal Characteristics. *Journal of Climate*, 18(14):2558–2574, 2005.

D. Weaver, K. Strong, K. A. Walker, C. Sioris, M. Schneider, C. T. McElroy, H. Vömel, M. Sommer, K. Weigel, A. Rozanov, J. P. Burrows, W. G. Read, E. Fishbein, and G.Stiller. Comparison of ground-based and satellite measurements of water vapour vertical profiles over ellesmere island, nunavut. *Atmospheric Measurement Techniques*, 12(7):4039–4063, 2019.

T.-K. Wee and Y.-H. Kuo. A perspective on the fundamental quality of GPS radio occultation data. *Atmospheric Measurement Techniques*, 8(10):4281–4294, 2015.

M. Wendisch, M. Brückner, J. Burrows, S. Crewell, K. Dethloff, K. Ebell, C.Lüpkes, A. Macke, J. Notholt, J. Quaas, A. Rinke, and I. Tegen. Understanding causes and effects of rapid warming in the arctic. *Eos*, 2017.

F. Weng and N. C. Grody. Retrieval of cloud liquid water using the special sensor microwave imager SSM/I. *JOURNAL OF GEOPHYSICAL RESEARCH*, 99(D12), 1992.

F. Weng, L. Zhao, R. R. Ferraro, G. Poe, X. Li, and N. C. Grody. Advanced microwave sounding unit cloud and precipitation algorithms. *Radio Science*, 38(4), 2003.

F. J. Wentz. User's Manual: SSM/I Antenna Temperature Tapes. Remote Sensing Systems, Inc., Santa Rosa, CA. RSS Technical Report 032588, 1991.

F. J. Wentz. Measurements of Oceanic Wind Vector Using Satellite Microwave Radiometers. *IEEE Transactions on Geoscience and Remote Sensing*, 30(5), 1992.

F. J. Wentz and R. W. Spencer. SSM/i rain retrievals within a unified all-weather ocean algorithm. *Journal of the Atmospheric Sciences*, 55(9):1613–1627, 1998.

E. R. Westwater, S.Crewell, C. Mätzler, and D. Cimini. Principles of surface-based microwave and millimeter wave radiometric remote sensing of the troposphere principles of surface-based microwave and millimeter wave radiometric remote sensing of the troposphere. *QUADERNI DELLA SOCIETÀ ITALIANA DI ELETTROMAGNETISMO*, 1(3), 2005.

B. A. Wilson, H. D. Bromwich, and K. M. Hines. Evaluation of Polar WRF forecasts on the Arctic System Reanalysis domain: Surface and upper air analysis. *J. Geophys. Res. Lett.*, 116:D11112, 2011.

B. A. Wilson, H. D. Bromwich, and K. M. Hines. Evaluation of polar WRF forecasts on the Arctic System Reanalysis Domain: 2. Atmospheric hydrologic cycle. *J. Geophys. Res. Lett.*, 117:D04107, 2012.

F. Winterstein and P. Jöckel. Methane chemistry in a nutshell - the new submodels CH4 (v1.0) and TRSYNC (v1.0) in MESSy (v2.54.0). jun 2020.

C. Woods and R. Caballero. The role of moist intrusions in winter arctic warming and sea ice decline. *Journal of Climate*, 29(12):4473–4485, 2016.

C. Woods, R. Caballero, and G. Svensson. Large-scale circulation associated with moisture intrusions into the arctic during winter. *Geophysical Research Letters*, 40 (17):4717–4721, 2013.

X. Xie, U. Löhnert, S. Kneifel, and S. Crewell. Snow particle orientation observed by ground-based microwave radiometry. *Journal of Geophysical Research: Atmospheres*, 117(D2), 2012.

E. V. Zabolotskikh. Contemporary Methods for Retrieving the Integrated Atmospheric Water-Vapor Content and the Total Cloud Liquid-Water Content. *Atmospheric and Oceanic Physics*, 53(3), 2017.

E. V. Zabolotskikh, I. A. Gurvich, and B. Chapron. New Areas of Polar Lows over the Arctic as a result of the Decrease in Sea Ice Extent. *Izvestiya, Atmospheric and Oceanic Physics*, 51:1021–1033, 2015.

M. Zahn and H. von Storch. A long term climatology of North Atlantic polar lows. *Geophys. Res. Lett.*, 35:L22702, 2008.

G. Zappa, L. Shaffrey, and K. Hodges. Can Polar Lows be Objectively Identified and Tracked in the ECMWF Operational Analysis and the ERA-Interim Reanalysis? *Monthly Weather Review*, 142:2596–2608, 2014.

J. Zhang, W. Tian, M. P. Chipperfield, F. Xie, and J. Huang. Persistent shift of the arctic polar vortex towards the eurasian continent in recent decades. *Nature Climate Change*, 6(12):1094–1099, 2016.

L. Zhao and F. Weng. Retrieval of ice cloud parameters using the advanced microwave sounding unit. *JOURNAL OF APPLIED METEOROLOGY*, 41:384–395, 2002.

Y. Zhu and R. E. Newell. A proposed algorithm for moisture fluxes from atmospheric rivers. *Monthly Weather Review*, 126(3):725–735, 1998.

Y. Zhu and R.E. Newell. Atmospheric rivers and bombs. *Geophysical Research Letters*, 21(18):1999–2002, 1994.

P. Zuidema and R. Joyce. Water vapor, cloud liquid water paths, and rain rates over northern high latitude open seas. *Journal of Geophysical Research: Atmospheres*, 113(D5), 2008.

Acknowledgments

I would like to thank my supervisors Prof. Susanne Crewell and Annete Rinke (AWI Potsdam) for their guidance, encouragement, advice and interest during the course of this research. I would also like to thank, Mario Mech and Erlend M. Knudsen for their help and valuable discussion throughout the process of writing my first publication and finishing my thesis. I gratefully acknowledge Mario's effort with explaining radiative transfer model PAMTRA and helping with other technical issues. I thank Marek Jacob for his help in programming and his patience whenever I had some question about it. I would like to thank Kerstin Ebell, Jan Chylik and Christoph Böhm for reading some of this thesis chapter drafts and their comments in helping to improve it.

I thank Gunnar Noer and Claud Chantal for their interest and discussion about polar lows dynamics. I thank Irina Gorodetskaya and Carolina Viceto for providing information on atmospheric rivers for polar low cases. I also thank Dave Bromwich and Shi Li for providing the ASRv2 data and answering my questions about its production.

I would like to express my gratitude for the funding by the Deutsche Forschungsgemeinschaft (DFG, German Research Foundation) – Projektnummer 268020496-TRR172, within the Transregional Collaborative Research Center "ArctiC Amplification: Climate Relevant Atmospheric and SurfaCe Processes, and Feedback Mechanisms (AC)^3 project under which work for this dissertation was performed.

I am grateful for having the opportunity to do aviation weather forecasting and research flight during Arctic CLoud Observations Using airborne measurements during polar Day (ACLOUD) campaign in Svalbard.

Big thank you goes to my uncles who were always there when I needed them.

Last but most important, I thank my beloved father for waking my interest in physics that led me to be an enthusiast in meteorology and for teaching me to never quit and always look for answers myself. I would express my deepest gratitude to my mother, my grandma and sisters for always being a support and source of prayers that are encouraging me.

Eigenständigkeitserklärung

Erklärung nach dem Wortlaut der Promotionsordnung der Mathematisch-Naturwisse--nschaftlichen Fakultät der Universität zu Köln vom 10. August 2020:

Hiermit versichere ich an Eides statt, dass ich die vorliegende Dissertation selbstständig und ohne die Benutzung anderer als der angegebenen Hilfsmittel und Literatur angefertigt habe. Alle Stellen, die wörtlich oder sinngemäß aus veröffentlichten und nicht veröffentlichten Werken dem Wortlaut oder dem Sinn nach entnommen wurden, sind als solche kenntlich gemacht. Ich versichere an Eides statt, dass diese Dissertation noch keiner anderen Fakultät oder Universität zur Prüfung vorgelegen hat; dass sie – abgesehen von unten angegebenen Teilpublikationen und eingebundenen Artikeln und Manuskripten – noch nicht veröffentlicht worden ist sowie, dass ich eine Veröffentlichung der Dissertation vor Abschluss der Promotion nicht ohne Genehmigung des Promotionsausschusses vornehmen werde. Die Bestimmungen dieser Ordnung sind mir bekannt. Darüber hinaus erkläre ich hiermit, dass ich die Ordnung zur Sicherung guter wissenschaftlicher Praxis und zum Umgang mit wissenschaftlichem Fehlverhalten der Universität zu Köln gelesen und sie bei der Durchführung der Dissertation zugrundeliegenden Arbeiten und der schriftlich verfassten Dissertation beachtet habe und verpflichte mich hiermit, die dort genannten Vorgaben bei allen wissenschaftlichen Tätigkeiten zu beachten und umzusetzen. Ich versichere, dass die eingereichte elektronische Fassung der eingereichten Druckfassung vollständig entspricht.

Datum	Ana Radovan